10-21-2024

Improving Ground-based Measurements and Understanding of Mineral Dust and Trace Elements in Ambient Particulate Matter on a Global Scale

Xuan Liu
Washington University – McKelvey School of Engineering

WASHINGTON UNIVERSITY IN ST. LOUIS

McKelvey School of Engineering
Department of Energy, Environmental and Chemical Engineering

Dissertation Examination Committee:
Randall Martin, Co-Chair
Jay Turner, Co-Chair
Rajan Chakrabarty
Jenny Hand
Jian Wang

Improving Ground-based Measurements and Understanding of Mineral Dust and Trace Elements in Ambient Particulate Matter on a Global Scale

by

Xuan Liu

A dissertation presented to
the McKelvey School of Engineering
of Washington University in
partial fulfillment of the
requirements for the degree
of Doctor of Philosophy

December 2024
St. Louis, Missouri

Table of Contents

List of Figures

List of Tables

Acknowledgments

First, I would like to express my greatest appreciation to my advisors, Dr. Jay Turner and Dr. Randall Martin, for their invaluable guidance, support, patience, and kindness. Their inspiration, trust, and generous feedback helped me grow in my academic pursuits by granting me freedom and fostering my confidence.

I extend my sincere thanks to my committee members, Dr. Rajan Chakrabarty, Dr. Jenny Hand, and Dr. Jian Wang, for their support and guidance throughout this process. I am especially grateful to Dr. Jenny Hand for her generous compliments and encouragement each time she attended my conference presentations.

I would also like to acknowledge my collaborators throughout my PhD research. Dr. Jenny Hand and Dr. Bret Schichtel provided valuable suggestions for Chapter 2. Collaborators at UC Davis Air Quality Research Center, including Dr. Nicole Hyslop, Jason Giacomo, and Dr. Ann Dillner, generously shared their expertise in elemental analysis and quality assurance for Chapter 3. Dr. Mansur Amonov contributed significantly to Chapter 4 by assisting with sample collection in Tashkent, Uzbekistan, and providing valuable insights. I am also grateful to him for hosting my visit to Uzbekistan. I thank Dr. Dhruv Mitroo for assisting with sample collection using his aerosol generation system for Chapter 5.

I would like to thank my colleagues in both the Turner group and the Martin group for creating a positive and supportive environment. Special thanks to Dr. Pradeep Prathibha and Jacob McNeill for their patience and encouragement while sharing their knowledge and skills on analytical instruments with me. I appreciate the support from both past and present members of the SPARTAN team, including Dr. Chris Oxford, Dr. Brenna Walsh, Emmie Le Roy, Yuxuan Ren,

Wenyu Liu, and Zilin Wei. A special note of thanks to Dr. Chris Oxford, whose guidance, meticulousness, patience, and sense of humor have made him not only an exceptional colleague but also a valued mentor.

I am also grateful to my friends at WashU for their kindness, support, and encouragement. Their friendship brought invaluable joy and companionship throughout this journey.

Lastly, I am thankful to my family for their love, support, and sacrifice. My deepest gratitude goes to my parents in China who wholeheartedly supported my academic pursuits abroad. I am also thankful to my partner, Siyuan Shen, who has been my constant source of support, celebrating my achievements and standing by me through challenges.

This work would not have been possible without all the wonderful people who supported me throughout this memorable journey.

Xuan Liu

Washington University in St. Louis

December 2024

ABSTRACT OF THE DISSERTATION

Improving Ground-based Measurements and Understanding of Mineral Dust and Trace Elements in Ambient Particulate Matter on a Global Scale

by

Xuan Liu

Doctor of Philosophy in Energy, Environmental and Chemical Engineering

Washington University in St. Louis, 2024

Professor Randall Martin, Co-Chair

Professor Jay Turner, Co-Chair

Mineral dust is a major component of ambient particulate matter (PM) globally, affecting visibility, air quality, human health, climate, and biogeochemistry. Dust mass cannot be directly measured and therefore is typically estimated using a dust equation to sum common oxides of major crustal elements based on measured elemental composition data. Both an accurate dust equation and reliable elemental data are essential to accurately estimate dust mass. However, most dust equations fail to account for all major dust compounds, exclude non-dust components of some elements, or account for regional variations in dust composition. Attenuation effects for light elements measured by the widely used X-ray fluorescence (XRF) technique can lead to underestimation of dust mass, yet correcting these effects in PM filter samples remains a significant challenge. Elemental characterization of PM also provides concentrations of trace elements, which can be strongly associated with morbidity and mortality. Ground-based monitoring of atmospheric elements is important to estimate the exposure to dust and trace elements, assess health risks, and investigate emission sources. However, many developing countries lack sufficient ground-based measurements of PM chemical composition. Uniform sampling protocols and reliable analyses are also needed to enable global comparisons.

This dissertation includes four studies aimed at improving measurements and understanding of mineral dust and trace elements in ambient PM. In the first study, a global-scale mineral dust equation with region-specific coefficients was developed and evaluated for various types of dust from different regions. The global equation reduced regional biases by about 6-10% for desert dust in source regions compared to an existing equation (IMPROVE) that was designed for the U.S. The second study presented the methodology and implications for the elemental characterization of ambient PM for a globally distributed monitoring network, the Surface PARTiculate mAtter Network (SPARTAN). Consistent protocols were applied to collect PM samples and analyze them at one central laboratory. Health risk assessment indicated significant airborne arsenic pollution at sites in South and Southeast Asia. The third study focused on characterizing dust contribution to PM in Central Asia, an understudied dust source region, using the first contemporary elemental composition data of PM samples collected from Tashkent, Uzbekistan. Large dust events originating from different deserts were identified by time series analysis, backward trajectory analysis, and satellite images. The fourth study assessed attenuation due to mass loading and particle size for light elements by comparing XRF and gravimetric measurements of samples with known compositions. Theoretical attenuation models were compared with measurements and applied to ambient PM samples to assess their impact on dust concentration estimates. These studies collectively advance the understanding of airborne mineral dust and trace elements and inform global air quality management.

Chapter 1: Introduction

1.1 Background

1.1.1 Mineral Dust Equation

Mineral dust is the most dominant global aerosol by mass (Knippertz & Stuut, 2014), which can strongly reduce visibility (e.g., Ashley et al., 2015; Hand et al., 2014, 2020; Kavouras et al., 2009), perturb climate systems (e.g., Miller & Tegen, 1998; Sokolik et al., 2001; Tegen, 2003), affect biogeochemistry (e.g., Jickells et al., 2005; Koren et al., 2006; Mahowald et al., 2010; Muhs et al., 2012), and cause adverse health effects (e.g., Goudie, 2014; Tong et al., 2017; Zhang et al., 2016). Also known as soil (Malm et al., 1994), geological minerals (Chow et al., 2015), and crustal material (Snider et al., 2016), mineral dust is commonly defined as airborne minerals originating from soil. It constitutes a major component of ambient particulate matter (PM), including $PM_{2.5}$ (aerodynamic diameter < 2.5 μm) and PM_{10} (aerodynamic diameter < 10 μm), and dominates the $PM_{10-2.5}$ fraction (aerodynamic diameter between 2.5 and 10 μm). Mineral dust has both natural (e.g., desert) and anthropogenic (e.g., roads, construction, and agricultural activities) sources.

The dust mass and therefore the dust fraction in PM cannot be measured directly because mineral dust is a complex mixture of many minerals, majorly quartz, feldspars, clays, calcite, and iron oxides (e.g., Nowak et al., 2018), and is often mixed with non-dust PM species that also contain crustal elements (e.g., Deboudt et al., 2010; Li et al., 2014). The practical and typical way to estimate dust mass is by applying a dust equation to sum oxides of major crustal elements by using measured elemental composition and assuming common oxide forms associated with dust. An accurate dust equation is essential to estimate the dust contribution to measured aerosols (e.g., Andrews et al., 2000; Chow et al., 2015; Malm et al., 1994; Snider et al., 2016), and to serve as a

reference to evaluate and improve atmospheric models (e.g., Appel et al., 2013; Kok et al., 2021; Zhang et al., 2013) and satellite remote sensing algorithms (e.g., Diner et al., 2018).

However, dust equations used in previous studies exhibit various sources of error. Most dust equations omit some important dust components such as carbonate. The calcite ($CaCO_3$) content of dust can exceed 20 weight percent (wt%) in some deserts such as the Sahara (e.g., Scheuvens et al., 2013) and the Middle East (e.g., Ahmady-Birgani et al., 2015; Awadh, 2012). Thus, neglecting carbonate when estimating dust mass for these areas can cause substantial errors. Some dust equations (Andrews et al., 2000; Hueglin et al., 2005; Pryor et al., 1997) include K or Mg directly into the equation without excluding the non-dust component of these elements such as K from biomass burning and Mg from sea salt, which will therefore overestimate dust K or Mg. The U.S. Interagency Monitoring of Protected Visual Environments (IMPROVE) network's "soil" formula (Soil = 2.20Al+2.49Si+1.63Ca+2.42Fe+1.94Ti) was developed to characterize mineral dust within the United States (Malm et al., 1994). Soil K is incorporated as a fraction (0.6) of Fe to avoid the influence of smoke K emitted by biomass burning (Eldred, 2003; Pachon et al., 2013). A correction factor of 1.16 is applied to all five elements to account for other missing compounds (mainly MgO, Na_2O, CO_2, and H_2O) based on the composition of average sediment (Eldred, 2003; Pettijohn, 1975). Although the IMPROVE equation is designed to address many of the challenges associated with dust characterization, Malm and Hand (2007) found that dust mass across the IMPROVE network may be underestimated by ~20%, suggesting that the IMPROVE equation needs further development. Some studies have applied the IMPROVE equation to natural or anthropogenic dust measured outside the US (e.g., Ho et al., 2003; Kim et al., 2001; Matawle et al., 2015; Pant et al., 2015; Shen et al., 2007; Wu et al., 2011), yet to our knowledge, none have

demonstrated its accuracy for that purpose. A more accurate dust equation is needed to estimate dust mass across different regions of the globe.

1.1.2 Attenuation Effects in X-ray Fluorescence Analysis

In addition to an accurate dust equation, reliable elemental composition data is essential for estimating dust mass, as elemental concentrations are directly used in the dust equation. Elemental characteristics (elemental ratios) are also commonly utilized to distinguish source areas of dust (Aldhaif et al., 2020; Cao et al., 2008; Hand et al., 2017; Scheuvens et al., 2013). A variety of techniques have been used for elemental analysis of PM samples, including both destructive and non-destructive techniques. Destructive techniques involve wet chemistry-based analytical methods that require digesting the sample into a liquid solution using acids, while non-destructive techniques do not require any digestion steps. The X-ray fluorescence (XRF) technique is widely used to characterize the elemental composition of PM samples collected on filters. Its non-destructive nature enhances analysis efficiency, reduces costs, enables additional speciation analysis, and avoids extraction efficiency issues compared to destructive techniques such as inductively coupled plasma mass spectrometry (ICP-MS). This advantage is particularly significant for large-scale monitoring networks (Liu et al., 2024; Solomon et al., 2014).

However, light elements are susceptible to attenuation effects in XRF analysis. Attenuation effects occur when part of the incoming X-rays and the fluorescent X-rays emitted by the target elements are absorbed by other components in the sample, resulting in a weaker detected signal than expected. Attenuation is more pronounced for light elements than for heavy elements because of the lower energy (“soft”) X-rays they emit. Light elements, particularly crustal elements like Si

and Al, are major elements in dust and are incorporated into the dust equation. Therefore, attenuation effects can lead to underestimation of dust mass and inaccuracies in elemental ratios.

The magnitude of attenuation in XRF analysis of PM filter samples depends on multiple factors, including mass loading, particle size, and chemical composition (Gutknecht et al., 2010). Greater attenuation is anticipated with high mass loading and large particles because of the increased path length of X-rays traveling through the deposit compared to low mass loading and small particles. High concentrations of heavy elements within the matrix can also contribute to increased attenuation. Attenuation resulting from particle penetration into the filter can be substantial for quartz fiber filters but is negligible for Teflon filters which are considered "surface filters" (Chiari et al., 2018).

Dzubay and Nelson (1974) established foundational theoretical models for estimating attenuation in PM filter samples. They utilized a homogeneous layer model for fine particles, assuming negligible attenuation within fine particles, and a particle size model for coarse particles, assuming these particles are collected as a monolayer on the filter. In the context of $PM_{2.5}$, Gutknecht et al. (2010) reviewed theoretical models developed to estimate attenuation and proposed using the particle size model for light elements (Na, Mg, Al, and Si) and the homogeneous layer model for heavier elements ($Z > 14$) in $PM_{2.5}$ based on Dzubay and Nelson's work as extended by Kellogg. Kellogg (2005) assumed that particles containing light elements are primarily at the high end of the $PM_{2.5}$ distribution and therefore used the particle size model to estimate attenuation for light elements in $PM_{2.5}$ by averaging the attenuations for potential mineral forms containing these elements. However, considering only attenuation due to particle size for light elements in $PM_{2.5}$

may be valid for filters with low mass loading where the monolayer assumption is applicable, but may not be suitable for filters with high dust loading such as those collected during dust events.

These models have not been thoroughly evaluated by experiments. Only a limited number of studies have applied experimental methods to estimate the attenuation effects of light elements for PM filter samples in XRF (Formenti et al., 2010; Turner & Brown, 2015), as well as in a similar technique, particle-induced X-ray emission (PIXE) (Calzolai et al., 2014; D'Alessandro et al., 2003; Maenhaut & Cafmeyer, 1998). Experimental assessments of the attenuation effects due to various factors and evaluations of these theoretical models are needed to better understand their impact on dust concentration estimates from XRF analysis of PM filter samples.

1.1.3 Ground-based Monitoring of Dust and Trace Elements

In addition to the major (crustal) elements used in dust estimation, the elemental characterization of PM also provides concentrations of trace elements. Trace elements are often concentrated in $PM_{2.5}$ and primarily emitted by anthropogenic sources such as fossil fuel combustion, industries, and traffic. Many of the trace elements (e.g., Pb, As, Cd, Cr) have strong associations with morbidity and mortality (Krall et al., 2017; Paithankar et al., 2021). Concentrations of hazardous trace elements are particularly high in low-income and middle-income countries (LMICs) because of unregulated activities during urbanization and industrialization (Fuller et al., 2022; Majumder et al., 2021; Zhu et al., 2020). Ground-level observations of atmospheric elements are important to estimate the exposure to dust and trace elements, assess health risks, and investigate emission sources, as well as improve atmospheric models. However, few monitoring networks of PM chemical composition exist in LMICs. Uniform sampling protocols and reliable analyses are also needed to enable comparisons across the world.

The Surface PARTiculate mAtter Network (SPARTAN, https://www.spartan-network.org/) is a long-term project that measures ground-based speciated PM at globally dispersed sites in densely populated regions (Snider et al., 2015). This network is designed to expand available global ground-based observations of PM composition and to provide information to evaluate and improve satellite-based estimates of $PM_{2.5}$. To our knowledge, SPARTAN is the only global monitoring network that measures the elemental composition of $PM_{2.5}$ and to a lesser extent, PM_{10}. Samples are collected from SPARTAN sites and analyzed for elemental composition at one central laboratory using consistent protocols, which ensures the comparability of data among the different sites. Beginning in 2019, the elemental measurements of SPARTAN samples have been conducted by energy-dispersive X-ray fluorescence (ED-XRF) spectroscopy, which is also used in the U.S. national $PM_{2.5}$ Chemical Speciation Network (CSN) and the U.S. IMPROVE network (Solomon et al., 2014). Prior analysis of SPARTAN filters for 2013−2019 identified large global variations in measured airborne metal concentrations, but this analysis used inductively coupled plasma mass spectrometry (ICP-MS) with nitric acid digestion that introduced uncertainty in extraction efficiencies for some crustal elements such as Fe and Al and could not measure Si (McNeill et al., 2020). There is a need to examine more recent filters using XRF to assess the robustness of prior conclusions and their degree of persistence over time.

Especially for networks that operate over long periods across multiple sites, high-quality and consistent data is needed to interpret the measurements (Solomon et al., 2014). Robust quality assurance (QA) measures are needed including appropriate calibration, filter acceptance testing, routine analyses of blanks and standards, and appropriate blank subtraction to obtain reliable elemental data. Method detection limits (MDLs) and uncertainties for elemental concentrations

are needed to evaluate the data quality. These QA measures must be developed, and MDLs and uncertainties should be estimated for XRF analysis in the SPARTAN network.

As a region not covered by the SPARTAN network, Central Asia has remained understudied concerning $PM_{2.5}$ concentration and chemical composition, despite experiencing severe air pollution (Amonov & Nishonov, 2020; Kerimray et al., 2020; Miller-Schulze et al., 2015; Tursumbayeva et al., 2023). Air pollution caused by dust storms is common in Central Asia, which is a major global dust source region with several large deserts, including the Kyzylkum Desert, the Karakum Desert, and the Aralkum Desert (Shen et al., 2016; Zhang et al., 2020). Aralkum, the desiccated lakebed of the former Aral Sea, generates salt dust containing pesticides and other chemicals, which adversely affects the environment and human health in the region (Breckle et al., 2012; Indoitu et al., 2015; Shen et al., 2019; Singer et al., 2003). Dust events occur frequently in Central Asia during spring, summer, and fall, with reduced frequency in winter (Zhang et al., 2020). Some studies have investigated dust deposition (Bazarbayev et al., 2022; Groll et al., 2013; Opp et al., 2017) and dust optical depth in Central Asia (Hofer et al., 2017; L. Li & Sokolik, 2018; Xi & Sokolik, 2015). However, few studies have conducted ground measurements of PM composition to quantify dust contributions to PM in this region (Miller-Schulze et al., 2015).

Uzbekistan, situated at the center of Central Asia, primarily relies on natural gas for power generation and heating, yet faces persistent air pollution challenges (Tursumbayeva et al., 2023). Given the frequent dust storms (Broomandi et al., 2023; Nishonov et al., 2023), dust is anticipated to be a major component of PM in Uzbekistan, but it has not been quantified. A previous long-term monitoring campaign at two urban sites during the summer and fall of 2008–2009 quantified the contributions of inorganic ions, elemental carbon, and organic carbon to PM in Uzbekistan

(Amonov et al., 2010). However, the contemporary composition and emission sources of PM in Uzbekistan remain unexplored.

1.2 Objectives

Given the significant environmental and health impacts of mineral dust and trace elements, this dissertation aims to improve their ground-based measurements and understanding by developing a global-scale mineral dust equation, assessing attenuation effects in XRF, and exploring implications of elemental measurements from a global monitoring network as well as from field campaigns in Central Asia. This dissertation presents four studies:

Chapter 2: *A Global-scale Mineral Dust Equation*

I developed a global-scale dust equation that builds upon the IMPROVE "soil" formula using analyses of the elemental composition and carbonate content of desert dust in different regions compared with that of continental crust. I evaluated the global equation for desert dust over source and non-source regions, dust in the U.S. IMPROVE monitoring network, and major types of anthropogenic dust.

Chapter 3: *Elemental Characterization of Ambient Particulate Matter for a Globally Distributed Monitoring Network: Methodology and Implications*

I improved QA methods and estimated MDLs and uncertainties for the elemental characterization of ambient PM in the SPARTAN network using XRF. I explored the implications of the global PM elemental dataset measured by XRF by examining the concentration levels of dust and trace element oxides across globally distributed sites,

evaluating health risks caused by hazardous trace elements, and exploring emission sources of trace elements at the site with the highest estimated health risk levels.

Chapter 4: *Characterizing Particulate Matter Composition in Central Asia: Dust Contribution in Tashkent, Uzbekistan*

I analyzed the elemental composition of the first contemporary $PM_{2.5}$ and PM_{10} filter samples collected from Tashkent, the capital of Uzbekistan, during dusty seasons in 2023. I estimated dust concentration levels to understand its contribution to $PM_{2.5}$, PM_{10}, and coarse PM ($PM_{10-2.5}$). I identified large dust events, investigated their source areas and elemental characteristics, and explored potential emission sources of major and trace elements in addition to dust.

Chapter 5: *Assessing Attenuation Effects in X-ray Fluorescence Analysis of Light Elements in Mineral Dust*

I assessed attenuation effects due to mass loading, particle size, and chemical composition for Si and Al by comparing XRF measurements with gravimetric data of samples generated using powder oxides and Arizona test dust (ATD). I compared the experimental results to estimates derived from the homogeneous layer and particle size models. I evaluated the potential impact of attenuation effects on dust concentration estimates for ambient dust-dominated $PM_{2.5}$ samples collected from SPARTAN.

Each chapter provides conclusions and recommendations for future work related to its specific study. Chapter 6 summarizes the key contributions of these studies.

Chapter 2: A Global-scale Mineral Dust Equation

This work was funded by the National Science Foundation (Grant 2020673), the Clean Air Fund, and internal funds at Washington University in St. Louis. This chapter has been published as: Liu, X., Turner, J. R., Hand, J. L., Schichtel, B. A., & Martin, R. V. (2022). A Global-Scale Mineral Dust Equation. Journal of Geophysical Research: Atmospheres, 127(18), e2022JD036937. https://doi.org/10.1029/2022JD036937.

2.1 Abstract

A robust method to estimate mineral dust mass in ambient particulate matter (PM) is essential, as the dust fraction cannot be directly measured but is needed to understand dust impacts on the environment and human health. In this study, a global-scale dust equation is developed that builds on the widely used Interagency Monitoring of Protected Visual Environments (IMPROVE) network's "soil" formula that is based on five measured elements (Al, Si, Ca, Fe, and Ti). We incorporate K, Mg, and Na into the equation using the mineral-to-aluminum (MAL) mass ratio of $(K_2O+MgO+Na_2O)/Al_2O_3$ and apply a correction factor (CF) to account for other missing compounds. We obtain region-specific MAL ratios and CFs by investigating the variation in dust composition across desert regions. To calculate reference dust mass for equation evaluation, we use total-mineral-mass (summing all oxides of crustal elements) and residual-mass (subtracting non-dust species from total PM) approaches. For desert dust in source regions, the normalized mean bias (NMB) of the global equation (within ±1%) is significantly smaller than the NMB of the IMPROVE equation (-6 to 10%). For $PM_{2.5}$ with high dust content measured by the IMPROVE network, the global equation estimates dust mass well (NMB within ±5%) at most sites. For desert dust transported to non-source regions, the global equation still performs well (NMB within ±2%).

The global equation can also represent paved road, unpaved road, and agricultural soil dust (NMB within ±5%). This global equation provides a promising approach for calculating dust mass based on elemental analysis of dust.

2.2 Introduction

Mineral dust, also referred to as soil (Malm et al., 1994), geological minerals (Chow et al., 2015), and crustal material (Snider et al., 2016), is commonly defined as airborne minerals originating from soil, and is a major component of ambient particulate matter (PM) including $PM_{2.5}$ (aerodynamic diameter < 2.5 μm) and PM_{10} (aerodynamic diameter < 10 μm). Mineral dust has both natural (e.g., desert) and anthropogenic (e.g., agricultural soil, roads, and industry) sources, affecting visibility (e.g., Ashley et al., 2015; Hand et al., 2014, 2020; Kavouras et al., 2009), human health (e.g., Goudie, 2014; Tong et al., 2017; Zhang et al., 2016), the climate system (e.g., Miller & Tegen, 1998; Sokolik et al., 2001; Tegen, 2003), and biogeochemistry (e.g., Jickells et al., 2005; Koren et al., 2006; Mahowald et al., 2010; Muhs et al., 2012). The dust mass and therefore the dust fraction in PM cannot be measured directly because mineral dust is a complex mixture of many minerals, majorly quartz, feldspars, clays, calcite, and iron oxides (e.g., Nowak et al., 2018), and is often mixed with non-dust PM species that also contain crustal elements (e.g., Deboudt et al., 2010; Li et al., 2014). The practical and typical way to estimate dust mass is by applying a dust equation to sum oxides of major crustal elements by using measured elemental composition and assuming common oxide forms associated with dust. An accurate dust equation is essential to estimate the dust contribution to measured aerosols (e.g., Andrews et al., 2000; Chow et al., 2015; Malm et al., 1994; Snider et al., 2016), and to serve as a reference to evaluate and improve atmospheric models (e.g., Appel et al., 2013; Kok et al., 2021; Zhang et al., 2013) and satellite remote sensing algorithms (e.g., Diner et al., 2018).

Table 2.1 summarizes dust equations used in previous studies and various sources of error. Most dust equations omit some important dust components such as carbonate. The calcite ($CaCO_3$) content of dust can exceed 20 weight percent (wt%) in some deserts such as the Sahara (e.g., Scheuvens et al., 2013) and the Middle East (e.g., Ahmady-Birgani et al., 2015; Awadh, 2012). Thus, neglecting carbonate when estimating dust mass for these areas can cause substantial errors. Some dust equations (Andrews et al., 2000; Hueglin et al., 2005; Pryor et al., 1997) include K or Mg directly into the equation without excluding the non-dust component of these elements such as K from biomass burning and Mg from sea salt, which will therefore overestimate dust K or Mg. The U.S. Interagency Monitoring of Protected Visual Environments (IMPROVE) network's "soil" formula (Soil = 2.20Al+2.49Si+1.63Ca+2.42Fe+1.94Ti) was developed to characterize mineral dust within the United States (Malm et al., 1994), but is used worldwide. The IMPROVE equation assumes that iron is split equally between Fe_2O_3 and FeO in soil according to their abundance in most rock types (Eldred, 2003). Soil K is incorporated as a fraction (0.6) of Fe to avoid the influence of smoke K emitted by biomass burning (Eldred, 2003; Pachon et al., 2013). A correction factor of 1.16 is applied to all five elements to account for other missing compounds (mainly MgO, Na_2O, CO_2, and H_2O) based on the composition of average sediment (Eldred, 2003; Pettijohn, 1975). Across the IMPROVE network, the elemental composition of $PM_{2.5}$ samples is measured using X-ray fluorescence (XRF) and the above equation is applied to estimate soil (dust) mass. Although the IMPROVE equation is designed to address many of the challenges associated with dust characterization, Malm and Hand (2007) found that dust mass across the IMPROVE network may be underestimated by ~20%, suggesting that the IMPROVE equation needs further development.

Table 2.1 Summary of dust equations used in previous studies

Reference	Dust Equation	Sources of Error
(Macias & Hopke, 1981)	1.89Al+2.14Si+1.4Ca+1.43Fe+1.2K	Missing carbonate, oxides of Na, Mg, Ti, etc.; K susceptible to biomass burning
(Chow et al., 1994; Solomon et al., 1989)	1.89Al+2.14Si+1.4Ca+1.43Fe	Missing carbonate, oxides of Na, Mg, K, Ti, etc.
(Malm et al., 1994)	[1.89Al+2.14Si+1.40Ca+(1.36+0.6×1.20)Fe+1.67Ti]×1.16 = 2.20Al+2.49Si+1.63Ca+2.42Fe+1.94Ti (**IMPROVE**)	Accuracy of the correction factor for missing compounds; Developed for the U.S.
(Pryor et al., 1997)	2.2Al+2.49Si+1.63Ca+1.5Fe+1.4K+1.94Ti	Accuracy of the correction factor for missing compounds; K susceptible to biomass burning
(Andrews et al., 2000; Kleindienst et al., 2010)	1.89Al+2.14Si+1.4Ca+1.43Fe+1.67Ti+1.2K	Missing carbonate, oxides of Na, Mg, etc.; K susceptible to biomass burning
(Hueglin et al., 2005)	1.89Al+2.14Si+1.40Ca+1.43Fe+1.21K+1.66Mg	Missing carbonate, oxides of Na, Ti, etc.; K susceptible to biomass burning; Mg susceptible to sea salt
(Terzi et al., 2010)	1.89Al+2.14Si+1.95Ca+1.43Fe+1.67Ti+1.2K+1.66Mg	Missing carbonate, oxides of Na, etc.; K susceptible to biomass burning; Mg susceptible to sea salt
(Ni et al., 2013)	1.89Al+2.14Si+1.40Ca+1.43Fe+1.67Ti+1.21K+1.66Mg	Missing carbonate, oxides of Na, etc.; K susceptible to biomass burning; Mg susceptible to sea salt

Several issues need to be addressed to further develop the IMPROVE equation for mineral dust on a global scale. First, the relationship between soil K and Fe may change in regions outside the US or even within the US because of the variation in dust composition (e.g., Journet et al., 2014). Second, although using Fe as a surrogate for soil K works well for natural dust at IMPROVE sites, for anthropogenic dust in urban areas, Al or Si should be a better choice than Fe given that the Fe concentration is more likely affected by non-dust sources such as combustion (e.g., Chen et al., 2012). Third, the fraction of missing compounds in dust may also differ inside or outside the US. Fourth, the data of average sediment (Pettijohn, 1975) used to derive the factor of 1.16 might not

represent natural dust composition which is usually represented using the data of continental crust from other sources (e.g., Cao et al., 2008; Choi et al., 2001; Contini et al., 2010; Ganor et al., 1991; Gao et al., 2018; Radhi et al., 2010a). Fifth, liquid water (different from crystal water) associated with special types of dust can be non-negligible. Dust is commonly assumed to be non-hygroscopic, but high hygroscopicity has been observed for saline dust in some regions (e.g., Gaston, 2020; Gaston et al., 2017; Koehler et al., 2007; Tang et al., 2019), some types of aged dust (e.g., Sullivan et al., 2009; Tang et al., 2016), and some types of anthropogenic dust (e.g., Peng et al., 2020). Sixth, special types of dust such as saline dust (e.g., Gaston et al., 2017), volcanic dust (e.g., Gislason et al., 2011; Taylor & Lichte, 1980), and aged dust (e.g., Tang et al., 2016) may contain salt minerals that are not considered for common desert dust. Some studies have applied the IMPROVE equation to natural or anthropogenic dust measured outside the US (e.g., Ho et al., 2003; Kim et al., 2001; Matawle et al., 2015; Pant et al., 2015; Shen et al., 2007; Wu et al., 2011), yet to our knowledge, none have demonstrated its accuracy for that purpose. The development of a global-scale dust equation should address the issues discussed above and assess its performance both within and outside the US.

In this study, we develop a global-scale dust equation that builds upon the IMPROVE "soil" formula using analyses of the elemental composition and carbonate content of desert dust in different regions compared with that of continental crust. The global equation is evaluated for desert dust over source/non-source regions, dust in the U.S. IMPROVE monitoring network, and major types of anthropogenic dust. The performance of the IMPROVE equation is treated as a well-respected benchmark to evaluate the global equation. The goal of this study is to develop a global dust equation with regional parameterization that reduces the regional bias in dust mass estimated using measured elemental data. The reduced bias is especially important to PM mass

closure (e.g., Ni et al., 2013; Terzi et al., 2010) and model evaluation (e.g., Appel et al., 2013; Meng et al., 2021; Zhang et al., 2013).

2.3 Data and Methods

2.3.1 Development of the Global Dust Equation

The five major crustal elements (Al, Si, Ca, Fe, and Ti) of the IMPROVE equation were used in the global equation assuming common oxide forms of Al_2O_3, SiO_2, CaO, FeO and Fe_2O_3 (in equal amounts), and TiO_2, respectively. However, in contrast to the use of Fe in the IMPROVE equation to estimate soil K, Al was investigated as the new surrogate and used to estimate dust components of K, Mg, and Na by defining a mineral-to-aluminum (MAL) mass ratio as $(K_2O+MgO+Na_2O)/Al_2O_3$. We combined these three elements into one coefficient because they are all major crustal elements that cannot be directly included due to their potentially significant sources from biomass burning and sea salt. We included only dust components of these elements by applying the MAL ratio obtained using dust data with negligible non-dust sources. The MAL ratio can be converted to:

$$\mathrm{MAL} = (1.20\mathrm{K}/\mathrm{Al} + 1.66\,\mathrm{Mg}/\mathrm{Al} + 1.35\,\mathrm{Na}/\mathrm{Al})/1.89 \quad (2.1)$$

where 1.20, 1.66, 1.35, and 1.89 are the oxide factors that convert elements to oxides for K_2O, MgO, Na_2O, and Al_2O_3, respectively. Thus, with elemental ratios of dust, the MAL ratio can be calculated and compared between regions. The MAL ratio is similar to the Chemical Index of Alteration (CIA) defined as $100\times Al_2O_3/(Al_2O_3+CaO+Na_2O+K_2O)$ and the Weathering Index of Parker (WIP) represented as $100\times(2Na_2O/0.35+MgO/0.9+2K_2O/0.25+CaO/0.7)$ (Price & Velbel, 2003), in the sense of representing the relative abundance of alkalis in dust.

We next examined the contribution from other elements. Although according to the composition of the upper continental crust (UCC) (Shaw et al., 1986), both CO_2 (decomposed from carbonate) and the sum of remaining compounds (mainly crystal H_2O, P_2O_5, and MnO) account for 1 wt% of UCC, for mineral dust in arid areas, the CO_2 content can reach up to 10 wt% or higher (Awadh, 2012; Modaihsh, 1997; Scheuvens et al., 2013). The abundance of bound H_2O, P_2O_5, and MnO is relatively consistent with that in the UCC (Mahowald et al., 2008; Mendez et al., 2010; Moreno et al., 2006; Moufti, 2013; Najafi et al., 2014; Zarasvandi et al., 2011). Therefore, we further investigated the regionally resolved CO_2 content at dry conditions but fixed the abundance of remaining compounds as 1 wt%. We derived an overall correction factor (CF) as:

$$CF = \frac{100\ \text{wt\%}}{100\ \text{wt\%} - [1\ \text{wt\%} + CO_2(\text{wt\%})]} \tag{2.2}$$

Including the MAL ratio and CF, we proposed a global-scale mineral dust equation:

$$\text{Dust} = [1.89\text{Al} \times (1 + \text{MAL}) + 2.14\text{Si} + 1.40\text{Ca} + 1.36\text{Fe} + 1.67\text{Ti}] \times \text{CF} \tag{2.3}$$

where 1.89, 2.14, 1.40, 1.36, and 1.67 are the oxide factors for Al_2O_3, SiO_2, CaO, FeO and Fe_2O_3 (in equal amounts), and TiO_2, respectively. Both the MAL ratio and CF vary regionally. Because the MAL ratio is estimated using dust data with negligible non-dust sources, the dust mass calculated by the global equation will exclude non-dust components of K, Mg, and Na when these elements are influenced by non-dust sources such as wildfire or sea salt. Similarly, we tested a mineral-to-silicon (MSI) ratio as $(K_2O+MgO+Na_2O)/SiO_2$ to examine the feasibility of using Si as the surrogate to estimate K, Mg, and Na.

To include adsorbed water and salt minerals for special types of dust such as saline dust, volcanic dust, and aged dust, we derived an expanded global equation with expanded MAL and CF as

described in the Supporting Information (Text 2.6.1). A water adjustment factor (WAF) was included in the CF based on the single hygroscopicity parameter κ (Kreidenweis et al., 2008; Snider et al., 2016). Although insufficient measured data were available to calculate the coefficients in the expanded global equation for these special types of dust, the expanded equation offers a framework to represent these special cases when detailed mineralogical information and hygroscopicity measurements are available in addition to elemental data. Dust hygroscopicity κ depends on many factors including the dust mineralogy or salinity (Tang et al., 2019), chemical mixing state (Sullivan et al., 2009), emission source (Peng et al., 2020), and particle size (Ibrahim et al., 2018). A review of the literature reveals that the κ of common desert dust is low (<0.1; (Gaston et al., 2017; Herich et al., 2009; Koehler et al., 2009; Tang et al., 2019), but for saline dust κ can be higher (>0.8; Gaston et al., 2017; Tang et al., 2019). For dust with high hygroscopicity, e.g., κ = 1.0, the resulting WAF will be 1.2, meaning adsorbed water can reach 20 wt% of the dry dust mass. For common desert dust, K, Mg, and Na exist mainly in feldspar or illite with low hygroscopicity (Tang et al., 2019), but they can exist mostly in salt minerals with high hygroscopicity for special types of dust such as saline dust. Salt minerals commonly observed in various special types of dust require the expanded global equation. For example, saline dust can have significant amounts of chlorides and sulfates besides carbonates, such as NaCl and Na_2SO_4 (Gaston et al., 2017). Volcanic dust has non-negligible sulfates, chlorides, and fluorides, such as $MgSO_4$, NaCl, and K_2SiF_6 (Gislason et al., 2011; Taylor and Lichte, 1980). Aged dust can contain nitrates, sulfates, and chlorides, such as $Ca(NO_3)_2$, $CaSO_4$, and $CaCl_2$ (Sullivan et al., 2009).

To investigate variation in the MAL and MSI ratios of desert dust across different regions, we collected elemental characteristics data (elemental ratios) of mineral dust in six major dust source regions (Sahara, Sahel, Middle East, East Asia, Australia, and Southwest US) as shown in Table

2.2. Other source regions such as South Africa and South America were not selected because insufficient measured data are available for these regions. Figure S2.9 summarizes the median and interquartile range of elemental ratios and MAL for each region. The data we used were obtained from various analysis techniques such as X-ray fluorescence (XRF), inductively coupled plasma-mass spectrometry (ICP-MS), and particle-induced X-ray emission (PIXE). These techniques have different detection limits and analytical errors, which can generate uncertainties on the elemental ratios, an inevitable problem for compiling different published analyses (Scheuvens et al., 2013), so we used the median value to reduce the influence of outliers. For the Southwest US, we used $PM_{2.5}$ data with dust mass (SOIL) > 50% of the reconstructed fine mass (RCFM) based on the IMPROVE algorithm (http://vista.cira.colostate.edu/Improve/reconstructed-fine-mass/) measured at IMPROVE rural sites. The measured data in other dust source regions were collected from literature and the Surface Particulate Matter Network (SPARTAN, Snider et al., 2015, https://www.spartan-network.org/). Given that Na and Mg potentially come from sea salt and K from biomass burning, to ensure negligible non-dust sources of Na, Mg, and K in the collected dust data from literature, we excluded the data affected by sea salt or biomass burning indicated by the dust origin analysis in their literature sources, which removed ~20 potential data sources. We incorporated different types of dust (aerosol, soil, and sediment) to augment the data set size. We neglected the difference in elemental ratios between different types of dust because insufficient previous studies are available to examine this concern. As a reference, the MAL and MSI ratios for average continental crust were calculated using elemental ratios from commonly cited sources for natural dust (Lide, 1995; Mason, 1952; Taylor & McLennan, 1995; Wedepohl, 1995). We applied the Kruskal-Wallis test to compare the MAL and MSI ratios in major dust source regions and continental crust. The criterion of a calculated probability with significance level < 0.05 (P <

0.05) was used as a measure of statistically significant differences between the groups. When the measurements of any element used in the global equation are not available or not well characterized, the median elemental ratios for each region shown in Table 2.2 could be applied to estimate the concentration of that element.

Measurements of the CO_2 content in dust are commonly omitted, which handicaps the investigation of its regional variability. Thus, an indirect way to estimate CO_2 content is needed. We obtained the worldwide distribution of $CaCO_3$ content in topsoil (0−30 cm) from the Harmonized World Soil Database (HWSD version 1.21, FAO & ISRIC, 2012). This distribution is generally consistent with the mineralogical maps from several modeling studies (Claquin et al., 1999; Journet et al., 2014; Nickovic et al., 2012). We estimated the average $CaCO_3$ content in major dust source regions using an embedded query Tool in the HWSD viewer. We also used mineralogical maps for carbonates in the topsoil (A horizon, 5−10 cm) of the conterminous US from the U.S. Geological Survey (USGS, Smith et al., 2019) as a reference. To account for other carbonates in dust, we calculated the mass ratio of total CO_2 to the CO_2 in $CaCO_3$ using available measured mineralogical data for major deserts worldwide from literature (Boose et al., 2016; Engelbrecht et al., 2016; Shen et al., 2009). Using the inferred total CO_2 abundance and fixing the remaining compounds as 1 wt% and WAF as unity, we calculated the corresponding CF in the global equation.

The measured data assembled from the literature for this study include various sizes of dust. Because the chemical composition of dust can be size-dependent (Cao et al., 2008; Pettijohn, 1975; Shen et al., 2007; Wu et al., 2011; Zarasvandi et al., 2011), we compared the differences of the elemental characteristics and carbonate content between PM_{10} and $PM_{2.5}$ using a data set of surface

soil from arid regions (Engelbrecht et al., 2016). Detailed information on data processing is provided in the Supporting Information (Text 2.6.2).

In addition to employing multiple major crustal elements to estimate dust mass, single crustal elements such as Si have also been used previously (Chow et al., 2015). As a comparison, Si alone with a coefficient M (Dust = Si×M) to account for all the major minerals was also investigated by calculating the coefficient M across dust source regions.

Table 2.2 Elemental Ratios of Dust in Major Dust Source Regions and Continental Crust

Region	Site	Type	Size (μm)	Si/Al	Fe/Al	Ca/Al	Ti/Al	K/Al	Mg/Al	Na/Al	MAL	K/Fe	Source	Method
Crust	Upper Continental Crust	rock		3.83	0.44	0.37	0.04	0.35	0.17	0.36	0.63	0.80	(S. R. Taylor & McLennan, 1995)	NA
	Upper Continental Crust	rock		3.92	0.40	0.38	0.04	0.33	0.17	0.33	0.60	0.83	(Wedepohl, 1995)	NA
	Continental Crust	rock		3.41	0.62	0.45	0.05	0.32	0.26	0.35	0.68	0.52	(Lide, 1995)	NA
	Continental Crust	rock		3.43	0.68	0.50	0.07	0.25	0.28	0.29	0.61	0.37	(Mason, 1952)	NA
	median			**3.63**	**0.53**	**0.42**	**0.05**	**0.33**	**0.22**	**0.34**	**0.62**	**0.66**		
Middle East	Southwest Iran	aerosol	0.8-50	NA	NA	1.15	0.08	0.22	0.29	0.13	0.49	NA	(Torghabeh et al., 2020)	ICP-OES
	Western Iran	aerosol	TSP	3.57	0.66	2.86	0.07	0.23	0.56	0.11	0.72	0.35	(Najafi et al., 2014)	XRF
	Central Iran 2008	aerosol	TSP	4.34	0.79	4.28	0.10	0.22	0.44	0.21	0.68	0.29	(Hojati et al., 2012)	ICP-MS
	Central Iran 2009	aerosol	TSP	3.29	0.76	5.36	0.14	0.22	0.46	0.32	0.78	0.29	(Hojati et al., 2012)	ICP-MS
	Ahvaz, Iran 2009	aerosol	TSP	NA	1.14	4.73	0.02	0.32	0.89	0.21	1.14	0.28	(Zarasvandi et al., 2011)	ICP-MS
	Israel[a]	aerosol	$PM_{2.5}$	2.71	0.61	0.68	0.06	0.37	0.21	0.37	0.68	0.60		XRF
	Abu Dhabi[a]	aerosol	$PM_{2.5}$	3.05	0.76	2.03	0.06	0.38	0.70	0.23	1.02	0.50		XRF
	median			**3.29**	**0.76**	**2.86**	**0.07**	**0.23**	**0.46**	**0.21**	**0.72**	**0.32**		
Sahara	Northern Algeria	aerosol	0.1-1	1.85	0.45	1.09	0.06	0.17	NA	NA	NA	0.38	(Gomes et al., 1990)	XRF
	Northern Algeria	aerosol	1-20	2.12	0.48	0.88	0.06	0.19	NA	NA	NA	0.40	(Gomes et al., 1990)	XRF
	Morocco	aerosol	TSP	4.97	0.64	5.22	0.09	0.40	0.86	NA	NA	0.63	(Khiri et al., 2004)	XRF
	Khamaseen dust	aerosol	5-20	4.05	0.73	3.60	0.13	0.25	0.58	0.13	0.77	0.33	(Abed et al., 2009)	ICP-MS
	Cairo	aerosol	<20	5.83	0.70	2.00	0.14	0.28	0.57	0.16	0.80	0.40	(Linke et al., 2006)	XRF
	Cairo	soil	<20	6.33	0.77	4.26	0.21	0.24	0.43	0.20	0.67	0.31	(Linke et al., 2006)	XRF
	Morocco	soil	<20	7.41	0.57	1.85	0.11	0.38	0.31	0.09	0.58	0.66	(Linke et al., 2006)	XRF
	Western Sahara site 1	soil	<30	6.26	0.66	1.98	0.08	0.34	0.37	0.15	0.66	0.52	(Moreno et al., 2006)	ICP-AES
	Western Sahara site 2	soil	<30	5.82	0.53	3.40	0.07	0.37	0.42	0.15	0.71	0.70	(Moreno et al., 2006)	ICP-AES
	Western Sahara site 3	soil	<30	9.88	1.10	3.24	0.20	0.42	0.43	0.23	0.80	0.38	(Moreno et al., 2006)	ICP-AES
	Hoggar Massif site 1	soil	<30	3.72	0.54	0.22	0.11	0.26	0.14	0.15	0.40	0.48	(Moreno et al., 2006)	ICP-AES
	Hoggar Massif site 2	soil	<30	4.06	0.50	0.20	0.10	0.28	0.13	0.20	0.44	0.56	(Moreno et al., 2006)	ICP-AES
	Tindouf, Algeria	soil	<63	4.68	0.65	6.52	0.11	0.34	0.96	0.48	1.40	0.52	(Criado & Dorta, 2003)	ICP-AES
	Tiris, Mauritania	soil	<63	7.07	0.53	0.25	0.17	0.42	0.14	0.20	0.53	0.79	(Criado & Dorta, 2003)	ICP-AES

	Northern Mali	soil	NA	NA	0.49	7.95	NA	0.27	0.65	0.13	0.84	0.57	(Washington et al., 2009)	NA
	median			**5.40**	**0.57**	**2.00**	**0.11**	**0.28**	**0.43**	**0.16**	**0.69**	**0.52**		
Sahel	Dakar, Senegal	aerosol	TSP	5.62	0.62	0.25	0.09	0.24	0.15	0.09	0.35	0.38	(Orange et al., 1993)	NA
	Mbour, Senegal	aerosol	TSP	6.69	0.68	0.14	0.10	0.16	0.16	0.02	0.26	0.24	(Orange et al., 1993)	NA
	Pete, Senegal	aerosol	TSP	6.59	0.67	0.12	0.10	0.16	0.15	0.01	0.24	0.25	(Orange et al., 1993)	NA
	Zaria, Northern Nigeria	aerosol	<2	2.23	0.42	0.01	0.06	0.10	0.09	0.00	0.14	0.23	(Møberg et al., 1991)	AAS
	Niger, local	aerosol	<40	2.50	0.57	0.21	0.11	0.17	0.10	0.04	0.22	0.29	(Formenti et al., 2008)	XRF
	Niger, advected	aerosol	<40	2.84	0.57	0.39	0.07	0.18	0.16	0.06	0.30	0.32	(Formenti et al., 2008)	XRF
	Agadez, Niger	soil	<20	6.10	0.23	0.08	0.03	0.49	0.04	0.27	0.54	2.13	(Linke et al., 2006)	XRF
	Niger, Monsoon	aerosol	<30	5.29	0.50	0.04	0.13	0.16	0.05	0.04	0.17	0.32	(Moreno et al., 2006)	ICP-AES
	Niger, Harmattan	aerosol	<30	4.84	0.62	0.18	0.11	0.23	0.08	0.07	0.27	0.37	(Moreno et al., 2006)	ICP-AES
	Chad Basin	soil	<30	4.00	0.63	0.13	0.08	0.16	0.10	0.11	0.27	0.26	(Moreno et al., 2006)	ICP-AES
	Bodélé, Chad	soil	NA	NA	0.64	0.04	NA	0.16	0.08	0.26	0.36	0.26	(Washington et al., 2009)	NA
	median			**5.07**	**0.62**	**0.13**	**0.09**	**0.16**	**0.10**	**0.06**	**0.27**	**0.29**		
Australia	Birdsville, Queensland	aerosol	TSP	3.42	0.77	0.11	0.09	0.19	NA	0.24	NA	0.24	(Radhi et al., 2010a)	PIXE, PIGE
	Muloorina Station	aerosol	TSP	3.16	0.96	0.58	0.08	0.26	NA	0.12	NA	0.27	(Radhi et al., 2010b)	PIXE, PIGE
	Ormiston Creek site 1	soil	PM_{10}	NA	0.47	0.09	0.04	0.24	0.10	0.06	0.28	0.51	(Moreno et al., 2009)	ICP-AES
	Ormiston Creek site 2	soil	PM_{10}	NA	0.44	0.05	0.04	0.17	0.05	0.05	0.19	0.40	(Moreno et al., 2009)	ICP-AES
	Wilpena Pound site 1	soil	PM_{10}	NA	0.62	0.03	0.05	0.11	0.05	0.01	0.13	0.18	(Moreno et al., 2009)	ICP-AES
	Wilpena Pound site 2	soil	PM_{10}	NA	0.26	0.03	0.08	0.26	0.07	0.03	0.25	0.99	(Moreno et al., 2009)	ICP-AES
	Silverton	soil	PM_{10}	NA	0.53	0.12	0.04	0.28	0.10	0.03	0.29	0.53	(Moreno et al., 2009)	ICP-AES
	Queensland	sediment	<80	3.45	0.59	0.09	0.09	0.14	0.10	0.06	0.23	0.23	(Kamber et al., 2005)	ICP-OES
	Autralian continent	sediment	<2, 000	8.47	0.53	0.08	0.08	0.23	0.07	0.05	0.25	0.44	(Reimann & de Caritat, 2012)	XRF
	median			**3.44**	**0.53**	**0.09**	**0.08**	**0.23**	**0.07**	**0.05**	**0.25**	**0.40**		
East Asia	Zhenbeitai, China	aerosol	TSP	4.14	0.52	0.79	0.08	0.25	0.26	NA	NA	0.48	(Zhang et al., 2003)	PIXE
	Zhenbeitai, China	aerosol	PM_9	2.79	0.63	0.79	0.05	0.31	0.32	0.19	0.62	0.49	(Alfaro, 2003)	XRF
	Zhenbeitai, China	aerosol	$PM_{2.5}$	1.90	0.59	1.00	0.05	0.32	0.35	0.15	0.62	0.54	(Arimoto, 2004)	PIXE
	Yulin, China	aerosol	$PM_{2.5}$	NA	0.51	0.81	0.07	0.46	0.24	0.19	0.64	0.90	(Xu, 2004)	ICP-MS

	Gansu, China	aerosol	TSP	2.94	0.35	0.74	0.03	0.27	0.31	0.11	0.52	0.77	(Ta et al., 2003)	XRF
	Desert area, China	soil	＜100	7.68	0.54	0.94	0.06	0.34	0.28	0.29	0.68	0.63	(Ta et al., 2003)	XRF
	Gobi area, China	soil	＜100	7.85	0.35	1.17	0.04	0.39	0.18	0.36	0.67	1.09	(Ta et al., 2003)	XRF
	Gansu, China	soil	＜30	4.61	0.49	0.97	0.06	0.32	0.26	0.22	0.59	0.66	(Nishikawa et al., 2000)	XRF, etc.[b]
	Ningxia, China	soil	＜30	4.76	0.51	0.91	0.08	0.29	0.27	0.23	0.59	0.56	(Nishikawa et al., 2000)	XRF, etc.
	Xi Feng, China	soil	TSP	4.56	0.78	2.25	0.07	0.41	0.28	0.06	0.55	0.52	(Wu et al., 2011)	XRF
	Xi Feng, China	soil	PM_{10}	2.03	0.71	2.30	0.06	0.39	0.29	0.08	0.56	0.55	(Wu et al., 2011)	XRF
	Xi Feng, China	soil	$PM_{2.5}$	1.78	0.65	1.56	0.05	0.29	0.29	0.07	0.49	0.44	(Wu et al., 2011)	XRF
	Xi Feng, China	soil	PM_{1}	1.88	0.68	1.77	0.05	0.29	0.29	0.06	0.49	0.43	(Wu et al., 2011)	XRF
	median			**3.54**	**0.54**	**0.97**	**0.06**	**0.32**	**0.28**	**0.17**	**0.59**	**0.55**		
Southwest US[c]	Jarbidge Wilderness	aerosol	$PM_{2.5}$	2.86	0.60	0.49	0.05	0.43	0.25	0.30	0.71	0.71		XRF
	Saguaro NM	aerosol	$PM_{2.5}$	2.33	0.58	0.68	0.05	0.36	0.22	0.24	0.59	0.61		XRF
	Meadview	aerosol	$PM_{2.5}$	2.40	0.63	0.78	0.06	0.36	0.30	0.26	0.68	0.57		XRF
	Owens Valley	aerosol	$PM_{2.5}$	2.50	0.60	0.78	0.05	0.38	0.37	0.27	0.76	0.64		XRF
	Tonto NM	aerosol	$PM_{2.5}$	2.32	0.58	0.63	0.05	0.34	0.26	0.24	0.62	0.59		XRF
	Chiricahua NM	aerosol	$PM_{2.5}$	2.36	0.53	0.63	0.05	0.35	0.20	0.27	0.59	0.65		XRF
	Petrified Forest NP	aerosol	$PM_{2.5}$	2.31	0.60	0.71	0.05	0.32	0.27	0.20	0.58	0.54		XRF
	Canyonlands NP	aerosol	$PM_{2.5}$	2.31	0.56	0.88	0.05	0.36	0.32	0.19	0.65	0.65		XRF
	White Mountain	aerosol	$PM_{2.5}$	2.40	0.57	1.10	0.05	0.33	0.42	0.21	0.73	0.58		XRF
	Capitol Reef NP	aerosol	$PM_{2.5}$	2.48	0.63	1.02	0.06	0.39	0.38	0.22	0.74	0.62		XRF
	Zion Canyon	aerosol	$PM_{2.5}$	2.44	0.60	1.01	0.06	0.37	0.40	0.27	0.77	0.61		XRF
	Gila Wilderness	aerosol	$PM_{2.5}$	2.29	0.55	0.78	0.05	0.34	0.26	0.18	0.58	0.62		XRF
	median			**2.38**	**0.59**	**0.78**	**0.05**	**0.36**	**0.29**	**0.24**	**0.66**	**0.61**		

Note. NA: not available; XRF: X-ray fluorescence; AAS: atomic absorption spectrometry; ICP-MS: inductively coupled plasma-mass spectrometry; ICP-OES: inductively coupled plasma-optical emission spectrometry; ICP-AES: inductively coupled plasma-atomic emission spectrometry; PIXE: particle-induced X-ray emission; PIGE: particle-induced gamma emission; TSP: total suspended particulate; NM: national monument; NP: national park.

[a]The Israel and UAE data are the ratios of mean element concentrations using $PM_{2.5}$ data in 2019 from the SPARTAN network. Only the data with Na/Al < 0.45 and K/Al < 0.5 were selected to avoid the effects of non-dust sources (Scheuvens et al., 2013). [b]This is a reference material certified using multiple techniques. [c]The Southwest US data are the ratios of mean element concentrations calculated using dust-dominated (SOIL > 50% RCFM) $PM_{2.5}$ data in 2011-2018 from the IMPROVE network.

2.3.2 Reference Dust Mass

To evaluate the performance of the global dust equation, we applied two approximate methods to obtain the reference dust mass since no absolute benchmark is available. One is called the total-mineral-mass approach, which is calculated by summing all the oxides of measured major crustal elements (Si, Al, Fe, Ca, Ti, Na, Mg, and K). Elemental concentrations were multiplied by corresponding common oxide factors (Reff et al., 2009) to obtain oxide concentrations. Measurements of Na, Mg, and K can be directly used to calculate dust mass only when they have negligible non-dust sources. Other dust components such as H_2O and carbonate are not commonly measured, so we applied the same CF used in the global equation to obtain "total mineral mass". The other method is the residual-mass approach, which is calculated by subtracting organic mass (OM), elemental carbon (EC), sulfate, nitrate, ammonium, sea salt, and particle-bound water (PBW) from the measured PM. OM was calculated by multiplying OC with spatiotemporally varying estimates of the OM/OC ratio (Philip et al., 2014). Sea salt was represented as $1.8Cl^-$, or as 1.8Cl when the Cl^- concentration was missing (Hand et al., 2012; Malm & Hand, 2007). PBW refers to water associated with sulfate, nitrate, ammonium, sea salt, and OM, which was estimated using a κ-Kohler framework (Kreidenweis et al., 2008) with specific parameters for each species at different RH conditions from Latimer & Martin (2019). Following the IMPROVE algorithm, we assumed sulfate exists as ammonium sulfate and nitrate as ammonium nitrate to calculate PBW. For anthropogenic dust such as road dust, non-dust trace metals were also subtracted because their influence on the residual mass may be non-negligible (Chow et al., 2015). Both approaches have limitations. The total-mineral-mass approach cannot directly test the accuracy of the CF because it is used in both the total mineral mass and the global equation. As for the residual-mass approach, uncertainties exist in the measurements of each PM component and related assumptions, especially

the uncertainty in estimating OM (Philip et al., 2014; Simon et al., 2011). Nevertheless, both approaches offer information to evaluate our global equation. To optimize the accuracy of the reference dust mass, we used dust-dominated samples where all measurements of mineral elements were well quantified and contributions from organics and other non-dust species were negligible. The data selection and the method of calculating the reference dust mass applied for different data sources are further discussed in the next section.

To carry out the evaluation, we applied several statistical metrics including the normalized mean bias (NMB), mean fractional bias (MFB), and normalized root mean square error (NRMSE):

$$\text{NMB}\ (\%) = 100 \times \sum (C_j\text{-}R_j) \Big/ \sum R_j \tag{2.4}$$

$$\text{MFB}\ (\%) = 100 \times 1/\text{N} \times \sum (C_j\text{-}R_j) \Big/ [(C_j\text{+}R_j)/2] \tag{2.5}$$

$$\text{NRMSE}\ (\%) = 100 \times 1/\sigma \times \sqrt{\sum \left(C_j\text{-}R_j\right)^2 \Big/ \text{N}} \tag{2.6}$$

where C_j represents the calculated dust mass, R_j is the reference dust mass obtained using the total-mineral-mass or residual-mass approach, j represents the pairing of the calculated dust mass and reference dust mass by site and time for N data points, and σ is the standard deviation of the reference dust mass. The NMB and MFB are also calculated with the IMPROVE equation to serve as a benchmark of our global equation. Some results with ratio form were plotted on a log scale so that deviations from unity are visually symmetrical.

2.3.3 Evaluation of the Global Dust Equation

First, we examined the performance of the global equation for desert dust in source regions and for the average global continental crust using the same data sources as those in Table 2.2. For the Australian dust data without Si measurements, the median Si/Al ratio (3.44) from available measurements was used. We also evaluated the global equation for desert dust (African and Asian) transported to non-source regions using measurements from the European Monitoring and Evaluation Programme (EMEP, https://www.emep.int/) and literature. We used dust data measured at southern EMEP sites during summer African dust events. To reduce the influence of sea salt and biomass burning, we selected the data with Na/Al < 0.45 and K/Al < 0.5 reflecting typical elemental ratios for Northern African dust (Scheuvens et al., 2013). After the selection, PM_{10} data from six sites during three dust episodes (Alastuey et al., 2016; Matassoni et al., 2009) were used for the evaluation. We also applied the global equation to available literature data of African dust over the Atlantic islands (Criado & Dorta, 2003; Engelbrecht et al., 2014; Formenti, 2003; Kandler et al., 2007) as well as Asian dust over Japan (Nishikawa et al., 1991) and Korea (Kim et al., 2003). We only used data with minimal influence of non-dust sources suggested in the literature. Because Si measurements were missing in the dust data over Japan and Korea, we used the median Si/Al ratio (3.54) in East Asian deserts from Table 2.2. For most of the above data, we were unable to apply the residual-mass approach owing to insufficient measurements of non-dust PM species, so the total-mineral-mass approach was the major method applied for the evaluation. According to the protocol of EMEP measurements, we used 50% RH to calculate PBW for EMEP data.

To further evaluate the global dust equation within the US, we utilized daily-integrated $PM_{2.5}$ speciation data from the IMPROVE network. Mineral elements are analyzed with XRF for samples from IMPROVE sites which are primarily located in rural areas (Solomon et al., 2014). Following

the IMPROVE data advisories (http://vista.cira.colostate.edu/Improve/data-advisories/), we used data collected in 2011−2018 to avoid the influence of data anomalies or potential problems such as non-quantitative Na data prior to 2011 (Hyslop et al., 2015). To balance avoiding uncertainties in the measurements of low dust content data while retaining sufficient data, we used dust-dominated $PM_{2.5}$ data (SOIL > 50% RCFM based on the IMPROVE algorithm). For cases with measured elemental concentration below the minimum detection limit (MDL), we substituted one-half of the MDL. The spatial distribution of the MAL ratio was investigated by calculating the ratio of the average K_2O+MgO+Na_2O to average Al_2O_3 concentrations. The NMB and MFB for the entire data set and for each site were calculated using both total-mineral-mass and residual-mass approaches. The NRMSE was also provided for the entire data set. For the residual-mass approach, we adopted the common humidity protocol (35%) for gravimetric mass analysis to calculate PBW. Following the IMPROVE advisory about increased variation of humidity after the weighing laboratory moved in 2011, we applied an RH of 45% for summer (June to August) data after the laboratory move. The average fraction of calculated PBW in measured total $PM_{2.5}$ was ~4 wt%. All IMPROVE sites including rural and urban sites were considered but only the sites with ≥5 daily-integrated $PM_{2.5}$ records that meet the criterion of SOIL > 50% RCFM were used in our maps to ensure representativeness. We neglected the data from the U.S. National $PM_{2.5}$ Chemical Speciation Monitoring Network (CSN) given that CSN dust concentrations were inconsistent with collocated IMPROVE dust concentrations, and comparisons between the two networks would be semiquantitative (Hand et al., 2012). Gorham et al. (2021) indicated that CSN has lower flow rate and larger sample deposit area than IMPROVE which makes quantification difficult, and particle size cut point efficiency also varies between the two networks. CSN has

higher MDLs for mineral elements than IMPROVE, and therefore some elements are poorly detected (e.g., Al).

We explored the applicability of the global equation for anthropogenic dust by evaluating its performance for paved road, unpaved road, and agricultural soil dust using measured $PM_{2.5}$ and PM_{10} data from the U.S. Environmental Protection Agency's (EPA) SPECIATE 5.0 database (https://www.epa.gov/air-emissions-modeling/speciate) and available data from two studies of paved road dust in Spain and China (Amato et al., 2009; Zhao et al., 2006). Both total-mineral-mass and residual-mass approaches were used to calculate the reference dust mass. All the data we used were dust-dominated (dust fraction > 50 wt%). More details about the data processing are described in the Supporting Information (Text 2.6.3). Insufficient dust-dominated data were available to evaluate the global equation for other types of anthropogenic dust including construction, combustion, and industrial dust (Pervez et al., 2018; Santacatalina et al., 2010; Shen et al., 2016).

2.4 Results and Discussion

2.4.1 Characteristics of Regional MAL and CF Coefficients

The use of Si alone is explored first given its dominant abundance in dust. Figure S2.10 shows that the single Si coefficient M can vary by more than a factor of two within a region especially East Asia and Sahara where the standard deviation of M was 27% and 21% of the mean respectively. This high variability in the soil composition within the selected regions will result in undue errors in dust estimated using a single tracer, such as Si. Only the multi-component dust model is examined further.

We subsequently examine the use of regional MAL ratios. Table 2.2 shows dust data with negligible non-dust sources. The corresponding K/Fe ratios of desert dust in the southwestern US and eastern Asia are ~0.6 as used in the IMPROVE equation (Malm et al., 1994), but tend to be lower (~0.4) in other regions, providing evidence that the K/Fe ratio varies regionally. Figure 2.1 shows the variation of the MAL ratio in six different dust source regions and the MAL ratio for the average global continental crust using the data in Table 2.2. The median MAL ratio is significantly different ($P < 0.05$ for the Kruskal-Wallis test) across regions. Australia and the Sahel have low MAL ratios (<0.3) due to high chemical weathering (Kamber et al., 2005; Moreno et al., 2006, 2009; Reimann & de Caritat, 2012), while the MAL ratio in other regions is close to the crustal MAL ratio. Dust with relatively high MAL ratios (~0.8) in the Sahara (Linke et al., 2006; Moreno et al., 2006) and the Middle East (Hojati et al., 2012) is enriched in dolomite and palygorskite leading to their high Mg/Al ratios (>0.4). Figure S2.11 shows that the MSI ratio varies more widely than the MAL ratio both across and within regions, indicating that the sum of (K_2O+MgO+Na_2O) may associate better with Al than Si. This could be because Si has an additional major mineral source besides aluminosilicate, i.e., quartz, which makes the MSI ratio sensitive to the variation of quartz content across and within regions (Nickovic et al., 2012) as well as the significant mineralogical fractionation effect on quartz (Ahmady-Birgani et al., 2015; Formenti et al., 2014; Jeong et al., 2014). Therefore, we used the MAL ratio instead of the MSI ratio to develop the global equation. No consistent difference of the MAL ratio among aerosol, soil, and sediment was observed. Thus, all the data were used to develop regional MAL ratios. The particle size effect is discussed below. The median values in Table 2.2 were used to represent regional MAL ratios in six dust source regions and the crustal MAL ratio listed in Table 2.3.

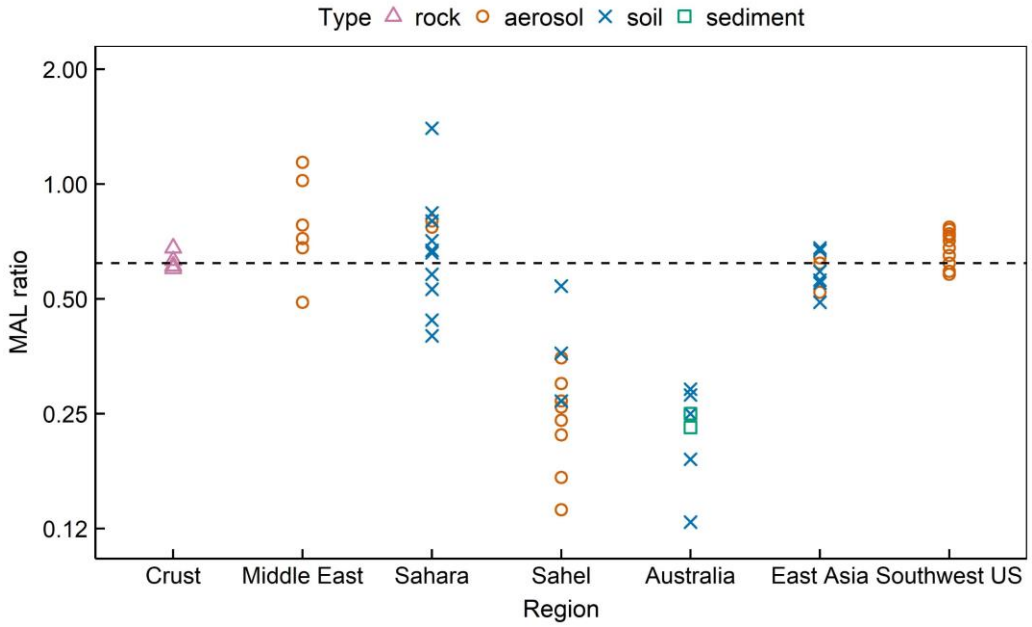

Figure 2.1 The MAL ratio of $(K_2O+MgO+Na_2O)/Al_2O_3$ in six dust source regions and the average global continental crust shown on a log scale. The dashed line indicates the median MAL ratio (0.62) in continental crust of four data sources. Each symbol represents a data record in **Table 2.2**.

The regional carbonate content and CF are thereafter investigated. Figure S2.12 demonstrates that $CaCO_3$ of topsoil is predominantly distributed in arid areas with variation in amounts across different deserts. The approximate content of $CaCO_3$ in topsoil for the six dust source regions is shown in Table 2.3, which generally agrees with available dust measurements in previous studies. Desert dust in the Middle East is commonly rich in carbonate due to abundant calcite and dolomite in local soils (Ahmady-Birgani et al., 2015; Awadh, 2012; Modaihsh, 1997). Saharan dust is considerably more carbonate-rich than Sahelian dust that is largely originated from the Chad Basin (Moreno et al., 2006; Scheuvens et al., 2013). The carbonate content of Australian dust is relatively low most likely linked to extensive and intense weathering of Australian soils (Moreno et al., 2009; Reimann & de Caritat, 2012). Asian dust in the Taklimakan Desert and Gobi area contains large amounts of carbonate (Cao, 2005; Wang et al., 2005). USGS reports somewhat higher calcite contents than the HWSD but they both show soils in the Southwest US are primarily carbonate-rich. Figure S2.13 shows that the mass ratio of total CO_2 to CO_2 in $CaCO_3$ is not significantly

different across regions (Kruskal-Wallis test, $P > 0.05$). Hence, we applied the median ratio (1.11) of total CO_2 to CO_2 in $CaCO_3$ to account for other carbonates of dust in all the regions. Sensitivity tests using 25th percentile (1.06) or 75th percentile (1.20) for this mass ratio show that this variation does not significantly change the CF. The resulting dust CO_2 content and the calculated CF across six dust source regions and the average global continental crust are shown in Table 2.3. Although regional-scale variation in MAL and CF is included, microscale or synoptic-scale variation cannot be resolved without sufficient measured data.

We then examine the effects of particle size on the elemental ratios and CO_2 content. Figure S2.14 shows that using surface soil data from arid regions worldwide, the particle size of dust has a significant effect (paired-sample Wilcoxon test, $P < 0.05$) on Si/Al, Fe/Al, Ti/Al, and K/Al, but not on Ca/Al, Mg/Al, and Na/Al. As natural mechanical weathering can have various effects on minerals with different properties (Boose et al., 2016), the size effect is expected to differ among elemental ratios. However, Figure 2.2 indicates that the size effect is not significant for the MAL ratio (paired-sample Wilcoxon test, $P = 0.14$) and the CO_2 content (paired-sample Wilcoxon test, $P = 1.00$) which are used in the global equation. A size-dependent dust equation appears unnecessary based on the available data. Nevertheless, more available data sets of measured size-fractionated elemental composition and carbonate content of dust samples are needed to assess the size effect and possibly develop a size-dependent global dust equation.

Table 2.3 Region-specific MAL Ratio and CF for Natural Dust

Type	Region	Regional MAL	95% CI of MAL[a]	$CaCO_3$ (wt%)	CO_2 (wt%)	Regional CF
	Crust	**0.62**	**(0.60, 0.68)**		**1**	**1.02**
source region	Middle East	0.72	(0.68, 1.00)	22	11	1.14
source region	Sahara	0.69	(0.56, 0.80)	22	11	1.14
source region	Sahel	0.27	(0.23, 0.35)	8	4	1.05
source region	Australia	0.24	(0.19, 0.28)	8	4	1.05
source region	East Asia	0.59	(0.54, 0.63)	18	9	1.11
source region	Southwest US	0.66	(0.58, 0.71)	22	11	1.14
within the US	East[b]	0.27				1.05
within the US	West	0.66				1.14
non-source region	South Europe & the Atlantic islands	0.48				1.10
non-source region	Korea & Japan	0.59				1.11

[a]The 95% confidence interval (CI) of the median MAL ratio for six dust source regions (deserts) and the average global continental crust are calculated. [b]Eastern and western regions are defined based on the dividing line shown in Figure 2.3.

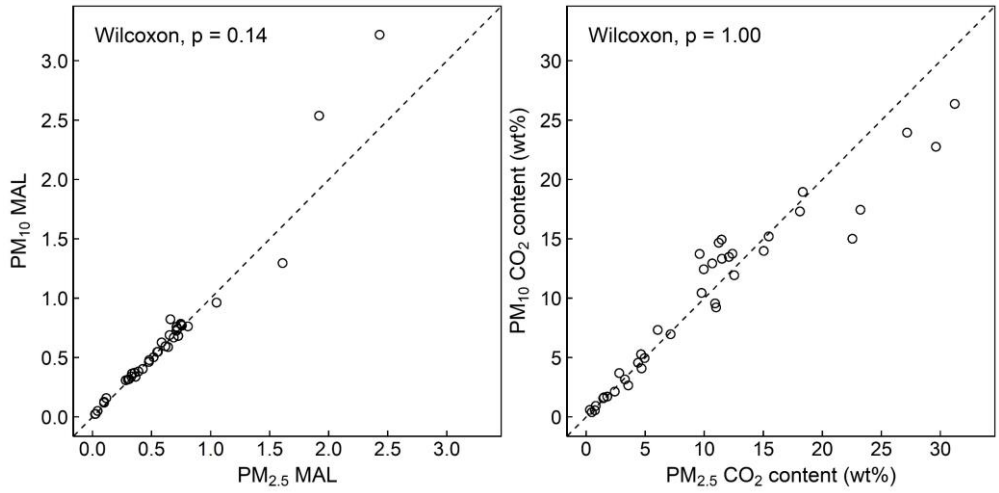

Figure 2.2 Particle size effect on the MAL ratio and CO_2 content of dust using a data set of surface soil from arid regions (Engelbrecht et al., 2016). Inset P-values are the results of the paired-sample Wilcoxon test.

The coefficients used within the US are further investigated. Figure 2.3 shows the distribution of the MAL ratio at IMPROVE sites. Most of the western sites have a similar MAL ratio with deserts in the Southwest, while the MAL ratio at eastern sites is close to that of Sahelian dust (~0.27). A previous study (Perry et al., 1997) found that African dust transported to the US has a characteristic Ca/Al ratio of <0.26, similar to that of Sahelian dust (median Ca/Al = 0.13 shown in Table 2.2). Thus, we applied the coefficients of Sahelian dust (MAL = 0.27, CF = 1.05) to eastern sites and

those of the Southwest (MAL = 0.66, CF = 1.12) to western sites using the longitude (103.2°W) of the Big Bend National Park site in Texas as an approximate dividing line based on the data pattern shown in Figure 2.3. Because we only use dust-dominated data to investigate the MAL pattern, using the Sahelian MAL may underestimate dust mass for months without the influence of African dust but the dust contribution to total $PM_{2.5}$ is small in those months.

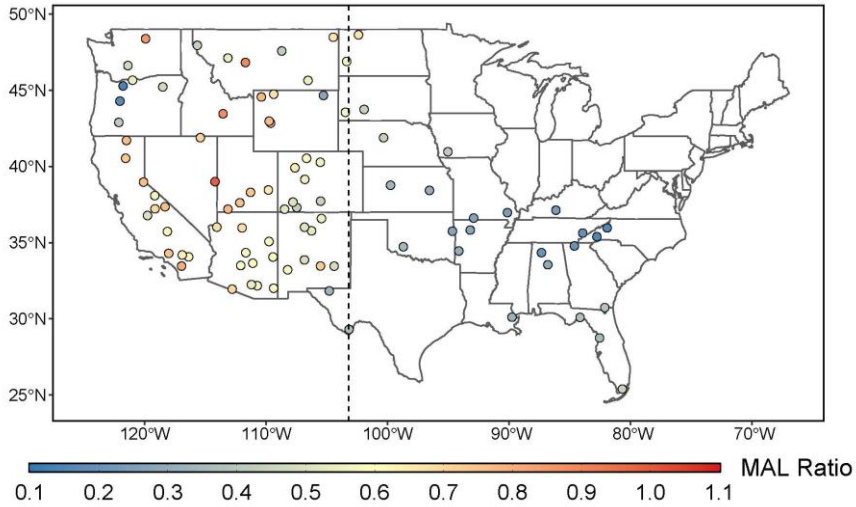

Figure 2.3 The MAL ratio of $(K_2O+MgO+Na_2O)/Al_2O_3$ at IMPROVE sites using daily-integrated dust-dominated (SOIL > 50% RCFM) $PM_{2.5}$ speciation data in 2011−2018 from the U.S. IMPROVE network. Only the sites with ≥5 data points were used to ensure representativeness. The number of selected IMPROVE sites is 95. The dashed line indicates the dividing line (103.2°W) through the Big Bend National Park site.

Coefficients for desert dust transported to non-source regions are assumed to be the same as those used for source regions. Elemental ratios (e.g., Al/Ca, K/Fe) are used as dust source tracers in many studies and the elemental ratios used to calculate MAL (i.e., K/Al, Mg/Al, and Na/Al) can remain similar during long-range transport (Cao et al., 2008; Hand et al., 2017; Mori, 2003; VanCuren, 2002), so we used the MAL ratio of source regions for non-source regions. Previous studies show that $CaCO_3$ may be converted to $Ca(NO_3)_2$ or $CaSO_4$ by reacting with acidic species if the dust plume passes over highly polluted regions (Huang et al., 2010; Scheuvens et al., 2013a). Asian dust transported eastwards passing over urban areas of China can become aged (Heim et al.,

2020), which may require a higher CF than that for Asian dust in the source region given the formation of secondary salts and adsorbed water due to increased hygroscopicity. The expanded expression of the global equation can be used in this case, but insufficient mineralogical information and hygroscopicity measurements are available to calculate the coefficients. Therefore, for Asian dust transported to Japan and Korea (Kim et al., 2003; Nishikawa et al., 1991), we still utilized the MAL ratio (0.59) and CF (1.11) of its source region. The loss of carbonate during long-range transport is not severe for African dust (Coz et al., 2009; Denjean et al., 2015; Scheuvens et al., 2013). African dust traveling to southern Europe (Alastuey et al., 2016; Escudero, 2005; Sánchez de la Campa et al., 2013; Stuut et al., 2009) and the Atlantic islands (Criado & Dorta, 2003; Engelbrecht et al., 2014; Formenti, 2003; Reid, 2003) can originate from both the Sahara and Sahel, so we employed the average MAL ratio (0.48) and average CF (1.10) of the two regions.

With limited data for different types of anthropogenic dust in various regions, we estimate the coefficients for anthropogenic dust more simplistically than for natural dust. The crustal MAL ratio (0.62) was applied to both paved road and unpaved road dust. Given that the road dust data are from areas (Texas, Illinois, northeastern Spain, and northern China) where local soils are enriched in carbonates or places affected by dust storms (Amato et al., 2009; Smith et al., 2019; Zhao et al., 2006), we used a high CF of 1.12 for both paved road and unpaved road dust. For agricultural soils, mobile elements (Na, K, and Mg) and carbonates can be leached by irrigation (Chow et al., 2003), so we applied a lower MAL ratio of 0.31 (half the crustal MAL) and the crustal CF (1.02).

2.4.2 Evaluation of the Global Dust Equation

Figure 2.4 shows the performance of the global equation and the IMPROVE equation for desert dust in six source regions and for the average global continental crust. The estimates by the global equation are consistent with the "total mineral mass" with a small NMB of -0.7 to 0.2% and a small MFB of -0.7 to 0.3% for all the source regions as well as the continental crust, while both the NMB and MFB of applying the IMPROVE equation are -6 to 10%. Because the same CF was used in both the global equation and "total mineral mass", the comparison between the two estimates indicates the accuracy of applying the region-specific MAL ratio. Although the MAL ratio can vary by more than a factor of 4 within a region (Figure 2.1), the resulting bias in using a median MAL in each region is within ±1%. The underestimation of US desert dust by the IMPROVE equation is also observed in previous studies (Hand et al., 2019; Simon et al., 2010, 2011). Therefore, it is necessary to consider the variation in dust composition to improve the accuracy of estimating dust mass. Using an equation with region-specific coefficients (MAL and CF) is found to be an effective approach, which reduced the regional bias by about 6-10% compared to the IMPROVE equation with universal coefficients. This reduction in bias matters to PM mass closure and model evaluation especially when dust mass is high during dust events. Although the global equation agrees well with the "total mineral mass", the total-mineral-mass approach cannot be used when Na, Mg, and K are significantly influenced by non-dust sources because they are directly added to the total dust mass. Thus, the advantage of the global equation is that it accounts for only the dust component of these elements by applying an average MAL ratio obtained from analyses of dust data with negligible non-dust sources.

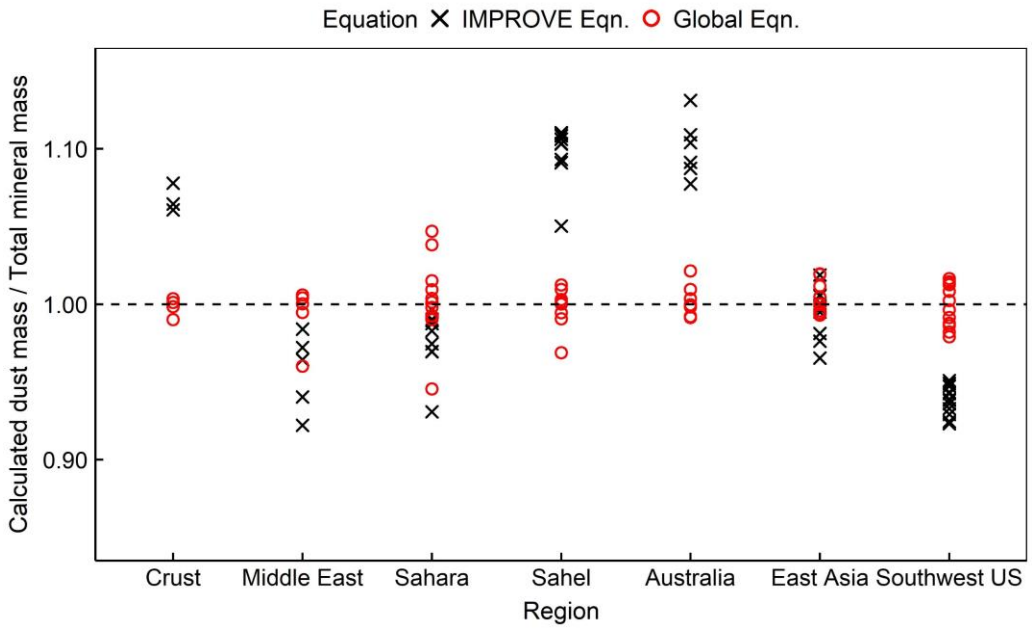

Figure 2.4 The ratio of the dust mass calculated by the global equation and the IMPROVE equation to the "total mineral mass" for desert dust in source regions and for the average global continental crust.

The performance of the global equation for the IMPROVE network is shown in Figure 2.5. Both equations show a small bias compared to the "total mineral mass" (NMB and MFB within ±4%), which is within experimental uncertainties for the five elements (Al, Si, Ca, Fe, and Ti) measured in the IMPROVE network (Gorham et al., 2021; Hyslop & White, 2009). The global equation shows a slightly smaller NRMSE (8.5%) than the IMPROVE equation (10%). Applying the bootstrapping method, the mean estimates from the two equations have no statistically significant difference (P = 0.30). We also attempted to use the residual-mass approach for evaluation but were stymied by possible biases in gravimetric and speciated measurements as well as related assumptions. The relative humidity is not rigorously controlled in the weighing laboratory (Simon et al., 2011), especially after the laboratory was relocated in 2011, and RH generally increased after 2011 (Hand et al., 2019). Opposing biases from the residual-mass approach were observed before and after the IMPROVE weighing laboratory move in 2011, with no net bias as shown in Figure S2.15. Over the high dust mass range (>10 μg/m^3), the "residual mass" tended to be larger

than estimates from the global equation after 2011, likely related to underestimated PBW, and tended to be smaller before 2011, possibly attributable to overestimated OM/OC ratio and the assumption of fully neutralized ammonium sulfate (AS) as discussed in Hand et al. (2019). The analytical changes in 2011 on dust could also contribute to the bias. Based on the IMPROVE advisory, the attenuation effect for light elements at high sample loadings was not corrected after the switch to the PANalytical XRF system and the implemented correction before 2011 could overcorrect the attenuation.

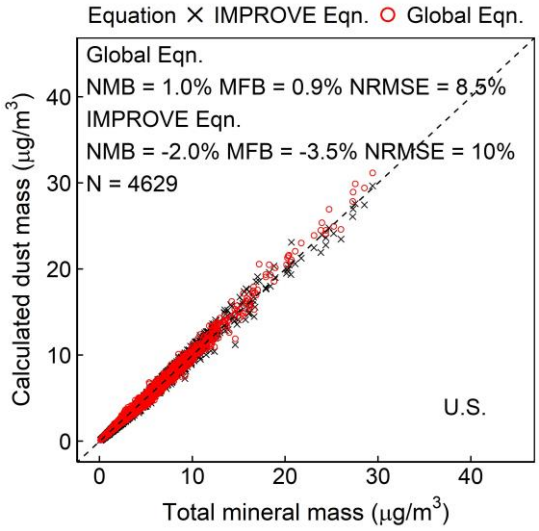

Figure 2.5 Comparison of the dust mass calculated by the global equation and the IMPROVE equation with the "total mineral mass" using dust-dominated (SOIL > 50% RCFM) $PM_{2.5}$ data in 2011−2018 from the U.S. IMPROVE network. Inset statistics are the normalized mean bias (NMB), mean fractional bias (MFB), and normalized root mean square error (NRMSE) of using the two equations for the entire data set. N is the number of speciation profiles.

Despite the overall systematic, yet unquantified, bias in the residual mass approach at IMPROVE sites, comparison across sites remains instructive because all sites are similarly affected by laboratory protocols. Figure 2.6 presents the performance of the global equation at individual U.S. IMPROVE sites including the Virgin Islands National Park site which is known to be impacted by African dust (Perry et al., 1997). Compared to the "total mineral mass", the global equation performs well at almost all sites (NMB within ±5%) and reduces the variable performance found

for the IMPROVE equation. The residual-mass approach shows similar improvement after using the global equation, although overestimation or underestimation was observed at some sites possibly related to the heterogeneity of soil carbonate content on a small scale (Smith et al., 2019). Soils in the West Coast region of the US are carbonate-poor due to Mediterranean climates (Machette, 1985; Smith et al., 2019), which may explain the overestimation at some sites in that region. The underestimation at the Pasayten site (48.4°N, 119.9°W) in the Northwest may be attributable to the influence of transported Asian dust (Hand et al., 2012, 2017). For the Virgin Islands National Park site, the global equation shows a much lower bias (NMB = 5.7%) than the IMPROVE equation (NMB = 15.9%). The overall improvement at IMPROVE sites is owing to the use of distinct MAL and CF for eastern and western sites in the global equation. Similar maps for MFB are shown in Figure S2.16.

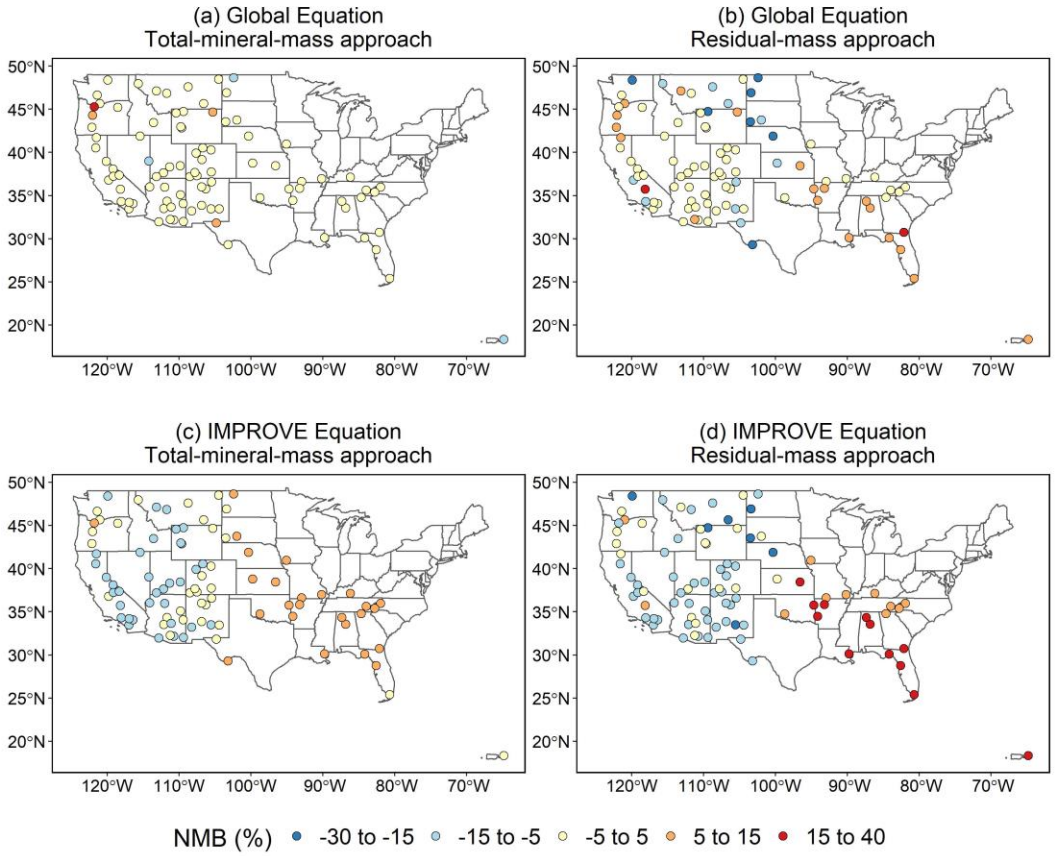

Figure 2.6 Normalized mean bias (NMB) for the dust mass calculated by (a, b) the global equation and (c, d) the IMPROVE equation compared to (a, c) the "total mineral mass" and (b, d) the "residual mass" at IMPROVE sites using daily-integrated dust-dominated (SOIL > 50% RCFM) $PM_{2.5}$ speciation data in 2011−2018 from the U.S. IMPROVE network. Only the sites with ≥5 data points were used to ensure representativeness. The number of selected IMPROVE sites is 95.

Evaluation of the global equation for Europe is challenging due to the paucity of complete analyses of PM speciation and the strong effect of sea salt and biomass burning on the data (Manders et al., 2010; Sigsgaard et al., 2015), as well as the transport of dust from both the Sahara and Sahel with different dust mineralogy. We identified a campaign in Italy with sufficient characterization to contribute to the evaluation of the global equation. Figure 2.7 shows that both the global equation and the IMPROVE equation perform well for African dust transported to Italy using the total-mineral-mass and residual-mass approaches. The global equation shows a somewhat lower NMB (-0.3% and -0.9% respectively) than the IMPROVE equation (2.8% and 2.1% respectively) for

both approaches. The MFB of using the global equation (-0.2% and -0.0% respectively) is also somewhat lower than the IMPROVE equation (2.8% and 3.0% respectively) for both approaches. The performance of the global equation at EMEP sites during other African dust episodes is shown in Figure S2.17. The high correlation between the estimates by the global equation and "total mineral mass" indicates that the MAL ratio (0.48) in the global equation used for African dust transported to southern Europe is appropriate for data examined in Figure S2.17. The small difference between the estimates by the global equation and IMPROVE equation indicates that the fractions of missing compounds considered in both equations are close to each other in this case. However, for desert dust significantly depleted or enriched in mobile elements and carbonate, the difference will be larger as shown in Figure 2.4.

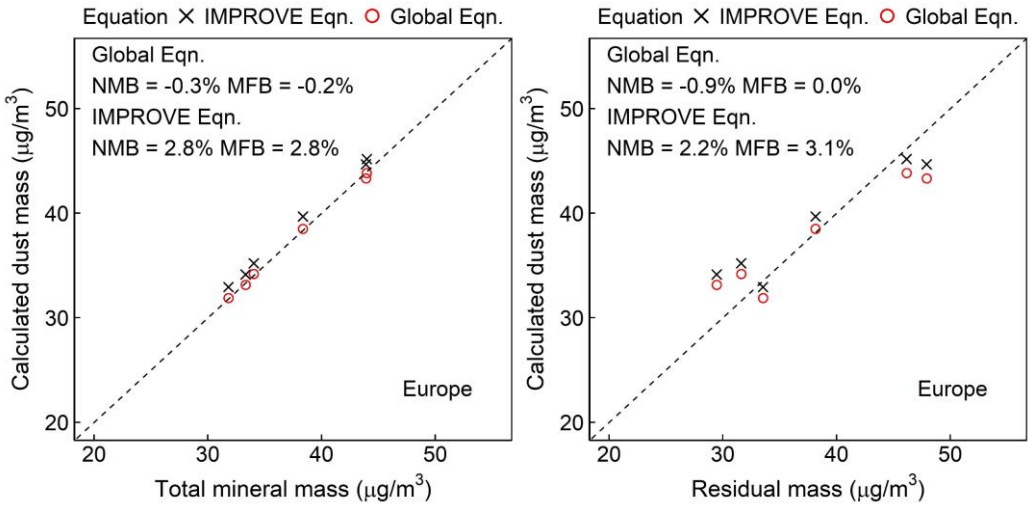

Figure 2.7 Comparison of dust mass calculated by the global equation and the IMPROVE equation with the "total mineral mass" (left) and the "residual mass" (right) for dust-dominated PM_{10} data (SOIL > 50% RCFM) measured at Montelibretti, Italy during an African dust event (20-30 June 2006). Data with Na/Al > 0.45 or K/Al > 0.5 are excluded to reduce the influence of non-dust sources. Inset statistics are the normalized mean bias (NMB) and mean fractional bias (MFB) of using the two equations.

We evaluated the global equation for transported African dust over the Atlantic islands as well as transported Asian dust over Japan and Korea shown in Figure S2.18. For African dust, the global equation shows a slightly lower bias (NMB = 1.4%, MFB = 1.6%) than the IMPROVE equation

(NMB = 2.0%, MFB = 1.7%). As for Asian dust, the global equation (NMB = -1.2%, MFB = -1.2%) performs similarly to the IMPROVE equation (NMB = -1.0%, MFB = -1.0%). The good performance of the global equation for desert dust over both source and non-source regions confirms that long-range transport does not substantially alter the MAL ratio of desert dust. However, the dust mass could be underestimated because the potential secondary salts and adsorbed water due to chemical aging are not included. Sufficient mineralogical information and hygroscopicity measurements are needed to better estimate transported dust that likely undergoes significant chemical aging.

Figure 2.8 shows the performance of the global equation and the IMPROVE equation for several major types of anthropogenic fugitive dust including paved road, unpaved road, and agricultural soil dust. Using the total-mineral-mass approach, the NMB for the global equation is similar to the IMPROVE equation for paved (3.3% vs 2.4%) and unpaved (-0.05% vs 1.1%) roads, while the bias for the global equation is much lower than the IMPROVE equation for agricultural soils (1.9% vs 15%). Similar results were found using the residual mass as the reference, although more noise was observed which is attributable to greater uncertainties in calculating the residual mass. The results suggest that the previously recognized overestimate by the IMPROVE equation of agricultural soil (Simon et al., 2010, 2011) can be remedied by accounting for the depletion of mobile elements and carbonates by irrigation. Because the evaluation is based on data with limited regional coverage, more measured data of anthropogenic dust in different regions are needed to further examine the performance of the global equation. It is difficult to derive general coefficients (MAL and CF) for other types of anthropogenic dust because their chemical composition can vary widely depending on the source and the area. However, an accurate dust equation is still important

to estimate the concentration of different types of anthropogenic dust if the missing compounds are not measured or some crustal elements have significant non-dust sources.

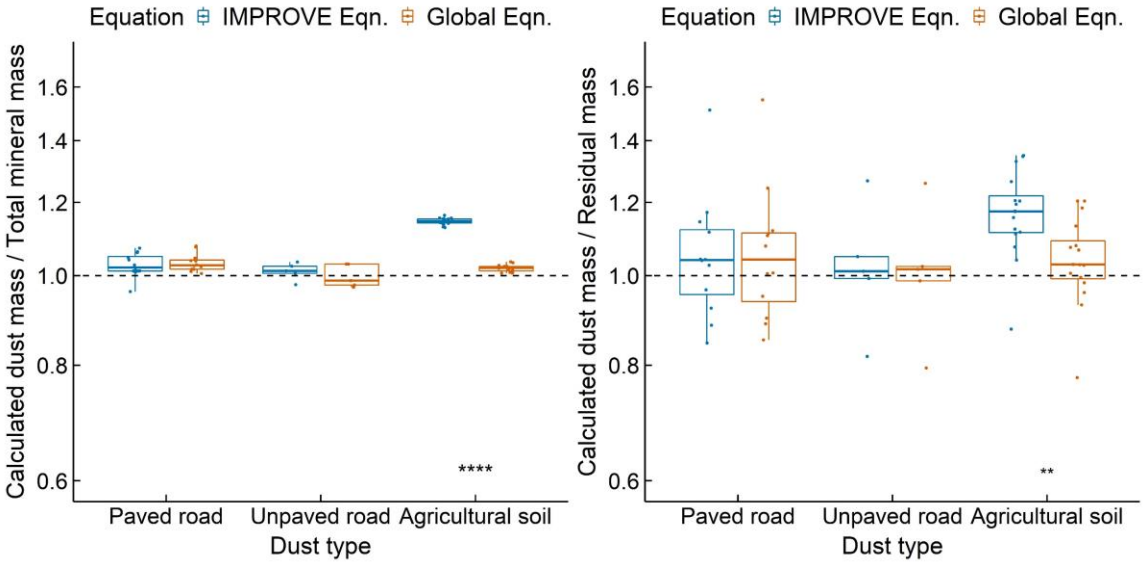

Figure 2.8 The ratio of the dust mass calculated by the global equation and the IMPROVE equation to the "total mineral mass" (left) and the "residual mass" (right) for paved road, unpaved road, and agricultural soil dust using $PM_{2.5}$ and PM_{10} data from the U.S. EPA's SPECIATE database and collected literature data (Amato et al., 2009; Zhao et al., 2006). Ratios are presented on a log scale. Data points are jittered to avoid overlap. The number of asterisks indicates the significance level (**P < 0.01, ****P < 0.0001) of the difference between two groups using the paired-sample Wilcoxon test.

2.5 Conclusions

This study develops a global-scale mineral dust equation used to estimate dust mass by building upon the IMPROVE equation that was designed for the U.S. The IMPROVE equation is widely used to calculate dust mass but prior work finds general underestimates in dust mass across the IMPROVE network, and had not been evaluated globally. Developing a global dust equation needs to address several issues especially the variation of dust composition across different regions. Three important mineral compounds, K_2O, MgO, and Na_2O, are usually either missing from previous dust equations or directly included without excluding biomass burning or sea salt sources. Our global dust equation incorporates the three compounds using Al as a surrogate by defining the MAL ratio as $(K_2O+MgO+Na_2O)/Al_2O_3$ that is specific to the dust components of K, Mg, and Na.

Analyses of dust data from major dust source regions of the world with negligible non-dust sources indicate that the MAL ratio is significantly different across regions with Australian and Sahelian dust exhibiting much lower MAL ratios than dust in other regions. A correction factor (CF) is used to account for other missing compounds, mainly CO_2 which is an important mineral compound but is commonly not measured and not included in previous dust equations. The amount of CO_2 in dust inferred from $CaCO_3$ content in topsoil and mineralogical data also varies substantially across regions. We provide flexible options for expanding the global equation to include adsorbed water and salt minerals in special types of dust such as saline dust, volcanic dust, and aged dust.

Applying the global dust equation with the region-specific coefficients (MAL and CF) to major dust source regions and using the IMPROVE equation as a benchmark demonstrates that the global equation provides evident improvement for estimating the dust mass. Compared to the reference dust mass, the resulting NMB and MFB of the estimates from the global equation are within ±1%, while those from the IMPROVE equation are -6 to 10%. The global equation also performs well (NMB and MFB within ±2%) for desert dust transported to non-source regions using coefficients that depend on their source regions and the pollution characteristics along the transport pathway. For major types of anthropogenic dust (paved road, unpaved road, and agricultural soil), the global equation generally performs well (NMB within ±5%) by applying the crustal MAL ratio and a high CF for road dust as well as a low MAL and CF for agricultural soil dust. Applying different coefficients to eastern and western IMPROVE sites, the global equation estimates the dust mass well (NMB within ±5%) at most sites.

Further improvement of the global equation would benefit from more complete and accurate measurements of mineral elements and CO_2 content in dust. More accurate estimation of organic

mass, sea salt, and particle-bound water can decrease the uncertainties in calculating the reference dust mass using the residual-mass approach. Assigning the coefficients on a finer spatial scale could further reduce the bias but would require much more data. Further examining the link of the MAL ratio and carbonate content between soil and aerosol is beyond the scope of our work but worthy of further study. Characteristics of different types of anthropogenic dust over various regions deserve further investigation. Despite the limitations, the global equation with region-specific coefficients has an absolute advantage over the IMPROVE equation with universal coefficients because it considers the variation in dust composition across different regions which is important for accurate estimation of dust mass on a global scale.

To our knowledge, this is the first study to develop and evaluate a region-specific global dust equation, which is challenging given the limitation of insufficient complete measurements of dust composition on a global scale and the lack of an absolute benchmark for reference dust mass. The use of regional coefficients for MAL and CF yields a promising method for estimating the dust mass not only outside the US but also within the US. This global equation can help future studies assess the measured dust contribution to aerosols more accurately when performing PM mass reconstruction and better understand the dust impacts on the environment and human health. More accurate representation of ground-based dust measurements can also benefit the development of atmospheric models and satellite remote sensing algorithms.

2.6 Supplementary Material

2.6.1 Expanded Global Equation

To develop a framework to address adsorbed water for special types of dust, we began with the single hygroscopicity parameter κ (Kreidenweis et al., 2008; Snider et al., 2016), and derived a water adjustment factor (WAF) as:

$$\mathrm{WAF} = 1 + \left(\kappa \frac{\mathrm{RH}}{100 - \mathrm{RH}}\right) \times \left(\frac{\rho_{\mathrm{water}}}{\rho_{\mathrm{dust}}}\right) \tag{S2.7}$$

where RH is relative humidity and ρ is density. The overall κ of dust can be obtained from hygroscopic growth measurements or estimated using mineralogical composition and known κ values of each mineral. For common desert dust, WAF approaches unity.

To account for salt minerals in special types of dust, we expanded the expressions of the MAL ratio, CF, and the global dust equation given that some elements can be associated with other anions besides carbonate and these anions are not considered for common desert dust.

The expanded expression of MAL is shown below:

$$\begin{aligned}\mathrm{MAL} &= \{[x + 1.20(1 - x)]\,\mathrm{K/Al} + [y + 1.66(1 - y)]\,\mathrm{Mg/Al} + [z + 1.35(1 - z)]\,\mathrm{Na/Al}\}/1.89 \\ &= [(1.20 - 0.20x)\mathrm{K/Al} + (1.66 - 0.66y)\,\mathrm{Mg/Al} + (1.35 - 0.35z)\,\mathrm{Na/Al}]/1.89\end{aligned} \tag{S2.8}$$

The variables x, y, and z represent mass ratios of K, Mg, and Na ions that exist in salt minerals apart from carbonates to total K, Mg, and Na, respectively. Specific mineralogical information is needed to estimate x, y, and z. For common desert dust, x, y, and z approach zero, which reduces the equation to the original expression of MAL where K, Mg, and Na are only included as oxides.

The expanded expression of CF combined with WAF is shown below:

$$CF=\frac{100\ wt\%}{100\ wt\%-\left[1\ wt\%+CO_2(wt\%)+Cl^-(wt\%)+F^-(wt\%)+SO_4{}^{2-}(wt\%)+NO_3{}^-(wt\%)\right]}\times WAF \quad (S2.9)$$

Carbonate is incorporated as CO_2 as in the original expression of CF. Specific mineralogical information is needed to estimate the abundance of all salt minerals. For common desert dust, the water content and salt minerals apart from carbonates are negligible, which reduces the equation to the original expression of CF.

The expanded global equation with expanded MAL and CF is shown below:

$$\begin{aligned}Dust&=\{1.89Al\times(1+MAL)+[\alpha+2.14(1-\alpha)]Si+[\beta+1.40(1-\beta)]Ca+1.36Fe+1.67Ti\}\times CF\\&=[1.89Al\times(1+MAL)+(2.14-1.14\alpha)Si+(1.40-0.40\beta)Ca+1.36Fe+1.67Ti]\times CF\end{aligned} \quad (S2.10)$$

The variable α represents the mass ratio of Si in fluorides to total Si for volcanic dust. The variable β represents the mass ratio of Ca ions that exist in salt minerals apart from carbonates to total Ca for saline dust, volcanic dust, aged dust, etc. Specific mineralogical information is needed to estimate α and β. For common desert dust, α and β approach zero, which reduces the equation to the original expression of the global equation.

2.6.2 Processing of a Soil Data Set

We used an available data set (Engelbrecht et al., 2016) with chemical and mineralogical measurements of PM_{10} and $PM_{2.5}$ surface soil samples from 65 sites worldwide to investigate the mass ratio of total CO_2 to CO_2 in $CaCO_3$ as well as the effects of particle size on the elemental ratios and CO_2 content. Since we are interested in desert dust, we excluded samples that are local

soils in Europe, lakebed or riverbed deposits, soils collected from roads and artillery firing pads, and special types of soil including red clay and green dust. We were therefore left with 38 samples in the final data set. This data set is missing measurements of Na, so we used available ICP-OES measurements of Na^+ as the substitute. For calculating the mass ratio of total CO_2 to CO_2 in $CaCO_3$ in dust source regions, we excluded the samples with desert soil in non-source regions (the Atlantic islands) and averaged the data of soils with the same particle size from the same site. Hence, 13 more samples were omitted.

2.6.3 Processing of Anthropogenic Dust Data from SPECIATE

We collected measured $PM_{2.5}$ and PM_{10} data of paved road, unpaved road, and agricultural soil dust from the EPA's SPECIATE5.0 database. The concentrations of species are given in the weight fraction form. Speciation profiles that are composites of other profiles were discarded to avoid double weighting. Data without information on the sampling date were excluded. We calculated the "residual mass" (RM) using the following equation:

$$\mathrm{RM} = 100\% - \mathrm{OC} \times (\mathrm{OM}/\mathrm{OC}) - \mathrm{EC} - {\mathrm{SO_4}}^{2-} - {\mathrm{NO_3}}^{-} - {\mathrm{NH_4}}^{+} - 1.8\mathrm{Cl}^{-}(\text{or Cl}) - \mathrm{PBW} \quad \text{(S2.11)}$$

When the measurement of ${\mathrm{NH_4}}^{+}$ is unavailable, we use $1.375\,{\mathrm{SO_4}}^{2-}$ and $1.29\ {\mathrm{NO_3}}^{-}$ in the equation assuming $(\mathrm{NH_4})_2\mathrm{SO_4}$ and $\mathrm{NH_4NO_3}$ referring to the IMPROVE algorithm. The common humidity protocol (35%) was adopted for calculating the PBW. Table S2.4 provides information about the selected data.

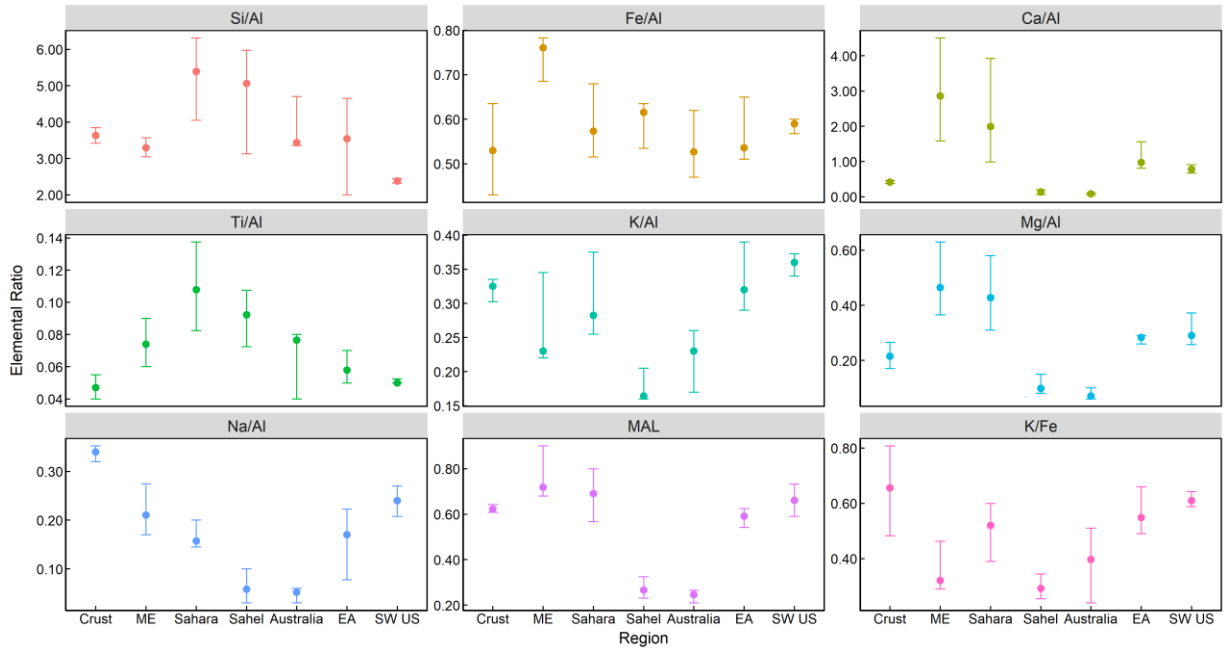

Figure S2.9 The median and interquartile range of elemental ratios and MAL in six dust source regions and the average global continental crust. The six dust source regions include the Middle East (ME), Sahara, Sahel, Australia, East Asia (EA), and Southwest US (SW US).

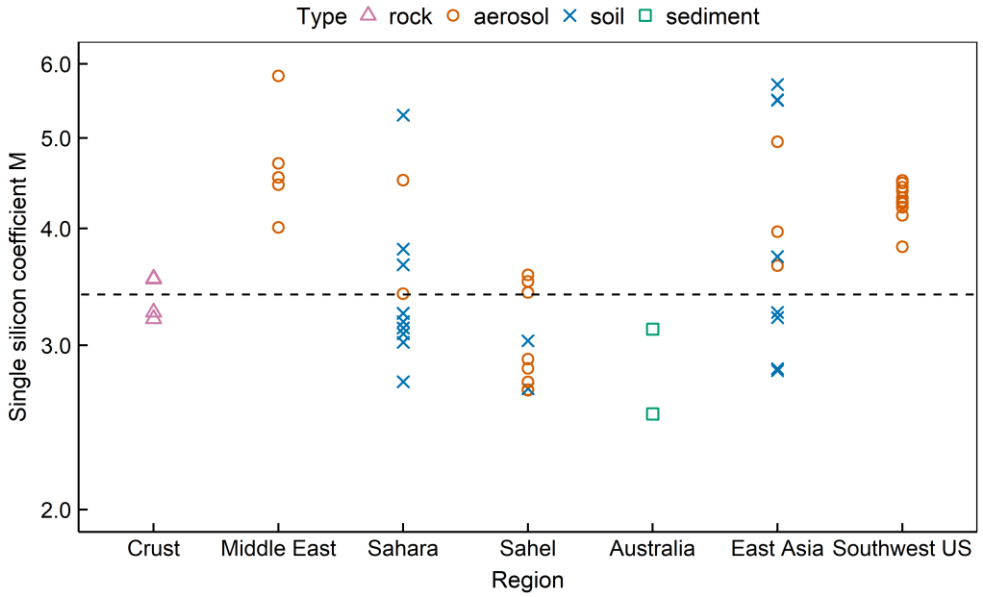

Figure S2.10 The single silicon coefficient M (total dust mass / Si) in six dust source regions and the average global continental crust shown on a log scale. The dashed line indicates the median coefficient M (3.4) in continental crust of four data sources.

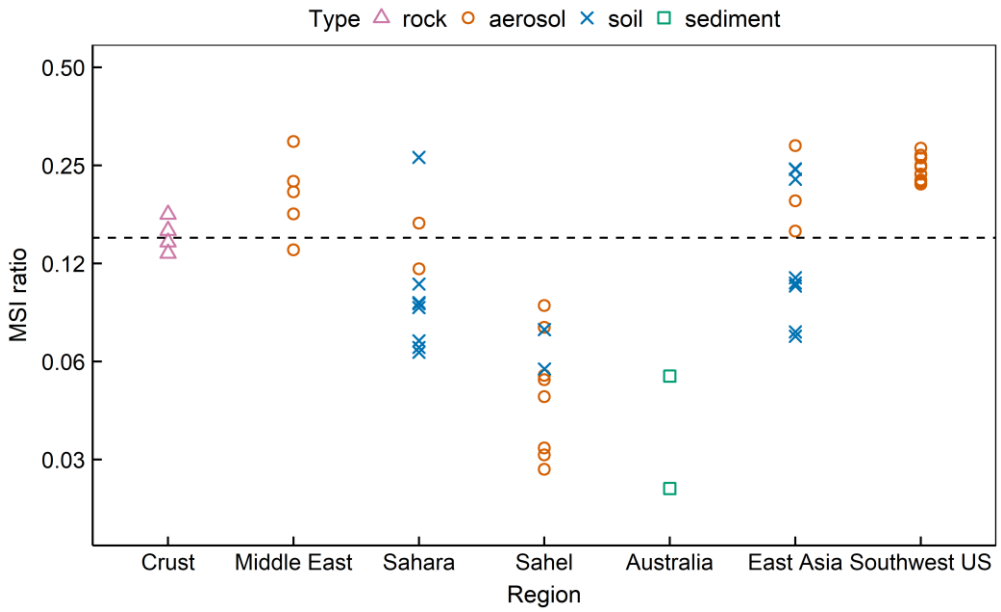

Figure S2.11 The MSI ratio of $(K_2O+MgO+Na_2O)/SiO_2$ in six dust source regions and the average global continental crust shown on a log scale. The dashed line indicates the median MSI ratio (0.15) in continental crust of four data sources.

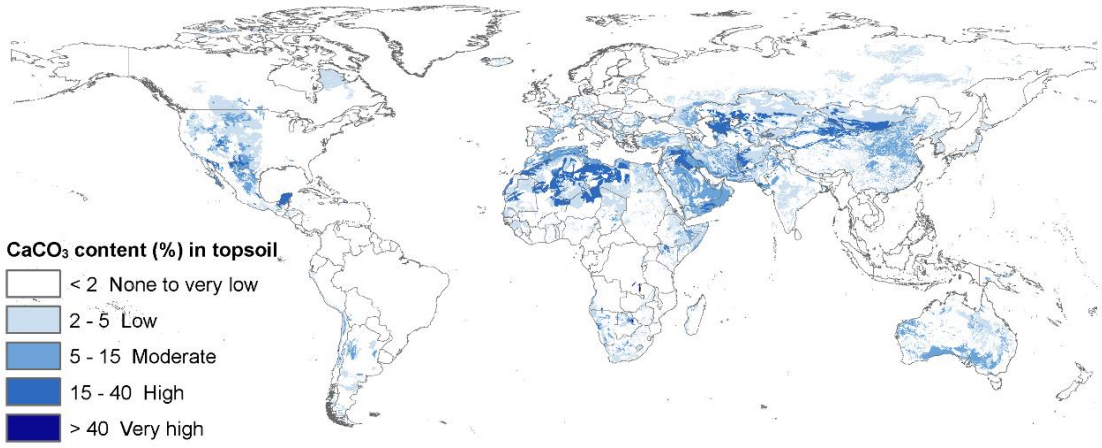

Figure S2.12 The distribution of $CaCO_3$ content (wt%) in topsoil from the Harmonized World Soil Database (HWSD version 1.21).

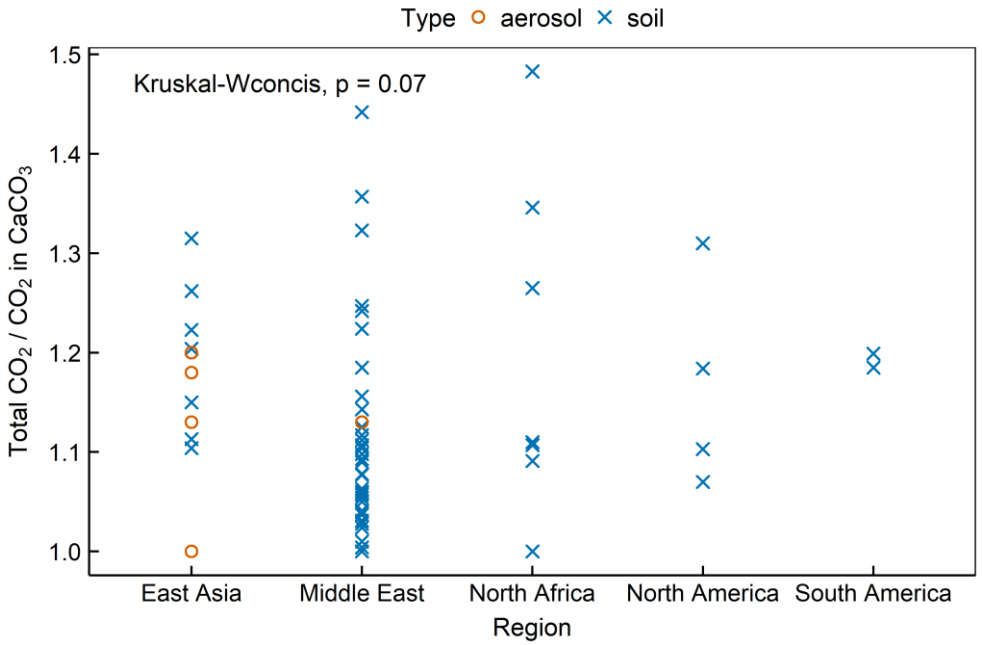

Figure S2.13 The mass ratio of total CO_2 to the CO_2 associated with $CaCO_3$ using measured data collected from the literature (Boose et al., 2016; Engelbrecht et al., 2016; Shen et al., 2009). Soils from islands were excluded and duplicated samples were averaged.

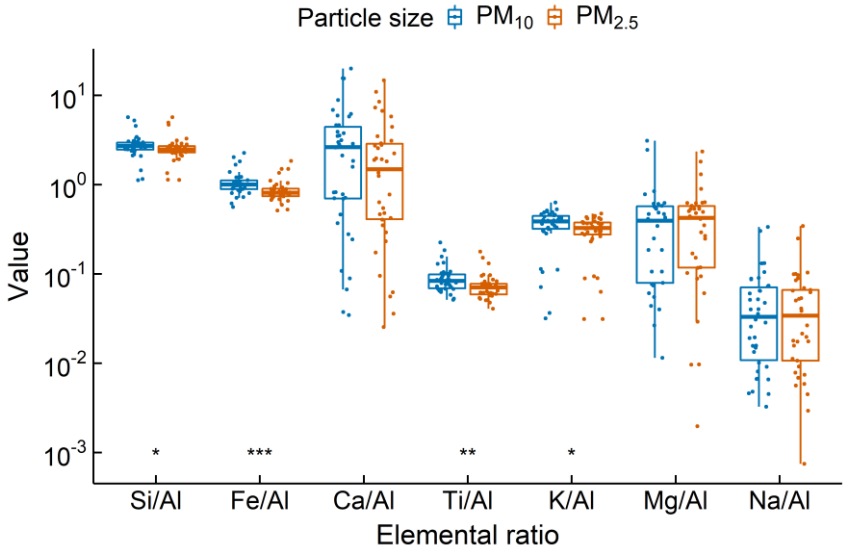

Figure S2.14 Particle size effect on elemental ratios of dust using a dataset of surface soil from arid regions (Engelbrecht et al., 2016). ICP-OES measurements of Na^+ were used to calculate Na/Al. Data points are jittered to avoid overlap. The number of asterisks indicates the significance level (*P < 0.05; **P < 0.01; ***P < 0.001) of the difference between two groups using the paired-sample Wilcoxon test.

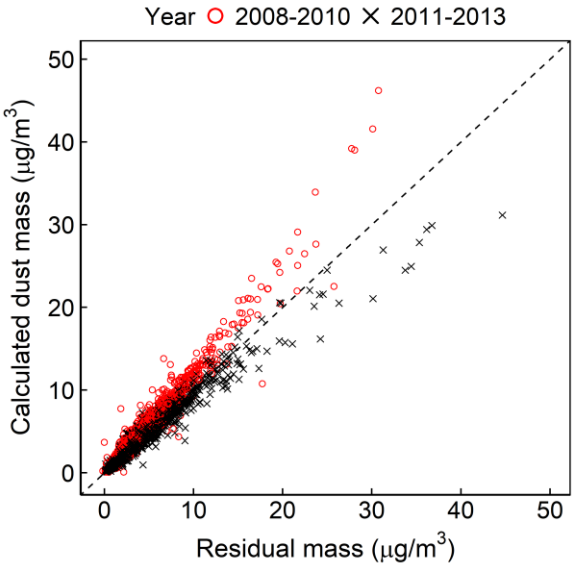

Figure S2.15 Comparison of the dust mass calculated by the global equation with the "residual mass" using dust-dominated (SOIL > 50% RCFM) $PM_{2.5}$ data during 2008-2010 (red circles) and 2011−2013 (black crosses) from the U.S. IMPROVE network.

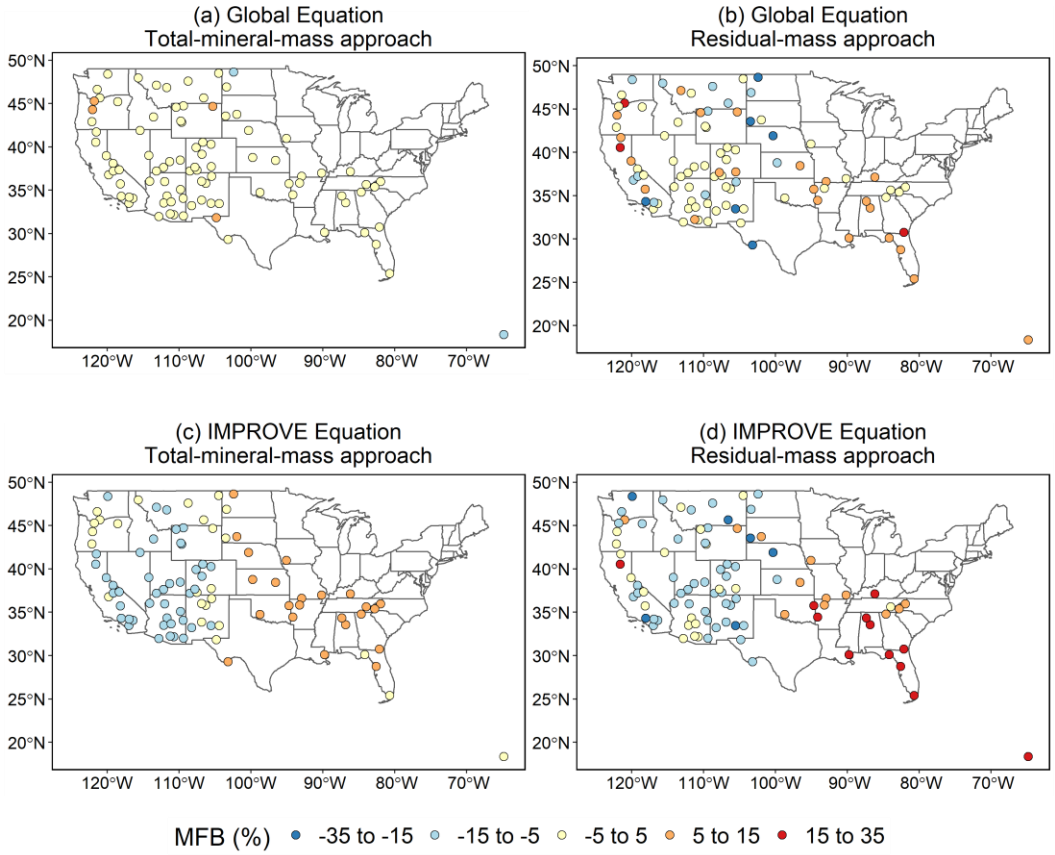

Figure S2.16 Mean fractional bias (MFB) for the dust mass calculated by (a, b) the global equation and (c, d) the IMPROVE equation compared to (a, c) the "total mineral mass" and (b, d) the "residual mass" at IMPROVE sites

using daily-integrated dust-dominated (SOIL > 50% RCFM) $PM_{2.5}$ speciation data in 2011−2018 from the U.S. IMPROVE network. Only the sites with ≥5 data points were used to ensure representativeness. The number of selected IMPROVE sites is 95.

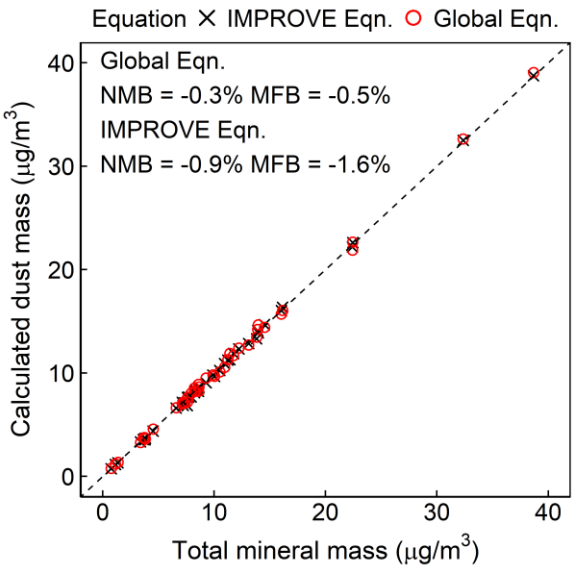

Figure S2.17 Comparison of the dust mass calculated by the global equation and the IMPROVE equation with the "total mineral mass" for PM_{10} data measured at EMEP sites during Saharan dust events (17-23 June 2012 and 28 June to 7 July 2012). Inset statistics are the normalized mean bias (NMB) and mean fractional bias (MFB) of using the two equations. The residual-mass approach was not applied because of insufficient measurements of other PM_{10} species.

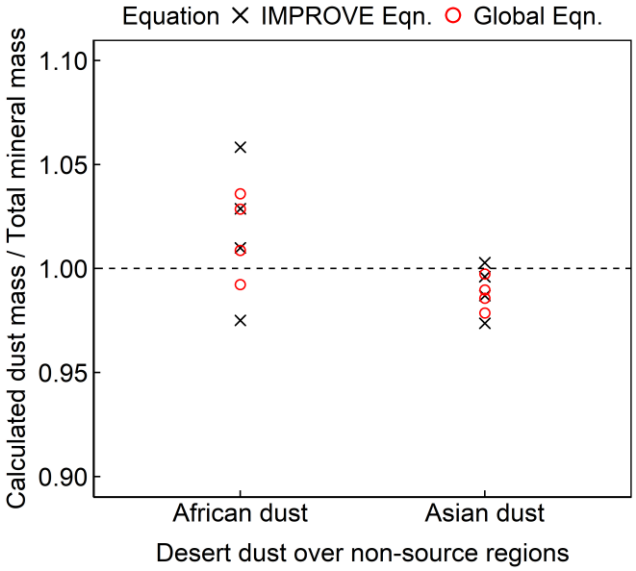

Figure S2.18 The ratio of the dust mass calculated by the global equation and the IMPROVE equation to the "total mineral mass" for African dust over the Atlantic islands as well as Asian dust over Japan and Korea. The amounts of dust elements are given in mass concentration or mass fraction, so only the mass ratios were shown in the plot for comparison.

Table S2.4 Anthropogenic dust data from the SPECIATE5.0 database used in this study

Dust Type	SPECIATE Profile Code	Sampling Region
Paved Road	4204, 4206, 4208, 4210, 4212	Texas
Unpaved Road	4217, 4219, 4221, 3966, 3968	Texas, Illinois
Agricultural Soil[a]	3297, 3298, 3307, 3308, 3312, 3313, 3332, 3333, 3337, 3338, 3357, 3358, 3392, 3393	California

[a]Mg and Na data are missing. The average elemental ratios of Mg/Al (0.07) and Na/Al (0.02) from another study (Chow et al., 2003) in the same location were therefore applied.

Chapter 3: Elemental Characterization of Ambient Particulate Matter for a Globally Distributed Monitoring Network: Methodology and Implications

This work was supported by the Clean Air Fund and the National Science Foundation (Grant 2020673), with additional contributions from NASA and the US Agency for International Development via the MAIA project at the Jet Propulsion Laboratory, California Institute of Technology. This chapter has been published as: Liu, X., Turner, J. R., Oxford, C. R., McNeill, J., Walsh, B., Le Roy, E., … Martin, R. V. (2024). Elemental Characterization of Ambient Particulate Matter for a Globally Distributed Monitoring Network: Methodology and Implications. ACS ES&T Air, 1(4), 283–293. https://doi.org/10.1021/acsestair.3c00069.

3.1 Abstract

Global ground-level measurements of elements in ambient particulate matter (PM) can provide valuable information to understand the distribution of dust and trace elements, assess health impacts, and investigate emission sources. We use X-ray fluorescence spectroscopy to characterize the elemental composition of PM samples collected from 27 globally distributed sites in the Surface PARTiculate mAtter Network (SPARTAN) over 2019−2023. Consistent protocols are applied to collect all samples and analyze them at one central laboratory which facilitates comparison across different sites. Multiple quality assurance measures are performed including applying reference materials that resemble typical PM samples, acceptance testing, and routine quality control. Method detection limits and uncertainties are estimated. Concentrations of dust and trace element oxides (TEO) are determined from the elemental dataset. In addition to sites in arid regions, a moderately high mean dust concentration (6 $\mu g/m^3$) in $PM_{2.5}$ is also found in Dhaka

(Bangladesh) along with a high average TEO level (6 μg/m^3). High carcinogenic risk (>1 cancer case per 100,000 adults) from airborne arsenic is observed in Dhaka (Bangladesh), Kanpur (India), and Hanoi (Vietnam). Industries of informal lead-acid battery and e-waste recycling as well as coal-fired brick kilns likely contribute to the elevated trace element concentrations found in Dhaka.

3.2 Introduction

Elemental characterization of ambient particulate matter (PM) provides concentrations of major (crustal) and trace elements, which can be used to estimate two PM components – mineral dust and trace element oxides (TEO) (Chow et al., 2015; Liu et al., 2022). As the most dominant global aerosol by mass, mineral dust can strongly reduce visibility, perturb climate systems, affect biogeochemistry, and cause adverse health effects (Knippertz & Stuut, 2014). Some epidemiological studies find that acute exposure to dust in PM_{10} (aerodynamic diameter <10 μm) or $PM_{2.5}$ (aerodynamic diameter <2.5 μm) during dust events as well as long-term exposure is associated with cardiovascular and respiratory events and diseases (Chan et al., 2008; Ostro et al., 2016; Soleimani et al., 2020; Stafoggia et al., 2016; Vedal et al., 2013; Vodonos et al., 2014). Dust has both natural and anthropogenic sources such as deserts, unpaved roads, construction, and agricultural activities. Trace elements are often more concentrated in $PM_{2.5}$ and primarily emitted by anthropogenic sources such as fossil fuel combustion, industries, and traffic. Many of the trace elements (e.g., Pb, As, Cd, Cr) have strong associations with morbidity and mortality (Krall et al., 2017; Paithankar et al., 2021). Concentrations of hazardous trace elements are particularly high in low-income and middle-income countries (LMICs) because of unregulated activities during urbanization and industrialization (Fuller et al., 2022; Majumder et al., 2021; Zhu et al., 2020). Ground-level observations of atmospheric elements are important to estimate the exposure to dust and trace elements, assess health risks, and investigate emission sources, as well as improve

atmospheric models. However, few monitoring networks of PM chemical composition exist in LMICs. Uniform sampling protocols and reliable analyses are also needed to enable comparisons across the world.

The Surface PARTiculate mAtter Network (SPARTAN, https://www.spartan-network.org/) is a long-term project that measures ground-based speciated PM at globally dispersed sites in densely populated regions (Snider et al., 2015). This network is designed to expand available global ground-based observations of PM composition and to provide information to evaluate and improve satellite-based estimates of $PM_{2.5}$. To our knowledge, SPARTAN is the only global monitoring network that measures the elemental composition of $PM_{2.5}$ and to a lesser extent, PM_{10}. Samples are collected from SPARTAN sites and analyzed for elemental composition at one central laboratory using consistent protocols, which ensures the comparability of data among the different sites. Beginning in 2019, the elemental measurements of SPARTAN samples have been conducted by Energy-Dispersive X-Ray Fluorescence (ED-XRF) spectroscopy, which is also used in the U.S. national $PM_{2.5}$ Chemical Speciation Network (CSN) and the U.S. Interagency Monitoring of PROtected Visual Environments (IMPROVE) network (Solomon et al., 2014). XRF is widely used to characterize the elemental composition of PM filters mainly because of its non-destructive nature that requires no acid digestion making the analysis less labor-intensive and allowing additional analysis such as Ion Chromatography (Galvão et al., 2018; Rodríguez et al., 2012). XRF can also measure the major dust element Si. Prior analysis of SPARTAN filters for 2013−2019 identified large global variations in measured airborne metal concentrations, but this analysis used Inductively Coupled Plasma Mass Spectrometry (ICP-MS) with nitric acid digestion that introduced uncertainty in extraction efficiencies for some crustal elements such as Fe and Al and

could not measure Si (McNeill et al., 2020). There is a need to examine more recent filters using XRF to assess the robustness of prior conclusions and their degree of persistence over time.

Especially for networks that operate over long periods across multiple sites, high-quality and consistent data is needed to interpret the measurements (Solomon et al., 2014). Robust quality assurance (QA) measures are needed including appropriate calibration, filter acceptance testing, routine analyses of blanks and standards, and appropriate blank subtraction to obtain reliable elemental data. Method detection limits (MDLs) and uncertainties for elemental concentrations are needed to evaluate the data quality.

Both high-quality elemental data and an accurate dust equation that sums dust compounds based on elemental data are essential to accurately estimate dust mass. However, most dust equations fail to account for all major dust compounds such as carbonate or fail to exclude non-dust components of some crustal elements such as K from biomass burning. A recently developed global dust equation with region-specific coefficients tackles these challenges and takes account of dust composition differences across regions (Liu et al., 2022), which allows calculating and comparing dust mass at globally distributed sites.

The objectives of this paper are to (1) describe the laboratory methods of measuring PM elemental composition with ED-XRF employed in the SPARTAN network; (2) describe QA methods and reported values; and (3) explore this new global PM elemental dataset from SPARTAN. The dataset is analyzed to examine the concentration levels of dust and TEO across globally distributed sites, evaluate health risks caused by hazardous trace elements, and explore emission sources of trace elements at the site with the highest estimated health risk levels.

3.3 Materials and Methods

3.3.1 Sampling Overview

Table 3.1 provides specific location information of 27 SPARTAN sites with available XRF data examined in this study. High population density and poorly sampled regions are two key factors in the selection of SPARTAN sites. Given SPARTAN's objective to evaluate and enhance $PM_{2.5}$ estimates derived from satellite retrievals of aerosol optical depth, site locations should have available sun photometers providing aerosol optical depth measurements. Site safety and access to electricity are also considered in the selection process. The chosen SPARTAN sites represent a variety of $PM_{2.5}$ concentrations and compositions. More details about early development of SPARTAN are provided by Snider et al. (Snider et al., 2015, 2016) and Weagle et al. (Weagle et al., 2018)

Sampling procedures and chemical analysis instrumentation have been updated over the last few years. Most sites retain the original standard sampling protocol, while select sites have more frequent sampling as part of the National Aeronautics and Space Administration (NASA)−Italian Space Agency (ASI) Multi-Angle Imager for Aerosols (MAIA) satellite mission (Diner et al., 2018). For the standard sampling protocol, AirPhoton (Baltimore, MD) SS5 sampling stations are employed to collect $PM_{2.5}$ and PM_{10} on 25 mm Teflon filters (PT25DMCAN-PF03A, Measurement Technology Laboratories) assembled in a cartridge as described by McNeill et al. (McNeill et al., 2020) The sampling station uses a sharp-cut cyclone that operates at the target flow rate of 5 L/min to collect $PM_{2.5}$ samples and 1.5 L/min to collect PM_{10} samples with a sampling period of 54 days for one filter cartridge. Each cartridge consists of six filters for $PM_{2.5}$, one for PM_{10}, and one for a field blank. The station collects $PM_{2.5}$ at staggered 3-hour intervals followed by 30-minute intervals of PM_{10} sampling over a 9-day period to generate one 24-hour $PM_{2.5}$ sample

covering one diel cycle (Figure S3.5). The entire 54-day period generates six 24-hour $PM_{2.5}$ samples and one 24-hour PM_{10} sample. The sampling time per day for the Canadian sites is doubled to increase filter mass loading given that the $PM_{2.5}$ concentration is typically low at these sites. Cartridges are assembled with pre-weighed filters in the central laboratory, shipped to each site for sampling, and shipped back to the central laboratory for a series of analyses including elemental analysis.

The SPARTAN sites that have been selected or established since 2021 as part of the MAIA mission are designed to collect $PM_{2.5}$ samples in the Primary Target Areas to study the health impacts of exposure to different types of airborne particles (Diner et al., 2018). These sites use the same instrumentation (AirPhoton SS5), Teflon filter, cyclone, and target flow rate of 5 L/min to collect $PM_{2.5}$ continuously for 24 hours from 9 am to 9 am at mission-defined frequency, currently every three days with a planned increase to every two days around the time of MAIA launch in 2025. The sites that apply the MAIA sampling protocol are indicated in **Table S3.2.**

About 1800 $PM_{2.5}$ samples and 140 PM_{10} samples collected during 2019−2023 as well as a few samples from December 2018 have been analyzed by XRF and are used in this study. The specific sampling period, seasons with samples, and number of samples for each site are summarized in Table S3.3 and Table S3.4.

3.3.2 Instrumentation and Standards

Pre- and post-sampling weighing of filters is performed using an automated weighing system (MTL AH500E). Prior to weighing, each filter is equilibrated for 24 hours in an environment where the temperature and relative humidity are controlled to 21.5 ± 1.0 °C and 35.0 ± 1.5%, respectively. Each filter is then weighed three times using a Mettler Toledo XPR6UD5 microbalance with a 0.5

µg readability within the controlled environment. The mean of these three measurements is calculated as pre- or post-weights and the difference between them provides the PM mass.

The Epsilon 4 ED-XRF instrument (Malvern PANalytical) is used to analyze the elemental composition of SPARTAN samples. Details about the Epsilon 4 configuration are provided in the Supporting Information (Text 3.6.1). Spectrum background subtraction (blank correction) is performed to obtain the net intensity of each element which is converted to mass loading (µg/cm^2) based on calibration curves established using a set of standards. Five analytical conditions with different mediums, X-ray filters, X-ray tube voltages and currents, and analysis time are applied to measure the 26 elements reported to SPARTAN as summarized in Table 3.1.

Table 3.1 Epsilon 4 ED-XRF application used to analyze SPARTAN samples

Reported Elements	Medium	X-ray filter[a]	Voltage[b] (kV)	Current (µA)	Analysis time (s)
Na, Mg, Al, Si, S, Cl	Helium	Ti	9	1666	720
K, Ca, Ti	Air	Al-50	12	1250	540
V, Cr, Mn, Ce	Air	Al-200	20	750	540
Fe, Co, Ni, Cu, Zn, As, Se, Rb, Sr, Pb	Air	Ag	50	300	540
Cd, Sn, Sb	Air	Cu	50	300	540

[a]Al-50 and Al-200 represent aluminum with a thickness of 50 and 200 µm, respectively. [b]The maximum X-ray tube voltage is 50 kV.

Calibration curves are established with 62 standards to include enough standards for each element preferably covering the mass loading range of SPARTAN samples. Commonly used and commercially available Micromatter (Surrey, Canada) single-element/compound reference materials (RMs) and the U.S. National Institute of Standards and Technology (NIST) standard reference material (SRM) 2783 are included in the standards. However, these RMs insufficiently represent filter material and mass loadings of common ambient PM samples (Yatkin et al., 2018).

Inter-laboratory evaluations show that the single compound and multi-element RMs generated recently by the University of California-Davis (UCD) are a useful resource to address this issue (Hyslop et al., 2019; Yatkin et al., 2018, 2020). Therefore, the UCD-made RMs are also included in our standards. Background subtraction is performed on all standards using corresponding blanks. The correlation coefficients of calibration curves determined by linear regression are ≥ 0.99 for all the elements except Mg with a correlation coefficient of 0.98.

3.3.3 Quality Assurance

Acceptance testing of filters is performed to ensure filter quality by evaluating the contamination level of elements on new filters from the manufacturer (Solomon et al., 2014). Five test filters from each new filter box (100 filters) are randomly selected and measured for elemental loadings using XRF. If the measurements are all within the acceptance limit, defined as the mean plus three times the standard deviation from measurements of 100 laboratory blank (LB) filters from multiple boxes, the new filter box is accepted for use in field sampling from the aspect of elemental analysis.

Routine quality control (QC) measures are conducted to verify calibration and monitor the long-term stability of the XRF instrument, which includes repeated analyses of one LB, RMs, and representative SPARTAN samples. The RMs include a UCD-made multi-element RM and NIST SRM 2783. The representative SPARTAN samples are nine selected samples that typify low, medium, and high loadings in the SPARTAN network. Details about the routine QC activities including frequencies, criteria, and corrective actions that are built on the QC methods used by IMPROVE (IMPROVE, 2022) are provided in the Supporting Information (Table S3.5 and Text 3.6.2). When new calibrations are performed, an additional quality check is performed by

conducting replicate measurements of Micromatter stoichiometric standards and ensuring the relative uncertainty is < 5%.

Background contamination levels from both the laboratory and field are considered in calculating the method detection limit (MDL) by using the greater of the MDL determined from either field blanks (FBs) or LBs. The FB filter is loaded along with the seven sample filters in one of the eight filter slots of a cartridge which is shipped to the field and installed in the sampling station without air pulled through the FB filter. Following methods used by the IMPROVE network (IMPROVE, 2022), the MDLs based on FBs (MDL_{FB}) and LBs (MDL_{LB} or analytical MDL) are calculated as the 95th percentile minus the median mass loading of 100 FBs and LBs, respectively. Concentrations below MDL including negative values are retained and posted on the SPARTAN website to avoid losing potentially useful data and to allow data users the flexibility to process these values. Both analytical MDLs and final MDLs are reported on the SPARTAN website.

The overall measurement uncertainties for elemental mass concentrations are estimated by combining additive and proportional (mass and volume) uncertainties:

$$\sigma = \sqrt{\left(\sigma_{\text{additive}} \times \frac{S}{V}\right)^2 + \sigma_{\text{proportion}}^2 \times C^2} = \sqrt{\left(\sigma_{\text{additive}} \times \frac{S}{V}\right)^2 + \left(\sigma_{\text{mass}}^2 + \sigma_{\text{volume}}^2\right) \times C^2} \quad (3.1)$$

where σ is the overall uncertainty for the elemental concentration (ng/m^3); σ_{additive} is the additive uncertainty (ng/cm^2); $\sigma_{\text{proportion}}$ is the total proportional uncertainty; C is the elemental concentration (ng/m^3); S is the known deposition area for 25 mm filters (3.53 cm^2); V is the sampled volume (m^3); σ_{mass} is the proportional mass uncertainty; and σ_{volume} is the proportional volume (flow rate) uncertainty. The additive uncertainty of each element is derived by dividing the MDL by 1.645 which is the critical value of the Z-score in a one-tailed test for a 5%

significance level. Deposition area and sampled volume are used to convert the unit of $\sigma_{additive}$ from mass loading (ng/cm^2) to mass concentrations (ng/m^3). σ_{mass} is estimated as the mean of relative standard deviations from monthly QC re-analyses of the representative SPARTAN samples using only the samples with mean > 3×MDL. σ_{volume} is estimated as the relative standard deviation from 120 flow rate measurements of six flow meters (3.5%).

3.3.4 Dataset Analysis

We use the XRF method described above at all SPARTAN sites and the global dust equation to estimate and compare concentration levels of dust and TEO at the global scale. First, ambient elemental mass concentrations (ng/m^3) are calculated using elemental mass loadings (ng/cm^2) measured by XRF and sampling flow measurements along with the deposition area on the filter. Dust concentrations are computed from concentrations of major crustal elements using the global-scale mineral dust equation as shown in Eq. (2.3) in Chapter 2. Region-specific coefficients are used for different SPARTAN sites (Table S3.6). TEO concentrations are calculated by summing all the oxides of measured elements retained after excluding S, Cl, and major crustal elements (Si, Al, Fe, Ca, Ti, Na, Mg, and K):

$$\begin{aligned}\mathrm{TEO} = {} & 1.79\mathrm{V} + 1.69\mathrm{Cr} + 1.63\mathrm{Mn} + 1.34\mathrm{Co} + 1.27\mathrm{Ni} + 1.25\mathrm{Cu} + 1.24\mathrm{Zn} + 1.43\mathrm{As} + \\ & 1.41\mathrm{Se} + 1.09\mathrm{Rb} + 1.18\mathrm{Sr} + 1.14\mathrm{Cd} + 1.20\mathrm{Sn} + 1.26\mathrm{Sb} + 1.20\mathrm{Ce} + 1.12\mathrm{Pb}\end{aligned} \tag{3.2}$$

where oxide factors summarized by Reff et al. (2009) are applied to calculate oxide concentrations by assuming common oxide forms of the trace elements.

The SPARTAN elemental dataset measured using this consistent methodology enables evaluation and comparison of health risks from exposure to deleterious trace elements in $PM_{2.5}$ across the set of globally distributed measurement sites. Both carcinogenic risk (CR) and non-carcinogenic risk

quantified by hazard quotient (HQ) are estimated by applying the U.S. Environmental Protection Agency (EPA) health risk assessment model (U.S. EPA, 2009), which includes the estimation of exposure concentration and the use of reference toxicity values (Table S3.7) (U.S. EPA, 2022). CR is estimated by multiplying exposure concentration and inhalation unit risk, while HQ is the ratio of exposure concentration to inhalation reference concentration (see details in Text 3.6.3). Summing the HQ for multiple elements yields the hazard index (HI). The mean elemental concentrations of available $PM_{2.5}$ samples from SPARTAN sites over the study period are used to estimate exposure concentrations. Elements with <50% of samples above MDLs at each site are excluded when calculating CR or HI for that site to ensure more reliable results.

We explore potential emission sources of $PM_{2.5}$ trace elements at the site with the highest estimated health risks based on measured elemental data. Correlation analysis is conducted first to examine relationships among the elements by calculating non-parametric Spearman's correlation coefficients. Elements that are used in the health risk assessment or have source specificity are selected to perform correlation analysis. Elements with <50% of samples above MDLs at the specific site are excluded. Principal component analysis (PCA) (Henry & Hidy, 1979) is thereafter applied to qualitatively explore putative emission sources of trace elements by extracting principal components (PCs) that represent most of the variance from normalized elemental data (see details in Text 3.6.4).

3.4 Results and Discussion

3.4.1 Quality Assurance

Figure S3.6 provides an example of acceptance testing where mass loadings of all elements on each test filter from six new filter boxes are within acceptance limits and therefore these new filter

boxes are considered “clean” in terms of elemental contamination level. The monthly measurements of a UCD-made multi-element RM, NIST SRM 2783, and representative SPARTAN samples within acceptance limits provide an indicator of instrument stability (Figure S3.7, Figure S3.8, Figure S3.9). These repeated measurements of the UCD-made multi-element RM over time also demonstrate high long-term precision (relative standard deviation within 6%) and high accuracy (relative bias within ±5%) by comparing with the certified or reference mass loading. The consistent positive or negative bias observed for some elements is attributable to the use of multiple types of standards in the calibration. SRM 2783 is difficult to keep flat, a requirement for it to receive consistent radiation during each analysis, because its filter membrane does not have a support ring (Hyslop et al., 2019), resulting in lower long-term precision than the UCD-made multi-element RM.

The field blank-based MDL is generally higher than the lab blank-based MDL (Table S3.8), reflecting the greater range of conditions to which the field blank is exposed. The relative difference between the two MDL estimates is small for most elements but significant for sulfur which is not yet well understood. About 90%−100% of the samples are above MDL for major (crustal) elements except for Mg, while about 10%−90% are above MDL for trace elements. The overall uncertainty integrating both additive and proportional uncertainties is reported for each measured elemental concentration on the SPARTAN website. The total proportional uncertainty is estimated to be 4−11% for elements that have at least one re-analyzed sample with a mean > 3×MDL (Table S3.9). For elements without estimated $\sigma_{\text{proportion}}$ (Cr, Ni, Cu, Cd, Sn, and Sb), σ_{additive} can approximate the overall expected uncertainty for most samples because the concentrations of these elements are usually low. In addition to this “bottom-up” approach, a “top-down” approach using collocated sampling (Hyslop & White, 2008, 2009) will be applied to provide more

comprehensive estimates of uncertainties when sufficient collocation data are available in the future.

3.4.2 Dust and TEO Levels

Table S3.10 and Table S3.11 summarize elemental concentration levels (mean ± standard deviation) in $PM_{2.5}$ and PM_{10} samples from SPARTAN sites, respectively. To understand the magnitude of elemental uncertainties, we use measured elemental concentrations for the Dhaka site as an example and compare standard deviations of the measured concentrations with uncertainties for the means. The uncertainty is much lower than the standard deviation by about one order of magnitude for most elements (Figure S3.10), indicating that the measurement uncertainty is negligible. For most sites, the uncertainty is significantly lower than the standard deviation for most elements (Table S3.12).

The mass concentration levels of dust and TEO calculated for $PM_{2.5}$ and PM_{10} samples from SPARTAN sites are listed in Table S3.3 and Table S3.4, respectively. The two tables also provide $PM_{2.5}$ and PM_{10} concentrations along with corresponding air quality levels by comparing with the World Health Organization's annual Air Quality Guideline and Interim Targets (WHO, 2021). Figure 3.1 shows the mean relative contributions of dust and TEO to $PM_{2.5}$ samples across globally distributed SPARTAN sites. Dust contributes about 20%−40% to $PM_{2.5}$ for sites located in deserts or otherwise impacted by dust events (Abu Dhabi, UAE; Ilorin, Nigeria; Fajardo, Puerto Rico; Rehovot, Israel; Haifa, Israel; and Addis Ababa, Ethiopia). The Abu Dhabi and Ilorin sites have the highest mean $PM_{2.5}$-dust concentrations of ~10 $\mu g/m^3$ as well as the highest mean PM_{10}-dust concentrations of ~50 $\mu g/m^3$. At the Kanpur (India) site, both natural dust (from the neighboring Thar Desert) and anthropogenic dust (e.g., road and agricultural dust) (Bhaskar & Sharma, 2008;

Misra et al., 2014; Prospero, 2002) contribute to a similarly high mean $PM_{2.5}$-dust concentration (9 $\mu g/m^3$, 21%) as that observed at desert sites. The Dhaka (Bangladesh) site, located in a humid region, also exhibits a moderately high mean concentration of dust (6 $\mu g/m^3$) that is likely driven by anthropogenic sources such as road dust or construction dust (Kabir et al., 2022). Nonetheless, the relative dust contribution to $PM_{2.5}$ in Dhaka is 16%, lower than that of desert sites because of the more significant $PM_{2.5}$ contribution from non-dust species in Dhaka. The highest mean TEO concentration in $PM_{2.5}$ is found in Dhaka (6 $\mu g/m^3$) followed by Hanoi, Vietnam (1 $\mu g/m^3$), while the TEO concentration at other sites is < 1 $\mu g/m^3$. The relative TEO contribution to $PM_{2.5}$ varies from <1% at most sites (e.g., Abu Dhabi, Rehovot, and Fajardo) to 4% in Hanoi, and reaches up to 16% in Dhaka. Prior analysis of SPARTAN filters for 2013-2019 using ICP-MS similarly identified high trace element concentrations at the same Dhaka and Hanoi sites, but mineral dust concentrations were uncertain due to weak acid digestion and lack of Si measurements, and the oxide forms of trace elements were not considered (McNeill et al., 2020). Our analysis finds that the TEO concentration at Dhaka not only persists but is even higher when oxide forms are included. This high average TEO level at Dhaka will be further discussed in Section 3.4.

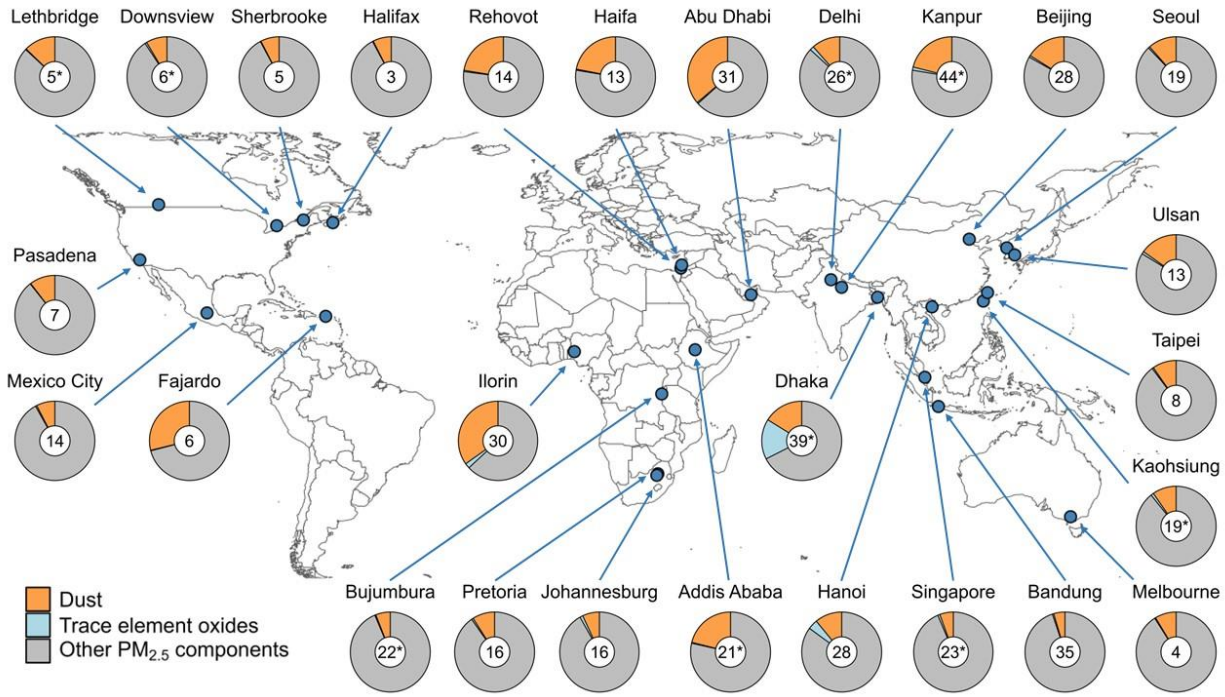

Figure 3.1 Mass fraction of dust and trace element oxides (TEO) in $PM_{2.5}$ based on mean concentrations at SPARTAN sites. Inset values are mean $PM_{2.5}$ concentrations ($\mu g/m^3$). Inset asterisks indicate sites that do not have samples from all four seasons.

3.4.3 Health Risk Assessment

Figure 3.2 shows the contributions of trace elements (As, Pb, Cd, Co, and Ni) to carcinogenic risk (CR, defined in Section 2.4) for adults across SPARTAN sites with ≥50% of samples above MDLs for at least three examined trace elements. The highest total CR of 7.7×10^{-5} for adults (about 77 cancer cases per 1,000,000 adults) occurs in Dhaka followed by Kanpur and Hanoi. The CR caused only by As in Dhaka, Kanpur, and Hanoi exceeds the benchmark (Choi et al., 2022; U.S. EPA, 1991) of 1×10^{-5} and is higher than the sum of CR caused by the remaining elements, suggesting a concerning level of atmospheric As at these sites. Estimates based on global simulation from Zhang et al. (2020) indicate similarly high CR caused by atmospheric As in several regions including Asian countries such as India and Bangladesh. Previous studies find that As pollution in groundwater is a serious problem in South and Southeast Asia (Fendorf et al., 2010; Podgorski & Berg, 2020; Shaji et al., 2021), while our measured data indicate that exposure to As through

inhalation of $PM_{2.5}$ may also be of concern in these regions. In addition to As, the CR caused by Co or Cd alone also exceeds 1×10^{-5} in Dhaka. As and Co are major contributors to CR for most examined SPARTAN sites, while Pb contributes significantly to CR mainly in Dhaka and Ni to CR in Singapore. Specific CR estimates for each element for both adults and children at different sites are provided in Table S3.13. The CR value for adults is four times as high as that for children because of the difference in exposure duration used for the CR calculation (Text 3.6.3). Dhaka is the only site where the combined CR exceeds the benchmark of 1×10^{-5} for both adults and children.

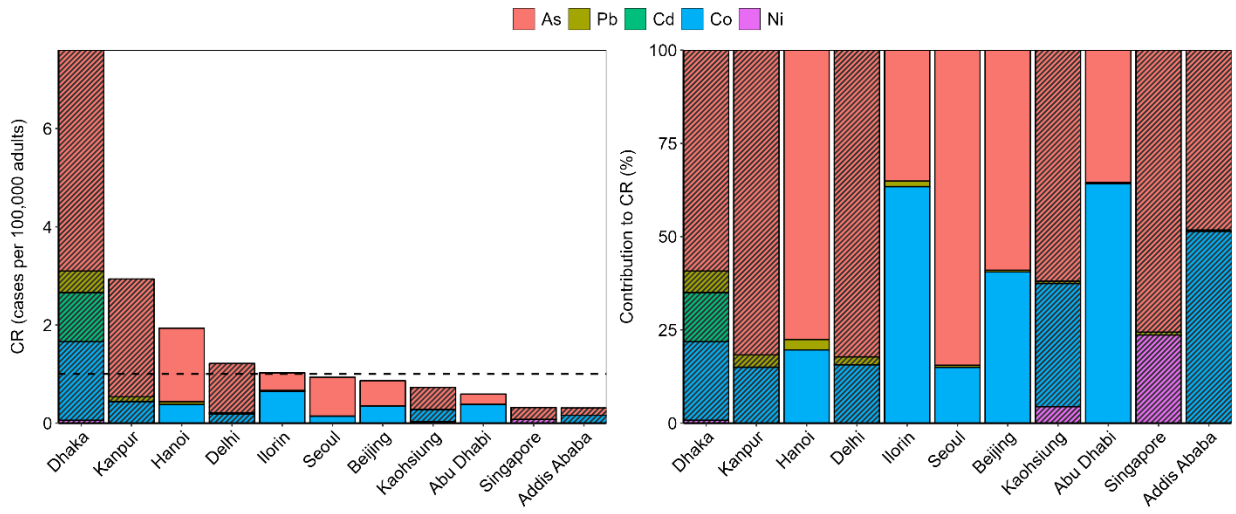

Figure 3.2 Absolute (left) and relative (right) contributions of trace elements to carcinogenic risk (CR) for adults estimated using mean elemental concentrations in $PM_{2.5}$ samples from SPARTAN sites with ≥50% of samples above MDLs for at least three examined trace elements. The black dashed line represents the 1×10^{-5} cancer benchmark for adults. Sites are sorted by the total CR. Sites with shading lines do not have samples from all four seasons.

Figure 3.3 displays the contributions of trace elements (As, Cd, Co, Ni, Mn, and V) to hazard index (HI, defined in Section 2.4) across SPARTAN sites with ≥50% of samples above MDLs for at least three examined trace elements. The inhalation reference concentration of Pb is not available to assess its hazard quotient (HQ, defined in Section 2.4). Specific HQ estimates for each element at different sites are provided in Table S3.14. Dhaka has the highest HI of 6.8, followed by Kanpur, Hanoi, Singapore, Beijing, and Kaohsiung all exceeding the threshold (U.S. EPA, 1991) of unity.

Similar to CR, the non-carcinogenic risk caused by As, Cd, or Mn alone exceeds the benchmark at the Dhaka site, which suggests that multiple large emission sources may exist and have significant adverse health impacts in Dhaka. Kanpur also has a high non-carcinogenic risk caused solely by As exceeding the threshold. The relative contributions of different elements to HI vary significantly across different sites. The highest absolute and relative contributions of V and Ni to HI are observed at the Singapore site. Given that V and Ni are often used as indicators for residual oil combustion and Singapore Strait has the highest density of emissions originating from shipping globally (Johansson et al., 2017), the high contribution of V and Ni to HI implies a considerable health impact of shipping emissions in Singapore.

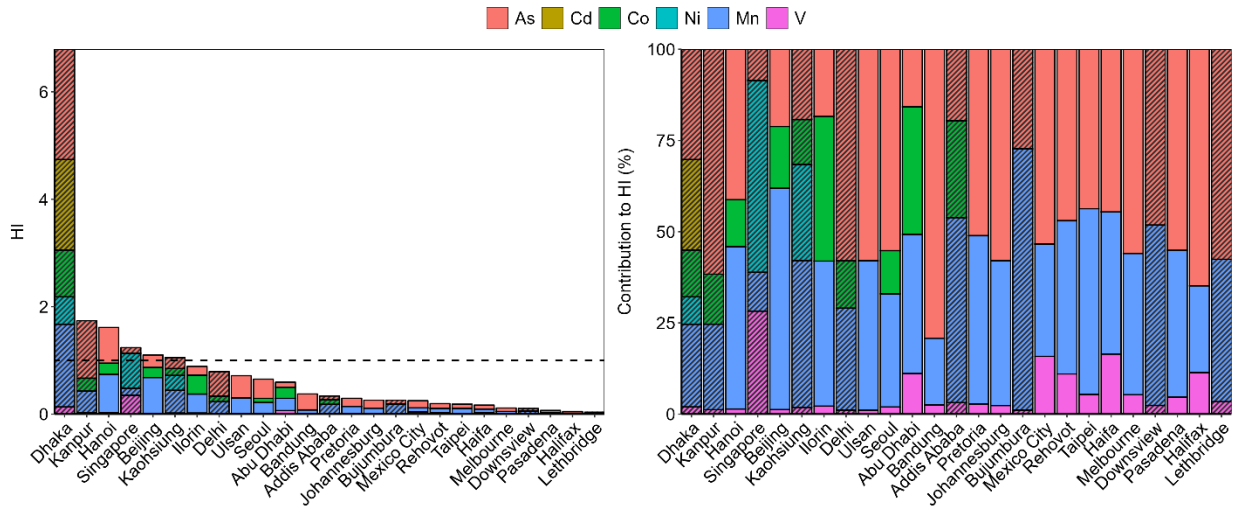

Figure 3.3 Absolute (left) and relative (right) contributions of trace elements to hazard index (HI) estimated using mean elemental concentrations in $PM_{2.5}$ samples from SPARTAN sites with ≥50% of samples above MDLs for at least three examined trace elements (As, Cd, Co, Ni, Mn, and V). The dashed line represents the threshold HI of 1. Sites are sorted by the total HI. Sites with shading lines do not have samples from all four seasons.

3.4.4 Investigation into TEO Sources in Dhaka

The high TEO concentration observed at the Dhaka site with the highest CR and HI caused by hazardous trace elements across SPARTAN warrants further investigation. The Dhaka site is in a busy area with mixed residential, commercial, and industrial uses where many emission sources

could contribute to its high TEO concentration. The breakdown of oxides of different trace elements in $PM_{2.5}$ samples from Dhaka indicates oxides of Zn (3.8 μg/m^3) and Pb (1.1 μg/m^3) are major contributors to this high TEO concentration (Figure S3.11). This $PM_{2.5}$-Pb level substantially exceeds the U.S. National Ambient Air Quality Standard (NAAQS) for Pb of 0.15 μg/m^3 in total suspended particles as a 3-month average (U.S. EPA, 2016b), suggesting a significant Pb pollution issue at Dhaka. High concentrations of Zn (6.0 μg/m^3) and Pb (5.4 μg/m^3) in $PM_{2.5}$ were also observed at a site located ~4 km north of the SPARTAN site in Dhaka from December 2012 to February 2013 (Rahman et al., 2020).

We explore potential emission sources of trace elements in $PM_{2.5}$ at the Dhaka site. Figure 3.4 shows correlation coefficients among different elements for $PM_{2.5}$ samples from the Dhaka site. High positive correlations ($r > 0.9$, $P < 0.0001$) are observed among Pb, Sb, Se, and As, and among crustal elements including Al, Si, Ca, Ti, and Fe. The strong correlation of As with Pb, Sb, and Se suggests that the high airborne As level at the Dhaka site is likely primarily driven by anthropogenic sources rather than natural dust sources. Significant correlations ($r > 0.8$, $P < 0.0001$) exist among Zn, Cd, and Co, while V is only significantly correlated with Ni ($r = 0.6$, $P < 0.01$) suggesting its unique emission source. In contrast to other trace elements, Cr correlates well with crustal elements ($r > 0.7$, $P < 0.0001$).

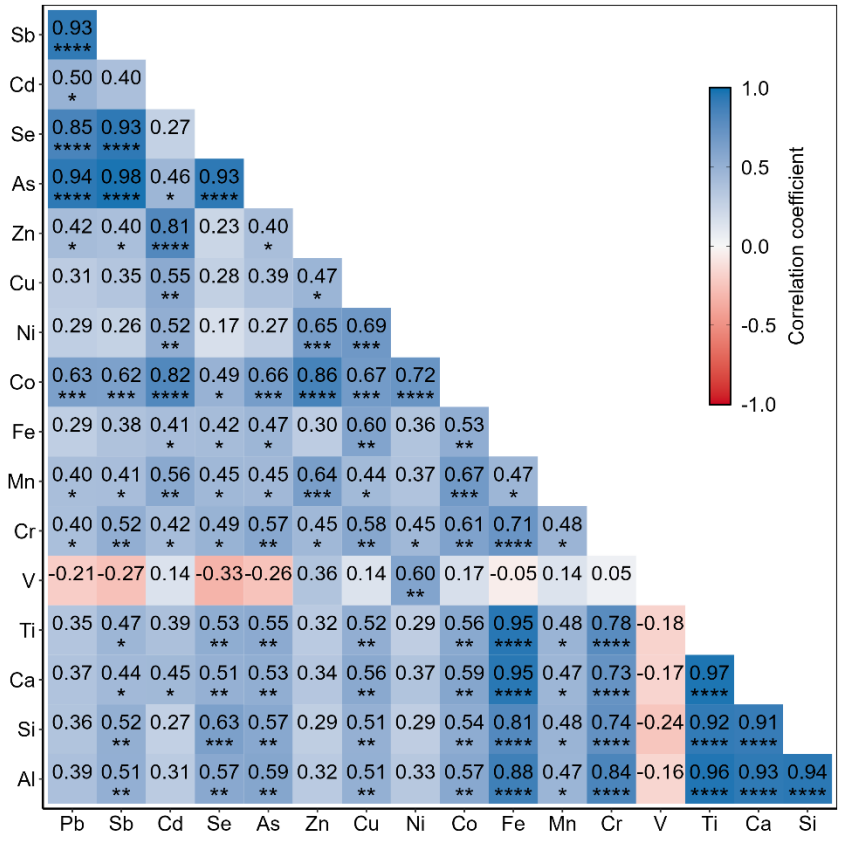

Figure 3.4 Correlation matrix for elemental concentrations of $PM_{2.5}$ samples from the Dhaka site. Elements are sorted by atomic mass. The number of asterisks indicates the significance level (*P < 0.05; **P < 0.01; ***P < 0.001; ****P < 0.0001). The color indicates the correlation coefficient.

The PCA results for the Dhaka site (Table S3.15) are consistent with patterns observed in the correlation analysis. Interpretation of each principal component (PC) is provided in the Supporting Information (Text 3.6.5). The PCA results interpreted with existing literature and an understanding of potential sources around the site location, indicate that coal-fired brick kiln industries (Guttikunda et al., 2013; Lee et al., 2021; Weyant et al., 2014) and unregulated lead-acid battery recycling (Kumar et al., 2022; Majumder et al., 2021) likely contribute to the elevated levels of Pb and As found in Dhaka, while traffic (Councell et al., 2004; Rahman et al., 2019) and the growing industries of informal e-waste recycling (Awasthi et al., 2016; Mowla et al., 2021) may be responsible for the elevated concentrations of Zn, Cd, and Co in Dhaka. Given the lack of surface wind data and a micro-scale emission inventory, further investigation of potential sources is

constrained. More samples from future sampling will help to better understand trace element levels and the emission sources in Dhaka.

3.5 Outlook

In summary, we described the methodology of PM elemental characterization with X-ray fluorescence for the SPARTAN network. Samples are collected from globally distributed urban cities and analyzed at one central laboratory using consistent protocols, which ensures the comparability of data across different sites. Reference materials that mimic filter material and mass loadings of typical PM samples are applied to calibrate the instrument. Acceptance testing is conducted to ensure filter quality and routine quality control measures are implemented to monitor instrument stability. Background levels from both the lab and field are considered to calculate method detection limits. Additive and proportional uncertainties are estimated to provide overall measurement uncertainties. Uncertainty is generally substantially lower than the standard deviation of measured concentrations, indicating that for most sites and elements measurement uncertainty is negligible. We applied this globally distributed PM elemental dataset to compare concentration levels of dust and trace element oxides (TEO) and health risks caused by hazardous trace elements across the SPARTAN sites. The average dust concentration contributes up to 40% to $PM_{2.5}$ for sites located in arid regions. The Dhaka site located in a humid region features both a moderate dust level (6 $\mu g/m^3$, 16%) and the highest TEO level (6 $\mu g/m^3$, 16%) of $PM_{2.5}$ contributed mainly by oxides of Zn and Pb. Dhaka has the highest total carcinogenic risk (~77 cancer cases per 1,000,000 adults) and the highest hazard index (6.8) exceeding the thresholds. High carcinogenic risk level caused only by As (>1 cancer case per 100,000 adults) in Dhaka, Kanpur, and Hanoi suggests significant airborne particulate As pollution. Growing industries of informal recycling of lead-acid batteries and e-waste as well as coal-fired brick kiln industries are identified

as likely sources contributing to the elevated concentrations of trace elements (Pb, As, Zn, Cd, and Co) in Dhaka.

More samples representative of all four seasons are needed to better estimate dust and TEO levels across different sites and enable time-series analyses. Both health risk assessments and source apportionment analyses in this paper are intended to provide qualitative information about health risk levels and emission sources at SPARTAN sites. As the elemental dataset grows in the future, more complete measurements of exposure concentrations can be used to estimate health risks. Uncertainties exist in exposure parameters and reference toxicity values used for the risk assessment. The bioavailability of trace elements may be useful to further evaluate health risks (Huang et al., 2018). Further investigation of the oxidation state of trace elements would better constrain their mass concentrations. Given the sample collection schedule of periodic sampling over nine days onto a single filter, considerable smearing across factors is likely present in the PCA analysis. In the future, other models such as Positive Matrix Factorization (PMF) (Paatero & Tapper, 1994), can be used to perform source apportionment based on the data of all PM components and associated uncertainties at sites applying the MAIA protocol with increased sampling frequency and a larger sample size. Despite the limitations, the concerning health risk level caused by hazardous trace elements observed at the Dhaka, Kanpur, and Hanoi sites demonstrates the need for urgent attention to survey elemental composition to identify regions with elevated trace elements and inform air quality management strategies.

3.6 Supplementary Material

3.6.1 Configuration of the Epsilon 4 ED-XRF Instrument

Epsilon 4 is equipped with a 15-Watt silver anode X-ray tube, a high-resolution silicon drift detector, X-ray filters, a sample spinner, and a helium purge facility. X-ray filters placed between the X-ray tube and the sample are used to improve the signal-to-noise ratio by reducing the intensity of interfering tube lines and background. The spinner rotates the sample holder during measurement to reduce the effects of sample heterogeneity and physical imperfections. Helium instead of air is used to measure elements lighter than K because air absorbs low-energy radiation from these elements. The spectrum of fluorescence intensities versus energy is fitted to individual line profiles of elements present in the sample through a deconvolution process. K-lines are used to determine intensities for most elements, while L-lines are used for Ce and Pb because the required energy of their K-lines exceeds the measurement range of the instrument. The deconvolution method in Epsilon 4 cannot resolve line profiles of Na and Mg well, so their K-lines are represented using assigned energy ranges.

3.6.2 Definition of Acceptance Limits in Quality Control Criteria

Acceptance limits in the quality control criteria for blanks and reference materials are defined differently following the IMPROVE method (IMPROVE, 2022). For PTFE blanks, the acceptance limit is defined as the mean plus three times the standard deviation from measurements of 100 lab blanks. For the UCD-made multi-element RM, uncertainties provided in the certification are used as the acceptance limit, i.e., ± 10% for certified loadings or 20% for reference loadings. For NIST SRM 2783, the acceptance limit is defined as root-mean-squared-relative-errors (RMSREs) plus three times the standard deviations of absolute relative biases from multiple measurements. The absolute relative bias is calculated using $|C - C_{cer/ref}|/C_{cer/ref}$ where C is the monthly

measurement of SRM 2783 and $C_{cer/ref}$ is the certified or reference mass loading. For representative SPARTAN samples, the acceptance limit is defined as ±1 for Z-score which is calculated using the following equation:

$$Z_i = \frac{C_i - C_{ref,i}}{\sqrt{U_i^2 + U_{ref,i}^2}} \quad \text{(S3.3)}$$

where C_i is the mass loading of each representative SPARTAN sample i; $C_{ref,i}$ is the reference loading represented using the mean from multiple measurements of the sample; U_i is the uncertainty (combining additive and proportional mass uncertainties) of C_i; and $U_{ref,i}$ is the standard deviation from multiple measurements of the sample.

3.6.3 Method of Health Risk Assessment

Both carcinogenic and non-carcinogenic risks are estimated by applying the U.S. EPA health risk assessment model (U.S. EPA, 2009). The exposure concentration (EC) through inhalation for each element is calculated first by the following equation:

$$\mathrm{EC} = \mathrm{CA} \times \frac{\mathrm{ET} \times \mathrm{EF} \times \mathrm{ED}}{\mathrm{AT}} \quad \text{(S3.4)}$$

where CA is the contaminant concentration in air (μg/m^3); ET is the exposure time (24 hours/day); EF is the exposure frequency (350 days/year); ED is the exposure duration (6 years for children and 24 years for adults); and AT is the averaging time (for carcinogens, AT = 70 years × 365 days/year × 24 hours/day; for non-carcinogens, AT = ED × 365 days/year × 24 hours/day). The carcinogenic risk (CR) and non-carcinogenic risk represented using hazard quotient (HQ) can be calculated as:

$$CR = EC \times IUR \tag{S3.5}$$

$$HQ = \frac{EC}{RfC} \tag{S3.6}$$

where IUR is the inhalation unit risk $(\mu g/m^3)^{-1}$ and RfC is the inhalation reference concentration ($\mu g/m^3$). The IUR and RfC values used in this study are obtained from the Regional Screening Level (RSL) Resident Ambient Air Table (U.S. EPA, 2022) and listed in Table S3.7. Summing the HQ for multiple elements yields the hazard index (HI). The CR benchmark of 1×10^{-5} (one cancer per 100,000 people) is used to identify significant carcinogenic risk, and HI > 1 is used to indicate significant non-carcinogenic risk (Choi et al., 2022; Huang et al., 2018; U.S. EPA, 1991).

3.6.4 Method of Principal Component Analysis (PCA)

The elemental data is first normalized by subtracting the mean from each data point and dividing by the standard deviation, generating a Z-score for each data point. A covariance matrix is then calculated for the normalized data, and eigenvalues and eigenvectors of the covariance matrix are computed to identify principal components (PCs). The number of retained PCs is selected based on both the scree plot that displays eigenvalues for individual PCs and the Kaiser criterion that recommends retaining PCs with eigenvalue > 1.0 (Cattell, 1966; Kaiser, 1960). Varimax rotation is performed to better interpret the results by trying to associate each element to primarily one PC. To conduct the analysis with a sufficient sample size (≥15), we relax the flow rate criteria (5 L/min ± 10%) and include samples collected at a start or end flow rate within 3.8−5.8 L/min which corresponds to a cyclone cut-point range of 2.1−3.4 μm. The correlations between elements are treated as similar in this size range.

3.6.5 Interpretation of PCA Results for Dhaka

Table S3.15 presents the PCA results for the Dhaka site. Four PCs are extracted accounting for 90% of the total variance and explaining 70%−100% of the variance for all elements except Mn (33%) which has an emission source different from the four PCs. The first PC (PC1) is strongly correlated with crustal elements and moderately correlated with Cr, potentially indicating mineral dust mixed with emissions from tannery industries. Soils and groundwater in the Hazaribagh area close to the sampling site were heavily contaminated with Cr by waste discharged from tannery industries (Khan et al., 2020; Rahman et al., 2019). PC2 has high loadings (> 0.95) of Pb, Sb, Se, and As, indicating a profile that may be related to emissions from coal combustion sources such as coal-fired brick kilns. Many elements including Pb, As, Se, and Sb are emitted during coal combustion (Tian et al., 2014). Across South Asia, bricks are widely produced in coal-fired kilns without pollution control to meet the high demand for construction materials due to rapid urbanization (Weyant et al., 2014). Hundreds of coal-fired brick kilns exist within and around Dhaka, significantly affecting air quality and human health (Guttikunda et al., 2013; Lee et al., 2021). Another major emission source is unregulated lead-acid battery (LAB) recycling. The rising demand for motor vehicles leads to the growth of LAB recycling industries, while recycling is performed mainly through unregulated and dangerous smelting processes in LMICs such as Bangladesh (Kumar et al., 2022). Dhaka is located in one of the Pb-contaminated hotspot areas in Bangladesh with a significant number of LAB recycling and lead smelting industries (Majumder et al., 2021). Other elements besides Pb such as Sb and As can also be emitted from LAB smelters (Johnston et al., 2019). PC3 is dominated by Zn, Cd, and Co, which suggests traffic and industrial emissions. The Dhaka site is surrounded by heavily congested roads within ~1 km and Zn is a typical tracer for traffic emissions such as tire wear, brake wear, and lubricant oil (Councell et al.,

2004). Zn, Cd, and Co can be emitted from numerous nearby paint, rubber, plastic, and printing industries as well as informal e-waste recycling shops (Leyssens et al., 2017; Mowla et al., 2021; Rahman et al., 2019). The rapid digitalization in Bangladesh and export from elsewhere cause increasing e-waste that is informally recycled through unregulated combustion such as open burning, which may contribute to the elevated elemental concentrations found here (Awasthi et al., 2016; Mowla et al., 2021). PC4 likely represents shipping emissions given its high loadings of V and Ni. Many ships travel on the Buriganga River in the southwestern part of Dhaka and ships use residual oil which emits V and Ni (Begum et al., 2011).

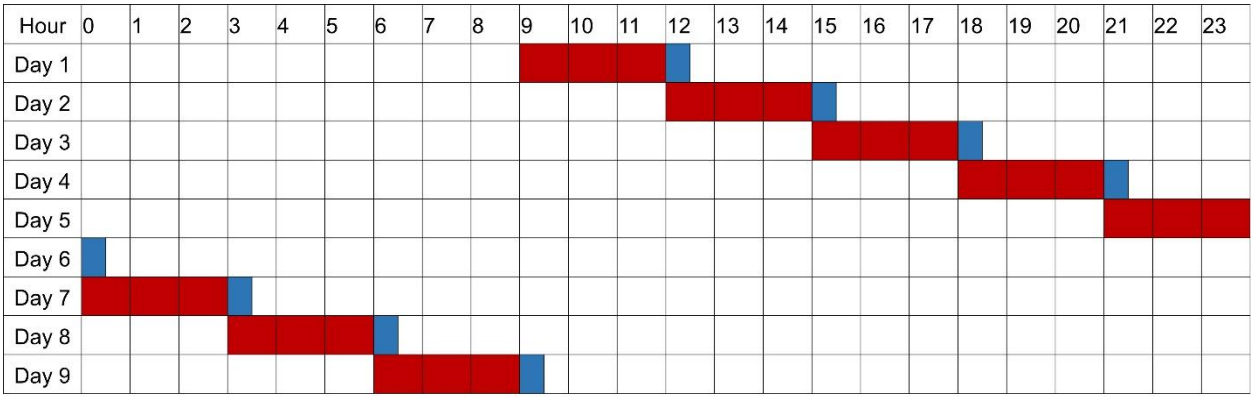

Figure S3.5 A 9-day sampling period following the SPARTAN standard sampling protocol. The red color indicates $PM_{2.5}$ sampling time while the blue color represents PM_{10} sampling time.

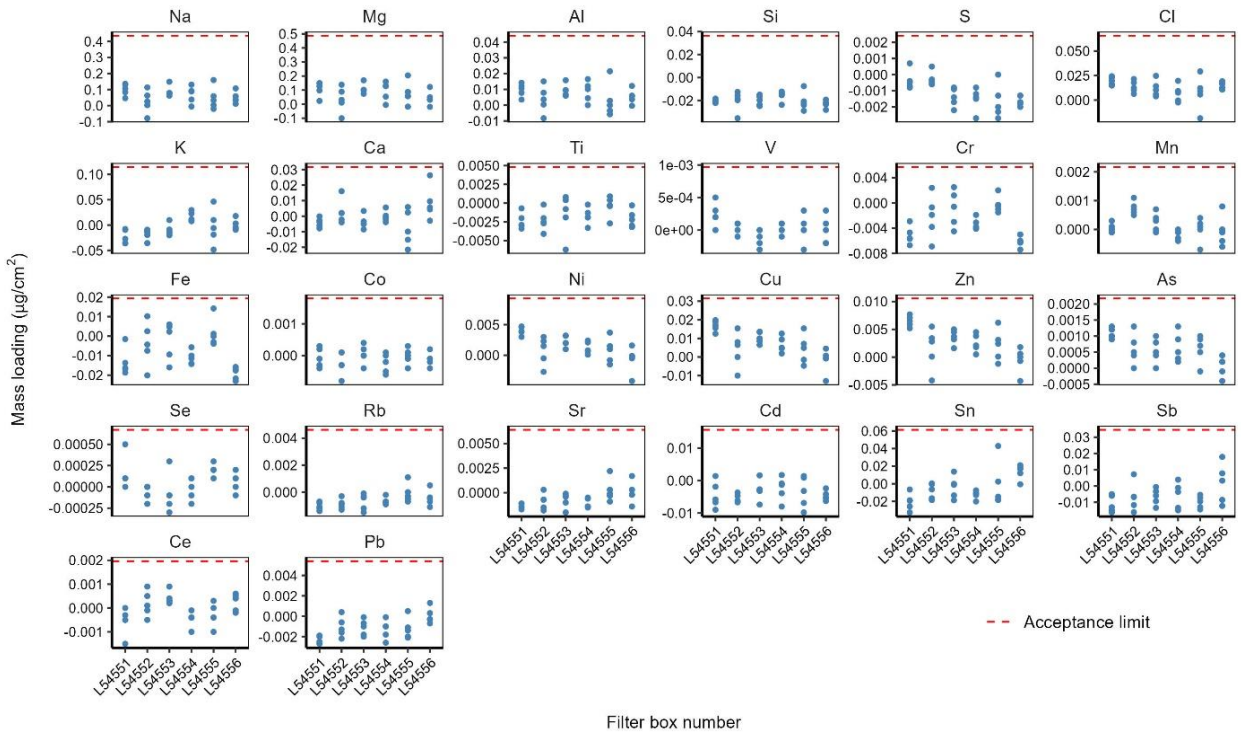

Figure S3.6 Acceptance testing results of six new filter boxes. The dashed red line represents the acceptance limit that is defined as the mean plus three times the standard deviation from measurements of 100 lab blanks.

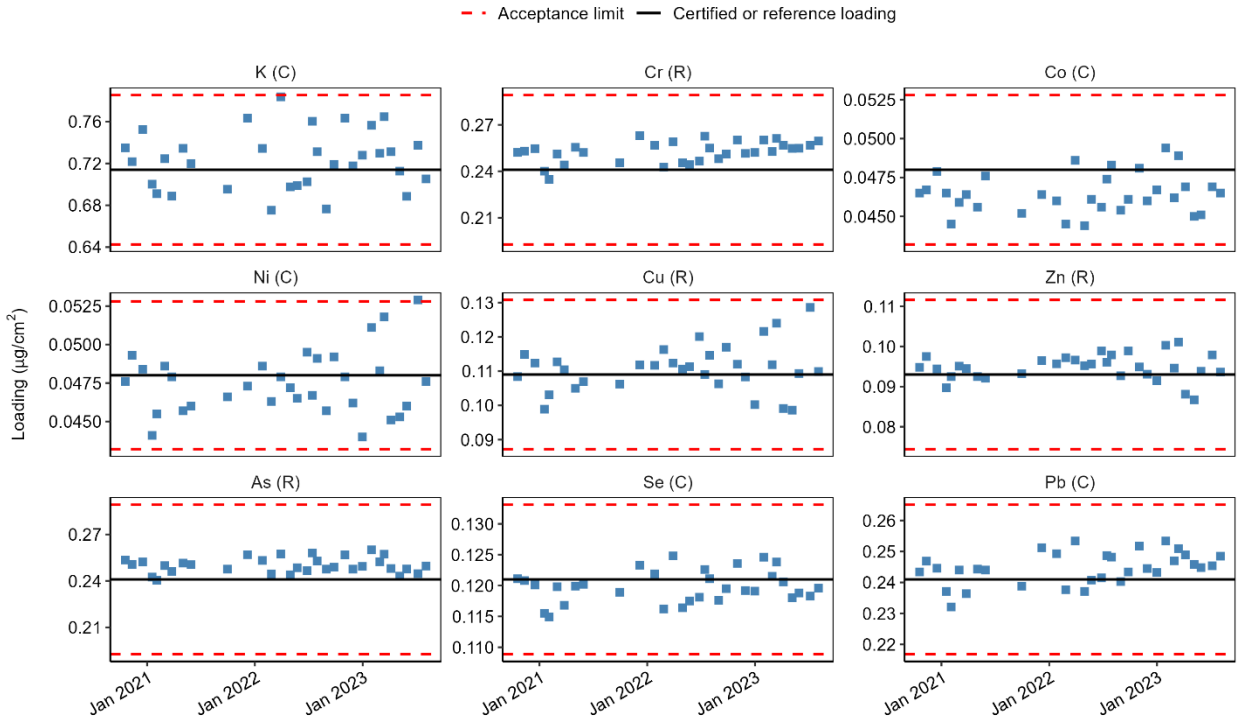

Figure S3.7 Quality control plots of a multi-element reference material made by the University of California-Davis. The solid black line represents the certified or reference mass loading and the dashed red line represents the acceptance

limit, i.e., ±10% uncertainty of certified loadings or ±20% of reference loadings. Elements that have certified or reference mass loadings are indicated by a (C) or (R), respectively, after the element symbol.

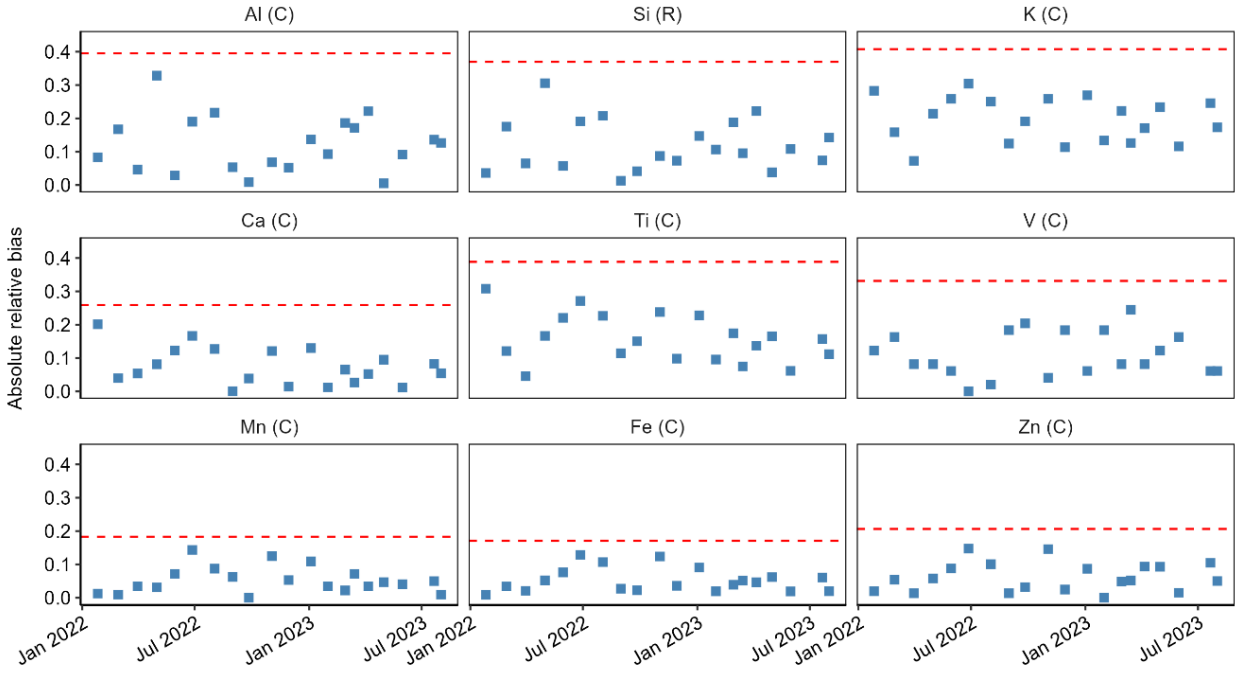

Figure S3.8 Quality control plots of absolute relative bias for NIST SRM 2783. The dashed red line represents the acceptance limit that is defined as the root mean squared relative error plus three times the standard deviation of the absolute relative bias from multiple measurements of NIST SRM 2783. Elements that have certified or reference mass loadings are indicated by a (C) or (R), respectively, after the element symbol.

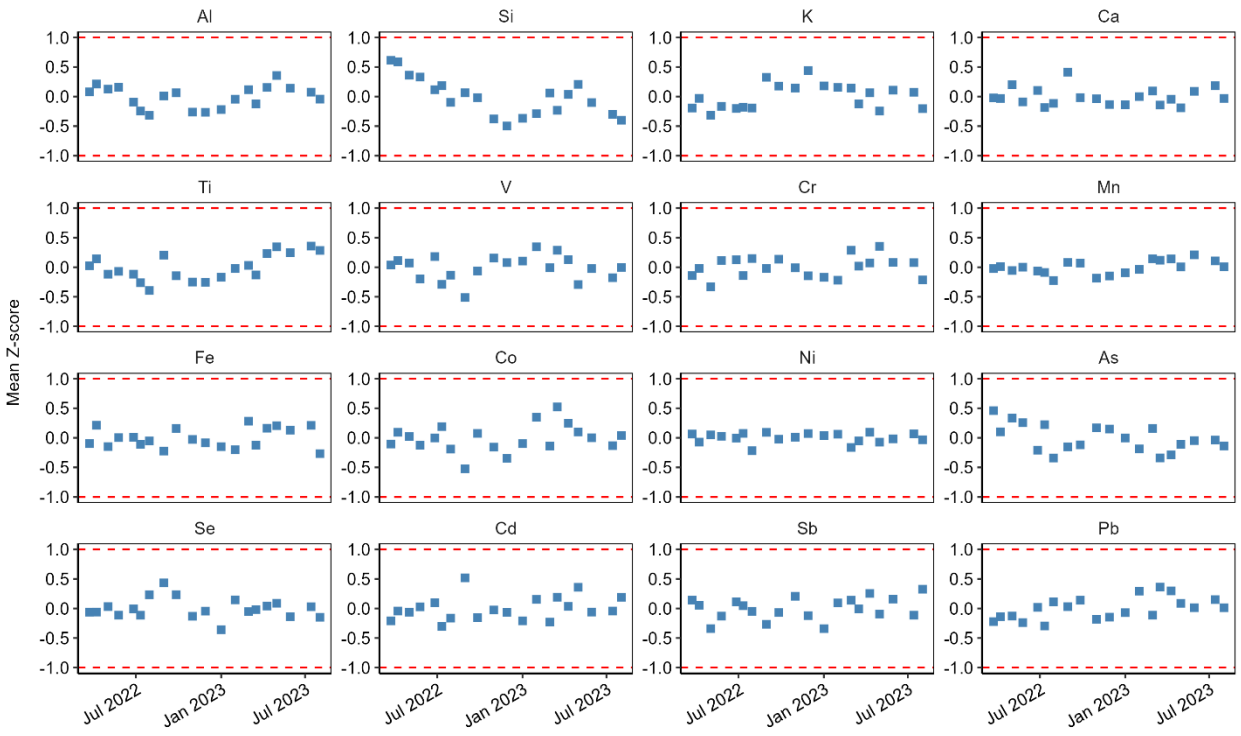

Figure S3.9 Quality control plots of mean Z-score for the representative SPARTAN samples. The dashed red line represents the acceptance limit of ± 1.

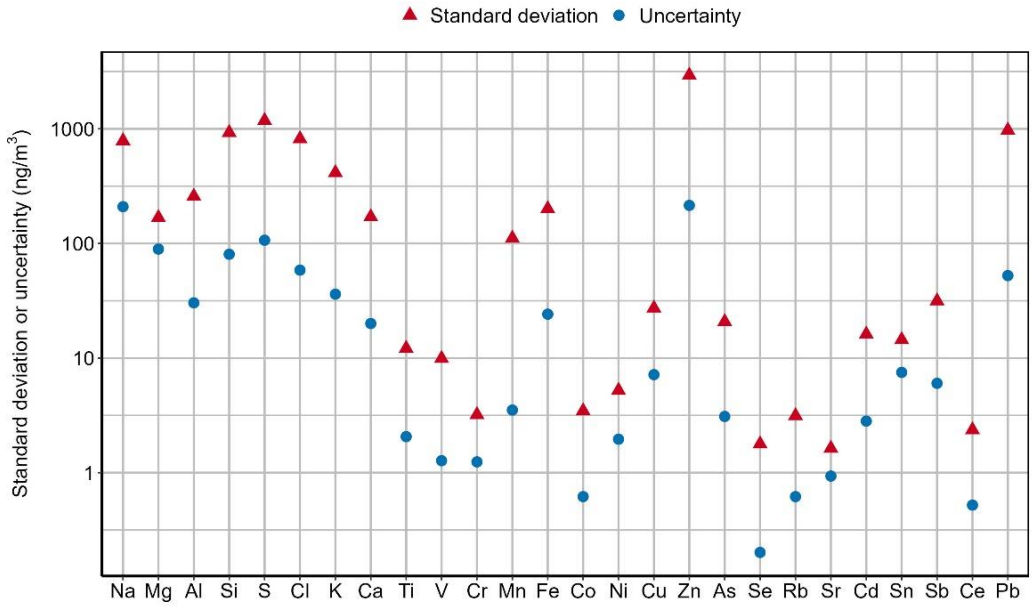

Figure S3.10 Comparison between the elemental standard deviations (ng/m^3) of available $PM_{2.5}$ samples collected from the Dhaka site and uncertainties (ng/m^3) for the mean elemental concentrations at the Dhaka site.

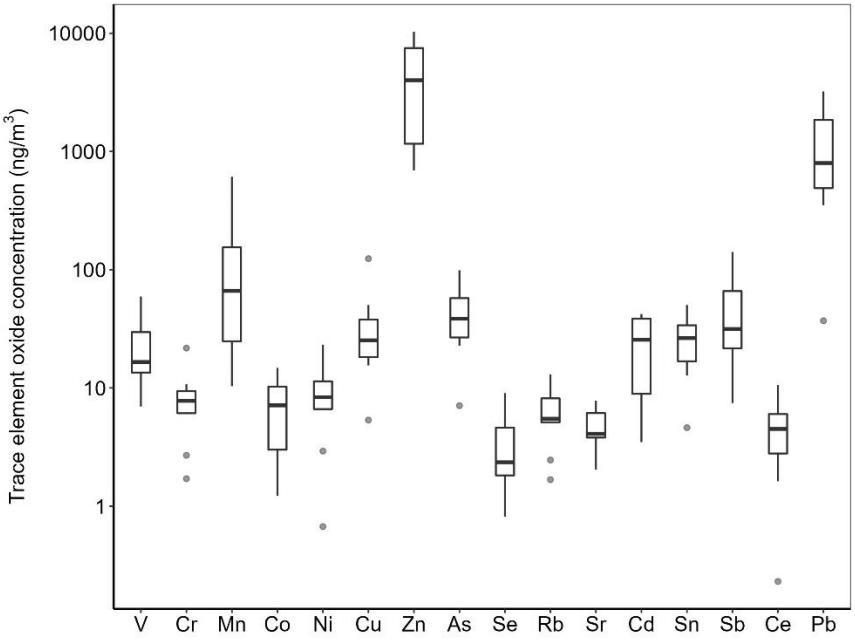

Figure S3.11 Boxplots for oxide concentrations of individual trace elements in $PM_{2.5}$ samples collected from the Dhaka site. The horizontal line indicates the median. The lower whisker extends from the first quartile to the smallest value greater than 1.5 times the interquartile range (IQR) below the first quartile. The upper whisker extends from the third quartile to the largest value smaller than 1.5 times the IQR above the third quartile. The dots represent outliers outside the range of the whiskers.

Table S3.2 Location information of SPARTAN sites used in this study sorted alphabetically

Site	Host Institute	Latitude	Longitude	Start date for MAIA sites
Abu Dhabi	Masdar Institute	24.44	54.62	
Addis Ababa[a]	Addis Ababa University	9.01	38.82	12/6/2022
Bandung	Institute of Technology Bandung	-6.89	107.61	
Beijing[a]	Tsinghua University	40.00	116.33	8/30/2022
Bujumbura	University of Burundi	-3.38	29.38	
Delhi[a]	American Center	28.63	77.22	6/28/2022
Dhaka	Dhaka University	23.73	90.40	
Downsview	Environment and Climate Change Canada	43.79	-79.47	
Fajardo	Cabezas de San Juan Nature Reserve	18.38	-65.62	
Haifa[a]	Technion Israel Institute of Technology	32.78	35.02	2/16/2022
Halifax	Dalhousie University	44.64	-63.59	
Hanoi	Vietnam Academy of Science and Technology	21.05	105.80	
Ilorin	Ilorin University	8.48	4.67	
Johannesburg[a]	University of Johannesburg	-26.18	28.00	4/7/2022
Kanpur	Indian Institute of Technology Kanpur	26.51	80.23	
Kaohsiung[a]	Kaohsiung Medical University	22.65	120.31	8/20/2022
Lethbridge	Lethbridge University	49.68	-112.87	
Melbourne	University of Melbourne	-37.80	144.97	
Mexico City	Universidad Nacional Autónoma de México	19.33	-99.18	
Pasadena[a]	Jet Propulsion Laboratory	34.20	-118.17	11/9/2021
Pretoria[a]	Council for Scientific and Industrial Research	-25.76	28.28	4/15/2021
Rehovot[a]	Weizmann Institute	31.91	34.81	11/5/2021
Seoul	Yonsei University	37.56	126.93	
Sherbrooke	Sherbrooke University	45.38	-71.93	
Singapore	National University of Singapore	1.30	103.78	
Taipei[a]	National Taiwan University	25.04	121.50	1/27/2022
Ulsan	Ulsan National Institute of Science and Technology	35.58	129.19	

[a]These sites began using the MAIA sampling protocol on the specified date.

Table S3.3 Sampling information and concentration levels (μg/m^3) of $PM_{2.5}$, dust, and trace element oxides (TEO) for $PM_{2.5}$ samples from SPARTAN sites used in this study

Site	Start date	Stop date	Sampling seasons[a]	*N*[b]	$PM_{2.5}$ level[c]	$PM_{2.5}$		Dust		TEO	
						mean	median	mean	median	mean	median
Kanpur	7/14/2021	5/24/2022	DJF, MAM, JJA	15	> 35	44	36	9.2	7.3	0.56	0.4
Dhaka	8/11/2020	8/18/2021	MAM, JJA	10	> 35	39	36	6.2	5.9	6.3	6.9
Bandung	7/4/2019	7/11/2021	DJF, MAM, JJA, SON	24	IT-1	35	34	1.6	1.4	0.19	0.15
Abu Dhabi	4/26/2019	6/19/2023	DJF, MAM, JJA, SON	95	IT-1	31	30	11	9.9	0.16	0.13
Ilorin	5/14/2019	12/1/2021	DJF, MAM, JJA, SON	40	IT-1	30	14	11	2.4	0.63	0.33
Hanoi	11/27/2018	8/12/2019	DJF, MAM, JJA, SON	13	IT-1	28	27	3.1	2.9	1.1	0.96
Beijing	5/8/2019	5/2/2023	DJF, MAM, JJA, SON	95	IT-1	28	18	4.5	3.3	0.21	0.18
Delhi	7/17/2022	3/27/2023	DJF, MAM, JJA	13	IT-1	26	24	3	1.6	0.43	0.21
Singapore	7/7/2019	12/17/2019	DJF, JJA, SON	12	IT-2	23	23	1.3	1.2	0.2	0.2
Bujumbura	12/9/2022	6/26/2023	DJF, MAM, JJA	8	IT-2	22	20	1.3	1.3	0.091	0.077
Addis Ababa	12/7/2022	6/26/2023	DJF, MAM, JJA	62	IT-2	21	19	4.4	3.7	0.075	0.064
Seoul	5/2/2019	5/14/2023	DJF, MAM, JJA, SON	68	IT-2	19	18	2.2	1.8	0.12	0.1
Kaohsiung	8/20/2022	2/16/2023	DJF, JJA, SON	63	IT-2	19	18	1.8	1.7	0.21	0.19
Pretoria	10/22/2020	6/4/2023	DJF, MAM, JJA, SON	178	IT-2	16	15	1.5	1.3	0.11	0.071
Johannesburg	4/7/2022	6/11/2023	DJF, MAM, JJA, SON	109	IT-2	16	14	1.1	1	0.2	0.11
Mexico City	3/7/2021	5/7/2023	DJF, MAM, JJA, SON	46	IT-3	14	14	1.1	0.95	0.078	0.067
Rehovot	2/22/2019	4/28/2023	DJF, MAM, JJA, SON	176	IT-3	14	13	3.1	1.4	0.071	0.055
Haifa	2/16/2022	5/27/2023	DJF, MAM, JJA, SON	136	IT-3	13	12	2.8	1.2	0.055	0.039
Ulsan	10/28/2021	6/17/2023	DJF, MAM, JJA, SON	56	IT-3	13	13	2	1.3	0.13	0.12
Taipei	1/27/2022	2/22/2023	DJF, MAM, JJA, SON	124	IT-4	8.5	7.9	0.82	0.64	0.049	0.042
Pasadena	11/9/2021	7/12/2023	DJF, MAM, JJA, SON	195	IT-4	6.6	6	0.69	0.66	0.016	0.012
Downsview	3/27/2019	8/12/2019	MAM, JJA	12	IT-4	6.4	6.3	0.55	0.48	0.048	0.039
Fajardo	3/18/2021	3/21/2023	DJF, MAM, JJA, SON	32	IT-4	5.8	5.1	1.7	0.9	0.013	0.0089
Lethbridge	3/8/2019	8/31/2019	MAM, JJA	13	AQG	5	4.9	0.64	0.49	0.015	0.014
Sherbrooke	4/3/2019	4/27/2023	DJF, MAM, JJA, SON	75	AQG	4.5	3.8	0.34	0.28	0.012	0.015
Melbourne	8/9/2022	7/1/2023	DJF, MAM, JJA, SON	29	AQG	4.2	3.6	0.36	0.31	0.016	0.016

Halifax	4/5/2019	3/14/2023	DJF, MAM, JJA, SON	113	AQG	3.1	2.7	0.23	0.2	0.0094	0.008

Note. Sites are sorted by mean $PM_{2.5}$ concentration. Only the sites with ≥3 samples are shown.

[a]DJF includes December, January, and February; MAM includes March, April, and May; JJA includes June, July, and August; SON includes September, October, and November. [b]*N* is the number of samples from each site included in this study. [c]$PM_{2.5}$ level indicates the achieved air quality level by comparing the mean concentration with the WHO annual Air Quality Guideline (AQG: 5 μg/m^3) and Interim Target X (IT-4: 10 μg/m^3; IT-3: 15 μg/m^3; IT-2: 25 μg/m^3; IT-1: 35 μg/m^3) for $PM_{2.5}$.

Table S3.4 Sampling information and concentration levels (μg/m^3) of PM_{10}, dust, and trace element oxides (TEO) for PM_{10} samples from SPARTAN sites used in this study

Site	Start date	Stop date	Sampling seasons[a]	*N*[b]	PM_{10} level[c]	PM_{10}		Dust		TEO	
						mean	median	mean	median	mean	median
Kanpur	7/14/2021	5/24/2022	DJF, MAM, JJA	3	> 70	110	95	41	30	0.62	0.54
Abu Dhabi	4/26/2019	10/3/2022	DJF, MAM, JJA, SON	16	> 70	110	100	53	47	0.43	0.42
Ilorin	5/14/2019	12/23/2021	DJF, MAM, JJA, SON	10	> 70	83	32	55	14	1.6	1.1
Hanoi	11/9/2018	11/22/2020	MAM, JJA, SON	4	IT-1	52	52	13	13	1.8	1.7
Rehovot	2/5/2019	4/13/2021	DJF, MAM, JJA, SON	8	IT-2	48	39	22	17	0.15	0.14
Beijing	5/8/2019	8/27/2022	DJF, MAM, JJA, SON	11	IT-2	47	43	21	21	0.36	0.38
Bandung	9/6/2019	7/11/2021	DJF, MAM, JJA, SON	4	IT-2	39	36	6.3	4.9	0.14	0.14
Seoul	5/2/2019	3/25/2023	DJF, MAM, JJA, SON	9	IT-2	31	34	8.3	7.5	0.19	0.21
Mexico City	8/27/2021	5/7/2023	DJF, MAM, JJA	7	IT-3	22	25	5.6	6.2	0.077	0.088
Ulsan	9/4/2021	6/17/2023	DJF, MAM, JJA, SON	10	IT-3	21	20	6.7	5.2	0.15	0.12
Fajardo	3/18/2021	3/21/2023	DJF, MAM, SON	5	IT-4	17	17	3.9	3.1	-0.0095	-0.0047
Melbourne	8/9/2022	7/1/2023	DJF, MAM, JJA, SON	6	AQG	12	12	1.7	1.5	0.048	0.046
Sherbrooke	5/27/2019	4/27/2023	DJF, MAM, JJA, SON	11	AQG	11	9.3	3	3.2	0.03	0.033
Halifax	4/5/2019	3/13/2023	DJF, MAM, JJA, SON	21	AQG	5.9	5.6	0.94	0.85	0.023	0.013

Note. Sites are sorted by mean PM_{10} concentration. Only the sites with ≥3 samples are shown.

[a]DJF includes December, January, and February; MAM includes March, April, and May; JJA includes June, July, and August; SON includes September, October, and November. [b]*N* is the number of samples from each site included in this study. [c]PM_{10} level indicates the achieved air quality level by comparing the mean concentration with the WHO annual Air Quality Guideline (AQG: 15 μg/m^3) and Interim Target X (IT-4: 20 μg/m^3; IT-3: 30 μg/m^3; IT-2: 50 μg/m^3; IT-1: 70 μg/m^3) for PM_{10}.

Table S3.5 Routine SPARTAN quality control (QC) frequencies, criteria, and corrective actions built upon the method used by IMPROVE

Analysis	Frequency	Criterion	Corrective Action
PTFE blank	Daily	≤ acceptance limits for all measured elements	If the criterion is exceeded: a. Remeasure the sample b. Check the sample for damage/contamination c. Replace the sample if necessary d. Remeasure field samples since last passing QC e. Recalibration if necessary
UCD-made multi-element RMs	Monthly	Within acceptance limits for K, Cr, Co, Ni, Cu, Zn, As, Se, and Pb	
NIST SRM 2783	Monthly	Absolute relative bias ≤ acceptance limits for Al, Si, K, Ca, Ti, V, Mn, Fe, and Zn	
Representative SPARTAN samples	Monthly	-1 ≤ mean Z-score ≤ 1 for Al, Si, K, Ca, Ti, V, Cr, Mn, Fe, Co, Ni, As, Se, Cd, Sb, and Pb	

Table S3.6 The mineral-to-aluminum ratio (MAL) and correction factor (CF) values used in the global dust equation to calculate dust mass for SPARTAN sites

Sites	MAL	CF
Addis Ababa, Bandung, Bujumbura, Delhi, Dhaka, Downsview, Halifax, Hanoi, Johannesburg, Kanpur, Kaohsiung, Lethbridge, Pretoria, Sherbrooke, Singapore, Taipei	0.62	1.02
Abu Dhabi, Haifa, Rehovot	0.72	1.14
Fajardo, Ilorin, Mexico City	0.27	1.05
Melbourne	0.24	1.05
Beijing, Seoul, Ulsan	0.59	1.11
Pasadena	0.66	1.14

Table S3.7 Inhalation unit risk (IUR) and inhalation reference concentration (RfC) values used in this study

Metal	IUR $(\mu g/m^3)^{-1}$	RfC $(\mu g/m^3)$
As	0.0043	0.015
Pb	0.000012[a]	NA[b]
Cd	0.0018	0.01
Cr (VI)	0.084	0.1
Co	0.009	0.006
Ni (Refinery Dust)	0.00024	0.014
Mn		0.05
V		0.1

[a]The IUR value of lead phosphate is used. [b]Not available.

Table S3.8 Method detection limit (MDL, ng/cm^2) estimates and percent of $PM_{2.5}$ samples above MDL for SPARTAN

Element	MDL_{FB}[a]	MDL_{LB}[b]	MDL[c]	Percent > MDL (%)
Na	208	164	208	92
Mg	269	163	269	58
Al	27	19	27	98
Si	24	15	24	99
S	6.7	1.1	6.7	100
Cl	49	27	49	32
K	71	42	71	85
Ca	23	16	23	98
Ti	5.3	2.8	5.3	88
V	0.5	0.4	0.5	85
Cr	4.2	3.7	4.2	50
Mn	1.8	1.0	1.8	91
Fe	15	11	15	99
Co	0.7	0.6	0.7	37
Ni	6.8	4.7	6.8	13
Cu	25	19	25	13
Zn	11	7.6	11	80
As	0.9	0.8	0.9	88
Se	0.3	0.5	0.5	82
Rb	1.8	1.7	1.8	43
Sr	2.7	3.1	3.1	30
Cd	9.8	8.3	9.8	10
Sn	25	26	26	16
Sb	21	18	21	13
Ce	1.2	1.1	1.2	52
Pb	2.4	2.6	2.6	66

[a]MDL determined using the 95th percentile minus the median mass loading of 100 field blanks. [b]MDL determined using the 95th percentile minus the median mass loading of 100 lab blanks. [c]The maximum of MDL_{FB} and MDL_{LB}.

Table S3.9 Estimates of proportional mass uncertainty (σ_{mass}), total proportional uncertainty ($\sigma_{proportion}$), and additive uncertainty ($\sigma_{additive}$) for SPARTAN

Element	N[a]	σ_{mass}[b] (%)	$\sigma_{proportion}$[c] (%)	$\sigma_{additive}$ (ng/cm^2)
Na	8	10	11	126
Mg	3	8	9	164
Al	8	4	5	16
Si	9	4	5	15
S	9	3	5	4.1
Cl	2	7	7	30
K	7	3	5	43
Ca	7	5	6	14
Ti	5	4	5	3.2
V	6	8	9	0.3
Cr	0	–	–	2.6
Mn	5	3	4	1.1
Fe	8	5	6	9.1
Co	3	10	11	0.4
Ni	0	–	–	4.1
Cu	0	–	–	15
Zn	5	4	6	6.7
As	4	9	10	0.6
Se	1	5	6	0.3
Rb	3	5	6	1.1
Sr	2	5	6	1.9
Cd	0	–	–	5.9
Sn	0	–	–	16
Sb	0	–	–	13
Ce	3	9	10	0.7
Pb	4	3	5	1.6

[a]N is the number of samples with the mean from 20 monthly measurements greater than 3×MDL out of the nine representative SPARTAN samples. [b]σ_{mass} is estimated as the mean of relative standard deviations from 20 monthly measurements of the representative SPARTAN samples with mean > 3×MDL. [c]$\sigma_{proportion}$ is estimated by combining σ_{mass} and the proportional volume uncertainty of 3.5%.

Table S3.10 Elemental mass concentrations (mean ± standard deviation, ng/m^3) measured for $PM_{2.5}$ samples from SPARTAN sites used in this study

site	Kanpur	Dhaka	Bandung	Abu Dhabi	Ilorin	Hanoi	Beijing	Delhi	Singapore	Bujumbura	Addis Ababa	Seoul	Kaohsiung
N[a]	15	10	24	95	40	13	95	13	12	8	62	68	63
Na	1000±600	1800±790	730±150	1400±680	450±330	740±210	550±360	740±590	680±200	170±110	340±150	390±130	670±190
Mg	560±360	480±170	260±90	750±380	240±250	180±74	290±250	290±210	220±64	27±100	220±130	150±86	270±100
Al	900±730	550±260	210±81	810±480	1000±1600	280±98	380±580	310±310	150±54	160±46	390±240	200±140	160±62
Si	2200±1800	1600±930	310±110	2100±1400	2800±4600	740±210	830±1300	660±710	250±79	270±82	990±560	450±330	350±150
S	2600±1500	2400±1200	2300±530	4500±2700	580±190	2300±700	1500±1100	1400±720	2100±920	420±210	670±360	1300±500	1500±650
Cl	110±160	760±820	52±16	36±100	100±170	120±98	90±210	480±950	17±11	23±6.5	49±38	35±31	63±66
K	1300±1300	620±410	600±260	310±200	650±680	570±220	370±440	780±530	450±150	690±380	380±120	210±110	250±140
Ca	580±620	300±170	92±36	1300±1100	350±580	190±58	290±290	190±190	64±12	46±15	390±240	91±46	100±36
Ti	49±46	25±12	7.2±4.1	41±28	68±110	16±4.7	24±37	17±17	6.8±6.4	6.7±2.1	30±17	13±7.8	11±7
V	2.2±1.5	14±9.9	0.98±0.43	6.9±5.8	2±2.3	2.3±0.98	1.4±1.4	0.88±0.58	36±20	0.28±0.18	1.1±0.56	1.3±1.8	2±0.99
Cr	9.5±9	5.5±3.2	3±6	2.8±1.9	3.3±3.6	2.7±1.2	4.2±2.9	2.8±2.9	0.12±1.8	1.4±0.68	1.4±1.4	3.1±2.8	11±9.6
Mn	21±13	80±110	3.6±1.6	12±6.2	18±22	37±24	35±45	12±10	6.9±2.6	9.6±4.7	8.9±4	11±4.1	22±27
Fe	600±480	390±200	110±52	520±330	650±1000	210±100	510±470	250±230	100±31	100±28	320±170	210±100	290±250
Co	1.5±1.2	5.4±3.5	0.01±0.38	1.3±1.1	2.2±3	1.3±0.59	1.2±1.3	0.64±0.68	0.09±0.34	0.028±0.23	0.56±0.48	0.48±0.34	0.81±0.69
Ni	1.4±1.2	7.5±5.2	1.9±1.8	3.3±2.8	1.3±2	2±1.1	0.59±1.8	1.2±2	9.5±4.8	0.25±0.9	-0.0±1.4	1.3±2.1	4±3.1
Cu	11±24	29±27	13±16	3±6.4	4±6.4	13±7.4	4.1±10	33±46	8±7.2	1.3±3.6	0.075±5	8.3±15	8.3±8
Zn	120±71	3800±2900	57±29	51±47	410±570	650±440	74±53	190±170	50±26	54±33	27±29	43±22	86±44
As	17±18	32±21	4.6±4	1.5±0.58	2.6±3	10±6.5	3.6±2.8	7.2±7.9	1.7±1.1	1.1±0.36	1±0.68	5.6±4.1	3.2±1.5
Se	2.7±2.2	2.4±1.8	0.73±0.31	1.2±0.64	0.25±0.15	1.7±0.61	2.2±1.5	1.3±2.2	1.5±1.3	0.31±0.049	0.41±0.2	1.1±0.47	1.5±0.72
Rb	5.1±4.9	5.7±3.1	3.6±1.3	1.9±1.3	2.7±2.8	3.6±1.2	1.5±1.5	3.4±2.9	2.2±1.4	3.3±1.4	1.8±0.74	0.95±0.94	1.2±0.63
Sr	5.5±7.6	3.7±1.6	0.97±0.87	18±21	3.7±6.3	1.1±0.61	3.5±9.5	1.8±1.7	1±1.6	-0.21±0.33	2.8±2	0.63±1.3	1.5±1.8
Cd	2.7±6.9	18±16	2.5±3.7	0.81±4.1	3.7±4.3	0.73±4.8	1.4±3.6	4±5.3	0.75±5	1.1±1	0.79±3.1	0.86±3.2	0.82±2.5
Sn	6.2±6.3	16±14	11±8.2	5.2±12	7.2±9.1	20±9.7	5.4±12	12±8.1	17±8.4	-4.1±2.5	2.8±8.4	1.1±9.6	5.1±12
Sb	8.9±7.6	35±32	5.5±6.4	4.2±10	1.7±7.9	7.4±5	5.6±6.4	12±11	3±6.8	-2.5±5.1	4.7±6.9	-0.75±6.9	0.89±6
Ce	3.3±2.7	4±2.4	-0.72±1.6	2.3±1.6	4.3±6.6	0.55±2.3	1.8±2.4	0.047±1.7	-0.95±2.9	0.99±0.48	1.4±1.1	1.9±1.8	0.55±1.3
Pb	250±430	1100±970	52±89	5.2±2.8	37±46	140±150	10±7.2	65±73	6±7.2	3.8±2.6	2.8±2.3	13±8.1	11±7.7

(continued)

site	Pretoria	Johannes-burg	Mexico City	Rehovot	Haifa	Ulsan	Taipei	Pasadena	Downs-view	Fajardo	Leth-bridge	Sher-brooke	Mel-bourne	Halifax
N[a]	178	109	46	176	136	56	124	195	12	32	13	75	29	113
Na	510±270	480±290	360±110	520±230	600±260	380±140	350±200	210±160	89±36	680±210	66±28	56±110	210±140	140±90
Mg	210±140	180±220	100±73	240±180	260±180	150±96	110±120	80±110	32±31	170±140	43±28	-6.7±130	3.4±100	42±47
Al	200±180	130±63	130±77	260±380	250±360	180±180	84±65	56±45	44±22	200±190	87±110	31±28	32±20	32±30
Si	280±140	220±98	230±140	560±900	520±850	400±430	160±130	110±82	92±39	400±450	120±62	69±65	71±33	38±19
S	1500±1000	1500±840	1300±320	1500±810	1600±870	1200±460	900±550	410±330	390±120	470±540	230±70	250±110	240±140	220±94
Cl	22±36	41±150	19±11	35±100	61±220	16±8.8	41±100	19±51	4.7±2.8	760±370	2.6±2.2	6.2±13	150±130	60±110
K	290±260	350±620	210±180	130±98	110±92	130±72	93±120	56±250	44±21	56±43	38±26	54±39	31±37	36±86
Ca	42±37	40±25	61±25	310±570	230±450	71±62	49±29	50±31	69±51	72±51	42±25	28±68	34±12	15±8.7
Ti	6.8±4.3	5.6±3.2	8.8±5.4	15±25	13±24	12±10	5.5±3.1	6.1±9.1	4.7±1.7	10±11	3.3±1	4.5±2.9	3.7±1.9	2.4±1.6
V	0.84±0.71	0.64±0.52	4.1±3.2	2.2±1.9	2.9±2.4	0.77±0.73	1±0.77	0.33±0.52	0.26±0.17	0.66±0.41	0.12±0.11	0.04±0.26	0.62±0.52	0.57±1.1
Cr	5.3±4.4	5.9±5.6	1.6±1.9	1.7±1.8	1.7±2	2.9±1.8	1.9±1.9	1.2±1.4	0.75±0.79	0.32±1.4	1.3±2.4	0.67±1.3	2.3±1.7	0.81±0.95
Mn	7.1±7	5.4±4.3	4±1.4	4.3±4.4	3.4±4.3	15±7.6	4.9±3.7	1.4±0.97	2.7±1.2	1.5±1.6	0.72±0.32	1.8±1.4	2.3±0.97	0.6±0.33
Fe	130±75	110±61	93±37	190±260	150±250	190±120	91±53	73±39	77±35	95±100	25±10	31±22	46±17	16±7.4
Co	0.28±0.37	0.39±0.7	0.1±0.18	0.37±0.71	0.34±0.67	0.28±0.34	0.22±0.31	0.13±0.19	0.15±0.14	0.18±0.29	0.02±0.08	0.1±0.2	0.11±0.25	0.07±0.12
Ni	0.0±2.5	-0.2±2.1	0.76±2	0.64±2.3	1±2.1	1.4±1.8	-0.01±2.6	-0.79±1.5	0.24±0.25	0.69±1.6	0.03±0.16	0.27±2.5	0.55±1.9	0.26±0.95
Cu	5.2±15	23±62	4.9±7.3	3.4±8.3	0.19±7	3.6±6.6	-0.19±9.6	-0.96±9.7	3.3±1.5	1.5±5.5	0.8±0.45	1.2±9.1	1.3±6.9	1.3±4.1
Zn	42±77	85±120	36±18	22±21	18±19	54±30	20±15	3.8±4.1	18±18	4.7±6.3	2.3±1.9	5.3±4.1	7±6.3	3.4±2.7
As	2.4±2.3	2.4±1.6	2.1±1.7	1.4±1.2	1.2±0.85	6.5±6.5	1.3±1	0.59±0.3	0.78±0.25	0.33±0.27	0.32±0.17	0.76±0.71	0.98±0.37	0.49±0.25
Se	1.4±2.4	1.3±1.7	1.3±0.71	0.56±0.3	0.43±0.22	1.2±0.87	0.59±0.44	0.57±0.75	0.45±0.2	0.14±0.12	0.37±0.22	0.17±0.15	0.48±0.38	0.13±0.09
Rb	1.5±0.94	1.5±1.7	0.22±0.67	0.91±1.5	0.63±0.88	0.35±0.6	0.68±0.79	0.45±0.49	0.24±0.3	0.17±0.65	0.17±0.28	0.02±0.73	-0.28±0.53	0.02±0.36
Sr	1±1.1	0.93±2	0.15±1.3	1.7±4.4	1.5±3.1	-0.08±0.91	0.96±2.7	1.3±5.8	0.27±0.57	0.61±1.1	0.07±0.44	-0.18±1.2	-0.31±1.3	0.12±1.9
Cd	0.74±2.8	1.1±4.2	-0.22±2.6	-0.01±6.8	1±3.1	-0.3±2.7	1.5±3.6	-0.0±2.4	-1.8±1.6	-0.67±2.8	-2.6±1.6	-0.36±3.5	-0.0±3.4	0.07±2.1
Sn	4.7±9.3	7±9.1	-1.9±6	4±11	0.79±9.1	0.1±7.5	-0.1±9.3	0.3±7.9	8±3.8	-2.1±8.9	6.1±3.5	-0.46±10	-3.1±6.6	-0.87±5.9
Sb	6.2±7.7	6.6±10	-0.0±5.7	2.9±11	1.3±6.2	-0.79±5.8	0.4±7.7	3.1±5.7	1.4±3.6	0.97±4.9	1.5±3.2	-1.4±7.3	-3.6±5	-0.89±3.2
Ce	0.0±1.1	0.49±2.7	2.9±3	0.73±2.1	0.42±1.5	2.7±1.7	0.53±1.2	0.41±0.95	0.95±1.4	1.0±1.6	0.43±0.75	0.98±1.4	3.0±1.8	0.89±1.1

Pb	9.1±17	13±15	3.3±2.8	7.6±15	6.8±9.8	10±8.9	2.9±3.7	0.27±0.70	1.8±2.6	-0.22±0.74	-0.12±0.28	0.2±1.4	-0.3±1.0	-0.17±0.55

Note. Sites are sorted by mean $PM_{2.5}$ concentration. Only the sites with ≥3 samples are shown.

[a]*N* is the number of samples from each site.

Table S3.11 Elemental mass concentrations (mean ± standard deviation, ng/m^3) measured for PM_{10} samples from SPARTAN sites used in this study

site	Kanpur	Abu Dhabi	Ilorin	Hanoi	Rehovot	Beijing	Bandung	Seoul	Mexico City	Ulsan	Fajardo	Mel-bourne	Sher-brooke	Halifax
N[a]	3	16	10	4	8	11	4	9	7	10	5	6	11	21
Na	1600±1100	3300±1200	1400±1200	1300±210	1300±540	1000±320	1200±320	740±200	390±200	520±180	2600±790	640±650	160±180	380±230
Mg	1300±1100	2700±1400	1000±1200	600±320	840±530	690±320	580±180	450±250	160±250	190±210	700±280	-200±310	92±160	91±150
Al	3800±3100	3000±1700	5200±6100	1100±250	1600±1200	1500±540	660±310	690±300	490±180	570±570	510±280	150±84	280±110	120±79
Si	9300±7500	8800±5200	15000±18000	2600±580	3500±2400	3900±1300	1200±660	1700±780	1300±450	1400±1400	880±660	360±180	670±240	170±87
S	2700±1600	6600±4000	750±190	2600±160	2000±900	2100±460	2500±220	1700±630	1100±260	1300±180	660±290	360±250	240±80	240±58
Cl	250±79	1200±1000	380±390	480±250	640±510	120±100	91±54	73±35	41±9.9	67±67	3700±1400	980±630	81±180	430±340
K	2400±2400	980±560	1400±1200	910±150	540±400	750±310	570±310	400±190	250±150	280±160	120±48	47±47	150±31	44±32
Ca	3000±3100	10000±7000	2300±2700	1800±370	3500±2700	2300±740	590±160	580±250	600±170	380±290	240±76	160±60	250±110	54±15
Ti	250±220	190±120	320±380	83±24	100±80	110±36	41±19	50±20	36±9.7	39±33	25±19	13±9	17±5.8	5.4±2.9
V	7.4±6	14±10	7.3±8	3.3±0.81	5.3±3.5	4.3±1.5	1±1.2	2.4±2.5	3.8±3	1.1±1.8	0.79±1.1	0.83±0.93	0.74±0.38	1.1±1
Cr	19±13	14±4.1	14±10	8.3±7.5	9.4±6.4	12±5.4	5.5±2.9	7±5.5	4.9±5.1	6.7±6.2	0.3±4	5.2±5.4	3.3±2.8	2.8±3
Mn	68±55	50±24	75±81	78±41	20±12	55±21	13±4.1	22±6.8	11±1.8	23±9.7	3.3±2.7	6.8±2.3	6.2±1.9	2.4±1
Fe	2800±2400	2400±1400	3100±3500	840±230	1200±840	1700±500	460±180	720±260	430±130	520±370	190±170	190±62	240±80	69±32
Co	7.4±5.9	6.1±4.4	9.1±9.7	2.4±1.9	1.9±2.9	3±1.6	0.4±1.7	1.5±0.8	0.2±0.65	0.63±0.82	0.48±0.12	0.7±1.3	0.32±0.43	0.32±0.39
Ni	2.5±6	10±9.6	0.027±7.5	2.9±7	-0±14	-1.5±6.1	-5.2±4	1.8±4.7	-2.7±8.8	0.34±5	1.4±2.4	-1±5.6	1.5±11	0.5±2.7

Cu	12±36	2±23	-4.5±27	18±23	6.4±44	3.2±25	-13±15	24±37	-4.7±30	0.95±15	3.2±11	-1.8±16	-2.4±10	3.3±9.5
Zn	160±40	87±64	990±1300	1100±560	42±18	110±45	48±18	64±23	39±14	71±20	4.9±4	8±6	5.7±3.7	5±3.8
As	14±6.1	3.3±2	4.9±7.2	12±3.4	2±1.3	4.5±1.7	4.7±1.7	6.8±3.5	2.4±1.4	7.2±3	1±1.1	1.5±1.3	0.79±0.47	0.58±0.66
Se	3±1.2	2.3±1.3	0.47±0.55	1.8±0.57	0.62±0.68	2.9±0.65	0.98±0.39	1.2±0.4	0.86±0.26	1.2±0.5	0.28±0.18	0.43±0.75	0.27±0.24	0.19±0.2
Rb	11±11	6.1±7.2	7.6±7.5	4.1±2.2	1.4±4.6	4.7±3.7	3±1	0.17±1.4	-0.4±1.9	0.18±1.7	0.23±2.1	-0.1±4.2	0.2±0.86	0.13±1.6
Sr	19±21	92±77	20±24	3.3±4.8	8.2±9.9	11±6.5	3.3±2.2	1.1±2.3	1.3±3.2	0.54±3.4	1.5±3.6	0.61±6.5	0.21±1.4	-0.1±2.3
Cd	7.8±17	1.8±21	7.9±13	6.8±26	3.4±12	5.7±17	2.8±15	-1.3±9.7	1.9±7.7	-2.1±7.4	-4.4±12	1.9±15	2.4±8.5	1.2±7
Sn	9.1±22	2.8±56	19±31	19±51	4.2±59	14±45	-10±11	0.1±25	-13±31	-12±31	-25±22	2.8±30	1.8±25	-4.3±23
Sb	9.7±13	14±49	5.7±26	-6.2±28	-11±40	16±33	6.7±15	-11±14	-1±23	-9.3±23	1.8±18	-0±32	-1.8±11	0.43±15
Ce	13±12	12±6.2	18±20	4.9±1	6.2±4	7.5±3.2	4.9±5.7	6.5±4.3	7.9±6.9	6.7±7.4	1.6±4	9.8±6.1	0.95±1.4	2.5±2.2
Pb	110±51	8.2±7.5	75±93	100±13	8.4±5.6	20±7.8	44±32	15±6.7	3.1±2.1	11±6.3	-1.6±2.6	-1±4	0.55±1.2	-0.2±1.8

Note. Sites are sorted by mean PM_{10} concentration. Only the sites with ≥3 samples are shown.

[a]*N* is the number of samples from each site.

Table S3.12 Uncertainties (ng/m^3) for the mean elemental concentration of $PM_{2.5}$ samples from SPARTAN sites included in this study

site	Kanpur	Dhaka	Bandung	Abu Dhabi	Ilorin	Hanoi	Beijing	Delhi	Singapore	Bujumbura	Addis Ababa	Seoul	Kaohsiung
N[a]	15	10	24	95	40	13	95	13	12	8	62	68	63
Na	130	210	100	160	79	100	86	100	96	63	71	74	95
Mg	93	89	82	100	81	80	82	82	81	78	81	79	82
Al	49	30	14	44	56	17	22	18	11	12	22	13	12
Si	110	80	17	110	140	38	42	34	15	16	51	24	19
S	120	110	100	200	26	100	69	64	94	19	30	57	68
Cl	17	58	15	14	16	17	16	39	14	14	15	14	15
K	66	36	35	25	37	34	27	42	30	39	27	23	24
Ca	36	20	8.7	83	23	14	19	13	7.7	7.2	25	8.7	9.1
Ti	3.1	2.1	1.6	2.7	4	1.8	2	1.8	1.6	1.6	2.2	1.7	1.7
V	0.24	1.3	0.17	0.64	0.23	0.25	0.19	0.16	3.3	0.15	0.17	0.19	0.23
Cr	1.2	1.2	1.2	1.2	1.2	1.2	1.2	1.2	1.2	1.2	1.2	1.2	1.2
Mn	1.1	3.5	0.55	0.73	0.96	1.7	1.6	0.73	0.61	0.67	0.65	0.7	1.1

Fe	37	24	7.9	32	39	14	31	16	7.7	7.4	20	13	18
Co	0.25	0.62	0.19	0.24	0.31	0.24	0.23	0.2	0.19	0.19	0.2	0.2	0.21
Ni	2	2	2	2	2	2	2	2	2	2	2	2	2
Cu	7.2	7.2	7.2	7.2	7.2	7.2	7.2	7.2	7.2	7.2	7.2	7.2	7.2
Zn	7.5	210	4.6	4.3	23	37	5.3	11	4.3	4.4	3.5	4	5.8
As	1.6	3.1	0.53	0.32	0.38	1	0.45	0.75	0.33	0.31	0.3	0.61	0.42
Se	0.22	0.2	0.15	0.16	0.14	0.17	0.19	0.16	0.17	0.14	0.15	0.16	0.17
Rb	0.6	0.62	0.56	0.54	0.55	0.57	0.53	0.56	0.54	0.56	0.54	0.53	0.53
Sr	0.96	0.93	0.91	1.4	0.93	0.91	0.93	0.91	0.91	0.91	0.92	0.91	0.91
Cd	2.8	2.8	2.8	2.8	2.8	2.8	2.8	2.8	2.8	2.8	2.8	2.8	2.8
Sn	7.5	7.5	7.5	7.5	7.5	7.5	7.5	7.5	7.5	7.5	7.5	7.5	7.5
Sb	6	6	6	6	6	6	6	6	6	6	6	6	6
Ce	0.47	0.52	0.34	0.41	0.55	0.34	0.38	0.33	0.35	0.35	0.36	0.39	0.34
Pb	12	52	2.6	0.8	1.9	6.5	0.91	3.2	0.82	0.79	0.78	0.98	0.94

(continued)

site	**Pretoria**	**Johannesburg**	**Mexico City**	**Rehovot**	**Haifa**	**Ulsan**	**Taipei**	**Pasadena**	**Downsview**	**Fajardo**	**Lethbridge**	**Sherbrooke**	**Melbourne**	**Halifax**
N[a]	178	109	46	176	136	56	124	195	12	32	13	75	29	113
Na	82	81	72	83	90	74	72	65	61	97	61	61	65	62
Mg	81	80	79	81	82	79	79	79	78	80	78	78	78	78
Al	13	11	11	16	15	12	9.1	8.4	8.2	13	9.2	8.1	8.1	8.1
Si	16	13	14	29	27	21	11	9.1	8.5	22	9.4	7.9	7.9	7.3
S	69	66	57	67	73	53	40	19	18	21	11	11	11	10
Cl	14	14	14	14	15	14	14	14	14	58	14	14	18	15
K	25	26	23	22	21	22	21	21	21	21	21	21	21	21
Ca	7.1	7.1	7.6	20	16	8	7.3	7.3	7.9	8	7.1	6.9	7	6.7
Ti	1.6	1.6	1.6	1.7	1.7	1.7	1.6	1.6	1.6	1.6	1.5	1.5	1.5	1.5
V	0.16	0.15	0.4	0.25	0.3	0.16	0.17	0.15	0.15	0.16	0.14	0.14	0.15	0.15

Cr	1.2	1.2	1.2	1.2	1.2	1.2	1.2	1.2	1.2	1.2	1.2	1.2	1.2	1.2
Mn	0.61	0.58	0.55	0.56	0.55	0.85	0.57	0.53	0.54	0.53	0.53	0.53	0.53	0.53
Fe	8.8	8	7.1	12	10	13	7	6.2	6.4	7.2	4.6	4.7	5.1	4.5
Co	0.19	0.2	0.19	0.2	0.19	0.19	0.19	0.19	0.19	0.19	0.19	0.19	0.19	0.19
Ni	2	2	2	2	2	2	2	2	2	2	2	2	2	2
Cu	7.2	7.2	7.2	7.2	7.2	7.2	7.2	7.2	7.2	7.2	7.2	7.2	7.2	7.2
Zn	4	5.8	3.8	3.4	3.4	4.4	3.4	3.2	3.4	3.2	3.2	3.2	3.2	3.2
As	0.36	0.36	0.35	0.32	0.31	0.69	0.31	0.29	0.3	0.29	0.29	0.3	0.3	0.29
Se	0.16	0.16	0.16	0.15	0.15	0.16	0.15	0.15	0.15	0.14	0.15	0.14	0.15	0.14
Rb	0.53	0.53	0.53	0.53	0.53	0.53	0.53	0.53	0.53	0.53	0.53	0.53	0.53	0.53
Sr	0.91	0.91	0.91	0.91	0.91	0.91	0.91	0.91	0.91	0.91	0.91	0.91	0.91	0.91
Cd	2.8	2.8	2.8	2.8	2.8	2.8	2.8	2.8	2.8	2.8	2.8	2.8	2.8	2.8
Sn	7.5	7.5	7.5	7.5	7.5	7.5	7.5	7.5	7.5	7.5	7.5	7.5	7.5	7.5
Sb	6	6	6	6	6	6	6	6	6	6	6	6	6	6
Ce	0.33	0.34	0.44	0.34	0.34	0.43	0.34	0.34	0.35	0.35	0.34	0.35	0.45	0.35
Pb	0.88	0.99	0.78	0.84	0.83	0.91	0.78	0.76	0.77	0.76	0.76	0.76	0.76	0.76

Note. Sites are sorted by mean $PM_{2.5}$ concentration. Only the sites with ≥3 samples are shown.

[a]*N* is the number of samples from each site.

Table S3.13 Carcinogenic risk of trace elements estimated using mean elemental concentrations in $PM_{2.5}$ samples from SPARTAN sites

Site	*N*[a]	Children					Adults				
		As	Pb	Cd	Co	Ni	As	Pb	Cd	Co	Ni
Dhaka	10	1.1E-05	1.1E-06	2.6E-06	4.0E-06	1.5E-07	4.5E-05	4.4E-06	1.0E-05	1.6E-05	5.9E-07
Kanpur	15	5.9E-06	2.4E-07	NA	1.1E-06	NA	2.4E-05	9.7E-07	NA	4.4E-06	NA
Hanoi	13	3.7E-06	1.4E-07	NA	9.6E-07	NA	1.5E-05	5.4E-07	NA	3.8E-06	NA
Delhi	13	2.5E-06	6.4E-08	NA	4.7E-07	NA	1.0E-05	2.6E-07	NA	1.9E-06	NA
Ilorin	40	9.0E-07	3.7E-08	NA	1.6E-06	NA	3.6E-06	1.5E-07	NA	6.5E-06	NA
Seoul	68	2.0E-06	1.3E-08	NA	3.6E-07	NA	7.9E-06	5.1E-08	NA	1.4E-06	NA
Beijing	95	1.3E-06	1.0E-08	NA	8.6E-07	NA	5.1E-06	4.1E-08	NA	3.5E-06	NA
Kaohsiung	63	1.1E-06	1.1E-08	NA	6.0E-07	8.0E-08	4.5E-06	4.5E-08	NA	2.4E-06	3.2E-07
Abu Dhabi	95	5.2E-07	5.2E-09	NA	9.6E-07	NA	2.1E-06	2.1E-08	NA	3.8E-06	NA
Singapore	12	5.9E-07	5.9E-09	NA	NA	1.9E-07	2.4E-06	2.4E-08	NA	NA	7.5E-07
Addis Ababa	62	3.6E-07	2.7E-09	NA	4.1E-07	NA	1.5E-06	1.1E-08	NA	1.6E-06	NA

Note. Sites are sorted by total carcinogenic risk. NA: not available.

[a]*N* is the number of samples from each site.

Table S3.14 Hazard quotient of trace elements estimated using mean elemental concentrations in $PM_{2.5}$ samples from SPARTAN sites

Site	*N*[a]	As	Cd	Co	Ni	Mn	V
Dhaka	10	2.1	1.7	0.87	0.51	1.5	0.13
Kanpur	15	1.1	NA	0.24	NA	0.41	0.021
Hanoi	13	0.67	NA	0.21	NA	0.72	0.022
Singapore	12	0.11	NA	NA	0.65	0.13	0.35
Beijing	95	0.23	NA	0.19	NA	0.67	0.014
Kaohsiung	63	0.2	NA	0.13	0.28	0.42	0.019
Ilorin	40	0.16	NA	0.35	NA	0.35	0.019
Delhi	13	0.46	NA	0.1	NA	0.22	0.0084
Ulsan	56	0.41	NA	NA	NA	0.29	0.0074
Seoul	68	0.36	NA	0.077	NA	0.2	0.013
Abu Dhabi	95	0.094	NA	0.21	NA	0.23	0.066
Bandung	24	0.3	NA	NA	NA	0.068	0.0094
Addis Ababa	62	0.066	NA	0.089	NA	0.17	0.011
Pretoria	178	0.15	NA	NA	NA	0.14	0.0081
Johannesburg	109	0.15	NA	NA	NA	0.1	0.0061
Bujumbura	8	0.07	NA	NA	NA	0.18	0.0027
Mexico City	46	0.13	NA	NA	NA	0.076	0.039
Rehovot	176	0.092	NA	NA	NA	0.082	0.021
Taipei	124	0.081	NA	NA	NA	0.094	0.01
Haifa	136	0.075	NA	NA	NA	0.065	0.027
Melbourne	29	0.063	NA	NA	NA	0.043	0.006
Downsview	12	0.05	NA	NA	NA	0.051	0.0025
Pasadena	195	0.038	NA	NA	NA	0.028	0.0032

Halifax	113	0.031	NA	NA	NA	0.011	0.0055
Lethbridge	13	0.02	NA	NA	NA	0.014	0.0012

Note. Sites are sorted by total HI. NA: not available.

[a]*N* is the number of samples from each site.

Table S3.15 Component matrix of the PCA analysis for $PM_{2.5}$ samples from the Dhaka site

Element	PC1	PC2	PC3	PC4	Communality
Pb	0.16	**0.97**	0.12	0.02	0.99
Sb	0.23	**0.96**	0.08	-0.02	0.98
Cd	0.24	0.15	**0.84**	-0.06	0.79
Se	0.24	**0.96**	0.01	-0.03	0.98
As	0.24	**0.96**	0.13	0.02	0.99
Zn	0.11	0.03	**0.90**	0.31	0.93
Cu	0.30	0.53	0.06	0.58	0.70
Ni	0.11	0.32	0.48	**0.75**	0.91
Co	0.32	0.55	**0.70**	0.26	0.97
Fe	**0.96**	0.03	0.12	0.14	0.95
Mn	0.21	-0.12	0.41	0.37	0.36
Cr	**0.80**	0.22	0.16	0.32	0.82
V	-0.22	-0.23	0.09	**0.91**	0.94
Ti	**0.96**	0.17	0.12	-0.04	0.97
Ca	**0.89**	0.25	0.27	-0.07	0.93
Si	**0.84**	0.35	0.18	-0.15	0.88
Al	**0.93**	0.32	0.14	0.01	0.98
Initial Eigenvalue	8.4	2.8	2.6	1.2	
Percent of variance	50	17	16	6.9	
Cumulative percent	50	66	82	89	

Note. Elemenzts are sorted by atomic mass. Loadings > 0.60 are shown in bold.

Chapter 4: Characterizing Particulate Matter Composition in Central Asia: Dust Contribution in Tashkent, Uzbekistan

This work was supported by the Global Incubator Seed Grant from the McDonnell International Scholars Academy Program at Washington University in St. Louis. We are grateful to the administration of the Agency for Hydrometeorological Service (Uzbekistan) for hosting the primary site. Sample collection was supported by Dr. Mansur Amonov and his students (Tashkent Institute of Irrigation and Agricultural Mechanization Engineers – National Research University).

4.1 Abstract

Insufficient ground-based measurements are available to understand particulate matter (PM) in Central Asia, a major global dust source region. Elemental characterization of PM is needed to examine dust contribution to PM and understand dust impacts in this region. We estimated the dust concentration levels using the first contemporary elemental composition data of both $PM_{2.5}$ and PM_{10} samples collected from Tashkent, Uzbekistan during the dusty seasons of 2023, compared to data from historical $PM_{2.5}$ samples collected in 2008–2010. Dust contributed an average of 6.8 μg/m³ (30%) to $PM_{2.5}$ in 2023, higher than in 2009 (4.9 μg/m³, 20%) and 2010 (5.3 μg/m³, 24%) but lower than in 2008 (13 μg/m³, 31%). A large dust event originating from the Kyzylkum Desert in 2023 and another from the Aralkum Desert in 2008 were identified by time series analysis of dust concentration, backward trajectory analysis, and satellite images. The two dust event days show lower Fe but higher Ca fractions in $PM_{2.5}$ than normal days. Compared to 2008–2010, elevated Zn concentrations were observed in 2023, likely driven by metalworking industries, transportation, and construction activities.

4.2 Introduction

Ambient air pollution by fine particulate matter ($PM_{2.5}$) is a leading risk factor for disease and premature death (Apte et al., 2015; Fuller et al., 2022). However, many developing countries lack sufficient ground-based measurements to understand $PM_{2.5}$ (Martin et al., 2019). Despite severe air pollution in developing countries of Central Asia (Amonov & Nishonov, 2020; Kerimray et al., 2020; Miller-Schulze et al., 2015; Tursumbayeva et al., 2023), the $PM_{2.5}$ concentration and chemical composition in this region remain understudied. Air pollution caused by dust storms is common in Central Asia, which is a major global dust source region with several large deserts, including the Kyzylkum Desert, the Karakum Desert, and the Aralkum Desert (Hao Shen et al., 2016; Zhang et al., 2020). Aralkum, the desiccated lakebed of the former Aral Sea, generates salt dust containing pesticides and other chemicals, which adversely affects the environment and human health in the region (Breckle et al., 2012; Indoitu et al., 2015; H. Shen et al., 2019; Singer et al., 2003). Dust events occur frequently in Central Asia during spring, summer, and fall, with reduced frequency in winter (Zhang et al., 2020). Dust can be a major component of ambient PM including fine particles ($PM_{2.5}$) and coarse particles ($PM_{10\text{-}2.5}$, with an aerodynamic diameter between 2.5 and 10 μm). Some studies have investigated dust deposition (Bazarbayev et al., 2022; Groll et al., 2013; Opp et al., 2017) and dust optical depth in Central Asia (Hofer et al., 2017; L. Li & Sokolik, 2018; Xi & Sokolik, 2015). However, few studies have conducted ground measurements of PM composition to quantify dust contributions to PM in this region (Miller-Schulze et al., 2015).

Elemental characterization of PM is needed to estimate concentration levels of mineral dust in Central Asia. Dust mass is typically calculated using a dust equation that sums oxides of major crustal elements based on elemental data (Chow et al., 2015; Liu et al., 2022). Elemental

characteristics (elemental ratios) can help investigate the influence from long-range transport of desert dust (Cao et al., 2008; Hand et al., 2017). Aside from crustal elements, trace element concentrations obtained through elemental analysis provide valuable insights into anthropogenic sources such as coal combustion and traffic (Chang et al., 2018; Querol et al., 2007). Certain elements (e.g., Fe, Cu, Mn, Zn) can considerably contribute to the oxidative potential of PM, which is associated with adverse health effects (Bates et al., 2019; Charrier & Anastasio, 2012).

Uzbekistan, situated at the center of Central Asia, primarily relies on natural gas for power generation and heating, yet faces persistent air pollution challenges (Tursumbayeva et al., 2023). Given the frequent dust storms (Broomandi et al., 2023; Nishonov et al., 2023), dust is anticipated to be a major component of PM in Uzbekistan, but it has not been quantified. A previous long-term monitoring campaign at two urban sites during the summer and fall of 2008–2009 quantified the contributions of inorganic ions, elemental carbon, and organic carbon to PM in Uzbekistan (Amonov et al., 2010). However, the contemporary composition and emission sources of PM in Uzbekistan remain unexplored.

In this study, we present the first contemporary elemental composition data of $PM_{2.5}$ and PM_{10} filter samples collected from Tashkent, the capital of Uzbekistan, during dusty seasons in 2023. We also include elemental data from available historical $PM_{2.5}$ samples collected during the same seasons in 2008–2010. Dust concentration levels are estimated using the elemental data to understand its contribution to $PM_{2.5}$, PM_{10}, and coarse PM ($PM_{10-2.5}$). We identify large dust events, investigate their source areas and elemental characteristics, and explore potential emission sources of major and trace elements in addition to dust.

4.3 Methods

4.3.1 Sample Collection and Chemical Analysis

The sampling site is located at the meteorological station “M-1 Tashkent-Observatory” (41°19'40.96"N, 69°17'42.98"E) of the Agency for Hydrometeorological Service in Tashkent, surrounded by residential and commercial areas with numerous construction activities and an active railroad within 2 km. Two MiniVol TAS samplers (AirMetrics, USA) with inertial impactors were collocated about two meters above the ground to collect $PM_{2.5}$ and PM_{10} on 47 mm Teflon filters at a flow rate of 5 L/min continuously for 24 hours every other day during dusty seasons (June–July and September–October) of 2023. Field blanks were collected after every 7 or 8 samples for each sampler, by installing a blank filter in the sampler and immediately removing it without pulling air through the filter. A QuantAQ MODULAIR-PM sensor was also collocated at the site to provide 1-minute average PM_1, $PM_{2.5}$, and PM_{10} concentrations.

A total of 37 pairs of $PM_{2.5}$ and PM_{10} samples were collected from the site and analyzed at Washington University in St. Louis. The filters were equilibrated for 24 h in an environment with controlled temperature (21.5 ± 1.0°C) and relative humidity (35.0 ± 1.5%) before weighing. Pre- and post-weighing of the filters were conducted using an automated weighing system (MTL AH500E) with a Mettler Toledo XPR6UD5 microbalance (0.5 μg readability). The elemental composition of the filter samples was analyzed using the Epsilon 4 (Malvern Panalytical) Energy-Dispersive X-ray Fluorescence (ED-XRF) instrument. Blank correction was conducted by subtracting the measurement of a laboratory blank filter from the sample measurement. Details about the instrument configuration and analytical application as well as measurement uncertainties for Teflon filters are provided by (Liu et al., 2024). The $PM_{10-2.5}$ concentration and elemental

concentrations in $PM_{10-2.5}$ were calculated as the differences between PM_{10} and $PM_{2.5}$ measurements.

Available historical Teflon filter samples from Tashkent were included in this study for analysis and comparison with the contemporary filter samples. A pioneering field campaign collected $PM_{2.5}$ Teflon filter samples from the same site during the dusty seasons of 2008−2009 (Amonov et al., 2009, 2010). Additional archived $PM_{2.5}$ samples were collected from both this primary site at "M-1 Tashkent-Observatory" and a secondary site at a major intersection with heavy traffic, approximately 4 km northwest of the primary site, during the same months of 2010. These samples from 2008–2010 were weighed using a Mettler Toledo XP-26DR microbalance at the Hydrometeorological Research Institute. The elemental composition of the samples from 2008–2009 was analyzed at the Desert Research Institute using the Epsilon 5 ED-XRF instrument, while the samples from 2010 were analyzed at Washington University in St. Louis using the Epsilon 4 ED-XRF instrument. To ensure comparability of the elemental data from the two instruments, only elements with >50% of measured samples above the method detection limits (MDLs) of both instruments, calculated using laboratory blank filters (U.S. EPA, 2016a), were included for comparison. The number of samples for different years is summarized in Table S4.2.

4.3.2 Dust Calculation

We calculated dust concentrations using a global mineral dust equation based on concentrations of major crustal elements (Liu et al., 2022):

$$\text{dust} = [1.89\text{Al} \times (1 + \text{MAL}) + 2.14\text{Si} + 1.40\text{Ca} + 1.36\text{Fe} + 1.67\text{Ti}] \times \text{CF} \qquad (4.1)$$

where the constants are oxide factors used to convert elements to oxides, MAL represents a mineral-to-aluminum mass ratio defined as $(K_2O+MgO+Na_2O)/Al_2O_3$, and CF is a correction

factor used to account for other missing compounds such as carbonate. The MAL and CF coefficients are developed for six major dust source regions (Middle East, Sahara, Sahel, Australia, East Asia, and Southwest US), but they are not available for Central Asia because of insufficient measured data from the dust source region required for developing the regional coefficients (Liu et al., 2022). To determine appropriate coefficients, we initially used those for the continental crust to calculate dust mass and compared the mean MAL ratio of dust-dominated (dust mass fraction > 50%) samples to the MAL ratios for the six major dust regions. The coefficients for the region with the closest MAL ratio were then applied to determine dust mass in this study.

4.3.3 Trajectory Analysis

We investigated source areas of large dust events characterized by high dust concentration and fraction in $PM_{2.5}$. To identify dust plumes for these events, we downloaded natural color images from the Moderate Resolution Imaging Spectroradiometer (MODIS) on board the National Aeronautics and Space Administration (NASA) Aqua satellite through the NASA Worldview website (https://worldview.earthdata.nasa.gov/). We computed 72-h air mass backward trajectories with arrival heights of 50, 100, and 500 m above ground level using the HYbrid Single Particle Lagrangian Integrated Trajectory (HYSPLIT) model (Rolph et al., 2017; Stein et al., 2015) with Global Data Assimilation System (GDAS) gridded meteorological files at 1° spatial resolution.

To examine the frequency of air masses passing over major desert areas, we also conducted a cluster analysis of backward trajectories using the "trajCluster" function in the "Openair" R package that applies the Partitioning Around Medoids algorithm (Carslaw & Ropkins, 2012). The Euclidean distance matrix is used to compute the similarity between different trajectories. The

optimal number of clusters was determined using the total spatial variance (TSV) method (Draxler et al., 2023).

4.3.4 Principal Component Analysis

We applied principal component analysis (PCA) to qualitatively explore potential emission sources of major and trace elements in $PM_{2.5}$. The covariance matrix was computed from the standardized elemental dataset, and the eigenvectors and eigenvalues were calculated from this matrix to determine the principal components (PCs). PCs with high eigenvalues were extracted to explain most of the total variance, and Varimax rotation was used to simplify interpretation. In the resulting component matrix, the component loadings represent the correlation of each element with each PC, while the communalities indicate the variance of each element explained by the extracted PCs.

4.4 Results and Discussion

4.4.1 Elemental Concentration Levels

Figure 4.1 shows the concentration levels of ten major and trace elements with >50% of measured samples above MDLs of both XRF instruments. Elevated levels of crustal elements, including Al, Si, K, Ca, Ti, Mn, and Fe, were observed in the summer of 2008, indicating large dust events during that year. S and Pb levels remained relatively consistent across different years, while Zn levels were significantly higher in 2023 than in 2008−2010. The mean $PM_{2.5}$-Zn concentration in 2023 (~200 ng/m^3) is comparable to levels observed in other polluted cities worldwide, such as Delhi, India, and Ilorin, Nigeria (Liu et al., 2024; Pant et al., 2017). The elemental comparison between $PM_{2.5}$ and $PM_{10\text{-}2.5}$ for 2023 (Figure S4.6) shows that crustal elements dominated the coarse mode, while Zn, Pb, and S were concentrated in the fine mode. Given that Zn from tire

wear and brake wear is often associated with the coarse mode, the notably higher concentration of Zn in the fine mode suggests the presence of additional major sources (Fussell et al., 2022; Harrison et al., 2012; Hays et al., 2011). No significant differences in elemental concentrations were found between the primary and secondary sites (Figure S4.7), except for Pb ($P < 0.05$), indicating the overall representativeness of the elemental composition across a few kilometers.

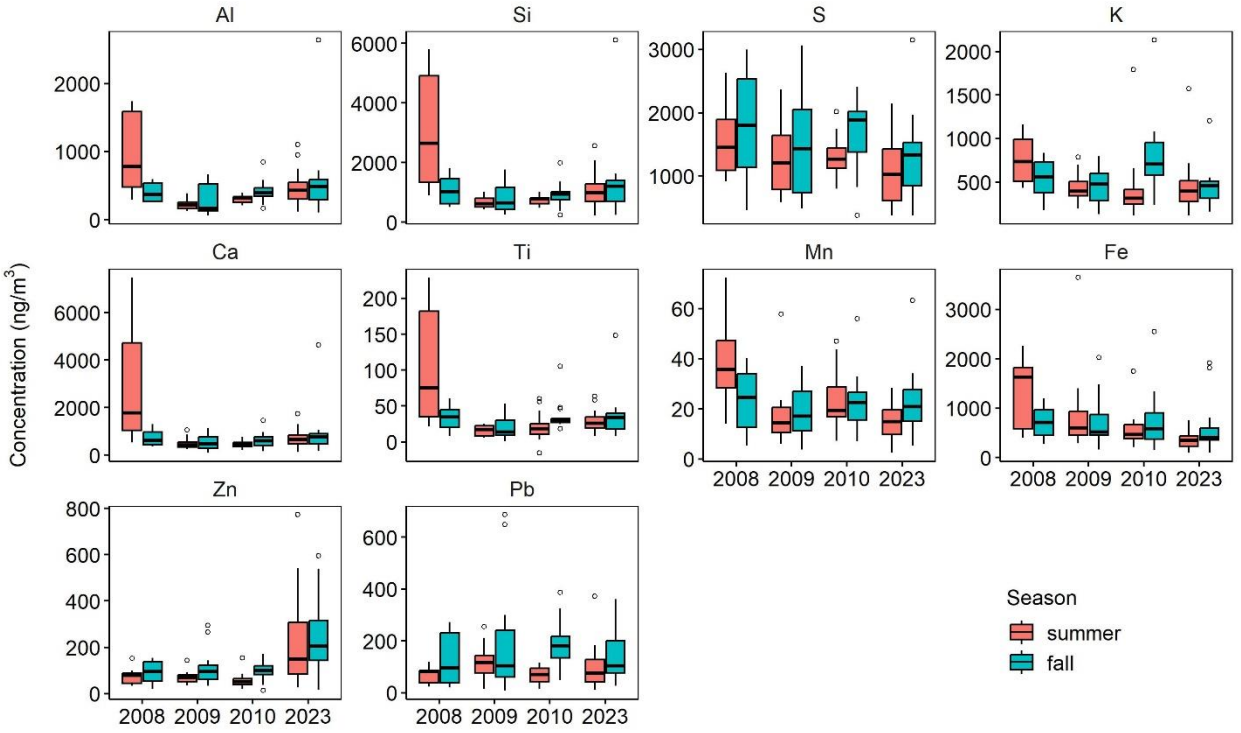

Figure 4.1 Elemental concentrations in $PM_{2.5}$ samples collected at the primary Tashkent site during the summer and fall of 2023 and 2008−2010. The box represents the interquartile range and the line inside indicates the median. The whiskers extend to the minimum and maximum within 1.5 times the interquartile range, and the dots represent outliers.

4.4.2 Dust Concentration Levels

For dust-dominated (dust mass fraction > 50%) samples determined using continental crust coefficients, the mean MAL ratio is 0.92, which is closest to the regional MAL ratio for the Middle East (0.72) and higher than those for other major dust source regions (Liu et al., 2022). Therefore, the MAL ratio of 0.72 and the CF of 1.14 for the Middle East were applied to calculate the dust mass for samples collected from Tashkent. The high MAL ratio found for dust-dominated PM in

Tashkent indicates that natural dust in Central Asia is likely more alkaline than dust in other source regions. Ground measurements of dust composition for deserts in Central Asia are needed to develop the coefficients specific to Central Asia and estimate dust mass in this region more accurately.

Table S4.2 summarizes the dust and total PM concentration levels (mean ± standard deviation) for the samples collected during the summer and fall of 2023 and 2008−2010. Figure 4.2 compares dust concentrations and dust fractions in $PM_{2.5}$ across different years. The mean $PM_{2.5}$-dust concentration in 2023 was 6.8 $\mu g/m^3$, higher than that in 2009 (4.9 $\mu g/m^3$) and 2010 (5.3 $\mu g/m^3$) but lower than that in 2008 (13 $\mu g/m^3$), a year characterized by low precipitation (Amonov et al., 2010). The mean $PM_{2.5}$-dust levels in different years all approach or exceed the World Health Organization (WHO) annual air quality guideline of 5 $\mu g/m^3$ for $PM_{2.5}$ (WHO, 2021), indicating a considerable contribution of dust to $PM_{2.5}$ levels in Tashkent. The mean PM_{10}-dust level of 37 $\mu g/m^3$ observed in 2023 also exceeds the WHO annual air quality guideline of 15 $\mu g/m^3$ for PM_{10}. These dust levels are comparable to those found in other dusty cities worldwide, such as Abu Dhabi, UAE, and Kanpur, India (Liu et al., 2024). In 2023, the mean dust contribution to $PM_{2.5}$ was 30%, close to that of 2008 (31%) but higher than those of 2009 (20%) and 2010 (24%). By deducting dust from the total $PM_{2.5}$, the calculated mean concentration of other $PM_{2.5}$ components in 2023 (15 $\mu g/m^3$, 70%) far exceeds the guideline (Figure S4.8), indicating that controllable sources, in addition to the uncontrollable desert dust, significantly contribute to $PM_{2.5}$ levels in Tashkent.

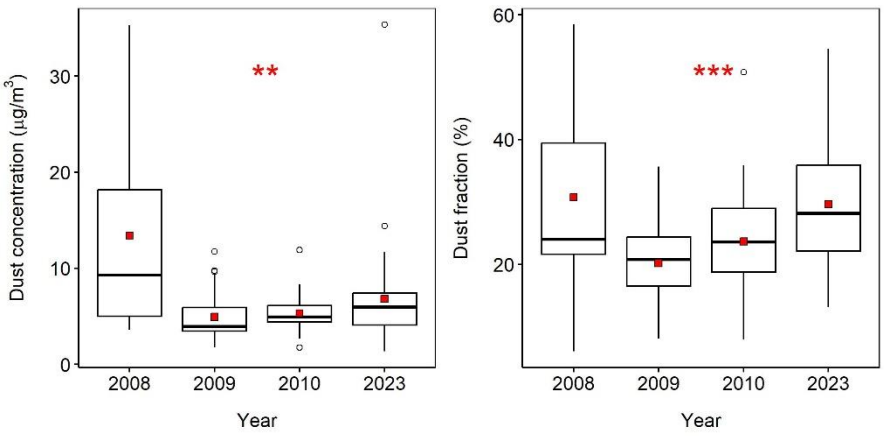

Figure 4.2 Dust concentration and dust fraction in $PM_{2.5}$ samples collected at the primary Tashkent site during the summer and fall of 2023 and 2008−2010. The number of asterisks indicates the significance level (**P < 0.01; ***P < 0.001) of the difference across different years using the Kruskal-Wallis test. The red square indicates the mean. The box represents the interquartile range and the line inside indicates the median. The whiskers extend to the minimum and maximum within 1.5 times the interquartile range, and the dots represent outliers.

Figure 4.3 presents the time series of dust concentrations and dust fractions in fine ($PM_{2.5}$) and coarse ($PM_{10\text{-}2.5}$) PM during the summer and fall of 2023 compared with 2008–2010. In the summer of 2008, multiple dust events, including the large event on 28 June with a peak dust concentration of 35 μg/m^3 and a peak dust fraction of 58%, contributed to the elevated mean $PM_{2.5}$-dust level for that year. A comparable large dust event also occurred on 11 September 2023, with both a high fine dust concentration of 35 μg/m^3 and a high coarse dust concentration of 110 μg/m^3. This event was confirmed by the 1-minute average PM data from the QuantAQ low-cost sensor, showing a sharp increase in PM_{10} concentration and a substantial decrease in the PM_1/PM_{10} ratio (Figure S4.9). The dust fraction in $PM_{2.5}$ increased to 55% during this dust event, while the dust fraction in $PM_{10\text{-}2.5}$ remained relatively constant, indicating that dust dominated the coarse mode during both dust event days and normal days. Throughout the 2023 sampling period, dust accounted for 60 ± 7% (mean ± standard deviation) of coarse PM, with the remaining 40% likely attributed to non-dust components and dust underestimation. A larger potential underestimation of dust was identified at sites in Kyrgyzstan through mass balance calculations (Miller-Schulze et al.,

2015). Higher MAL and CF coefficients may be necessary to calculate dust mass in Central Asia, especially when dust originates from Aralkum, which emits salts such as chlorides and sulfates in addition to carbonates (Orlovsky et al., 2001; Singer et al., 2003). Dust can also absorb acidic species in urban areas forming secondary salts (Heim et al., 2020; Kakavas & Pandis, 2021; Zhai et al., 2023), and adsorbed water can be non-negligible for salt minerals with high hygroscopicity. The expanded global dust equation, which incorporates salt minerals and adsorbed water (Liu et al., 2022), should be applied when sufficient mineralogical and hygroscopicity information for natural dust in Central Asia becomes available in the future. Dust underestimation could also be due to the attenuation effect of light elements in XRF analysis, which can be significant for coarse PM and heavily loaded filter samples (Formenti et al., 2010; Gutknecht et al., 2010).

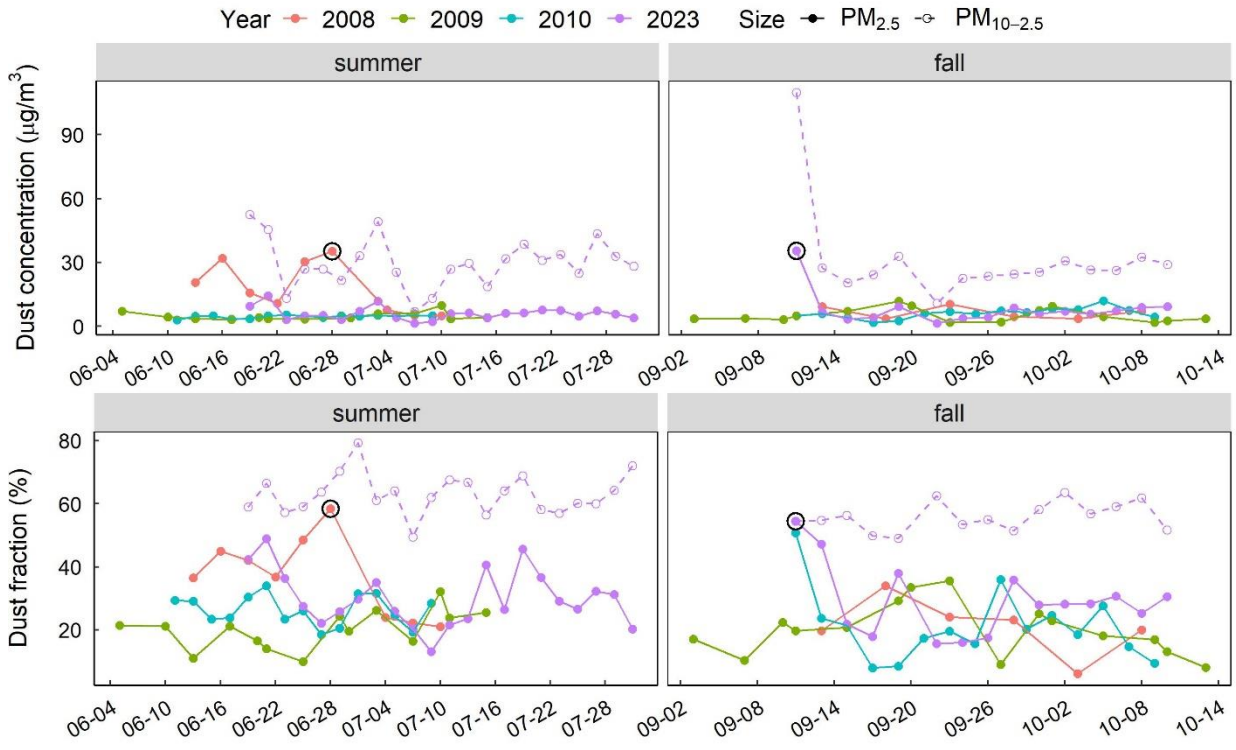

Figure 4.3 Time series of dust concentration and dust fraction in $PM_{2.5}$ and $PM_{10-2.5}$ at the primary Tashkent site during the summer and fall of 2023 and 2008−2010. The dust events on 11 September 2023 and 28 June 2008 with the highest dust concentrations and dust fractions in $PM_{2.5}$ are highlighted in black circles.

4.4.3 Characteristics of Two Large Dust Events

We further investigated the source areas of the large dust events on 11 September 2023 and 28 June 2008. The 3-day backward trajectories and satellite images shown in Figure 4.4 indicate different dust source areas for the two events, with the 2008 event originating from the Aralkum Desert and the 2023 event originating from the Kyzylkum Desert. The satellite image from the day before the 2008 event shows a whitish salt dust plume emitted from Aralkum and transported southeastward, while the satellite image for the 2023 event day shows a yellow dust plume along the edge of a cyclone over Kyzylkum. The backward trajectories for different arrival heights are similar and intersect with the two dust plumes. The cluster analysis results of backward trajectories for the entire year of 2023 (Figure S4.10) show that 22.7% of the air masses originated from the northwest, passing over Aralkum and Kyzylkum, and 17.5% originated from the southwest, passing over Karakum, indicating a high frequency (~40%) of air masses from major desert areas arriving in Tashkent. Similar results were obtained from the cluster analysis for the entire year of 2008 (Figure S4.11).

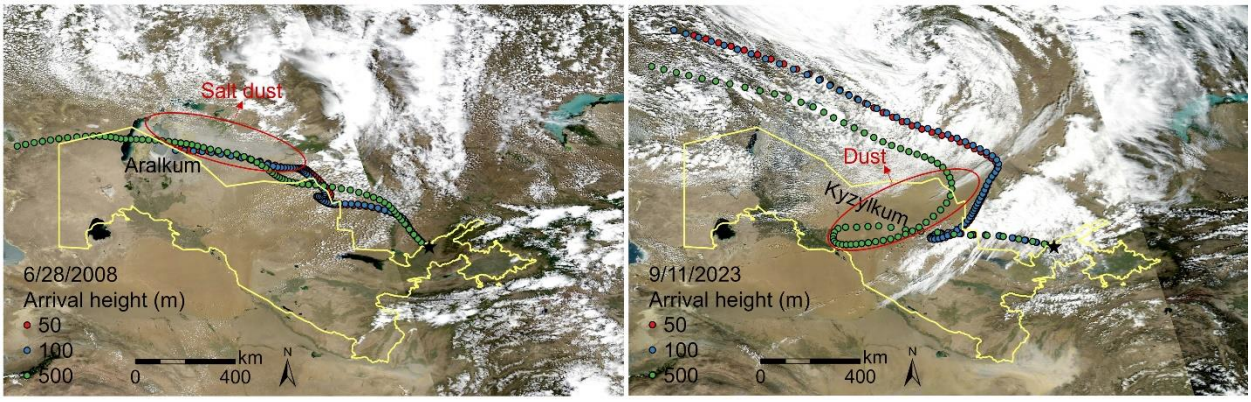

Figure 4.4 The 72-h HYSPLIT backward trajectories with arrival heights of 50, 100, and 500 m for the dust events observed at the primary Tashkent site on (left) 28 June 2008 and (right) 11 September 2023. The background images are MODIS/Aqua images for (left) 27 June 2008 and (right) 11 September 2023 (source: NASA Worldview).

We also examined the elemental characteristics of the two large dust events using the ternary diagram of Ca-Fe-Al. Figure 4.5 shows that $PM_{2.5}$ from both dust event days, especially the 2008 event, exhibits lower Fe but higher Ca abundance than normal days, suggesting a high carbonate content in the desert dust of Central Asia. The elevated Fe fraction observed on some normal days is likely attributable to large anthropogenic sources. The 2008 event originating from Aralkum has a higher Ca fraction (0.68) than the 2023 event (0.50) originating from Kyzylkum, confirming their different origins. Compared to major dust source regions and continental crust, the elemental characteristics of the two events are similar to those of the Middle East and Saraha, which produce carbonate-rich dust (Liu et al., 2022). Elemental characterization of dust across various source areas in Central Asia is important to help identify the origins of desert dust transported to urban areas within the region and beyond.

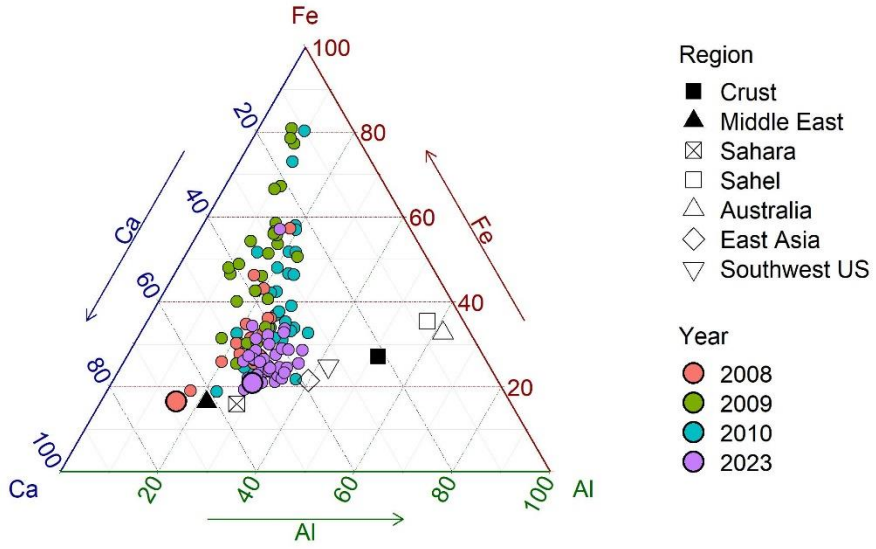

Figure 4.5 Ternary diagram (Ca-Fe-Al) of $PM_{2.5}$ samples collected from the primary Tashkent site during the summer and fall of 2023 and 2008−2010. Representative elemental compositions for major dust source regions and continental crust summarized by Liu et al. (2022) are included for comparison. The dust events on 11 September 2023 and 28 June 2008 are highlighted with large dots.

4.4.4 Source Apportionment of Major and Trace Elements

We qualitatively explored contemporary putative emission sources, in addition to dust, for major and trace elements using elemental data of $PM_{2.5}$ samples collected from Tashkent during the summer and fall of 2023. The correlation analysis results (Figure S4.12) show strong positive correlations ($r > 0.8$, $P < 0.0001$) among major crustal elements including Al, Si, Ca, Ti, and Fe, indicating dust sources. Moderate correlations ($r > 0.6$, $P < 0.0001$) were found between K and major crustal elements, as well as between Mn and major crustal elements, suggesting the presence of both natural and anthropogenic sources for K and Mn. Zn strongly correlates with Mn ($r = 0.7$, $P < 0.0001$), while S and Pb did not show strong correlations ($r \geq 0.7$) with the examined elements. Table 4.1 presents the PCA results with three PCs explaining 87% of the total variance and >70% of the variance for each element, except for K, which may have other sources such as wood burning for traditional cooking and the burning of leaves and plant residues in fall (Uzhydromet, 2020). PC1 is dominated by crustal elements, representing mineral dust emission. In addition to natural dust, anthropogenic sources such as road and construction dust also notably contribute to the crustal elements in Tashkent. PC2 is highly associated with Pb and S, implying possible combustion sources, while PC3 is strongly loaded with Zn, suggesting potential industrial and vehicle emissions. The elevated Zn concentrations observed in 2023 (Figure 4.1) could be attributed to various sources, including numerous metalworking factories in Tashkent, as well as lubricant oil combustion, tire wear, and brake wear from the increasing number of vehicles (Dallmann et al., 2014; Fussell et al., 2022). In addition to the large number of natural gas vehicles in Tashkent, diesel engines in construction equipment and railroad locomotives could also contribute to the high Zn concentrations (Reff et al., 2009), given the widespread construction activities and the busy railroad network across the city. Further investigation of potential emission

sources for these elements is constrained by the lack of a microscale emission inventory and samples covering all four seasons.

Table 4.1 Component matrix of the PCA analysis for $PM_{2.5}$ samples collected at the primary Tashkent site during the summer and fall of 2023

Element	PC1	PC2	PC3	Communality
Pb	0.11	**0.93**	0.03	0.87
Zn	0.02	0.17	**0.97**	0.97
Fe	**0.83**	0.09	0.10	0.71
Mn	**0.82**	0.23	0.44	0.92
Ti	**0.97**	0.16	-0.03	0.96
Ca	**0.98**	0.02	0.03	0.97
K	**0.70**	0.37	-0.07	0.63
S	0.16	**0.84**	0.24	0.80
Si	**0.98**	0.09	0.03	0.97
Al	**0.97**	0.13	0.02	0.96
Initial Eigenvalue	6.1	1.7	0.9	
Percent of variance	61	17	9	
Cumulative percent	61	78	87	

Note. Loadings ≥ 0.70 are shown in bold.

4.5 Conclusions

Overall, this study quantified the dust contribution to ambient PM in Tashkent, Uzbekistan using the first contemporary elemental composition data of PM samples collected during dust storm seasons in 2023. The available historical (2008−2010) $PM_{2.5}$ samples were also included for analysis and comparison. We found that the mean dust contribution to $PM_{2.5}$ was 30% in 2023, similar to 2008 (31%) but higher than in 2009 (20%) and 2010 (24%). Both dust and non-dust components in $PM_{2.5}$ exceeded the WHO annual guideline. Two large dust events in 2008 and 2023 were identified by their high dust concentrations (35 $\mu g/m^3$) and dust fractions (~60%) in $PM_{2.5}$. Backward trajectory analysis and satellite images indicate that the 2008 event originated from the Aralkum Desert, while the 2023 event originated from the Kyzylkum Desert. $PM_{2.5}$ samples from both dust event days exhibit lower Fe but higher Ca content than normal days. The

Zn concentration level in 2023 was significantly higher than the levels observed in 2008–2010. In addition to natural dust, anthropogenic sources including construction, combustion, metalworking industries, and transportation also potentially contribute to the major and trace elements in Tashkent.

Ground measurements of dust composition including elemental and mineralogical characterization across the source areas in Central Asia are needed to estimate dust contribution to PM more accurately in this region. Quantifying the attenuation effects of light elements in XRF analysis could further enhance the accuracy of dust estimation from XRF measurements. The health effects of contaminated salt dust in $PM_{2.5}$ from the Aralkum Desert deserve to be investigated, given the role of Aralkum as a source area for large dust events in urban cities. The considerable contribution of non-dust components to $PM_{2.5}$ suggests an urgent need to investigate anthropogenic sources of $PM_{2.5}$ in Uzbekistan. Characterization of other $PM_{2.5}$ components, samples representative of all seasons, and detailed emission inventories are needed to conduct comprehensive source apportionment of $PM_{2.5}$. This study helps fill the gap in understanding dust contribution to PM in Central Asia, providing evidence to guide air pollution management strategies in the region.

4.6 Supplementary Material

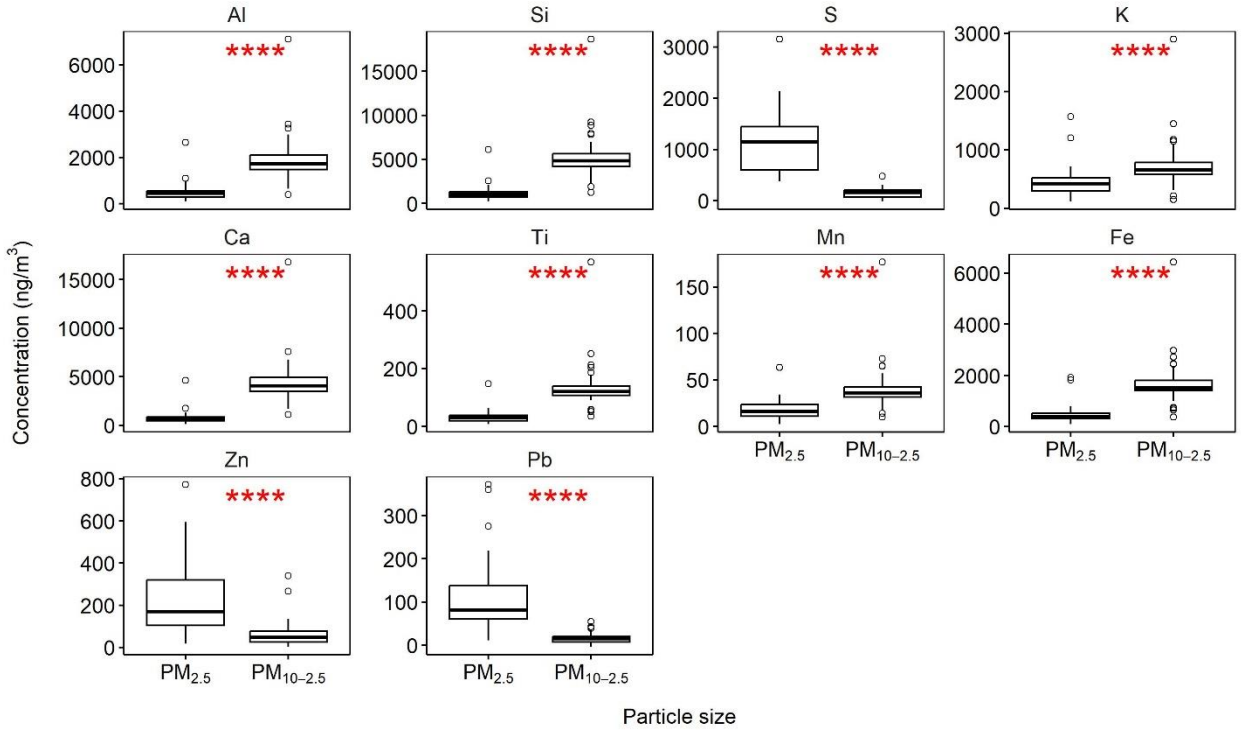

Figure S4.6 Comparison of elemental concentrations between $PM_{2.5}$ and $PM_{10–2.5}$ at the primary Tashkent site during the summer and fall of 2023. The number of asterisks indicates the significance level (****P < 0.0001) of the difference between the two sites using the Wilcoxon test. The box represents the interquartile range (IQR) and the line inside indicates the median. The whiskers extend to the minimum and maximum within 1.5 times the IQR, and the dots represent outliers.

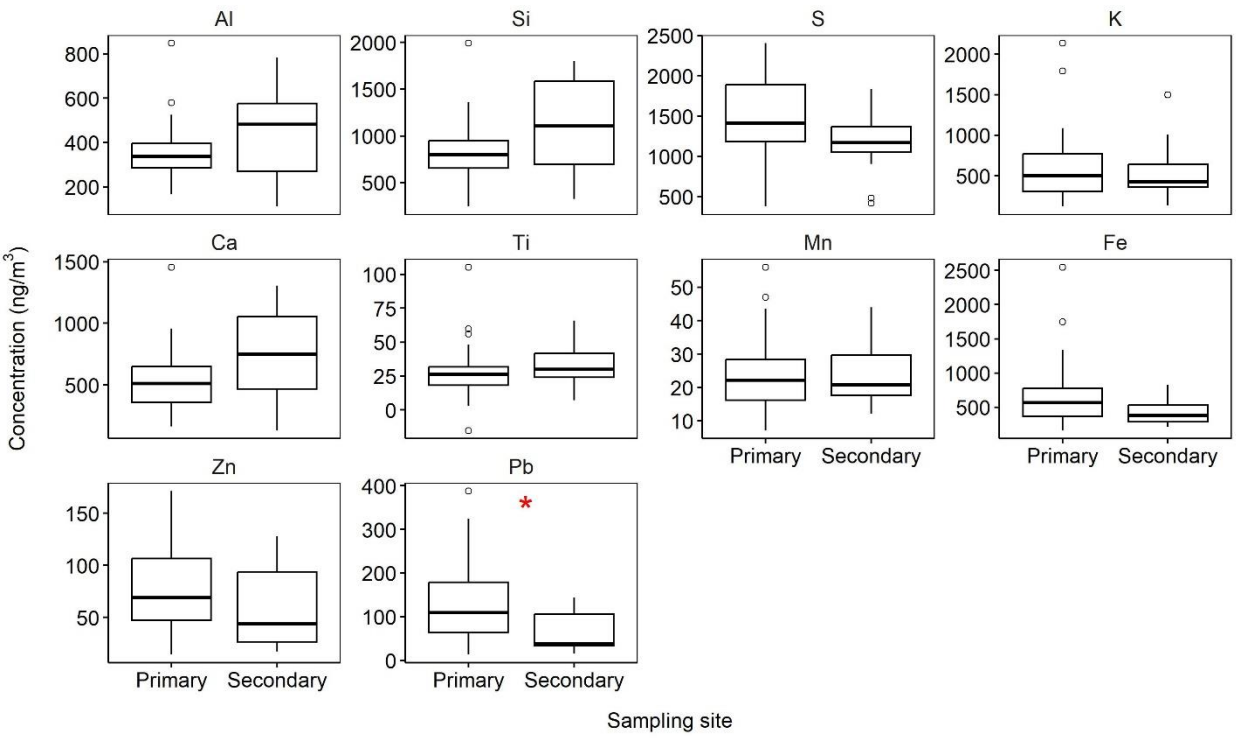

Figure S4.7 Comparison of elemental concentrations in $PM_{2.5}$ samples between the primary and secondary Tashkent sites during the summer and fall of 2010. The number of asterisks indicates the significance level (*$P < 0.05$) of the difference between the two sites using the Wilcoxon test. The box represents the IQR and the line inside indicates the median. The whiskers extend to the minimum and maximum within 1.5 times the IQR, and the dots represent outliers.

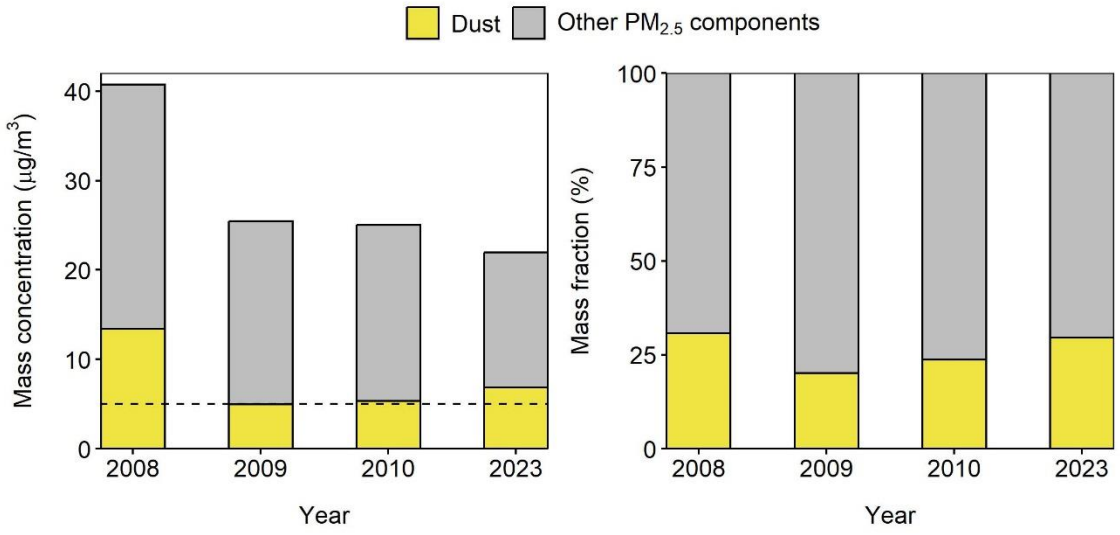

Figure S4.8 Mass concentration and fraction of dust and other components in $PM_{2.5}$ samples collected at the primary Tashkent site during the summer and fall of 2023 and 2008−2010. The dashed line represents the World Health Organization (WHO) annual air quality guideline of 5 µg/m^3 for $PM_{2.5}$.

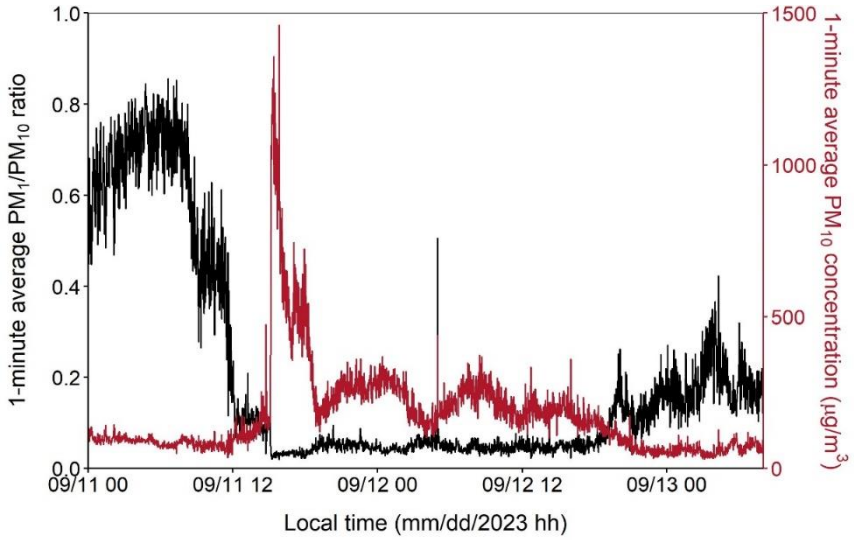

Figure S4.9 The 1-minute average PM_1/PM_{10} ratio and PM_{10} concentration from the MODULAIR-PM sensor at the primary Tashkent site for the dust event on September 11th, 2023.

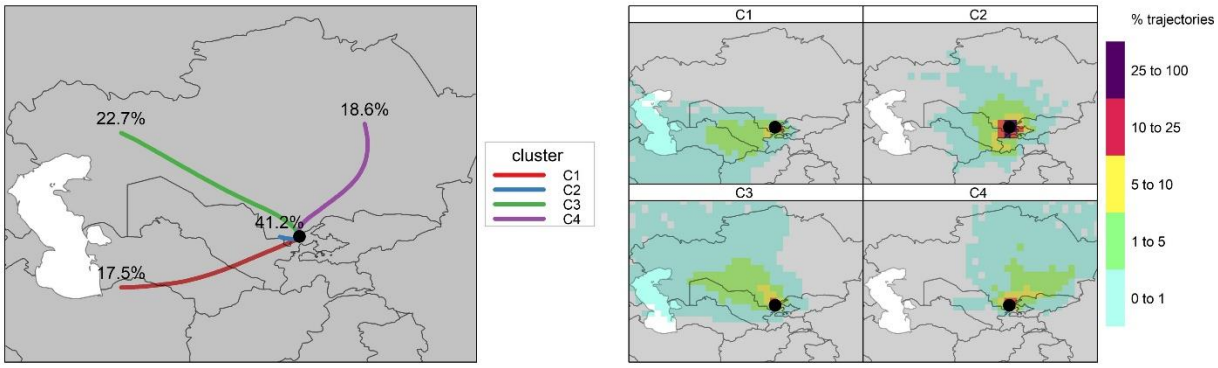

Figure S4.10 The mean trajectory of each cluster (left) and trajectory frequencies for each cluster (right) based on 72-h HYSPLIT backward trajectories with an arrival height of 100 m for the primary Tashkent site in 2023.

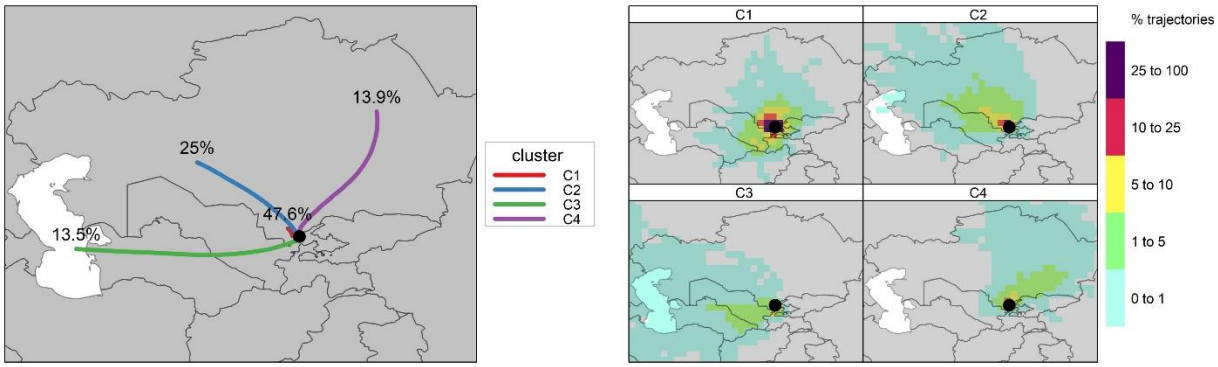

Figure S4.11 The mean trajectory of each cluster (left) and trajectory frequencies for each cluster (right) based on 72-h HYSPLIT backward trajectories with an arrival height of 100 m for the primary Tashkent site in 2008.

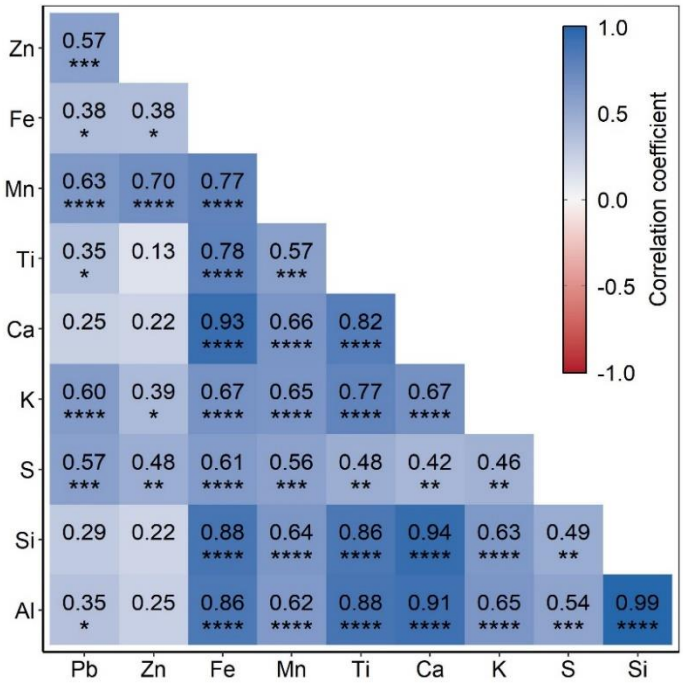

Figure S4.12 Nonparametric Spearman's correlation coefficients among elements for $PM_{2.5}$ samples collected at the primary Tashkent site during the summer and fall of 2023. The number of asterisks indicates the significance level (*P < 0.05; **P < 0.01; ***P < 0.001; ****P < 0.0001).

Table S4.2 Sampling information and mass concentrations (mean ± standard deviation) of PM and dust for PM samples collected at the primary and secondary sites

Site	Year	Particle size	N_{summer}	N_{fall}	N_{total}	XRF instrument	PM (μg/m^3)	Dust (μg/m^3)
Primary	2023	PM_{10}	22	15	37	Epsilon 4	73±39	37±22
Primary	2023	$PM_{2.5}$	22	15	37	Epsilon 4	22±9.8	6.8±5.5
Primary	2010	$PM_{2.5}$	15	15	30	Epsilon 4	25±11	5.3±2.0
Primary	2009	$PM_{2.5}$	14	15	29	Epsilon 5	25±9.7	4.9±2.6
Primary	2008	$PM_{2.5}$	9	6	15	Epsilon 5	41±18	13±11
Secondary	2010	$PM_{2.5}$	6	6	12	Epsilon 4	24±10	6.4±2.8

Note. N indicates the number of collected samples.

Chapter 5: Assessing Attenuation Effects in X-ray Fluorescence Analysis of Light Elements in Mineral Dust

This work was supported by NOAA (Grants NA230AR4310464 and NA24NESX432C001) and NSF (Grant 2020673). Sample collection was supported by Dr. Dhruv Mitroo and Yuxuan Ren (Washington University in St. Louis). Filter weighing was supported by Dr. Christopher Oxford, Wenyu Liu, and Zilin Wei (Washington University in St. Louis).

5.1 Abstract

Reliable elemental analysis is important for understanding mineral dust sources, mass concentrations, composition, and atmospheric processing. Attenuation effects for light elements measured by the widely used X-ray fluorescence (XRF) technique can lead to an underestimation of dust mass. However, correcting for these effects in filter samples of ambient particulate matter (PM) remains a significant challenge. This study assesses attenuation due to mass loading, particle size, and chemical composition for silicon and aluminum by comparing XRF and gravimetric measurements of samples with known compositions. Micron-sized powder oxides, SiO_2 and Al_2O_3, and Arizona test dust (ATD) were aerosolized and collected on Teflon filters to generate samples with varying mass loadings and particle size ranges. The results from the oxide samples validated that attenuation increases with both mass loading and particle size, while the significantly higher attenuation in ATD samples than in SiO_2 samples with the same mass loading and size range indicated the composition dependence of attenuation. The combined attenuation estimated by two theoretical models incorporating composition, mass loading, and particle size agreed well (slope = 1.01, R^2 = 0.99) with the measured attenuation for silicon in collected $PM_{2.5}$ ATD samples.

Applying attenuation corrections based on theoretical models to ambient $PM_{2.5}$ samples from a global monitoring network (SPARTAN) revealed an average increase of 30% in estimated dust concentrations. This work demonstrates the importance of considering attenuation effects in XRF analysis for accurate dust measurements.

5.2 Introduction

Atmospheric mineral dust has a widespread impact on climate, ecosystems, human health, and socio-economic sectors (Cuevas-Agulló et al., 2024; Kok et al., 2023; Salvador et al., 2022). Exposure to dust in ambient fine particulate matter ($PM_{2.5}$) with aerodynamic diameter <2.5 μm is associated with respiratory and cardiovascular diseases (Ostro et al., 2016; Vedal et al., 2013). In ground-based PM measurements, elemental composition is typically analyzed to estimate dust mass using a dust equation that sums common oxides of major crustal elements, such as Si and Al (Chow et al., 2015; Liu et al., 2022; Malm et al., 1994). Elemental ratios (e.g., Ca/Al) are commonly utilized to distinguish source areas of dust (Aldhaif et al., 2020; Scheuvens et al., 2013). Thus, reliable elemental composition is essential for estimating dust contributions to ambient PM and understanding dust characteristics.

The X-ray fluorescence (XRF) technique is widely used to characterize the elemental composition of PM samples collected on filters. Its non-destructive nature, requiring no acid digestion, enhances analysis efficiency, reduces costs, enables additional speciation analysis, and avoids extraction efficiency issues compared to destructive techniques such as inductively coupled plasma mass spectrometry. This advantage is particularly significant for large-scale monitoring networks (Liu et al., 2024; Solomon et al., 2014). However, light elements are susceptible to attenuation effects in XRF analysis. Attenuation effects occur when part of the incoming X-rays and the

fluorescent X-rays emitted by the target elements are absorbed by other components in the sample, weakening the detected signal. Attenuation is more pronounced for light elements than for heavy elements because of the lower energy ("soft") X-rays that light elements emit. Light elements, particularly crustal elements like Si and Al, are major elements in dust that are incorporated into dust equations used to infer dust mass. Therefore, attenuation effects can lead to underestimation of dust mass and inaccuracies in elemental ratios.

The magnitude of attenuation in XRF analysis of PM filter samples depends on multiple factors, including mass loading, particle size, and chemical composition (Gutknecht et al., 2010). Greater attenuation is anticipated with high mass loading and large particles because of the increased path length of X-rays traveling through the deposit compared to low mass loading and small particles (Chiapello et al., 1997; Formenti et al., 2010). Attenuation resulting from particle penetration into the filter can be substantial for quartz fiber filters but is negligible for "surface filters" such as Teflon (Chiari et al., 2018).

Dzubay and Nelson (1974) established foundational theoretical models for estimating attenuation in PM filters. They utilized a homogeneous layer model for fine particles, assuming negligible attenuation within fine particles, and a particle size model for coarse particles, assuming these particles are collected as a monolayer on the filter. In the context of $PM_{2.5}$, Gutknecht et al. (2010) reviewed theoretical models developed to estimate attenuation and proposed using the particle size model for light elements (Na, Mg, Al, and Si) and the homogeneous layer model for heavier elements ($Z > 14$) in $PM_{2.5}$ based on Dzubay and Nelson's work as extended by Kellogg. Kellogg (2005) assumed that particles containing light elements are primarily at the high end of the $PM_{2.5}$ size distribution and therefore used the particle size model to estimate attenuation for light

elements in $PM_{2.5}$ by averaging the attenuations for potential mineral forms containing these elements. However, considering only attenuation due to particle size for light elements in $PM_{2.5}$ may be valid for filters with low mass loading where the monolayer assumption is applicable, but may not be suitable for filters with high dust loading such as those collected during dust events. These models have not been thoroughly evaluated by experiments. Only a limited number of studies have applied experimental methods to estimate the attenuation effects of light elements for PM filter samples in XRF (Chiapello et al., 1997; Formenti et al., 2010; Turner & Brown, 2015), as well as in a similar technique, particle-induced X-ray emission (PIXE) (Calzolai et al., 2014; D'Alessandro et al., 2003; Maenhaut & Cafmeyer, 1998).

This study aims to experimentally assess the attenuation effects with a specific focus on Si and Al in $PM_{2.5}$. We examine attenuation due to mass loading, particle size, and chemical composition for Si and Al by comparing XRF measurements with gravimetric data of samples with known compositions. PM samples with varying mass loadings and particle size ranges are generated by aerosolizing micron-sized powder oxides (SiO_2 and Al_2O_3) and Arizona test dust, which are then collected on Teflon filters. The experimental results are compared to estimates derived from the homogeneous layer and particle size models. These theoretical models are also applied to ambient $PM_{2.5}$ samples with elevated dust content collected from the global monitoring network, Surface Particulate Matter Network (SPARTAN, Snider et al., 2015). The potential impact of attenuation effects on dust concentration estimates is evaluated.

5.3 Materials and Methods

5.3.1 Materials

We used commercially available 5-μm Al_2O_3 and SiO_2 powder with a high purity of >99.5% (US Research Nanomaterials, Inc.) and Arizona Test Dust (ATD, ISO 12103-1 A1 Ultrafine Grade, Powder Technology Inc.) with a volume mean diameter of 4.76 μm. The size distribution data for the micron powder oxides is not available from the manufacturer. The chemical composition of ATD measured by XRF following the ASTM C114-15 norm (ISO, 2024) and its size distribution determined by a laser diffraction analyzer (Microtrac, Inc.) were provided by the manufacturer. ATD primarily consists of SiO_2 (69–77%) along with smaller amounts of other crustal element oxides (Table S5.1).

5.3.2 Sample Collection and Analysis

The micron powder oxides and ATD were aerosolized using a recently developed benchtop system, which contains a wrist-action shaker, custom-made flask, sharp-cut cyclone (BGI, SCC1.829), neutralizer, and dilution drum (Mitroo et al., 2021). An AirPhoton (Baltimore, MD) SS5 sampling station was connected to the dilution drum to collect aerosolized particles on 25 mm Teflon filters. PM_1, $PM_{2.5}$, and PM_{10} samples were collected by operating the cyclone at flow rates of 11 L/min, 5 L/min, and 1.5 L/min, respectively. Varying mass loadings were achieved by adjusting the sampling time. The cyclone was regularly checked for clogging, and samples collected with a severely clogged cyclone were excluded from the analysis. The system was cleaned with methanol-wetted Kimwipes^{TM} and compressed air before collecting new material. Method blanks were collected after cleaning to assess potential contamination from the system. These blanks followed all procedures without adding powder or ATD.

Filters were weighed before and after the sampling using a Mettler Toledo XPR6UD5 microbalance with a high readability of 0.5 μg in an automated weighing system (MTL AH500E). Prior to weighing, the filters were conditioned for 24 h in a controlled environment (temperature = 21.5 ± 1.0°C, relative humidity = 35.0 ± 1.5%). Each filter was weighed three times, and the mean and standard deviations were recorded. The elemental composition of the collected filters was analyzed by the Epsilon 4 instrument (Malvern Panalytical), which employs the Energy-Dispersive X-ray Fluorescence (ED-XRF) technique. The Epsilon 4 configuration and analytical conditions for analyzing PM composition on Teflon filters have been previously described (Liu et al., 2024).

5.3.3 Experimental Assessment of Attenuation

The attenuation effect for element *i* can be represented using the attenuation factor (A_i):

$$I_{measured,i} = I_i \times A_i \tag{5.1}$$

where I_i and $I_{measured,i}$ are the intensities before and after attenuation for element *i*. For all cases $A_i \leq 1$ and smaller values of A_i correspond to greater attenuation. The experimental A_i in this study was obtained by comparing XRF and gravimetric measurements:

$$A_i = \frac{M_{\mathrm{XRF},i}}{M_{\mathrm{grav},i}} = \frac{M_{\mathrm{XRF},i}}{m \times w_i / \mathrm{S}} \tag{5.2}$$

where $M_{\mathrm{XRF},i}$ and $M_{\mathrm{grav},i}$ are the mass loadings (μg/cm^2) for element *i* from XRF and gravimetric measurements, *m* is the total mass of the deposit, w_i is the mass fraction of element *i* in the total mass, and S is the known deposition area. The uncertainty of the measured A_i ($\sigma_{A,i}$) was calculated by considering the elemental uncertainties from both XRF and gravimetric measurements:

$$\sigma_{A,i} = A_i \times \sqrt{\left(\frac{\sigma_{\mathrm{XRF},i}}{M_{\mathrm{XRF},i}}\right)^2 + \left(\frac{\sigma_{\mathrm{grav},i}}{M_{\mathrm{grav},i}}\right)^2} \tag{5.3}$$

For micron powders of pure oxides, w_i was determined by stoichiometry, and $\sigma_{\mathrm{grav},i}$ was determined by the uncertainty from measurements of m (σ_m), which can be calculated using the standard deviations of pre- and post-sampling weights from the microbalance (σ_{pre} and σ_{post}):

$$\sigma_{\mathrm{grav},i} = \sigma_m \times \frac{w_i}{\mathrm{S}} = \sqrt{\sigma_{\mathrm{pre}}^2 + \sigma_{\mathrm{post}}^2} \times \frac{w_i}{\mathrm{S}} \tag{5.4}$$

For ATD containing multiple oxides, $\sigma_{\mathrm{grav},i}$ was determined by both σ_m and the uncertainty in w_i ($\sigma_{w,i}$) derived from the ATD composition data provided by the manufacturer:

$$\sigma_{\mathrm{grav},i} = \sqrt{\left(\sigma_m \times \frac{w_i}{\mathrm{S}}\right)^2 + \left(\sigma_{w,i} \times \frac{m}{\mathrm{S}}\right)^2} \tag{5.5}$$

Given only the lower and upper limits of the oxide mass fractions in ATD, w_i was calculated using stoichiometry and the mean mass fraction of the corresponding oxide based on the limits, and $\sigma_{w,i}$ was roughly estimated using stoichiometry and half of the range between the limits. The calculated w_i and $\sigma_{w,i}$ are provided in the Supporting Information (Table S5.1). The elemental uncertainty and method detection limit (MDL) for XRF measurements of Teflon filters using the Epsilon 4 are from Liu et al. (2024). The MDL for mass measurements was calculated using the mean plus three times the standard deviation from the collected method blanks. Only samples with mass above the MDL were included for analysis.

5.3.4 Theoretical Estimation of Attenuation

The theoretical models developed by Dzubay and Nelson (1974) were applied to calculate theoretical A for $PM_{2.5}$. Assuming the sample can be considered as a homogeneous layer where

particle size is smaller than the layer thickness and attenuation within particles is negligible, the theoretical A due to mass loading (A_{mass}) can be calculated as:

$$A_{\text{mass}} = \frac{1-\exp(-\bar{\mu}M)}{\bar{\mu}M} \tag{5.6}$$

where M is the total mass loading (g/cm^2) and $\bar{\mu}$ is the total mass absorption coefficient (cm^2/g). The calculation of $\bar{\mu}$ involves elemental mass fractions, elemental mass absorption coefficients for incoming and emitted fluorescent X-rays, and the geometry of the sample relative to the X-ray source and detector, as shown in the Supporting Information (Text 5.6.1).

To determine the attenuation due to particle size, Dzubay and Nelson (1974) assumed particles could be treated as equivalent spheres and were collected as a monolayer on the filter. The attenuation factor for a sphere, A(sphere), can be calculated as a function of geometric particle diameter, particle density, and parameters used in the $\bar{\mu}$ calculation, which is shown in the Supporting Information (Text 5.6.1). The theoretical A due to particle size (A_{size}) for a sample can be calculated by averaging A(sphere) over the size distribution:

$$A_{\text{size}} = \frac{\int A(\text{sphere})\frac{\mathrm{d}V}{\mathrm{d}\log D}\eta(D)\mathrm{d}\log D}{\int \frac{\mathrm{d}V}{\mathrm{d}\log D}\eta(D)\mathrm{d}\log D} \tag{5.7}$$

where D is the geometric diameter, dV/dlog$D$ is the volume size distribution, and $\eta(D)$ is the penetration efficiency. $\eta(D)$ for collected $PM_{2.5}$ samples was calculated using the equation and parameters developed by Peters et al. (2001) for the cyclone model used in this study. However, the parameters for collecting PM_1 and PM_{10} were not available. When calculating $\eta(D)$, the geometric diameter was converted to aerodynamic diameter (D_a) using particle density and dynamic shape factor for nonspherical particles (Hinds & Zhu, 2022):

$$D_a = D\sqrt{\frac{\rho_p}{\rho_0 \chi}} \tag{5.8}$$

where χ is the dynamic shape factor, ρ_p is the particle density, and ρ_0 is the standard particle density (1 g/cm^3). For ATD, ρ_p is 2.65 g/cm^3 according to the manufacturer, matching the density of quartz. Therefore, the χ of quartz (1.36) was used for ATD (Boose et al., 2016; Hinds & Zhu, 2022).

5.3.5 Application to Ambient Dust

The theoretical models were also applied to ambient $PM_{2.5}$ samples collected from the SPARTAN network to assess the potential attenuation impact on dust concentrations. The SPARTAN samples were collected and analyzed using the same sampler, cyclone, Teflon filters, and XRF as used for powder oxides and ATD in this study. The early development, site locations, sampling procedures, quality assurance, and applications for SPARTAN have been described in previous studies (McNeill et al., 2020; Snider et al., 2015, 2016; Weagle et al., 2018). Dust concentrations were calculated using a global mineral dust equation with regional coefficients based on concentrations of major crustal elements (Liu et al., 2022).

We estimated theoretical attenuation factors for dust-dominated (dust > 50% of total mass) $PM_{2.5}$ SPARTAN samples collected over 2019−2024. The composition and mass loading for each sample were represented by the oxides of crustal elements and relatively abundant trace elements (Na, Mg, Al, Si, K, Ca, Ti, Mn, Fe, Zn, and Pb), which approximate the dust components. The effect of including additional $PM_{2.5}$ species on the attenuation factors was evaluated. Since the size distribution of SPARTAN samples was not available, the size distribution for emitted dust aerosols developed by Kok (2011) was applied. A typical dust density of 2.5 g/cm^3 was used, and a 45% increase was applied to convert aerodynamic diameter to geometric diameter for dust particles, as

suggested by a previous study (Huang et al., 2021). Attenuation factors estimated for Si and Al were used to correct the concentrations:

$$C_{corr,i} = \frac{C_{no\ corr,i}}{A_i} \tag{5.9}$$

where $C_{corr,i}$ and $C_{no\ corr,i}$ are the concentrations (μg/m^3) of element *i* with and without attenuation correction, respectively. The resulting dust concentrations were calculated after applying the attenuation correction.

5.4 Results and Discussion

5.4.1 Experimental Assessment of Attenuation

Figure 5.1 presents the measured attenuation factors for Al (A_{Al}) in Al_2O_3 samples with varying size ranges and total mass loadings based on XRF and gravimetric measurements. A decreasing trend in A_{Al} with increasing mass loading was observed across all size ranges, validating that Al attenuation increases with mass loading. For $PM_{2.5}$ Al_2O_3 samples, A_{Al} decreased from 0.93±0.06 at a total mass loading of 7.5 μg/cm^2 to 0.82±0.04 at 92 μg/cm^2. Despite the limited number of samples, a slight increase in Al attenuation with particle size was also observed. A_{Al} showed only a minor difference between PM_1 and $PM_{2.5}$ but decreased by approximately 0.05 as the size range increased from $PM_{2.5}$ to PM_{10}. The A_{Al} in ATD samples is not shown because of the low Al mass fraction (~6%) and significant associated uncertainty (~28%) from the ATD composition data (Table S5.1), which results in substantial error bars for the calculated attenuation factor and hinders meaningful comparison.

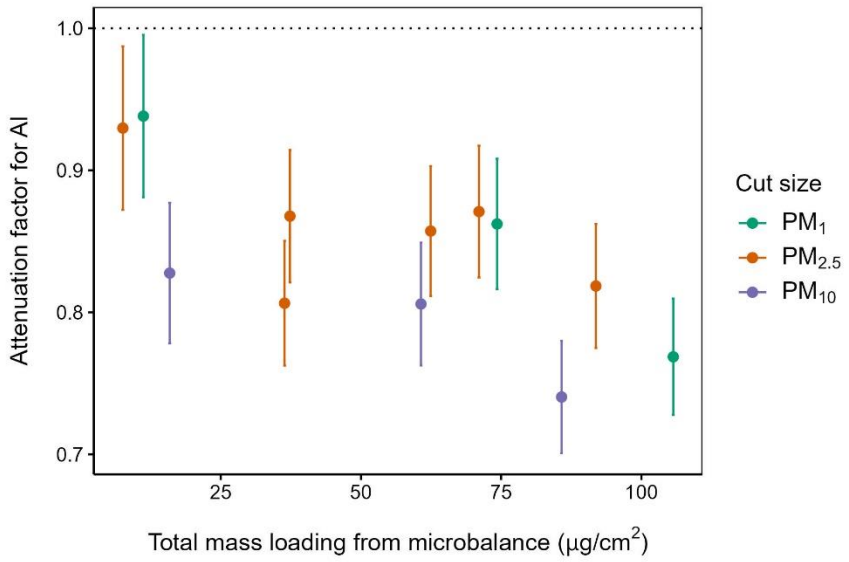

Figure 5.1 Attenuation factors for Al in Al_2O_3 powder samples. The error bars indicate the combined uncertainties from both XRF and gravimetric measurements. The dotted line denotes an attenuation factor of 1, indicating no attenuation.

Figure 5.2 shows the measured attenuation factors for Si (A_{Si}) in SiO_2 and ATD samples across various size ranges and total mass loadings. A decreasing trend in A_{Si} (increasing attenuation) with increasing mass loading was observed for both SiO_2 and ATD samples across all size ranges. For $PM_{2.5}$ ATD samples, A_{Si} decreased from 0.72±0.05 at a total mass loading of 59 μg/cm^2 to 0.33±0.02 at 923 μg/cm^2. A significant decrease (~0.1) in A_{Si} for ATD samples compared to SiO_2 samples at equivalent total mass loadings and size ranges was observed, indicating that attenuation is composition dependent. The presence of other oxides in ATD can absorb more fluorescent X-rays emitted by Si than pure SiO_2, leading to greater Si attenuation in ATD. The non-linear relationship of Si mass loadings between XRF and gravimetric measurements for $PM_{2.5}$ samples of SiO_2 and ATD is presented in Figure S5.5. A greater deviation from the one-to-one line was observed in ATD samples than in SiO_2 samples at the same Si mass loading. Since the ATD samples better match the matrix of ambient PM than the pure SiO_2 samples, their attenuation is expected to reflect real-world samples more closely.

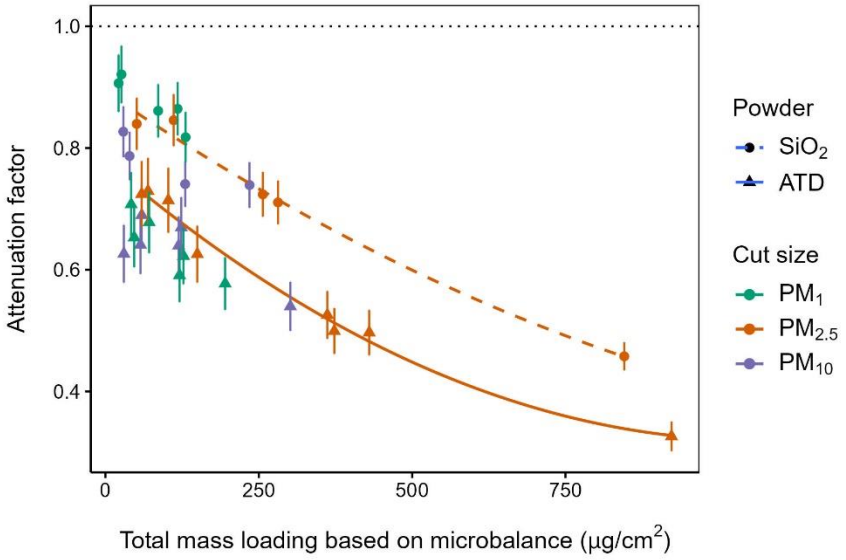

Figure 5.2 Attenuation factors for Si in SiO_2 powder and Arizona Test Dust (ATD) samples. The error bars indicate the combined uncertainties from both XRF and gravimetric measurements. The dotted line denotes an attenuation factor of 1, indicating no attenuation. The dashed and solid curves represent quadratic regression for $PM_{2.5}$ SiO_2 powder and ATD samples, respectively.

A size dependence of A_{Si} similar to that observed in the Al_2O_3 samples was found in the SiO_2 samples but not in the ATD samples (Figure 5.2). The PM_1 ATD samples exhibited slightly lower A_{Si} than the $PM_{2.5}$ ATD samples, potentially due to the size dependence of dust composition. Quartz (SiO_2) has a higher Mohs hardness and lower cleavage than other minerals, and therefore it is less affected by mechanical processes and tends to dominate larger size fractions (Boose et al., 2016; Nousiainen, 2009). Thus, PM_1 samples may contain less SiO_2 and more other oxides than $PM_{2.5}$ samples, which can enhance Si attenuation and lead to a slightly lower A_{Si}, as suggested by the comparison between ATD and pure SiO_2. The difference in A_{Si} between PM_{10} and $PM_{2.5}$ is also likely reduced because the attenuation decrease due to higher SiO_2 content in PM_{10} offsets the attenuation increase due to larger particle sizes. Figure S5.6 provides evidence of the size-dependent composition of ATD by examining the Si/Fe ratio across different particle size ranges. If the composition were size-independent, the Si/Fe ratio would decrease with increasing particle

size due to the increased attenuation of Si and negligible attenuation of Fe. However, a reverse trend was observed, indicating a higher Si content in the larger particle size fractions.

5.4.2 Theoretical Estimation of Attenuation

We compared the measured attenuation factors with estimates derived from the homogeneous layer and particle size models for Si in $PM_{2.5}$ ATD samples as shown in Figure 5.3. The theoretical estimates best aligned with the measured values (slope = 1.01, R^2 = 0.99) when attenuation factors due to mass loading and particle size were combined ($A_{mass} \times A_{size}$). The ATD composition was incorporated into the calculations of both A_{mass} and A_{size}. Gutknecht et al. (2010) proposed using the particle size model for light elements in $PM_{2.5}$. However, A_{size} calculated from the particle size model is a volume-weighted average that does not vary with mass loading for a given size distribution. Thus, considering only A_{size} cannot capture the observed decrease in the Si attenuation factor with increasing mass loading. This model assumed particles were collected as a monolayer on the filter, which may hold for filters with low mass loading but not for those with heavy loading. Dzubay and Nelson (1974) suggested using the homogeneous layer model for fine PM. However, when considering only A_{mass} derived from the homogeneous layer model, the theoretical estimates were ~26% higher than the measured Si attenuation factor (R^2 = 0.99) as shown in Figure S5.7, indicating a significant underestimation of the Si attenuation. The good agreement between $A_{mass} \times A_{size}$ and the measured values could suggest that considering the deposit as a homogeneous layer contributing to A_{mass} with a monolayer on top contributing to A_{size} is a more appropriate assumption than either a purely homogeneous layer or a monolayer alone. The multiplier of A_{size} applied to A_{mass} could be interpreted as an adjustment factor to account for assumptions made in the homogeneous layer model.

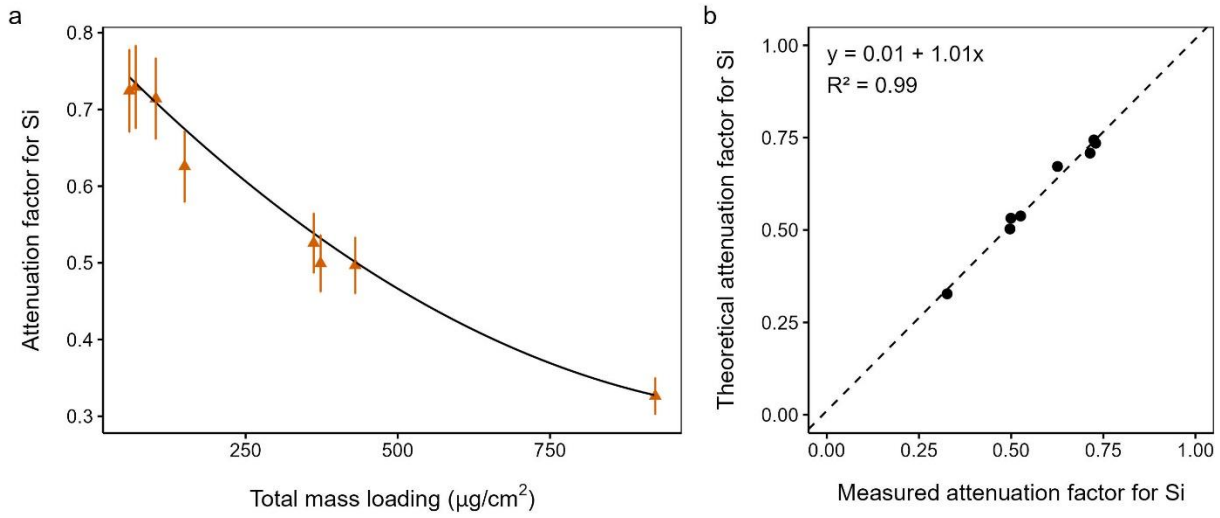

Figure 5.3 Comparison between theoretically estimated and measured attenuation factors for Si in $PM_{2.5}$ Arizona Test Dust samples. (a) The solid curve represents theoretical attenuation factors due to both mass loading and particle size ($A_{mass} \times A_{size}$), while the triangles and error bars indicate measured attenuation factors. (b) The dashed line shows the linear regression for the agreement between theoretical ($A_{mass} \times A_{size}$) and measured attenuation factors.

Multiple sources of uncertainty exist in the assumptions and model calculations. First, particles were assumed as equivalent spheres to calculate the attenuation due to particle size, which may not represent the attenuation for irregularly shaped dust particles. Second, the same elemental composition was used to calculate attenuation across all particle sizes, although dust composition is size dependent (Boose et al., 2016; Nousiainen, 2009). Third, the ATD composition used in calculating total mass absorption coefficients has significant uncertainty for elements other than Si, based on the data provided by the manufacturer (Table S5.1). We examined the effect of using an iterative process to deduce elemental composition and the resulting attenuation factor from the XRF measurements and found that the attenuation factor stabilized after three iterations with changes of <3%. The performance of the models for PM_1 and PM_{10} was not examined because penetration efficiency data for the cyclone at these size ranges were unavailable.

5.4.3 Dust Underestimation Due to Attenuation

Given the good agreement between $A_{mass} \times A_{size}$ and the measured values for $PM_{2.5}$ ATD samples (Figure 5.3), we also calculated $A_{mass} \times A_{size}$ for ambient dust-dominated $PM_{2.5}$ samples from the SPARTAN network. The theoretical attenuation factors estimated for Si and Al in dust-dominated $PM_{2.5}$ SPARTAN samples are summarized in Table S5.2. The combined $A_{mass} \times A_{size}$ values are 0.74±0.02 for Si and 0.71±0.02 for Al, similar to those observed for $PM_{2.5}$ ATD samples with comparable mass loading (<120 μg/cm^2) in Figure 5.3. The small standard deviations in $A_{mass} \times A_{size}$ indicate minor differences in attenuation factors due to variations in elemental composition and mass loading across most SPARTAN samples.

Figure 5.4 evaluates the impact on dust concentrations after correcting for estimated attenuation effects. The dust concentration increased by 30% on average based on linear regression results for dust-dominated $PM_{2.5}$ samples, demonstrating the importance of considering attenuation effects for $PM_{2.5}$ dust measured by XRF. We assessed the validity of using only elemental oxides to represent composition and mass loading for each sample. We calculated the change in estimated attenuation after including other species and found no significant difference when adding measured sulfate, nitrate, ammonium, chloride, or elemental carbon. Since organic matter was not measured, we assumed an organic matter to organic carbon ratio of 1.8 (Hand et al., 2012; Malm & Hand, 2007), with the organic matter mass approximated by summing organic carbon and oxygen, and found a resulting difference of <5%. The small effect of other species on attenuation in dust-dominated samples suggests that using only elemental oxides is appropriate. Future measurements of organic matter concentration could further refine the attenuation calculations and extend their applicability to samples that are not dust-dominated.

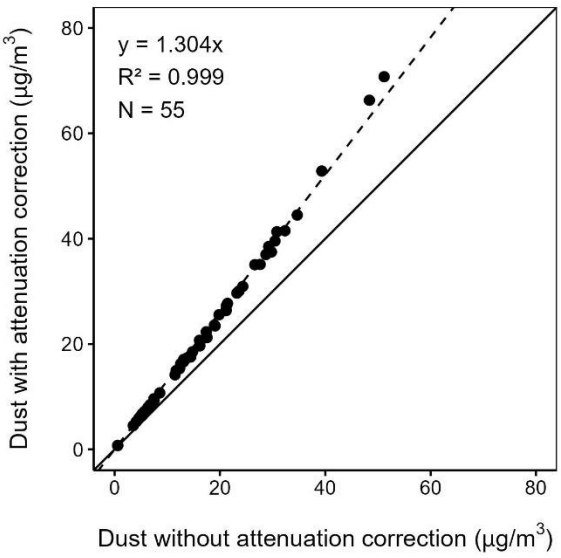

Figure 5.4 Comparison between dust mass with attenuation correction and dust mass without attenuation correction for dust-dominated (dust > 50% of total mass) $PM_{2.5}$ samples at SPARTAN sites. The dashed line shows the linear regression with zero intercept.

5.5 Conclusions

The XRF technique is widely used to analyze the elemental composition of PM filter samples to understand dust composition and estimate dust mass. Attenuation effects for light elements in XRF analysis can cause inaccurate elemental composition and dust underestimation, yet correcting these effects has often been overlooked in previous studies and remains a significant challenge. Here, we experimentally assessed attenuation due to mass loading, particle size, and chemical composition for Si and Al by comparing XRF and gravimetric measurements of samples generated using powder oxides and Arizona test dust (ATD). Results show that attenuation increased with both mass loading and particle size in the oxide samples. The attenuation for Si in ATD samples was significantly higher than in SiO_2 samples with the same mass loading and size range, verifying that attenuation is composition dependent. We compared the attenuation factors measured for ATD samples to estimates derived from a homogeneous layer model and a particle size model. Theoretical estimates for Si in $PM_{2.5}$ ATD samples aligned best with the measured values when

using combined estimates from both models, rather than a single model suggested by previous studies. Applying these models to ambient dust-dominated $PM_{2.5}$ samples from the SPARTAN network indicated an average increase of 30% in estimated dust concentrations after correcting for attenuation effects.

The uncertainty introduced by the spherical particle assumption in the particle size model requires further evaluation. The effect of particle morphology, such as shape, on attenuation should also be considered. A comprehensive analysis of all species in ambient PM samples and their particle size distribution would enable more accurate attenuation estimates using the models. Size-segregated dust composition could further reduce uncertainty in theoretical estimates. Further evaluation of the models is needed for coarse PM or PM_{10}, which experiences greater attenuation of light elements than fine PM, although the difference may not be substantial based on our experiments. Other experimental methods could be used to assess attenuation effects, such as comparing XRF with an attenuation-free technique suitable for light elements (e.g., particle-induced gamma-ray emission, PIGE), which allows the use of samples with unknown compositions.

This study provides experimental evidence for the significant attenuation of light elements in dust samples and its variations with mass loading, particle size, and composition. Correcting for attenuation effects will enhance understanding of dust characteristics and provide more accurate estimates of dust contributions to PM, which is important for PM mass closure, especially for samples collected during dust events. More accurate ground-based dust measurements are important for improving atmospheric models and satellite remote sensing algorithms, leading to a better understanding of dust impacts on the environment and human health.

5.6 Supplementary Material

5.6.1 Details for Theoretical Attenuation Calculations

The total mass absorption coefficient ($\bar{\mu}$) was calculated as:

$$\bar{\mu} = \mu \csc\theta + \mu' \csc\theta' \tag{S5.10}$$

where μ and μ' are the total mass absorption coefficients (cm^2/g) of all elements for the incoming and emitted fluorescent X-rays respectively, and θ and θ' are the angles between the sample surface and the incoming X-rays or emitted X-rays that reach the detector. μ and μ' were calculated as:

$$\mu = \sum(\mu_i w_i) \tag{S5.11}$$

$$\mu' = \sum\left(\mu_{ij} w_i\right) \tag{S5.12}$$

where μ_i and μ_{ij} are the mass absorption coefficients (cm^2/g) of element i for the incoming X-ray and the emitted fluorescent X-ray from element j respectively, and w_i is the mass fraction of element i in the sample.

The attenuation factor for a sphere, A(sphere) was calculated as:

$$A(\text{sphere}) = \frac{3}{2Y^3}\left[Y^2 - 2 + (2Y+2)\exp(-Y)\right]\left[\exp\left(-\mathrm{K}Y\left(\theta+\theta'\right)^2\right)\right] \tag{S5.13}$$

where $K = 4\times10^{-6}$ (degrees)$^{-2}$, and

$$Y = (\mu + \mu')D\rho_p \tag{S5.14}$$

where D is the geometric particle diameter and ρ_p is the particle density.

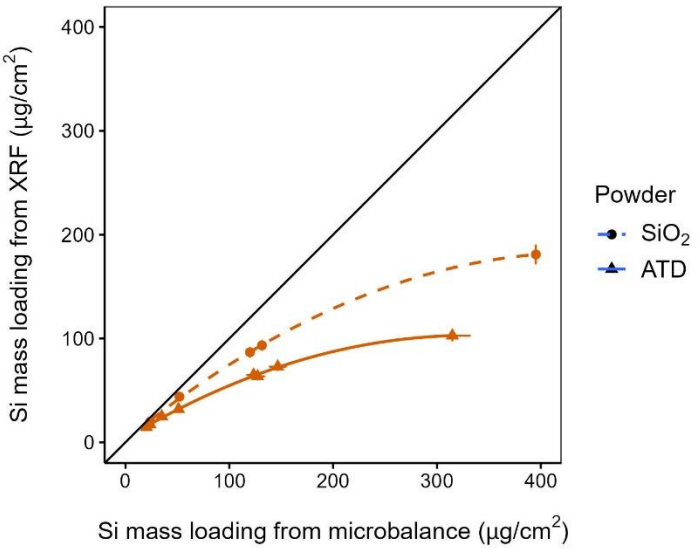

Figure S5.5 Comparison of Si mass loading based on XRF and gravimetric measurements for $PM_{2.5}$ SiO_2 powder and Arizona Test Dust (ATD) samples. The vertical and horizontal error bars indicate uncertainties from XRF and gravimetric measurements, respectively. The dashed and solid curves represent quadratic regression for $PM_{2.5}$ SiO_2 powder and ATD samples, respectively. The one-to-one line indicates no attenuation.

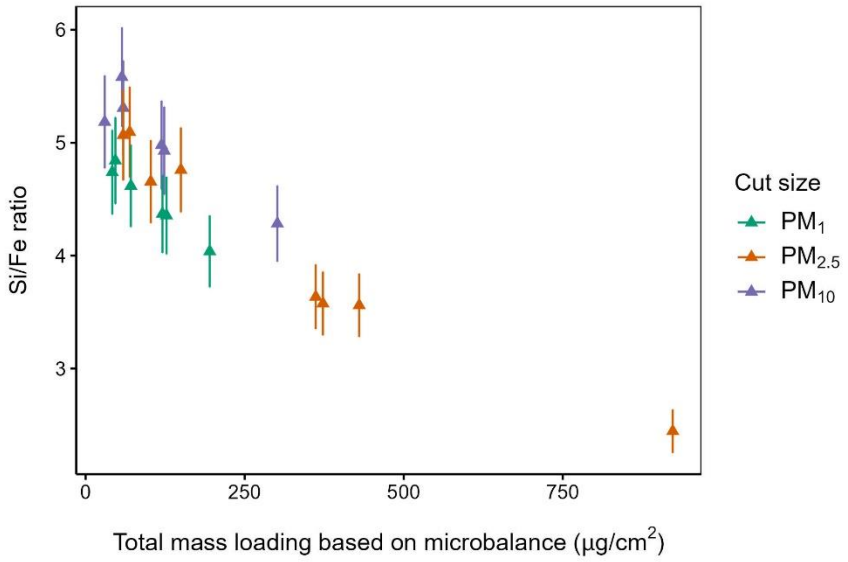

Figure S5.6 The mass ratio of Si/Fe for Arizona Test Dust samples. The error bars indicate the combined uncertainties from XRF measurements of both Si and Fe.

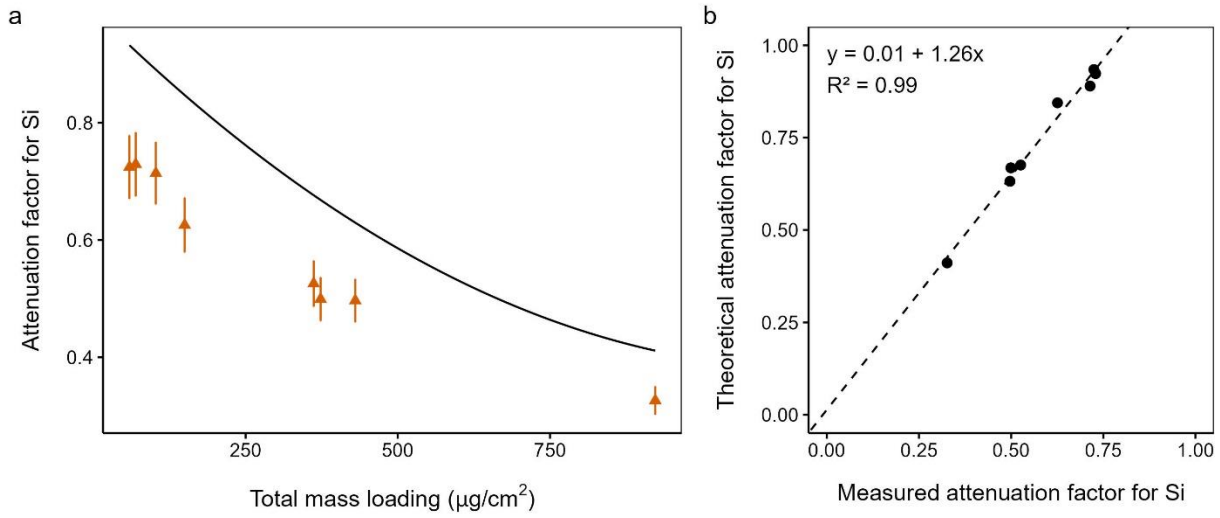

Figure S5.7 Comparison between theoretically estimated and measured attenuation factors for Si in $PM_{2.5}$ Arizona Test Dust samples. (a) The solid curve represents theoretical attenuation factors accounting only for mass loading, while the triangles and error bars indicate measured attenuation factors. (b) The dashed line shows the linear regression for the agreement between theoretical and measured attenuation factors.

Table S5.1 Chemical composition of ISO 12103-1 A1 Ultrafine Arizona Test Dust

Compound	Oxide mass fraction (%)	Mean[a] (%)	σ[b] (%)	Element-to-oxide ratio	Element, *i*	w_i[c] (%)	$\sigma_{w,i}$[d] (%)
SiO_2	69.0 – 77.0	73.0	4.0	0.47	Si	34.3	1.9
Al_2O_3	8.0 – 14.0	11.0	3.0	0.53	Al	5.8	1.6
Fe_2O_3	4.0 – 7.0	5.5	1.5	0.70	Fe	3.9	1.1
CaO	2.5 – 5.5	4.0	1.5	0.71	Ca	2.8	1.1
K_2O	2.0 – 5.0	3.5	1.5	0.83	K	2.9	1.2
Na_2O	1.0 – 4.0	2.5	1.5	0.74	Na	1.9	1.1
MgO	1.0 – 2.0	1.5	0.5	0.60	Mg	0.9	0.3
TiO_2	0.0 – 1.0	0.5	0.5	0.60	Ti	0.3	0.3

Note. Only the oxide mass fractions were provided by the manufacturer (Powder Technology Inc.).

[a]Mean is the average of the lower and upper limits of the oxide mass fraction range. [b]σ represents half the range between the upper and lower limits of the oxide mass fraction range. [c]w_i is the mass fraction of element *i* in the total mass calculated by multiplying the Mean by the element-to-oxide ratio. [d]$\sigma_{w,i}$ is the uncertainty in w_i calculated by multiplying σ by the element-to-oxide ratio.

Table S5.2 Theoretically estimated attenuation factors (mean ± standard deviation) for dust-dominated (dust > 50% of total mass) $PM_{2.5}$ samples from SPARTAN

Element	A_{mass}[a]	A_{size}[b]	$A_{size} \times A_{mass}$
Si	0.96±0.03	0.78±0.01	0.74±0.02
Al	0.95±0.03	0.75±0.01	0.71±0.02

[a]A_{mass} is the attenuation factor due to mass loading. [b]A_{size} is the attenuation factor due to particle size.

Chapter 6: Conclusions

Chapters 2 through 5 each present conclusions and recommendations for future work related to its specific study. This chapter summarizes the key contributions of these studies.

Chapter 2: *A Global-scale Mineral Dust Equation*

This study developed a global-scale mineral dust equation with region-specific coefficients, which provides a promising approach for calculating dust mass based on elemental analysis of dust. The global equation performed well for different types of dust over different regions. To our knowledge, this is the first study to develop and evaluate a region-specific global dust equation, which is challenging given the limitation of insufficient complete measurements of dust composition on a global scale and the lack of an absolute benchmark for reference dust mass. Further improvement of the global equation would benefit from more complete and accurate measurements of crustal elements and carbonate content in dust at a finer spatial scale. Sufficient mineralogical and hygroscopicity measurements are needed to account for adsorbed water and salt minerals in special types of dust (e.g., saline dust, volcanic dust, and aged dust).

Chapter 3: *Elemental Characterization of Ambient Particulate Matter for a Globally Distributed Monitoring Network: Methodology and Implications*

This study presented a detailed methodology for elemental analysis of ambient PM in the SPARTAN network. The global PM elemental dataset from SPARTAN was obtained using consistent protocols for sample collection and chemical analysis, which enabled the comparison of mineral dust and trace elements across globally distributed sites. Significant

airborne arsenic pollution was identified at sites in South and Southeast Asia using this dataset. This work draws attention to the need for sustained consistent monitoring of the elemental composition of fine PM in urban areas worldwide. More representative samples are needed to better estimate long-term levels of dust and trace elements, assess health risks, and identify emission sources.

Chapter 4: *Characterizing Particulate Matter Composition in Central Asia: Dust Contribution in Tashkent, Uzbekistan*

This study analyzed the elemental composition of the first contemporary PM filter samples collected from Uzbekistan in Central Asia, a region that suffers from severe air pollution but remains understudied. This work addresses the gap in estimating dust contribution to PM and understanding the source areas of major dust events in Central Asia, providing essential evidence to inform air pollution management strategies in the region. Ground measurements of dust composition including elemental and mineralogical characterization across source areas in Central Asia are needed to estimate dust contribution to PM more accurately. More representative samples and comprehensive analyses of PM species are needed to better understand anthropogenic sources in the region.

Chapter 5: *Assessing Attenuation Effects in X-ray Fluorescence Analysis of Light Elements in Mineral Dust*

This study provided experimental evidence of attenuation effects due to mass loading, particle size, and composition in XRF analysis of light elements for PM filter samples. Significant underestimation of dust mass in fine PM due to potential attenuation effects was found by applying theoretical models evaluated against experimental data. This work

demonstrates the importance of considering attenuation effects in XRF analysis for accurate dust measurements. Further evaluation of the models is needed for coarse PM. Comprehensive analyses of all PM species, accurate particle size distribution, and size-segregated composition would enable more accurate attenuation estimates using the models. The effect of particle morphology, such as shape, on attenuation should also be considered.

References

Abed, A. M., Al Kuisi, M., & Khair, H. A. (2009). Characterization of the Khamaseen (spring) dust in Jordan. *Atmospheric Environment*, *43*(18), 2868–2876. https://doi.org/10.1016/j.atmosenv.2009.03.015

Ahmady-Birgani, H., Mirnejad, H., Feiznia, S., & McQueen, K. G. (2015). Mineralogy and geochemistry of atmospheric particulates in western Iran. *Atmospheric Environment*, *119*, 262–272. https://doi.org/10.1016/j.atmosenv.2015.08.021

Alastuey, A., Querol, X., Aas, W., Lucarelli, F., Pérez, N., Moreno, T., et al. (2016). Geochemistry of PM10 over Europe during the EMEP intensive measurement periods in summer 2012 and winter 2013. *Atmospheric Chemistry and Physics*, *16*(10), 6107–6129. https://doi.org/10.5194/acp-16-6107-2016

Aldhaif, A. M., Lopez, D. H., Dadashazar, H., & Sorooshian, A. (2020). Sources, frequency, and chemical nature of dust events impacting the United States East Coast. *Atmospheric Environment*, *231*, 117456. https://doi.org/10.1016/j.atmosenv.2020.117456

Alfaro, S. C. (2003). Chemical and optical characterization of aerosols measured in spring 2002 at the ACE-Asia supersite, Zhenbeitai, China. *Journal of Geophysical Research*, *108*(D23), 8641. https://doi.org/10.1029/2002JD003214

Amato, F., Pandolfi, M., Viana, M., Querol, X., Alastuey, A., & Moreno, T. (2009). Spatial and chemical patterns of PM10 in road dust deposited in urban environment. *Atmospheric Environment*, *43*(9), 1650–1659. https://doi.org/10.1016/j.atmosenv.2008.12.009

Amonov, M., & Nishonov, B. (2020). Seasonal variability of PM concentration in Tashkent. *IOP Conference Series: Materials Science and Engineering*, *869*, 022030. https://doi.org/10.1088/1757-899X/869/2/022030

Amonov, M., Claiborn, C., Narbayev, N., & Nishonov, B. (2009). PM10 and PM2.5 concentration in ambient air of Tashkent city, the 2008 study results. *Ecological Herald of Uzbekistan*, *9*, 36–39.

Amonov, M. O., Claiborn, S. C., & Narbayev, N. (2010). Air quality monitoring and PM study results in Tashkent city. *Proceedings of the AWMA International Specialty Conference: "Leapfrogging Opportunities for Air Quality Improvement,"* 181–186.

Andrews, E., Saxena, P., Musarra, S., Hildemann, L. M., Koutrakis, P., McMurry, P. H., et al. (2000). Concentration and Composition of Atmospheric Aerosols from the 1995 SEAVS Experiment and a Review of the Closure between Chemical and Gravimetric Measurements. *Journal of the Air & Waste Management Association*, *50*(5), 648–664. https://doi.org/10.1080/10473289.2000.10464116

Appel, K. W., Pouliot, G. A., Simon, H., Sarwar, G., Pye, H. O. T., Napelenok, S. L., et al. (2013). Evaluation of dust and trace metal estimates from the Community Multiscale Air

Quality (CMAQ) model version 5.0. *Geoscientific Model Development*, *6*(4), 883–899. https://doi.org/10.5194/gmd-6-883-2013

Apte, J. S., Marshall, J. D., Cohen, A. J., & Brauer, M. (2015). Addressing Global Mortality from Ambient PM2.5. *Environmental Science & Technology*, *49*(13), 8057–8066. https://doi.org/10.1021/acs.est.5b01236

Arimoto, R. (2004). Chemical composition of atmospheric aerosols from Zhenbeitai, China, and Gosan, South Korea, during ACE-Asia. *Journal of Geophysical Research*, *109*(D19), D19S04. https://doi.org/10.1029/2003JD004323

Ashley, W. S., Strader, S., Dziubla, D. C., & Haberlie, A. (2015). Driving Blind: Weather-Related Vision Hazards and Fatal Motor Vehicle Crashes. *Bulletin of the American Meteorological Society*, *96*(5), 755–778. https://doi.org/10.1175/BAMS-D-14-00026.1

Awadh, S. M. (2012). Geochemistry and mineralogical composition of the airborne particles of sand dunes and dust storms settled in Iraq and their environmental impacts. *Environmental Earth Sciences*, *66*(8), 2247–2256. https://doi.org/10.1007/s12665-011-1445-6

Awasthi, A. K., Zeng, X., & Li, J. (2016). Relationship between e-waste recycling and human health risk in India: a critical review. *Environmental Science and Pollution Research*, *23*(12), 11509–11532. https://doi.org/10.1007/s11356-016-6085-7

Bates, J. T., Fang, T., Verma, V., Zeng, L., Weber, R. J., Tolbert, P. E., et al. (2019). Review of Acellular Assays of Ambient Particulate Matter Oxidative Potential: Methods and Relationships with Composition, Sources, and Health Effects. *Environmental Science & Technology*, *53*(8), 4003–4019. https://doi.org/10.1021/acs.est.8b03430

Bazarbayev, R., Zhou, B., Allaniyazov, A., Zeng, G., Mamedov, D., Ivanitskaya, E., et al. (2022). Physical and chemical properties of dust in the Pre-Aral region of Uzbekistan. *Environmental Science and Pollution Research*, *29*(27), 40893–40902. https://doi.org/10.1007/s11356-022-18827-6

Begum, B. A., Biswas, S. K., & Hopke, P. K. (2011). Key issues in controlling air pollutants in Dhaka, Bangladesh. *Atmospheric Environment*, *45*(40), 7705–7713. https://doi.org/10.1016/j.atmosenv.2010.10.022

Bhaskar, V. S., & Sharma, M. (2008). Assessment of fugitive road dust emissions in Kanpur, India: A note. *Transportation Research Part D: Transport and Environment*, *13*(6), 400–403. https://doi.org/10.1016/j.trd.2008.06.003

Boose, Y., Welti, A., Atkinson, J., Ramelli, F., Danielczok, A., Bingemer, H. G., et al. (2016). Heterogeneous ice nucleation on dust particles sourced from nine deserts worldwide – Part 1: Immersion freezing. *Atmospheric Chemistry and Physics*, *16*(23), 15075–15095. https://doi.org/10.5194/acp-16-15075-2016

Breckle, S.-W., Wucherer, W., Dimeyeva, L. A., & Ogar, N. P. (Eds.). (2012). *Aralkum - a Man-Made Desert* (Vol. 218). Springer Berlin Heidelberg. https://doi.org/10.1007/978-3-642-21117-1

Broomandi, P., Mohammadpour, K., Kaskaoutis, D. G., Fathian, A., Abdullaev, S. F., Maslov, V. A., et al. (2023). A Synoptic- and Remote Sensing-based Analysis of a Severe Dust Storm Event over Central Asia. *Aerosol and Air Quality Research*, *23*(2), 220309. https://doi.org/10.4209/aaqr.220309

Calzolai, G., Chiari, M., Lucarelli, F., Nava, S., Taccetti, F., Becagli, S., et al. (2014). PIXE–PIGE analysis of size-segregated aerosol samples from remote areas. *Nuclear Instruments and Methods in Physics Research Section B: Beam Interactions with Materials and Atoms*, *318*, 125–129. https://doi.org/10.1016/j.nimb.2013.05.097

Cao, J. J. (2005). Characterization of airborne carbonate over a site near Asian dust source regions during spring 2002 and its climatic and environmental significance. *Journal of Geophysical Research*, *110*(D3), D03203. https://doi.org/10.1029/2004JD005244

Cao, J. J., Chow, J. C., Watson, J. G., Wu, F., Han, Y. M., Jin, Z. D., et al. (2008). Size-differentiated source profiles for fugitive dust in the Chinese Loess Plateau. *Atmospheric Environment*, *42*(10), 2261–2275. https://doi.org/10.1016/j.atmosenv.2007.12.041

Carslaw, D. C., & Ropkins, K. (2012). openair — An R package for air quality data analysis. *Environmental Modelling & Software*, *27–28*, 52–61. https://doi.org/10.1016/j.envsoft.2011.09.008

Cattell, R. B. (1966). The scree test for the number of factors. *Multivariate Behavioral Research*, *1*(2), 245–276.

Chan, C.-C., Chuang, K.-J., Chen, W.-J., Chang, W.-T., Lee, C.-T., & Peng, C.-M. (2008). Increasing cardiopulmonary emergency visits by long-range transported Asian dust storms in Taiwan. *Environmental Research*, *106*(3), 393–400. https://doi.org/10.1016/j.envres.2007.09.006

Chang, Y., Huang, K., Xie, M., Deng, C., Zou, Z., Liu, S., & Zhang, Y. (2018). First long-term and near real-time measurement of trace elements in China's urban atmosphere: temporal variability, source apportionment and precipitation effect. *Atmospheric Chemistry and Physics*, *18*(16), 11793–11812. https://doi.org/10.5194/acp-18-11793-2018

Charrier, J. G., & Anastasio, C. (2012). On dithiothreitol (DTT) as a measure of oxidative potential for ambient particles: evidence for the importance of soluble transition metals. *Atmospheric Chemistry and Physics*, *12*(19), 9321–9333. https://doi.org/10.5194/acp-12-9321-2012

Chen, H., Laskin, A., Baltrusaitis, J., Gorski, C. A., Scherer, M. M., & Grassian, V. H. (2012). Coal Fly Ash as a Source of Iron in Atmospheric Dust. *Environmental Science & Technology*, *46*(4), 2112–2120. https://doi.org/10.1021/es204102f

Chiapello, I., Bergametti, G., Quisefit, J. P., & De Chateaubourg, P. (1997). Control and correction of the sample absorption effect in the analysis of atmospheric aerosol by X-ray fluorescence spectrometry. *Analusis*, *25*, 141–147.

Chiari, M., Yubero, E., Calzolai, G., Lucarelli, F., Crespo, J., Galindo, N., et al. (2018). Comparison of PIXE and XRF analysis of airborne particulate matter samples collected on Teflon and quartz fibre filters. *Nuclear Instruments and Methods in Physics Research Section B: Beam Interactions with Materials and Atoms*, *417*, 128–132. https://doi.org/10.1016/j.nimb.2017.07.031

Choi, E., Yi, S.-M., Lee, Y. S., Jo, H., Baek, S.-O., & Heo, J.-B. (2022). Sources of airborne particulate matter-bound metals and spatial-seasonal variability of health risk potentials in four large cities, South Korea. *Environmental Science and Pollution Research*, *29*(19), 28359–28374. https://doi.org/10.1007/s11356-021-18445-8

Choi, J. C., Lee, M., Chun, Y., Kim, J., & Oh, S. (2001). Chemical composition and source signature of spring aerosol in Seoul, Korea. *Journal of Geophysical Research: Atmospheres*, *106*(D16), 18067–18074. https://doi.org/10.1029/2001JD900090

Chow, J. C., Watson, J. G., Fujita, E. M., Lu, Z., Lawson, D. R., & Ashbaugh, L. L. (1994). Temporal and spatial variations of PM2.5 and PM10 aerosol in the Southern California air quality study. *Atmospheric Environment*, *28*(12), 2061–2080. https://doi.org/10.1016/1352-2310(94)90474-X

Chow, J. C., Watson, J. G., Ashbaugh, L. L., & Magliano, K. L. (2003). Similarities and differences in PM10 chemical source profiles for geological dust from the San Joaquin Valley, California. *Atmospheric Environment*, *37*(9–10), 1317–1340. https://doi.org/10.1016/S1352-2310(02)01021-X

Chow, J. C., Lowenthal, D. H., Chen, L.-W. A., Wang, X., & Watson, J. G. (2015). Mass reconstruction methods for PM2.5: a review. *Air Quality, Atmosphere & Health*, *8*(3), 243–263. https://doi.org/10.1007/s11869-015-0338-3

Claquin, T., Schulz, M., & Balkanski, Y. J. (1999). Modeling the mineralogy of atmospheric dust sources. *Journal of Geophysical Research: Atmospheres*, *104*(D18), 22243–22256. https://doi.org/10.1029/1999JD900416

Contini, D., Genga, A., Cesari, D., Siciliano, M., Donateo, A., Bove, M. C., & Guascito, M. R. (2010). Characterisation and source apportionment of PM10 in an urban background site in Lecce. *Atmospheric Research*, *95*(1), 40–54. https://doi.org/10.1016/j.atmosres.2009.07.010

Councell, T. B., Duckenfield, K. U., Landa, E. R., & Callender, E. (2004). Tire-Wear Particles as a Source of Zinc to the Environment. *Environmental Science & Technology*, *38*(15), 4206–4214. https://doi.org/10.1021/es034631f

Coz, E., Gómez-Moreno, F. J., Pujadas, M., Casuccio, G. S., Lersch, T. L., & Artíñano, B. (2009). Individual particle characteristics of North African dust under different long-

range transport scenarios. *Atmospheric Environment*, *43*(11), 1850–1863. https://doi.org/10.1016/j.atmosenv.2008.12.045

Criado, C., & Dorta, P. (2003). An unusual 'blood rain' over the Canary Islands (Spain). The storm of January 1999. *Journal of Arid Environments*, *55*(4), 765–783. https://doi.org/10.1016/S0140-1963(02)00320-8

Cuevas-Agulló, E., Barriopedro, D., García, R. D., Alonso-Pérez, S., González-Alemán, J. J., Werner, E., et al. (2024). Sharp increase in Saharan dust intrusions over the western Euro-Mediterranean in February–March 2020–2022 and associated atmospheric circulation. *Atmospheric Chemistry and Physics*, *24*(7), 4083–4104. https://doi.org/10.5194/acp-24-4083-2024

D'Alessandro, A., Lucarelli, F., Mando, P. A., Marcazzan, G., Nava, S., Prati, P., et al. (2003). Hourly elemental composition and sources identification of fine and coarse PM10 particulate matter in four Italian towns. *Journal of Aerosol Science*, *34*(2), 243–259. https://doi.org/10.1016/S0021-8502(02)00172-6

Dallmann, T. R., Onasch, T. B., Kirchstetter, T. W., Worton, D. R., Fortner, E. C., Herndon, S. C., et al. (2014). Characterization of particulate matter emissions from on-road gasoline and diesel vehicles using a soot particle aerosol mass spectrometer. *Atmospheric Chemistry and Physics*, *14*(14), 7585–7599. https://doi.org/10.5194/acp-14-7585-2014

Deboudt, K., Flament, P., Choël, M., Gloter, A., Sobanska, S., & Colliex, C. (2010). Mixing state of aerosols and direct observation of carbonaceous and marine coatings on African dust by individual particle analysis. *Journal of Geophysical Research: Atmospheres*, *115*(D24).

Denjean, C., Caquineau, S., Desboeufs, K., Laurent, B., Maille, M., Quiñones Rosado, M., et al. (2015). Long-range transport across the Atlantic in summertime does not enhance the hygroscopicity of African mineral dust. *Geophysical Research Letters*, *42*(18), 7835–7843. https://doi.org/10.1002/2015GL065693

Diner, D. J., Boland, S. W., Brauer, M., Bruegge, C., Burke, K. A., Chipman, R., Di Girolamo, L., Garay, M. J., Hasheminassab, S., & Hyer, E. (2018). Advances in multiangle satellite remote sensing of speciated airborne particulate matter and association with adverse health effects: from MISR to MAIA. *Journal of Applied Remote Sensing*, *12*(04), 1. https://doi.org/10.1117/1.JRS.12.042603

Diner, D. J., Boland, S. W., Brauer, M., Bruegge, C., Burke, K. A., Chipman, R., Di Girolamo, L., Garay, M. J., Hasheminassab, S., Hyer, E., et al. (2018). Advances in multiangle satellite remote sensing of speciated airborne particulate matter and association with adverse health effects: from MISR to MAIA. *Journal of Applied Remote Sensing*, *12*(04), 1. https://doi.org/10.1117/1.JRS.12.042603

Draxler, R., Stunder, B., Rolph, G., Stein, A., Taylor, A., Zinn, S., et al. (2023). HYSPLIT User's Guide. *National Oceanic and Atmospheric Administration Air Resources Laboratory*. https://www.arl.noaa.gov/documents/reports/hysplit_user_guide.pdf

Dzubay, T., & Nelson, R. (1974). Self absorption corrections for X-ray fluorescence analysis of aerosols. *Advances in X-Ray Analysis*, *18*, 619–631.

Eldred, B. (2003). Evaluation of the equation for soil composite: Internal memo to IMPROVE staff.

Engelbrecht, J. P., Menéndez, I., & Derbyshire, E. (2014). Sources of PM2.5 impacting on Gran Canaria, Spain. *Catena*, *117*, 119–132. https://doi.org/10.1016/j.catena.2013.06.017

Engelbrecht, J. P., Moosmüller, H., Pincock, S., Jayanty, R. K. M., Lersch, T., & Casuccio, G. (2016). Technical note: Mineralogical, chemical, morphological, and optical interrelationships of mineral dust re-suspensions. *Atmospheric Chemistry and Physics*, *16*(17), 10809–10830. https://doi.org/10.5194/acp-16-10809-2016

Escudero, M. (2005). Wet and dry African dust episodes over eastern Spain. *Journal of Geophysical Research*, *110*(D18), D18S08. https://doi.org/10.1029/2004JD004731

FAO, I., & ISRIC, I. (2012). JRC: harmonized world soil database (version 1.2). *FAO, Rome, Italy and IIASA, Laxenburg, Austria*.

Fendorf, S., Michael, H. A., & van Geen, A. (2010). Spatial and Temporal Variations of Groundwater Arsenic in South and Southeast Asia. *Science*, *328*(5982), 1123–1127. https://doi.org/10.1126/science.1172974

Formenti, P. (2003). Chemical composition of mineral dust aerosol during the Saharan Dust Experiment (SHADE) airborne campaign in the Cape Verde region, September 2000. *Journal of Geophysical Research*, *108*(D18), 8576. https://doi.org/10.1029/2002JD002648

Formenti, P., Rajot, J. L., Desboeufs, K., Caquineau, S., Chevaillier, S., Nava, S., et al. (2008). Regional variability of the composition of mineral dust from western Africa: Results from the AMMA SOP0/DABEX and DODO field campaigns. *Journal of Geophysical Research: Atmospheres*, *113*(D23). https://doi.org/10.1029/2008JD009903

Formenti, P., Nava, S., Prati, P., Chevaillier, S., Klaver, A., Lafon, S., et al. (2010). Self-attenuation artifacts and correction factors of light element measurements by X-ray analysis: Implication for mineral dust composition studies. *Journal of Geophysical Research: Atmospheres*, *115*(D1). https://doi.org/10.1029/2009JD012701

Fuller, R., Landrigan, P. J., Balakrishnan, K., Bathan, G., Bose-O'Reilly, S., Brauer, M., et al. (2022). Pollution and health: a progress update. *The Lancet Planetary Health*, *6*(6), e535–e547. https://doi.org/10.1016/S2542-5196(22)00090-0

Fussell, J. C., Franklin, M., Green, D. C., Gustafsson, M., Harrison, R. M., Hicks, W., et al. (2022). A Review of Road Traffic-Derived Non-Exhaust Particles: Emissions, Physicochemical Characteristics, Health Risks, and Mitigation Measures. *Environmental Science & Technology*, *56*(11), 6813–6835. https://doi.org/10.1021/acs.est.2c01072

Galvão, E. S., Santos, J. M., Lima, A. T., Reis, N. C., Orlando, M. T. D., & Stuetz, R. M. (2018). Trends in analytical techniques applied to particulate matter characterization: A critical review of fundaments and applications. *Chemosphere, 199*, 546–568. https://doi.org/10.1016/j.chemosphere.2018.02.034

Ganor, E., Foner, H. A., Brenner, S., Neeman, E., & Lavi, N. (1991). The chemical composition of aerosols settling in Israel following dust storms. *Atmospheric Environment. Part A. General Topics*, *25*(12), 2665–2670. https://doi.org/10.1016/0960-1686(91)90196-E

Gao, J., Wang, K., Wang, Y., Liu, S., Zhu, C., Hao, J., et al. (2018). Temporal-spatial characteristics and source apportionment of PM2.5 as well as its associated chemical species in the Beijing-Tianjin-Hebei region of China. *Environmental Pollution*, *233*, 714–724. https://doi.org/10.1016/j.envpol.2017.10.123

Gaston, C. J. (2020). Re-examining Dust Chemical Aging and Its Impacts on Earth's Climate. *Accounts of Chemical Research*, *53*(5), 1005–1013. https://doi.org/10.1021/acs.accounts.0c00102

Gaston, C. J., Pratt, K. A., Suski, K. J., May, N. W., Gill, T. E., & Prather, K. A. (2017). Laboratory Studies of the Cloud Droplet Activation Properties and Corresponding Chemistry of Saline Playa Dust. *Environmental Science & Technology*, *51*(3), 1348–1356. https://doi.org/10.1021/acs.est.6b04487

Gislason, S. R., Hassenkam, T., Nedel, S., Bovet, N., Eiriksdottir, E. S., Alfredsson, H. A., et al. (2011). Characterization of Eyjafjallajökull volcanic ash particles and a protocol for rapid risk assessment. *Proceedings of the National Academy of Sciences*, *108*(18), 7307–7312. https://doi.org/10.1073/pnas.1015053108

Gomes, L., Bergametti, G., Coudé-Gaussen, G., & Rognon, P. (1990). Submicron desert dusts: A sandblasting process. *Journal of Geophysical Research*, *95*(D9), 13927. https://doi.org/10.1029/JD095iD09p13927

Gorham, K. A., Raffuse, S. M., Hyslop, N. P., & White, W. H. (2021). Comparison of recent speciated PM2.5 data from collocated CSN and IMPROVE measurements. *Atmospheric Environment*, *244*, 117977. https://doi.org/10.1016/j.atmosenv.2020.117977

Goudie, A. S. (2014). Desert dust and human health disorders. *Environment International*, *63*, 101–113. https://doi.org/10.1016/j.envint.2013.10.011

Groll, M., Opp, Chr., & Aslanov, I. (2013). Spatial and temporal distribution of the dust deposition in Central Asia – results from a long term monitoring program. *Aeolian Research*, *9*, 49–62. https://doi.org/10.1016/j.aeolia.2012.08.002

Gutknecht, W., Flanagan, J., McWilliams, A., Jayanty, R. K. M., Kellogg, R., Rice, J., et al. (2010). Harmonization of Uncertainties of X-Ray Fluorescence Data for PM $_{2.5}$ Air Filter Analysis. *Journal of the Air & Waste Management Association*, *60*(2), 184–194. https://doi.org/10.3155/1047-3289.60.2.184

Guttikunda, S. K., Begum, B. A., & Wadud, Z. (2013). Particulate pollution from brick kiln clusters in the Greater Dhaka region, Bangladesh. *Air Quality, Atmosphere & Health*, *6*(2), 357–365. https://doi.org/10.1007/s11869-012-0187-2

Hand, J. L., Schichtel, B. A., Pitchford, M., Malm, W. C., & Frank, N. H. (2012). Seasonal composition of remote and urban fine particulate matter in the United States: COMPOSITION OF REMOTE AND URBAN AEROSOLS. *Journal of Geophysical Research: Atmospheres*, *117*(D5), n/a-n/a. https://doi.org/10.1029/2011JD017122

Hand, J. L., Schichtel, B. A., Malm, W. C., Copeland, S., Molenar, J. V., Frank, N., & Pitchford, M. (2014). Widespread reductions in haze across the United States from the early 1990s through 2011. *Atmospheric Environment*, *94*, 671–679. https://doi.org/10.1016/j.atmosenv.2014.05.062

Hand, J. L., Gill, T. E., & Schichtel, B. A. (2017). Spatial and seasonal variability in fine mineral dust and coarse aerosol mass at remote sites across the United States: Fine Mineral Dust and Coarse Mass. *Journal of Geophysical Research: Atmospheres*, *122*(5), 3080–3097. https://doi.org/10.1002/2016JD026290

Hand, J. L., Prenni, A. J., Schichtel, B. A., Malm, W. C., & Chow, J. C. (2019). Trends in remote PM2.5 residual mass across the United States: Implications for aerosol mass reconstruction in the IMPROVE network. *Atmospheric Environment*, *203*, 141–152. https://doi.org/10.1016/j.atmosenv.2019.01.049

Hand, J. L., Prenni, A. J., Copeland, S., Schichtel, B. A., & Malm, W. C. (2020). Thirty years of the Clean Air Act Amendments: Impacts on haze in remote regions of the United States (1990–2018). *Atmospheric Environment*, *243*, 117865. https://doi.org/10.1016/j.atmosenv.2020.117865

Harrison, R. M., Jones, A. M., Gietl, J., Yin, J., & Green, D. C. (2012). Estimation of the Contributions of Brake Dust, Tire Wear, and Resuspension to Nonexhaust Traffic Particles Derived from Atmospheric Measurements. *Environmental Science & Technology*, *46*(12), 6523–6529. https://doi.org/10.1021/es300894r

Hays, M. D., Cho, S.-H., Baldauf, R., Schauer, J. J., & Shafer, M. (2011). Particle size distributions of metal and non-metal elements in an urban near-highway environment. *Atmospheric Environment*, *45*(4), 925–934. https://doi.org/10.1016/j.atmosenv.2010.11.010

Heim, E. W., Dibb, J., Scheuer, E., Jost, P. C., Nault, B. A., Jimenez, J. L., et al. (2020). Asian dust observed during KORUS-AQ facilitates the uptake and incorporation of soluble pollutants during transport to South Korea. *Atmospheric Environment*, *224*, 117305. https://doi.org/10.1016/j.atmosenv.2020.117305

Henry, R., & Hidy, G. (1979). Multivariate analysis of particulate sulfate and other air quality variables by principal components-Part I: Annual data from Los Angeles and New York. *Atmospheric Environment (1967)*, *13*(11), 1581–1596.

Herich, H., Tritscher, T., Wiacek, A., Gysel, M., Weingartner, E., Lohmann, U., et al. (2009). Water uptake of clay and desert dust aerosol particles at sub- and supersaturated water vapor conditions. *Physical Chemistry Chemical Physics*, *11*(36), 7804. https://doi.org/10.1039/b901585j

Hinds, W. C., & Zhu, Y. (2022). *Aerosol technology: properties, behavior, and measurement of airborne particles*. John Wiley & Sons.

Ho, K. F., Lee, S. C., Chow, J. C., & Watson, J. G. (2003). Characterization of PM10 and PM2.5 source profiles for fugitive dust in Hong Kong. *Atmospheric Environment*, *37*(8), 1023–1032. https://doi.org/10.1016/S1352-2310(02)01028-2

Hofer, J., Althausen, D., Abdullaev, S. F., Makhmudov, A. N., Nazarov, B. I., Schettler, G., et al. (2017). Long-term profiling of mineral dust and pollution aerosol with multiwavelength polarization Raman lidar at the Central Asian site of Dushanbe, Tajikistan: case studies. *Atmospheric Chemistry and Physics*, *17*(23), 14559–14577. https://doi.org/10.5194/acp-17-14559-2017

Hojati, S., Khademi, H., Faz Cano, A., & Landi, A. (2012). Characteristics of dust deposited along a transect between central Iran and the Zagros Mountains. *Catena*, *88*(1), 27–36. https://doi.org/10.1016/j.catena.2011.09.002

Huang, K., Zhuang, G., Li, J., Wang, Q., Sun, Y., Lin, Y., & Fu, J. S. (2010). Mixing of Asian dust with pollution aerosol and the transformation of aerosol components during the dust storm over China in spring 2007. *Journal of Geophysical Research*, *115*, D00K13. https://doi.org/10.1029/2009JD013145

Huang, R., Cheng, R., Jing, M., Yang, L., Li, Y., Chen, Q., et al. (2018). Source-Specific Health Risk Analysis on Particulate Trace Elements: Coal Combustion and Traffic Emission As Major Contributors in Wintertime Beijing. *Environmental Science & Technology*, *52*(19), 10967–10974. https://doi.org/10.1021/acs.est.8b02091

Huang, Y., Adebiyi, A. A., Formenti, P., & Kok, J. F. (2021). Linking the Different Diameter Types of Aspherical Desert Dust Indicates That Models Underestimate Coarse Dust Emission. *Geophysical Research Letters*, *48*(6), e2020GL092054. https://doi.org/10.1029/2020GL092054

Hueglin, C., Gehrig, R., Baltensperger, U., Gysel, M., Monn, C., & Vonmont, H. (2005). Chemical characterisation of PM2.5, PM10 and coarse particles at urban, near-city and rural sites in Switzerland. *Atmospheric Environment*, *39*(4), 637–651. https://doi.org/10.1016/j.atmosenv.2004.10.027

Hyslop, N., & White, W. (2008). An evaluation of interagency monitoring of protected visual environments (IMPROVE) collocated precision and uncertainty estimates. *Atmospheric Environment*, *42*(11), 2691–2705. https://doi.org/10.1016/j.atmosenv.2007.06.053

Hyslop, N. P., & White, W. H. (2009). Estimating Precision Using Duplicate Measurements. *Journal of the Air & Waste Management Association*, *59*(9), 1032–1039. https://doi.org/10.3155/1047-3289.59.9.1032

Hyslop, N. P., Trzepla, K., & White, W. H. (2015). Assessing the Suitability of Historical $PM_{2.5}$ Element Measurements for Trend Analysis. *Environmental Science & Technology*, *49*(15), 9247–9255. https://doi.org/10.1021/acs.est.5b01572

Hyslop, N. P., Trzepla, K., Yatkin, S., White, W. H., Ancelet, T., Davy, P., et al. (2019). An inter-laboratory evaluation of new multi-element reference materials for atmospheric particulate matter measurements. *Aerosol Science and Technology*, *53*(7), 771–782. https://doi.org/10.1080/02786826.2019.1606413

Ibrahim, S., Romanias, M. N., Alleman, L. Y., Zeineddine, M. N., Angeli, G. K., Trikalitis, P. N., & Thevenet, F. (2018). Water Interaction with Mineral Dust Aerosol: Particle Size and Hygroscopic Properties of Dust. *ACS Earth and Space Chemistry*, *2*(4), 376–386. https://doi.org/10.1021/acsearthspacechem.7b00152

IMPROVE. (2022). X-Ray Fluorescence Analysis of Aerosol Deposits on PTFE Filters (with PANalytical Epsilon 5). Retrieved from http://vista.cira.colostate.edu/improve/wp-content/uploads/2023/02/IMPROVE_SOP_301_v2.5_XRF_Analysis_of_Aerosol_Deposits_on_PTFE_Filters_E5.pdf

Indoitu, R., Kozhoridze, G., Batyrbaeva, M., Vitkovskaya, I., Orlovsky, N., Blumberg, D., & Orlovsky, L. (2015). Dust emission and environmental changes in the dried bottom of the Aral Sea. *Aeolian Research*, *17*, 101–115. https://doi.org/10.1016/j.aeolia.2015.02.004

ISO. (2024). Road Vehicles—Test Contaminants for Filter Evaluation—Part 1: Arizona Test Dust. Retrieved from https://www.iso.org/standard/85949.html

Jickells, T. D. (2005). Global Iron Connections Between Desert Dust, Ocean Biogeochemistry, and Climate. *Science*, *308*(5718), 67–71. https://doi.org/10.1126/science.1105959

Johansson, L., Jalkanen, J.-P., & Kukkonen, J. (2017). Global assessment of shipping emissions in 2015 on a high spatial and temporal resolution. *Atmospheric Environment*, *167*, 403–415. https://doi.org/10.1016/j.atmosenv.2017.08.042

Johnston, J. E., Franklin, M., Roh, H., Austin, C., & Arora, M. (2019). Lead and Arsenic in Shed Deciduous Teeth of Children Living Near a Lead-Acid Battery Smelter. *Environmental Science & Technology*, *53*(10), 6000–6006. https://doi.org/10.1021/acs.est.9b00429

Journet, E., Balkanski, Y., & Harrison, S. P. (2014). A new data set of soil mineralogy for dust-cycle modeling. *Atmospheric Chemistry and Physics*, *14*(8), 3801–3816. https://doi.org/10.5194/acp-14-3801-2014

Kabir, M. H., Wang, Q., Rashid, M. H., Wang, W., & Isobe, Y. (2022). Assessment of Bioaccessibility and Health Risks of Toxic Metals in Roadside Dust of Dhaka City, Bangladesh. *Atmosphere*, *13*(3), 488. https://doi.org/10.3390/atmos13030488

Kaiser, H. F. (1960). The application of electronic computers to factor analysis. *Educational and Psychological Measurement*, *20*(1), 141–151.

Kakavas, S., & Pandis, S. N. (2021). Effects of urban dust emissions on fine and coarse PM levels and composition. *Atmospheric Environment*, *246*, 118006. https://doi.org/10.1016/j.atmosenv.2020.118006

Kamber, B. S., Greig, A., & Collerson, K. D. (2005). A new estimate for the composition of weathered young upper continental crust from alluvial sediments, Queensland, Australia. *Geochimica et Cosmochimica Acta*, *69*(4), 1041–1058. https://doi.org/10.1016/j.gca.2004.08.020

Kandler, K., Benker, N., Bundke, U., Cuevas, E., Ebert, M., Knippertz, P., et al. (2007). Chemical composition and complex refractive index of Saharan Mineral Dust at Izaña, Tenerife (Spain) derived by electron microscopy. *Atmospheric Environment*, *41*(37), 8058–8074. https://doi.org/10.1016/j.atmosenv.2007.06.047

Kavouras, I. G., Etyemezian, V., DuBois, D. W., Xu, J., & Pitchford, M. (2009). Source reconciliation of atmospheric dust causing visibility impairment in Class I areas of the western United States. *Journal of Geophysical Research: Atmospheres*, *114*(D2). https://doi.org/10.1029/2008JD009923

Kellogg, R. B. (2005). *X-Ray Fluorescence Analysis of Fine Ambient Aerosols at the USEPA, RTP, NC* (Internal Report). McLean, VA: Alion Science and Technology.

Kerimray, A., Assanov, D., Kenessov, B., & Karaca, F. (2020). Trends and health impacts of major urban air pollutants in Kazakhstan. *Journal of the Air & Waste Management Association*, *70*(11), 1148–1164. https://doi.org/10.1080/10962247.2020.1813837

Khan, A., Michelsen, N., Marandi, A., Hossain, R., Hossain, M. A., Roehl, K. E., et al. (2020). Processes controlling the extent of groundwater pollution with chromium from tanneries in the Hazaribagh area, Dhaka, Bangladesh. *Science of The Total Environment*, *710*, 136213. https://doi.org/10.1016/j.scitotenv.2019.136213

Khiri, F., Ezaidi, A., & Kabbachi, K. (2004). Dust deposits in Souss–Massa basin, South-West of Morocco: granulometrical, mineralogical and geochemical characterisation. *Journal of African Earth Sciences*, *39*(3–5), 459–464. https://doi.org/10.1016/j.jafrearsci.2004.07.019

Kim, K. H., Choi, G. H., Kang, C. H., Lee, J. H., Kim, J. Y., Youn, Y. H., & Lee, S. R. (2003). The chemical composition of fine and coarse particles in relation with the Asian Dust events. *Atmospheric Environment*, *37*(6), 753–765. https://doi.org/10.1016/S1352-2310(02)00954-8

Kim, K. W., Kim, Y. J., & Oh, S. J. (2001). Visibility impairment during Yellow Sand periods in the urban atmosphere of Kwangju, Korea. *Atmospheric Environment*, *35*(30), 5157–5167. https://doi.org/10.1016/S1352-2310(01)00330-2

Kleindienst, T. E., Lewandowski, M., Offenberg, J. H., Edney, E. O., Jaoui, M., Zheng, M., et al. (2010). Contribution of Primary and Secondary Sources to Organic Aerosol and PM $_{2.5}$ at SEARCH Network Sites. *Journal of the Air & Waste Management Association*, *60*(11), 1388–1399. https://doi.org/10.3155/1047-3289.60.11.1388

Knippertz, P., & Stuut, J. B. W. (Eds.). (2014). *Mineral dust—A key player in the Earth system*. Dordrecht: Springer Netherlands. https://doi.org/10.1007/978-94-017-8978-3

Koehler, K. A., Kreidenweis, S. M., DeMott, P. J., Petters, M. D., Prenni, A. J., & Carrico, C. M. (2009). Hygroscopicity and cloud droplet activation of mineral dust aerosol. *Geophysical Research Letters*, *36*(8), L08805. https://doi.org/10.1029/2009GL037348

Koehler, Kirsten A., Kreidenweis, S. M., DeMott, P. J., Prenni, A. J., & Petters, M. D. (2007). Potential impact of Owens (dry) Lake dust on warm and cold cloud formation. *Journal of Geophysical Research*, *112*(D12), D12210. https://doi.org/10.1029/2007JD008413

Kok, J. F. (2011). A scaling theory for the size distribution of emitted dust aerosols suggests climate models underestimate the size of the global dust cycle. *Proceedings of the National Academy of Sciences*, *108*(3), 1016–1021. https://doi.org/10.1073/pnas.1014798108

Kok, J. F., Adebiyi, A. A., Albani, S., Balkanski, Y., Checa-Garcia, R., Chin, M., et al. (2021). Improved representation of the global dust cycle using observational constraints on dust properties and abundance. *Atmospheric Chemistry and Physics*, *21*(10), 8127–8167. https://doi.org/10.5194/acp-21-8127-2021

Kok, J. F., Storelvmo, T., Karydis, V. A., Adebiyi, A. A., Mahowald, N. M., Evan, A. T., et al. (2023). Mineral dust aerosol impacts on global climate and climate change. *Nature Reviews Earth & Environment*, *4*(2), 71–86. https://doi.org/10.1038/s43017-022-00379-5

Koren, I., Kaufman, Y. J., Washington, R., Todd, M. C., Rudich, Y., Martins, J. V., & Rosenfeld, D. (2006). The Bodélé depression: a single spot in the Sahara that provides most of the mineral dust to the Amazon forest. *Environmental Research Letters*, *1*(1), 014005. https://doi.org/10.1088/1748-9326/1/1/014005

Krall, J. R., Mulholland, J. A., Russell, A. G., Balachandran, S., Winquist, A., Tolbert, P. E., et al. (2017). Associations between Source-Specific Fine Particulate Matter and Emergency Department Visits for Respiratory Disease in Four U.S. Cities. *Environmental Health Perspectives*, *125*(1), 97–103. https://doi.org/10.1289/EHP271

Kreidenweis, S. M., Petters, M. D., & DeMott, P. J. (2008). Single-parameter estimates of aerosol water content. *Environmental Research Letters*, *3*(3), 035002. https://doi.org/10.1088/1748-9326/3/3/035002

Kumar, S., Rahman, Md. A., Islam, Md. R., Hashem, Md. A., & Rahman, M. M. (2022). Lead and other elements-based pollution in soil, crops and water near a lead-acid battery recycling factory in Bangladesh. *Chemosphere*, *290*, 133288. https://doi.org/10.1016/j.chemosphere.2021.133288

Latimer, R. N. C., & Martin, R. V. (2019). Interpretation of measured aerosol mass scattering efficiency over North America using a chemical transport model. *Atmospheric Chemistry and Physics*, *19*(4), 2635–2653. https://doi.org/10.5194/acp-19-2635-2019

Lee, J., Brooks, N. R., Tajwar, F., Burke, M., Ermon, S., Lobell, D. B., et al. (2021). Scalable deep learning to identify brick kilns and aid regulatory capacity. *Proceedings of the National Academy of Sciences*, *118*(17), e2018863118. https://doi.org/10.1073/pnas.2018863118

Leyssens, L., Vinck, B., Van Der Straeten, C., Wuyts, F., & Maes, L. (2017). Cobalt toxicity in humans—A review of the potential sources and systemic health effects. *Toxicology*, *387*, 43–56. https://doi.org/10.1016/j.tox.2017.05.015

Li, L., & Sokolik, I. (2018). Analysis of Dust Aerosol Retrievals Using Satellite Data in Central Asia. *Atmosphere*, *9*(8), 288. https://doi.org/10.3390/atmos9080288

Li, W., Shao, L., Shi, Z., Chen, J., Yang, L., Yuan, Q., et al. (2014). Mixing state and hygroscopicity of dust and haze particles before leaving Asian continent. *Journal of Geophysical Research: Atmospheres*, *119*(2), 1044–1059. https://doi.org/10.1002/2013JD021003

Lide, D. R. (1995). *CRC handbook of chemistry and physics: a ready-reference book of chemical and physical data*. CRC press.

Linke, C., Möhler, O., Veres, A., Mohácsi, A., Bozóki, Z., Szabó, G., & Schnaiter, M. (2006). Optical properties and mineralogical composition of different Saharan mineral dust samples: a laboratory study. *Atmos. Chem. Phys.*, 10.

Liu, X., Turner, J. R., Hand, J. L., Schichtel, B. A., & Martin, R. V. (2022). A Global-Scale Mineral Dust Equation. *Journal of Geophysical Research: Atmospheres*, *127*(18), e2022JD036937. https://doi.org/10.1029/2022JD036937

Liu, X., Turner, J. R., Oxford, C. R., McNeill, J., Walsh, B., Le Roy, E., et al. (2024). Elemental Characterization of Ambient Particulate Matter for a Globally Distributed Monitoring Network: Methodology and Implications. *ACS ES&T Air*, *1*(4), 283–293. https://doi.org/10.1021/acsestair.3c00069

Machette, M. N. (1985). Calcific soils of the southwestern United States. *Soils and Quaternary Geology of the Southwestern United States: Geological Society of America Special Paper*, *203*, 1–21.

Macias, E. S., & Hopke, P. K. (Eds.). (1981). *Atmospheric Aerosol: Source/Air Quality Relationships* (Vol. 167). WASHINGTON, D. C.: AMERICAN CHEMICAL SOCIETY. https://doi.org/10.1021/bk-1981-0167

Maenhaut, W., & Cafmeyer, J. (1998). Long-term atmospheric aerosol study at urban and rural sites in Belgium using multi-elemental analysis by particle-induced x-ray emission spectrometry and short-irradiation instrumental neutron activation analysis. *X-Ray*

Spectrometry, *27*(4), 236–246. https://doi.org/10.1002/(SICI)1097-4539(199807/08)27:4<236::AID-XRS292>3.0.CO;2-F

Mahowald, N. M., Kloster, S., Engelstaedter, S., Moore, J. K., Mukhopadhyay, S., McConnell, J. R., et al. (2010). Observed 20th century desert dust variability: impact on climate and biogeochemistry. *Atmospheric Chemistry and Physics*, *10*(22), 10875–10893. https://doi.org/10.5194/acp-10-10875-2010

Majumder, A. K., Al Nayeem, A., Islam, M., Akter, M. M., & Carter, W. S. (2021). Critical Review of Lead Pollution in Bangladesh. *Journal of Health and Pollution*, *11*(31), 210902. https://doi.org/10.5696/2156-9614-11.31.210902

Malm, W. C., & Hand, J. L. (2007). An examination of the physical and optical properties of aerosols collected in the IMPROVE program. *Atmospheric Environment*, *41*(16), 3407–3427. https://doi.org/10.1016/j.atmosenv.2006.12.012

Malm, W. C., Sisler, J. F., Huffman, D., Eldred, R. A., & Cahill, T. A. (1994). Spatial and seasonal trends in particle concentration and optical extinction in the United States. *Journal of Geophysical Research*, *99*(D1), 1347. https://doi.org/10.1029/93JD02916

Manders, A. M. M., Schaap, M., Querol, X., Albert, M. F. M. A., Vercauteren, J., Kuhlbusch, T. A. J., & Hoogerbrugge, R. (2010). Sea salt concentrations across the European continent. *Atmospheric Environment*, *44*(20), 2434–2442. https://doi.org/10.1016/j.atmosenv.2010.03.028

Martin, R. V., Brauer, M., van Donkelaar, A., Shaddick, G., Narain, U., & Dey, S. (2019). No one knows which city has the highest concentration of fine particulate matter. *Atmospheric Environment: X*, *3*, 100040. https://doi.org/10.1016/j.aeaoa.2019.100040

Mason, B. (1952). Principles of Geochemistry. *Soil Science*, *74*(3), 262.

Matawle, J. L., Pervez, S., Dewangan, S., Shrivastava, A., Tiwari, S., Pant, P., et al. (2015). Characterization of PM2.5 Source Profiles for Traffic and Dust Sources in Raipur, India. *Aerosol and Air Quality Research*, *15*(7), 2537–2548. https://doi.org/10.4209/aaqr.2015.04.0222

McNeill, J., Snider, G., Weagle, C. L., Walsh, B., Bissonnette, P., Stone, E., et al. (2020). Large global variations in measured airborne metal concentrations driven by anthropogenic sources. *Scientific Reports*, *10*(1), 21817. https://doi.org/10.1038/s41598-020-78789-y

Meng, J., Martin, R. V., Ginoux, P., Hammer, M., Sulprizio, M. P., Ridley, D. A., & van Donkelaar, A. (2021). Grid-independent high-resolution dust emissions (v1.0) for chemical transport models: application to GEOS-Chem (12.5.0). *Geoscientific Model Development*, *14*(7), 4249–4260. https://doi.org/10.5194/gmd-14-4249-2021

Miller, R. L., & Tegen, I. (1998). Climate Response to Soil Dust Aerosols. *JOURNAL OF CLIMATE*, *11*, 21.

Miller-Schulze, J. P., Shafer, M., Schauer, J. J., Heo, J., Solomon, P. A., Lantz, J., et al. (2015). Seasonal contribution of mineral dust and other major components to particulate matter at two remote sites in Central Asia. *Atmospheric Environment*, *119*, 11–20. https://doi.org/10.1016/j.atmosenv.2015.07.011

Misra, A., Gaur, A., Bhattu, D., Ghosh, S., Dwivedi, A. K., Dalai, R., et al. (2014). An overview of the physico-chemical characteristics of dust at Kanpur in the central Indo-Gangetic basin. *Atmospheric Environment*, *97*, 386–396. https://doi.org/10.1016/j.atmosenv.2014.08.043

Mitroo, D., Gill, T. E., Haas, S., Pratt, K. A., & Gaston, C. J. (2021). Development of a bench scale method for constant output of mineral dust. *Aerosol Science and Technology*, *55*(6), 692–702. https://doi.org/10.1080/02786826.2021.1888866

Møberg, J. P., Esu, I. E., & Malgwi, W. B. (1991). Characteristics and constituent composition of Harmattan dust falling in Northern Nigeria. *Geoderma*, *48*(1–2), 73–81. https://doi.org/10.1016/0016-7061(91)90007-G

Modaihsh, A. S. (1997). Characteristics and composition of the falling dust sediments on Riyadh city, Saudi Arabia. *Journal of Arid Environments*, *36*(2), 211–223. https://doi.org/10.1006/jare.1996.0225

Moreno, T., Querol, X., Castillo, S., Alastuey, A., Cuevas, E., Herrmann, L., et al. (2006). Geochemical variations in aeolian mineral particles from the Sahara–Sahel Dust Corridor. *Chemosphere*, *65*(2), 261–270. https://doi.org/10.1016/j.chemosphere.2006.02.052

Moreno, T., Amato, F., Querol, X., Alastuey, A., Elvira, J., & Gibbons, W. (2009). Bedrock controls on the mineralogy and chemistry of PM10 extracted from Australian desert sediments. *Environmental Geology*, *57*(2), 411–420. https://doi.org/10.1007/s00254-008-1312-2

Mori, I. (2003). Change in size distribution and chemical composition of kosa (Asian dust) aerosol during long-range transport. *Atmospheric Environment*, *37*(30), 4253–4263. https://doi.org/10.1016/S1352-2310(03)00535-1

Moufti, A. M. B. (2013). Mineralogy, geochemistry and possible provenance of desert sand dunes from western Rub' al Khali area, southeastern Saudi Arabia. *International Journal of Basic and Applied Sciences*, *2*(4), 399–407. https://doi.org/10.14419/ijbas.v2i4.1292

Mowla, M., Rahman, E., Islam, N., & Aich, N. (2021). Assessment of heavy metal contamination and health risk from indoor dust and air of informal E-waste recycling shops in Dhaka, Bangladesh. *Journal of Hazardous Materials Advances*, *4*, 100025. https://doi.org/10.1016/j.hazadv.2021.100025

Muhs, D. R., Budahn, J. R., Prospero, J. M., Skipp, G., & Herwitz, S. R. (2012). Soil genesis on the island of Bermuda in the Quaternary: The importance of African dust transport and

deposition: AFRICAN DUST IN BERMUDA SOILS. *Journal of Geophysical Research: Earth Surface*, *117*(F3). https://doi.org/10.1029/2012JF002366

Najafi, M. S., Khoshakhllagh, F., Zamanzadeh, S. M., Shirazi, M. H., Samadi, M., & Hajikhani, S. (2014). Characteristics of TSP Loads during the Middle East Springtime Dust Storm (MESDS) in Western Iran. *Arabian Journal of Geosciences*, *7*(12), 5367–5381. https://doi.org/10.1007/s12517-013-1086-z

Ni, T., Li, P., Han, B., Bai, Z., Ding, X., Wang, Q., et al. (2013). Spatial and Temporal Variation of Chemical Composition and Mass Closure of Ambient PM10 in Tianjin, China. *Aerosol and Air Quality Research*, *13*(6), 1832–1846. https://doi.org/10.4209/aaqr.2012.10.0283

Nickovic, S., Vukovic, A., Vujadinovic, M., Djurdjevic, V., & Pejanovic, G. (2012). Technical Note: High-resolution mineralogical database of dust-productive soils for atmospheric dust modeling. *Atmospheric Chemistry and Physics*, *12*(2), 845–855. https://doi.org/10.5194/acp-12-845-2012

Nishikawa, M., Kanamori, S., Kanamori, N., & Mizoguchi, T. (1991). Kosa aerosol as eolian carrier of anthropogenic material. *Science of The Total Environment*, *107*, 13–27. https://doi.org/10.1016/0048-9697(91)90247-C

Nishikawa, M., Hao, Q., & Morita, M. (2000). Preparation and Evaluation of Certified Reference Materials for Asian Mineral Dust. *Global Environmental Research*, *4*, 1037113.

Nishonov, B. E., Kholmatjanov, B. M., Labzovskii, L. D., Rakhmatova, N., Shardakova, L., Abdulakhatov, E. I., et al. (2023). Study of the strongest dust storm occurred in Uzbekistan in November 2021. *Scientific Reports*, *13*(1), 20042. https://doi.org/10.1038/s41598-023-42256-1

Nousiainen, T. (2009). Optical modeling of mineral dust particles: A review. *Journal of Quantitative Spectroscopy and Radiative Transfer*, *110*(14–16), 1261–1279. https://doi.org/10.1016/j.jqsrt.2009.03.002

Nowak, S., Lafon, S., Caquineau, S., Journet, E., & Laurent, B. (2018). Quantitative study of the mineralogical composition of mineral dust aerosols by X-ray diffraction. *Talanta*, *186*, 133–139. https://doi.org/10.1016/j.talanta.2018.03.059

Opp, C., Groll, M., Aslanov, I., Lotz, T., & Vereshagina, N. (2017). Aeolian dust deposition in the southern Aral Sea region (Uzbekistan): Ground-based monitoring results from the LUCA project. *Quaternary International*, *429*, 86–99. https://doi.org/10.1016/j.quaint.2015.12.103

Orange, D., Gac, J.-Y., & Diallo, M. (1993). Geochemical assessment of atmospheric deposition including Harmattan dust in continental West Africa. *IAHS PUBLICATION*, 303–303.

Orlovsky, N., Glantz, M., & Orlovsky, L. (2001). Irrigation and land degradation in the Aral Sea basin (pp. 115–125). Presented at the Sustainable land use in deserts, Springer, Berlin, Heidelberg. https://doi.org/10.1007/978-3-642-59560-8_11

Ostro, B., Malig, B., Hasheminassab, S., Berger, K., Chang, E., & Sioutas, C. (2016). Associations of Source-Specific Fine Particulate Matter With Emergency Department Visits in California. *American Journal of Epidemiology*, *184*(6), 450–459. https://doi.org/10.1093/aje/kwv343

Paatero, P., & Tapper, U. (1994). Positive matrix factorization: A non-negative factor model with optimal utilization of error estimates of data values. *Environmetrics*, *5*(2), 111–126.

Pachon, J. E., Weber, R. J., Zhang, X., Mulholland, J. A., & Russell, A. G. (2013). Revising the use of potassium (K) in the source apportionment of PM2.5. *Atmospheric Pollution Research*, *4*(1), 14–21. https://doi.org/10.5094/APR.2013.002

Paithankar, J. G., Saini, S., Dwivedi, S., Sharma, A., & Chowdhuri, D. K. (2021). Heavy metal associated health hazards: An interplay of oxidative stress and signal transduction. *Chemosphere*, *262*, 128350. https://doi.org/10.1016/j.chemosphere.2020.128350

Pant, P., Shukla, A., Kohl, S. D., Chow, J. C., Watson, J. G., & Harrison, R. M. (2015). Characterization of ambient PM2.5 at a pollution hotspot in New Delhi, India and inference of sources. *Atmospheric Environment*, *109*, 178–189. https://doi.org/10.1016/j.atmosenv.2015.02.074

Pant, P., Habib, G., Marshall, J. D., & Peltier, R. E. (2017). PM2.5 exposure in highly polluted cities: A case study from New Delhi, India. *Environmental Research*, *156*, 167–174. https://doi.org/10.1016/j.envres.2017.03.024

Peng, C., Gu, W., Li, R., Lin, Q., Ma, Q., Jia, S., et al. (2020). Large Variations in Hygroscopic Properties of Unconventional Mineral Dust. *ACS Earth and Space Chemistry*, *4*(10), 1823–1830. https://doi.org/10.1021/acsearthspacechem.0c00219

Perry, K. D., Cahill, T. A., Eldred, R. A., Dutcher, D. D., & Gill, T. E. (1997). Long-range transport of North African dust to the eastern United States. *Journal of Geophysical Research: Atmospheres*, *102*(D10), 11225–11238. https://doi.org/10.1029/97JD00260

Pervez, S., Bano, S., Watson, J. G., Chow, J. C., Matawle, J. L., Shrivastava, A., et al. (2018). Source Profiles for PM10-2.5 Resuspended Dust and Vehicle Exhaust Emissions in Central India. *Aerosol and Air Quality Research*, *18*(7), 1660–1672. https://doi.org/10.4209/aaqr.2017.08.0259

Peters, T. M., Gussman, R. A., Kenny, L. C., & Vanderpool, R. W. (2001). Evaluation of $PM_{2.5}$ Size Selectors Used in Speciation Samplers. *Aerosol Science and Technology*, *34*(5), 422–429. https://doi.org/10.1080/02786820119266

Pettijohn, F. J. (1975). *Sedimentary rocks* (Vol. 3). Harper & Row New York.

Philip, S., Martin, R. V., Pierce, J. R., Jimenez, J. L., Zhang, Q., Canagaratna, M. R., et al. (2014). Spatially and seasonally resolved estimate of the ratio of organic mass to organic carbon. *Atmospheric Environment*, *87*, 34–40. https://doi.org/10.1016/j.atmosenv.2013.11.065

Podgorski, J., & Berg, M. (2020). Global threat of arsenic in groundwater. *Science*, *368*(6493), 845–850. https://doi.org/10.1126/science.aba1510

Price, J. R., & Velbel, M. A. (2003). Chemical weathering indices applied to weathering profiles developed on heterogeneous felsic metamorphic parent rocks. *Chemical Geology*, *202*(3–4), 397–416. https://doi.org/10.1016/j.chemgeo.2002.11.001

Prospero, J. M. (2002). Environmental characterization of global sources of atmospheric soil dust identified with the NIMBUS 7 Total Ozone Mapping Spectrometer (TOMS) absorbing aerosol product. *Reviews of Geophysics*, *40*(1), 1002. https://doi.org/10.1029/2000RG000095

Pryor, S. C., Simpson, R., Guise-Bagley, L., Hoff, R., & Sakiyama, S. (1997). Visibility and Aerosol Composition in the Fraser Valley During Reveal. *Journal of the Air & Waste Management Association*, *47*(2), 147–156. https://doi.org/10.1080/10473289.1997.10464432

Querol, X., Viana, M., Alastuey, A., Amato, F., Moreno, T., Castillo, S., et al. (2007). Source origin of trace elements in PM from regional background, urban and industrial sites of Spain. *Atmospheric Environment*, *41*(34), 7219–7231. https://doi.org/10.1016/j.atmosenv.2007.05.022

Radhi, M., Box, M. A., Box, G. P., Mitchell, R. M., Cohen, D. D., Stelcer, E., & Keywood, M. D. (2010a). Optical, physical and chemical characteristics of Australian continental aerosols: results from a field experiment. *Atmospheric Chemistry and Physics*, *10*(13), 5925–5942. https://doi.org/10.5194/acp-10-5925-2010

Radhi, M., Box, M. A., Box, G. P., Mitchell, R. M., Cohen, D. D., Stelcer, E., & Keywood, M. D. (2010b). Size-resolved mass and chemical properties of dust aerosols from Australia's Lake Eyre Basin. *Atmospheric Environment*, *44*(29), 3519–3528. https://doi.org/10.1016/j.atmosenv.2010.06.016

Rahman, M. S., Khan, M. D. H., Jolly, Y. N., Kabir, J., Akter, S., & Salam, A. (2019). Assessing risk to human health for heavy metal contamination through street dust in the Southeast Asian Megacity: Dhaka, Bangladesh. *Science of The Total Environment*, *660*, 1610–1622. https://doi.org/10.1016/j.scitotenv.2018.12.425

Rahman, M. S., Akhter, S., Rahman, R., Choudhury, T. R., Jolly, Y. N., Akter, S., et al. (2020). Identification of sources of PM2.5 at Farmgate Area, Dhaka using reconstructed mass calculation and statistical approaches. *Nuclear Sci Appl*, *28*(1), 2.

Reff, A., Bhave, P. V., Simon, H., Pace, T. G., Pouliot, G. A., Mobley, J. D., & Houyoux, M. (2009). Emissions Inventory of PM $_{2.5}$ Trace Elements across the United States. *Environmental Science & Technology*, *43*(15), 5790–5796. https://doi.org/10.1021/es802930x

Reid, E. A. (2003). Characterization of African dust transported to Puerto Rico by individual particle and size segregated bulk analysis. *Journal of Geophysical Research*, *108*(D19), 8591. https://doi.org/10.1029/2002JD002935

Reimann, C., & de Caritat, P. (2012). New soil composition data for Europe and Australia: Demonstrating comparability, identifying continental-scale processes and learning lessons for global geochemical mapping. *Science of The Total Environment*, *416*, 239–252. https://doi.org/10.1016/j.scitotenv.2011.11.019

Rodríguez, S., Alastuey, A., & Querol, X. (2012). A review of methods for long term in situ characterization of aerosol dust. *Aeolian Research*, *6*, 55–74. https://doi.org/10.1016/j.aeolia.2012.07.004

Rolph, G., Stein, A., & Stunder, B. (2017). Real-time Environmental Applications and Display sYstem: READY. *Environmental Modelling & Software*, *95*, 210–228. https://doi.org/10.1016/j.envsoft.2017.06.025

Salvador, P., Pey, J., Pérez, N., Querol, X., & Artíñano, B. (2022). Increasing atmospheric dust transport towards the western Mediterranean over 1948–2020. *Npj Climate and Atmospheric Science*, *5*(1), 34. https://doi.org/10.1038/s41612-022-00256-4

Sánchez de la Campa, A., García-Salamanca, A., Solano, J., de la Rosa, J., & Ramos, J.-L. (2013). Chemical and Microbiological Characterization of Atmospheric Particulate Matter during an Intense African Dust Event in Southern Spain. *Environmental Science & Technology*, *47*(8), 3630–3638. https://doi.org/10.1021/es3051235

Santacatalina, M., Reche, C., Minguillón, M. C., Escrig, A., Sanfelix, V., Carratalá, A., et al. (2010). Impact of fugitive emissions in ambient PM levels and composition: A case study in Southeast Spain. *Science of The Total Environment*, *408*(21), 4999–5009. https://doi.org/10.1016/j.scitotenv.2010.07.040

Scheuvens, D., Schütz, L., Kandler, K., Ebert, M., & Weinbruch, S. (2013). Bulk composition of northern African dust and its source sediments — A compilation. *Earth-Science Reviews*, *116*, 170–194. https://doi.org/10.1016/j.earscirev.2012.08.005

Shaji, E., Santosh, M., Sarath, K. V., Prakash, P., Deepchand, V., & Divya, B. V. (2021). Arsenic contamination of groundwater: A global synopsis with focus on the Indian Peninsula. *Geoscience Frontiers*, *12*(3), 101079. https://doi.org/10.1016/j.gsf.2020.08.015

Shaw, D. M., Cramer, J. J., Higgins, M. D., & Truscott, M. G. (1986). Composition of the Canadian Precambrian shield and the continental crust of the earth. *Geological Society, London, Special Publications*, *24*(1), 275–282. https://doi.org/10.1144/GSL.SP.1986.024.01.24

Shen, H., Abuduwaili, J., Samat, A., & Ma, L. (2016). A review on the research of modern aeolian dust in Central Asia. *Arabian Journal of Geosciences*, *9*(13), 625. https://doi.org/10.1007/s12517-016-2646-9

Shen, H., Abuduwaili, J., Ma, L., & Samat, A. (2019). Remote sensing-based land surface change identification and prediction in the Aral Sea bed, Central Asia. *International Journal of Environmental Science and Technology*, *16*(4), 2031–2046. https://doi.org/10.1007/s13762-018-1801-0

Shen, Z., Caquineau, S., Cao, J., Zhang, X., Han, Y., Gaudichet, A., & Gomes, L. (2009). Mineralogical characteristics of soil dust from source regions in northern China. *Particuology*, *7*(6), 507–512. https://doi.org/10.1016/j.partic.2009.10.001

Shen, Z., Sun, J., Cao, J., Zhang, L., Zhang, Q., Lei, Y., et al. (2016). Chemical profiles of urban fugitive dust PM2.5 samples in Northern Chinese cities. *Science of The Total Environment*, *569–570*, 619–626. https://doi.org/10.1016/j.scitotenv.2016.06.156

Shen, Z. X., Cao, J. J., Arimoto, R., Zhang, R. J., Jie, D. M., Liu, S. X., & Zhu, C. S. (2007). Chemical composition and source characterization of spring aerosol over Horqin sand land in northeastern China. *Journal of Geophysical Research*, *112*(D14), D14315. https://doi.org/10.1029/2006JD007991

Sigsgaard, T., Forsberg, B., Annesi-Maesano, I., Blomberg, A., Bølling, A., Boman, C., et al. (2015). Health impacts of anthropogenic biomass burning in the developed world. *European Respiratory Journal*, *46*(6), 1577–1588. https://doi.org/10.1183/13993003.01865-2014

Simon, H., Beck, L., Bhave, P. V., Divita, F., Hsu, Y., Luecken, D., et al. (2010). The development and uses of EPA's SPECIATE database. *Atmospheric Pollution Research*, *1*(4), 196–206. https://doi.org/10.5094/APR.2010.026

Simon, H., Bhave, P. V., Swall, J. L., Frank, N. H., & Malm, W. C. (2011). Determining the spatial and seasonal variability in OM/OC ratios across the US using multiple regression. *Atmospheric Chemistry and Physics*, *11*(6), 2933–2949. https://doi.org/10.5194/acp-11-2933-2011

Singer, A., Zobeck, T., Poberezsky, L., & Argaman, E. (2003). The PM10 and PM2.5 dust generation potential of soils/sediments in the Southern Aral Sea Basin, Uzbekistan. *Journal of Arid Environments*, *54*(4), 705–728. https://doi.org/10.1006/jare.2002.1084

Smith, D. B., Solano, F., Woodruff, L. G., Cannon, W. F., & Ellefsen, K. J. (2019). *Geochemical and mineralogical maps, with interpretation, for soils of the conterminous United States* (Report No. 2017–5118). Reston, VA. https://doi.org/10.3133/sir20175118

Snider, G., Weagle, C. L., Martin, R. V., van Donkelaar, A., Conrad, K., Cunningham, D., et al. (2015). SPARTAN: a global network to evaluate and enhance satellite-based estimates of ground-level particulate matter for global health applications. *Atmospheric Measurement Techniques*, *8*(1), 505–521. https://doi.org/10.5194/amt-8-505-2015

Snider, G., Weagle, C. L., Murdymootoo, K. K., Ring, A., Ritchie, Y., Stone, E., et al. (2016). Variation in global chemical composition of $PM_{2.5}$: emerging results from SPARTAN.

Atmospheric Chemistry and Physics, *16*(15), 9629–9653. https://doi.org/10.5194/acp-16-9629-2016

Sokolik, I. N., Winker, D. M., Bergametti, G., Gillette, D. A., Carmichael, G., Kaufman, Y. J., et al. (2001). Introduction to special section: Outstanding problems in quantifying the radiative impacts of mineral dust. *Journal of Geophysical Research: Atmospheres*, *106*(D16), 18015–18027. https://doi.org/10.1029/2000JD900498

Soleimani, Z., Teymouri, P., Darvishi Boloorani, A., Mesdaghinia, A., Middleton, N., & Griffin, D. W. (2020). An overview of bioaerosol load and health impacts associated with dust storms: A focus on the Middle East. *Atmospheric Environment*, *223*, 117187. https://doi.org/10.1016/j.atmosenv.2019.117187

Solomon, P. A., Fall, T., Salmon, L., Cass, G. R., Gray, H. A., & Davidson, A. (1989). Chemical Characteristics of PM $_{10}$ Aerosols Collected in the Los Angeles Area. *JAPCA*, *39*(2), 154–163. https://doi.org/10.1080/08940630.1989.10466515

Solomon, P. A., Crumpler, D., Flanagan, J. B., Jayanty, R. K. M., Rickman, E. E., & McDade, C. E. (2014). U.S. National PM $_{2.5}$ Chemical Speciation Monitoring Networks—CSN and IMPROVE: Description of networks. *Journal of the Air & Waste Management Association*, *64*(12), 1410–1438. https://doi.org/10.1080/10962247.2014.956904

Stafoggia, M., Zauli-Sajani, S., Pey, J., Samoli, E., Alessandrini, E., Basagaña, X., et al. (2016). Desert Dust Outbreaks in Southern Europe: Contribution to Daily PM_{10} Concentrations and Short-Term Associations with Mortality and Hospital Admissions. *Environmental Health Perspectives*, *124*(4), 413–419. https://doi.org/10.1289/ehp.1409164

Stein, A. F., Draxler, R. R., Rolph, G. D., Stunder, B. J. B., Cohen, M. D., & Ngan, F. (2015). NOAA's HYSPLIT Atmospheric Transport and Dispersion Modeling System. *Bulletin of the American Meteorological Society*, *96*(12), 2059–2077. https://doi.org/10.1175/BAMS-D-14-00110.1

Stuut, J.-B., Smalley, I., & O'Hara-Dhand, K. (2009). Aeolian dust in Europe: African sources and European deposits. *Quaternary International*, *198*(1–2), 234–245. https://doi.org/10.1016/j.quaint.2008.10.007

Sullivan, R. C., Moore, M. J. K., Petters, M. D., Kreidenweis, S. M., Roberts, G. C., & Prather, K. A. (2009). Effect of chemical mixing state on the hygroscopicity and cloud nucleation properties of calcium mineral dust particles. *Atmospheric Chemistry and Physics*, *9*(10), 3303–3316. https://doi.org/10.5194/acp-9-3303-2009

Ta, W., Xiao, Z., Qu, J., Yang, G., & Wang, T. (2003). Characteristics of dust particles from the desert/Gobi area of northwestern China during dust-storm periods. *Environmental Geology*, *43*(6), 667–679. https://doi.org/10.1007/s00254-002-0673-1

Tang, M., Cziczo, D. J., & Grassian, V. H. (2016). Interactions of Water with Mineral Dust Aerosol: Water Adsorption, Hygroscopicity, Cloud Condensation, and Ice Nucleation. *Chemical Reviews*, *116*(7), 4205–4259. https://doi.org/10.1021/acs.chemrev.5b00529

Tang, M., Zhang, H., Gu, W., Gao, J., Jian, X., Shi, G., et al. (2019). Hygroscopic Properties of Saline Mineral Dust From Different Regions in China: Geographical Variations, Compositional Dependence, and Atmospheric Implications. *Journal of Geophysical Research: Atmospheres*, *124*(20), 10844–10857. https://doi.org/10.1029/2019JD031128

Taylor, H. E., & Lichte, F. E. (1980). Chemical composition of Mount St. Helens volcanic ash. *Geophysical Research Letters*, *7*(11), 949–952. https://doi.org/10.1029/GL007i011p00949

Taylor, S. R., & McLennan, S. M. (1995). The geochemical evolution of the continental crust. *Reviews of Geophysics*, *33*(2), 241. https://doi.org/10.1029/95RG00262

Tegen, I. (2003). Modeling the mineral dust aerosol cycle in the climate system. *Quaternary Science Reviews*, *22*(18–19), 1821–1834. https://doi.org/10.1016/S0277-3791(03)00163-X

Terzi, E., Argyropoulos, G., Bougatioti, A., Mihalopoulos, N., Nikolaou, K., & Samara, C. (2010). Chemical composition and mass closure of ambient PM10 at urban sites. *Atmospheric Environment*, *44*(18), 2231–2239. https://doi.org/10.1016/j.atmosenv.2010.02.019

Tian, H., Liu, K., Zhou, J., Lu, L., Hao, J., Qiu, P., et al. (2014). Atmospheric Emission Inventory of Hazardous Trace Elements from China's Coal-Fired Power Plants—Temporal Trends and Spatial Variation Characteristics. *Environmental Science & Technology*, *48*(6), 3575–3582. https://doi.org/10.1021/es404730j

Tong, D. Q., Wang, J. X. L., Gill, T. E., Lei, H., & Wang, B. (2017). Intensified dust storm activity and Valley fever infection in the southwestern United States: Dust and Valley Fever Intensification. *Geophysical Research Letters*, *44*(9), 4304–4312. https://doi.org/10.1002/2017GL073524

Torghabeh, A. K., Pradhan, B., & Jahandari, A. (2020). Assessment of geochemical and sedimentological characteristics of atmospheric dust in Shiraz, southwest Iran. *Geoscience Frontiers*, *11*(3), 783–792. https://doi.org/10.1016/j.gsf.2019.08.004

Turner, J. R., & Brown, S. G. (2015). *Pilot Study on Coarse PM Monitoring* (No. EPA-454/R-15-001). U.S. EPA. Retrieved from https://www.epa.gov/sites/default/files/2020-06/documents/pmc_reportepa454r-15-001.pdf

Tursumbayeva, M., Muratuly, A., Baimatova, N., Karaca, F., & Kerimray, A. (2023). Cities of Central Asia: New hotspots of air pollution in the world. *Atmospheric Environment*, *309*, 119901. https://doi.org/10.1016/j.atmosenv.2023.119901

U.S. EPA. (1991). Risk Assessment Guidance for Superfund: Volume I Human Health Evaluation Manual (Part B, Development of Risk-Based Preliminary Remediation Goals). Retrieved from https://semspub.epa.gov/src/document/HQ/156739

U.S. EPA. (2009). Risk Assessment Guidance for Superfund Volume I: Human Health Evaluation Manual. (Part F, Supplemental Guidance for Inhalation Risk Assessment). Retrieved from https://semspub.epa.gov/src/document/HQ/140530

U.S. EPA. (2016a). Definition and Procedure for the Determination of the Method Detection Limit, Revision 2. *United States Environmental Protection Agency*. https://www.epa.gov/sites/default/files/2016-12/documents/mdl-procedure_rev2_12-13-2016.pdf

U.S. EPA. (2016b). National Ambient Air Quality Standards (NAAQS) for Lead (Pb). Retrieved from https://www.epa.gov/lead-air-pollution/national-ambient-air-quality-standards-naaqs-lead-pb

U.S. EPA. (2022). Regional Screening Levels (RSLs) - Generic Tables as of May 2023. Retrieved from https://semspub.epa.gov/src/document/HQ/404069

Uzhydromet. (2020). What is the scent of an autumn? *Hydrometeorological Service Agency under the Ministry of Ecology, Environmental Protection and Climate Change of the Republic of Uzbekistan*. https://monitoring.meteo.uz/en/news/what-is-the-scent-of-an-autumn

VanCuren, R. A. (2002). Asian aerosols in North America: Frequency and concentration of fine dust. *Journal of Geophysical Research*, *107*(D24), 4804. https://doi.org/10.1029/2002JD002204

Vedal, S., Kim, S., Miller, K., Fox, J., Bergen, S., Gould, T., et al. (2013). Section 1. NPACTepidemiologic study of components of fine particulate matter and cardiovascular disease in the MESA and WHI-OS cohorts. *National Particle Component Toxicity (NPACT) Initiative Report on Cardiovascular Effects, Research Report*, *178*, 9–128.

Vodonos, A., Friger, M., Katra, I., Avnon, L., Krasnov, H., Koutrakis, P., et al. (2014). The impact of desert dust exposures on hospitalizations due to exacerbation of chronic obstructive pulmonary disease. *Air Quality, Atmosphere & Health*, *7*(4), 433–439. https://doi.org/10.1007/s11869-014-0253-z

Wang, Y., Zhang, X., Arimoto, R., Cao, J., & Shen, Z. (2005). Characteristics of carbonate content and carbon and oxygen isotopic composition of northern China soil and dust aerosol and its application to tracing dust sources. *Atmospheric Environment*, *39*(14), 2631–2642. https://doi.org/10.1016/j.atmosenv.2005.01.015

Washington, R., Bouet, C., Cautenet, G., Mackenzie, E., Ashpole, I., Engelstaedter, S., et al. (2009). Dust as a tipping element: The Bodele Depression, Chad. *Proceedings of the National Academy of Sciences*, *106*(49), 20564–20571. https://doi.org/10.1073/pnas.0711850106

Weagle, C. L., Snider, G., Li, C., van Donkelaar, A., Philip, S., Bissonnette, P., et al. (2018). Global Sources of Fine Particulate Matter: Interpretation of $PM_{2.5}$ Chemical Composition

Observed by SPARTAN using a Global Chemical Transport Model. *Environmental Science & Technology*, *52*(20), 11670–11681. https://doi.org/10.1021/acs.est.8b01658

Wedepohl, K. H. (1995). The composition of the continental crust. *Geochimica et Cosmochimica Acta*, *59*(7), 1217–1232. https://doi.org/10.1016/0016-7037(95)00038-2

Weyant, C., Athalye, V., Ragavan, S., Rajarathnam, U., Lalchandani, D., Maithel, S., et al. (2014). Emissions from South Asian Brick Production. *Environmental Science & Technology*, *48*(11), 6477–6483. https://doi.org/10.1021/es500186g

WHO. (2021). WHO global air quality guidelines: particulate matter (PM2.5 and PM10), ozone, nitrogen dioxide, sulfur dioxide and carbon monoxide. *World Health Organization*. https://iris.who.int/handle/10665/345329

Wu, F., Chow, J. C., An, Z., Watson, J. G., & Cao, J. (2011). Size-Differentiated Chemical Characteristics of Asian Paleo Dust: Records from Aeolian Deposition on Chinese Loess Plateau. *Journal of the Air & Waste Management Association*, *61*(2), 180–189. https://doi.org/10.3155/1047-3289.61.2.180

Xi, X., & Sokolik, I. N. (2015). Dust interannual variability and trend in Central Asia from 2000 to 2014 and their climatic linkages. *Journal of Geophysical Research: Atmospheres*, *120*(23), 12,175-12,197. https://doi.org/10.1002/2015JD024092

Xu, J. (2004). Aerosol chemical, physical, and radiative characteristics near a desert source region of northwest China during ACE-Asia. *Journal of Geophysical Research*, *109*(D19), D19S03. https://doi.org/10.1029/2003JD004239

Yatkin, S., Trzepla, K., White, W. H., & Hyslop, N. P. (2018). Generation of multi-element reference materials on PTFE filters mimicking ambient aerosol characteristics. *Atmospheric Environment*, *189*, 41–49. https://doi.org/10.1016/j.atmosenv.2018.06.034

Yatkin, S., Trzepla, K., White, W. H., Spada, N. J., & Hyslop, N. P. (2020). Development of single-compound reference materials on polytetrafluoroethylene filters for analysis of aerosol samples. *Spectrochimica Acta Part B: Atomic Spectroscopy*, *171*, 105948. https://doi.org/10.1016/j.sab.2020.105948

Zarasvandi, A., Carranza, E. J. M., Moore, F., & Rastmanesh, F. (2011). Spatio-temporal occurrences and mineralogical–geochemical characteristics of airborne dusts in Khuzestan Province (southwestern Iran). *Journal of Geochemical Exploration*, *111*(3), 138–151. https://doi.org/10.1016/j.gexplo.2011.04.004

Zhai, S., Jacob, D. J., Pendergrass, D. C., Colombi, N. K., Shah, V., Yang, L. H., et al. (2023). Coarse particulate matter air quality in East Asia: implications for fine particulate nitrate. *Atmospheric Chemistry and Physics*, *23*(7), 4271–4281. https://doi.org/10.5194/acp-23-4271-2023

Zhang, L., Li, Q. B., Gu, Y., Liou, K. N., & Meland, B. (2013). Dust vertical profile impact on global radiative forcing estimation using a coupled chemical-transport–radiative-transfer

model. *Atmospheric Chemistry and Physics*, *13*(14), 7097–7114. https://doi.org/10.5194/acp-13-7097-2013

Zhang, Lei, Gao, Y., Wu, S., Zhang, S., Smith, K. R., Yao, X., & Gao, H. (2020). Global impact of atmospheric arsenic on health risk: 2005 to 2015. *Proceedings of the National Academy of Sciences*, *117*(25), 13975–13982. https://doi.org/10.1073/pnas.2002580117

Zhang, X., Zhao, L., Tong, D., Wu, G., Dan, M., & Teng, B. (2016). A Systematic Review of Global Desert Dust and Associated Human Health Effects. *Atmosphere*, *7*(12), 158. https://doi.org/10.3390/atmos7120158

Zhang, X.-X., Claiborn, C., Lei, J.-Q., Vaughan, J., Wu, S.-X., Li, S.-Y., et al. (2020). Aeolian dust in Central Asia: Spatial distribution and temporal variability. *Atmospheric Environment*, *238*, 117734. https://doi.org/10.1016/j.atmosenv.2020.117734

Zhang, XY, Gong, S., Shen, Z., Mei, F., Xi, X., Liu, L., et al. (2003). Characterization of soil dust aerosol in China and its transport and distribution during 2001 ACE-Asia: 1. Network observations. *Journal of Geophysical Research: Atmospheres*, *108*(D9).

Zhao, P., Feng, Y., Zhu, T., & Wu, J. (2006). Characterizations of resuspended dust in six cities of North China. *Atmospheric Environment*, *40*(30), 5807–5814. https://doi.org/10.1016/j.atmosenv.2006.05.026

Zhu, C., Tian, H., & Hao, J. (2020). Global anthropogenic atmospheric emission inventory of twelve typical hazardous trace elements, 1995–2012. *Atmospheric Environment*, *220*, 117061. https://doi.org/10.1016/j.atmosenv.2019.117061